AN INVESTIGATION

OF

THE DYNAMICS OF ABRASIVE WATERJET FORMATION

by

MD. EKRAMUL HASAN KHAN

Thesis submitted to the Faculty of the Graduate School of the New Jersey Institute of Technology in partial fulfillment of the requirements for the degree of Master of Science in Mechanical Engineering

1989 90

APPROVAL SHEET

Title of Thesis: An Investigation of the Dynamics of Abrasive Waterjet Formation

Name of Candidate: Md. Ekramul Hasan Khan
Master of Science in Mechanical Engineering
December, 1989

Thesis and Abstract Approved:

_____ _____
Dr. E. S. Geskin Date
Associate Professor
Mechanical Engineering Dept.

_____ _____

_____ _____

VITA

Name: Md. Ekramul Hasan Khan

Address: 351, Broad St., Apt. 1708, Newark, NJ 07104

Degree to be conferred and date: M.S.M.E., December, 1989

Collegiate institutions attended	Dates	Degree	Date of Degree
B.U.E.T	1979-1983	B.S.M.E.	July 1983
N.J.I.T	1988-1989	M.S.M.E.	Dec. 1989

Positions held: Research Assistant
Department of Mechanical Engineering
N.J.I.T, May 1988- Present

Lecturer
Department of Mechanical Engineering
B.U.E.T, Janu. 1984- Dec. 1987.

ABSTRACT

Title of Thesis: An Investigation of the Dynamics of Abrasive Waterjet Formation

Md. Ekramul Hasan Khan, M.S.M.E., 1989 90

Thesis directed by: Dr. E. S. Geskin

The aim of this research was to investigate the jet formation and the jet behavior, as characterized by the velocity field, the force exerted by the jet on a work-piece and the jet geometry. The velocity and force distributions were measured using a laser transit anemometer (LTA) and a piezoelectric force transducer (PFT) respectively for constant water pressure (334.6 MPa) supply. The jet structure and its instantaneous behavior were visualized by the use of high speed filming. LTA and PFT measuring techniques were established and verified. The measurements were performed under different operating conditions. It was found that at a constant pressure,

1. The sapphire nozzle diameter is a principal process variable.
2. The addition of abrasives substantially decreases the water velocity.
3. The force distribution has a peak about 8-20mm from the nozzle tip.
4. The flow discontinuity causes particle accumulation.
5. Ring vortices are present at the boundary of the waterjet but for abrasive waterjet the vortices break away.
6. Increasing the carbide diameter, or abrasive flow, or decreasing the abrasize size causes an increase of overall jet diameter.

ACKNOWLEDGEMENT

I would like to take this oppurtunity to express my deepest gratitude to Dr. Ernest S. Geskin, Associate Professor of Mechanical Engineering at New Jersey Institute of Technology for his valuable guidance throughout the course of this work. It was an honor to work under the guidance of such an esteemed researcher.

TABLE OF CONTENTS

LIST OF TABLES

LIST OF FIGURES

NOMENCLATURE

Symbols	Meaning
A	area of sapphire nozzle
d	sapphire nozzle diameter
d'	jet core diameter
D	carbide nozzle diameter
f	water force for sapphire nozzle
F	water force for sapphire carbide nozzle
F'	abrasive water force
P	supply water pressure
r	radial distance from jet axis
u	center line velocity of water for sapphire nozzle
U	ideal velocity from Bernoullis equation
v	axial velocity component while distribution is made across jet
V	center line velocity of water for sap-carb nozzle
W	center line velocity of abrasive particles
x	stand off distance from sapphire nozzle
X	stand off distance from carbide nozzle
ρ	water density

Abbreviations

AWJ	abrasive waterjet

Carb	carbide nozzle
LTA	laser transit anemometer
mv	milivolt
ns	nano second
Noz	nozzle
Noz 7-43W	nozzle consists of 0.007in. sapphire and 0.043in carbide tubes and flow media is water
Noz 7-43A	nozzle consists of 0.007in. sapphire and 0.043in carbide tubes and flow media is abrasive water
oscl	oscilloscope reading
PFT	piezoelectric force transducer
Sap	sapphire nozzle
Sap 7	sapphire nozzle of diameter 0.007 in.
um	micro meter
volt	voltmeter reading
WJ	waterjet

Chapter I

INTRODUCTION

1.1 General

During the past few years, high speed waterjets (WJ) and abrasive waterjets (AWJ) have found extensive applications in industrial cleaning, cutting and drilling. A number of publications citations have reported tests of the jet performance under different conditions, the but fluid dynamic characteristics of the jet, its structure and the determination of its corrosive properties have not been extensively studied.

A necessary step in the energy analysis of abrasive waterjet machining is the development of reliable techniques for the measurement of the jet characteristics, such as the forces developed in the impingement zone, the velocities of the water and the abrasive particles and the particle distribution. The high speed filming of WJs and AWJs is also a new technique to visualize the jet structure. The development of such techniques as well as the preliminary analysis of the data acquired in the course of the application of these techniques are investigated in this thesis.

1.2 Motivation Behind the Present Investigation

In the past, most, experimental studies relied on the results of AWJ applications in cutting, cleaning and drilling. Some research work on the cavijet and other special jets, different because of different shape of the

nozzles and their application in industry were also carried out. However, very little research was concerned with measuring the velocities and the forces generated during the interaction between a high-speed two-phase jet and a solid.

The present research was conducted to investigate the dynamics of WJs and AWJs which are characterized by the velocity distribution along and across the jet and the forces developed with jet-workpiece interaction. A laser transit anemometer and a piezoelectric force transducer were used for velocity and force measurements respectively. High speed filming of WJs and AWJs were also investigated to add to the present knowledge of jet structure and behavior.

1.3 Features of the present work

The work presented in this thesis has been divided into the following parts:

a) the measurement of axial velocities of WJs and AWJs using LTA

b) the measurement of the velocity distribution across the jet at different stand-off distances for WJs and AWJs by using LTA

c) the measurement of the forces caused by WJs and AWJs at different stand-off distances using a piezoelectric force transducer

d) the investigation of the jet structure of WJs and AWJs using high speed filming.

Chapter II

LITERATURE SURVEY

2.1 General

Waterjet cutting (WJC)- also known as water cutting, and hydrodynamic machining- involves the removal of material by the cutting action of high-velocity, water or water with abrasive additives. Most of the researches has been carried out in regards to its application in industry. Unfortunately there are only a few published papers citations which attempt to establish the dynamics of the waterjet and the abrasive waterjets.

2.2 Velocity Measurement of the WJ and AWJ

The characteristics of water flow in air were investigated by Yanaida and Ohashi [42]. The authors gave a theoretical analysis of the breakup characteristics of high-speed waterjets in air and verified their results by the electric method and the laser velocimeter. They showed that the statistical variation of the break up length is reasonably described as Gaussian distribution. From their axial velocity distributions, it was found that velocity is constant in the continuous flow region, velocity diminishes slightly in the droplet flow region and the velocity drops abruptly in the diffused flow region. They were unable to measure the axial velocity in the diffused flow region because of jet instability. The results in the breakup region of the jet give agreement between analytical and experimental results.

Hishida, Nakano and Maeda experimentally investigated the turbulent structure of a liquid-solid two-phase jet to examine turbulence models of the phases [18]. A modified LVD with particle size discrimination permitted the detailed measurements of velocity for each phase. The authors observed that the liquid velocity increases in two-phase flow since the slip velocity between the solid and liquid phases becomes larger in the down stream direction. The ratio of velocity fluctuation and turbulent Reynolds shear stress to local velocity difference between the centerline and the outer flow region decreases due to the existance of particles.

Swanson et al. determined experimentally the abrasive particle velocity [36]. Here conventional garnet sand was mixed with magnetic particles of comparable size. This mixture was injected into a conventional waterjet and the resultant cutting streams directed by a pair of current-carrying coils spaced at a fixed distance apart. Measurement of the time between the signal response from each of the coils yielded a measure of the particle velocity. The authors found that the particles which enter the jet at its periphery tend to stay at the periphery without further penetration. Their work shows that a considerable gain in the effectiveness of abrasive waterjet cutting can be achieved if a more effective means of accelerating the abrasive particles could be developed.

Givler and Mikatarian developed a fluid-particle flow

model [13]. Their primary concern was to calculate solid particle concentration within a flow field to indicate the initiation of a particle plug.

Amano and Neusen [1] carried out theoretical and experimental studies on the characteristics of turbulent axisymmetric jets impinging on a flat plate. They used a hybrid scheme of central and backward finite differencing techniques to solve the Navier-Stokes equations. The turbulence model used in this computation is a two-equation turbulence model which provides a turbulent kinetic energy equation and a turbulent energy dissipation equation, the so called k-e model. Their velocity coefficient of 0.9 and their 5.5 power velocity profile give good agreement with the measured values. The turbulence intensity produced in the nozzle did not affect the total force but only the stagnation pressure.

Edwards et al. [7] developed a mechanism where the droplets separating from the jet boundary in air may be dispersed rapidly from the central core in a manner detrimental to jet velocity based on Magnus-effect.

Davies et al. [6] carried out experiments concerned with the anatomy and impact characteristics of large scale waterjets. These authors used 3 different nozzles. Velocity decay along the jet from nozzle to impact site was determined by measuring the relative displacement of the packets between subsequent frames of a film.

A computer study of the flow pattern, which calculated velocity distributions during the impingement of a plain

jet on a rigid target material were conducted by Janakiram and Syamala Rao [20]. These authors solved the equations of motion for an incompressible, viscous flow in cylindrical coordinates using a finite difference technique. They used different plain jets from 4mm to 12mm in diameter and also cavijets varying from 7.59mm to 11.16mm in diameter in order to study the growth of the area of erosion due to the impingement of the plain jets with varying jet velocities.

2.3 Force Measurement of WJ and AWJ

Ben Wu, Summers and Tzeng [40] studied the fluctuating dynamic force exerted by a waterjet during impact- in the time and the frequency domains. They found that the frequency of the pulsation does not depend on magnitude of the impact force, and that an optimum standoff distance assuring the maximum impact force exists for each pumping system. The peak frequency in which the energy of the jet is concentrated must be different from the resonant frequencies in order to reduce the possibility of amplified vibrations.

Li [24] investigated the dynamic interaction between the waterjet and the workpiece. He found that the force is principally determined by the diameter of the sapphire nozzle.

Edwards et al. [7] carried out experiments to assess the progressive loss of the potential cutting effectiveness of impulsive waterjets with increasing standoff distance from nozzle to target, both in air and vacuum. Impulsive

high-speed waterjets produced in, and travelling through atmospheric air lack coherence even at short distances from the nozzle but they exhibit coherence in vacuum, even at relatively large stand off distances, and they offer appreciably greater potential for jet cutting.

Davies et al. [6] used a piezoelectric pressure transducer flush mounted in the target plate to measure impact forces.. The results are interpreted in terms of the excavation effectiveness of the jets and related to small scale experimental work on pulse jets. They found that tapered nozzles produce the most coherent jets over the standoff distance range in question. The impact characteristics for this nozzle design were found to be significantly higher than the other designs tested.

Yanaida and Ohashi developed a mathematical expression for the axial dynamic pressure of waterjets in air. They found that the axial jet momentum flux remained essentially constant at the various distances downstream of the nozzle.

A jet developed through the entrainment of solid particles in the water becomes the abrasive waterjet. A waterjet exiting from a sapphire nozzle guides the particles into a carbide nozzle where mixing takes place and the water-particle mixture is formed. In the carbide nozzle the particles are accelerated, that is the kinetic energy of the particles is increased, and a two-phase stream, assuring high cutting capability, is developed [16,17, 38].

Additional research work related to WJ and AWJ applications in industry is discussed in other publications [9,19,28,33].

2.4 High Speed Filming of WJ and AWJ

Szyczak et al. [37] developed special instrumentation for the visualization of high speed, submerged waterjets. These authors obtained short (1us) exposures of the jet using plane illumination. Their results showed the jet consists of the regions of cavity generation, growth and collapse. The effect of increased jet speed on cavitation was also presented.

Zauner [43] examined a laminar flow, circular, glycerol jet emerging from a plane wall. The flow field was visualized by means of very small bubbles suspended in the fluid. It was found that significant viscosity effects existed in the outer flow. These results confirmed the assymptotic theory of Schneider [30,31] for sufficiently large Reynolds numbers. At larger Reynolds numbers, a viscous toroidal eddy was observed.

Baker and Selberg [2] designed 5 different nozzles to produce a coherent jet structure for large stand-off distances. Photographs of the jet were taken utilizing parallel light illumination similar to the method used by Leach and Walker [23]. Jets which display solid coherent cores with minimal stripping action at large standoff distances possess high cutting capability. On the other hand, jets which appear to be breaking up in the

photographs has a limited cutting capability at that distance from the nozzle.

Although a substantial part of data concerning the behavior of WJs and AWJs has been acquired, the available information is not sufficient to predict the optimal design of the nozzle and the optimal cutting strategy. It is still necessary to determine a comprehensive set of data characterizing the kinetics and the geometry of the flow, in order to obtain the information necessary for process design and control. The development of such a system for the acquisition of such information is the objective of this study.

Chapter III

THEORY

3.1 General

Abrasive waterjet cutting is the process in which abrasive particles are accelerated by a small diameter orifice to a high velocity waterjet and directed towards the material to be cut. The general structure of a turbulent free jet is well known but that of turbulent waterjets and turbulent abrasive waterjets in air have never been determined. The jet consists of (i) an initial region with constant axial dynamic pressure; (ii) a main region with constant axial velocity and (iii) a final region. The part of the jet in which there are potential core region is termed the continuous flow region. These regions are illustrated in Fig. 3.1. These initial and continuous flow regions are the basic domains which characteristize high speed, abrasive waterjets in air.

Models of turbulent two-phase flows are classified into two types. One is based on the continuum approximation [5,8,27] and the other on the stochastic approach [15,29,35]. In the stochastic approach, the equations of the particle motion are solved, providing the interaction between the particles and the continuous phase, and taking into account the influence of the turbulent scale on the particle motion. It requires substantial calculation time to investigate whole region of flow field. Conversely, the continum approximation is useful to calculate both phases

with less computing time.

However, information acquired for high Reynolds number (Re) flows in various experiments,the development of various experimental techniques, become principal avenues for the advancement of knowledge in this field.

The author has experimentally investigated the water and particle motion using Laser transit anemometer (LTA), and the force fields in the impingement zone using a piezoelectric force transducer, and the jet structure using high speed filming.

3.2 Principle of Laser Transit Anemometry

A laser transit anemometer (LTA) provides a method for obtaining flow field information [22,25,32]. Particles entrained in the flow provide scattering centers for the incident light. There are two common techniques for optically coding the measurement region. The laser doppler anemometer (LDA) employs a sinousidally varying fringe pattern. Knowledge of the fringe spacing and the detected frequency of particles traversing the measurement region permits the determination of the velocity component normal to the fringes. Another technique for encoding the measurement region uses closely spaced spots, where the flow velocity component parallel to the axis connecting the spots is obtained from the time-of-flight (TOF) of the particles traversing the two spots. The distance between the two foci is 300-600um which is far greater than the distance between the interference fringes, which are of the

order 1um (Fig. 3.2).

The signal obtained from a TOF system consists of two noisy Gaussian- shaped pulses separated by the transit time of a particle traversing the two light spots in the measurement region. An estimate of the peak-to-peak time of flight and knowledge of the spot spacing then yields the particle velocity component along the axis of the two spots. A good method of estimating the time of flight for noisy pulses can be obtained by transforming the unipolar pulse into a bipolar pulse. The zero crossings of the bipolar pulses yield the estimated time of flight. The transformation from a unipolar to a bipolar pulse ideally should not introduce additional noise to the signal. Unfortunately, most particles do not travel directly from one focus to the other focus. There are five possible cases for the motion of the particles as shown in Fig. A.1 and how to get correct signal is discussed in Appendix A. For homogeneous turbulence, if the distance between the two foci, L, is small enough the turbulence parameters within a distance 2L can be considered as constant. The average distance between particles is assumed to be far greater than L. The direction of flow is always from one focus towards the other focus.

3.3 Principle of the Piezoelectric Force Transducer

Piezoelectric force transducer can be used to measure the momentum distribution along the axis of the jet. The previous studies using piezoelectric force transducers

[3,4,10,14,21,26,34] show that it is ideally suited to the measurement of high frequency dynamic processes and it can be used for the investigation of high pressure jets.

Piezoelectricity is defined as electric polarization produced upon the application of mechanical strain or deformation to piezoelectric materials. The polarization is proportional to the strain and changes sign with it. This is generally referred to as the direct piezoelectric effect. The application of electric an field (voltage or charge) to the material exhibiting stress, or strain, is defined as the reciprocal, or converse, piezoelectric effect. Piezoelectric phenomenon was first observed by the Curie, Pierre and Jacques [4] in 1880 when they placed a weight on the surface of a crystal and found that a charge appeared on the surface with a magnitude proportional to the weight.

The inverse piezoelectric effect, discovered in 1881 by Lippmann and verified by Curie, is when an electric field is applied to a crystal stress, and strain, in this crystal, result.

The direction of the current generated in a crystal is determined by "one wayness" in the crystal internal structure. This means that the crystal has a structure bias which can determine whether a given region on the structure should follow a positive, or negative, charge under compression load. In the inverse effect, the same "one-wayness" determines the sign of the deformation when an

electric field is applied to the crystal [3]. Considering the symmetry of crystal, there are 32 possible changes among which 20 create "one wayness". The equations related to piezoelectric effects are discussed in Appendix B.

The piezoelectricity of a crystal is determined by its longitudinal, transverse, and shear effects. These three effects are distinguished according to the position of the quartz crystal axes in relation to the force sustained .

With the longitudinal effect, the negative lattice points in the crystal lattice are displaced by the force imposed towards the positive lattice points such that the equilibrium is disturbed. Measurable charge differences result on the surfaces of the crystal plates. The resulting charge depends solely on the applied force. The simplified longitudinal effect crystal is shown in Fig.3.3 a.

When the force, F_Z is applied in the direction the neutral crystal axes Z, an electric charge is set up on the surfaces of the axes perpendicular to it. This is known as the transverse effect (Fig.3.3b). The magnitude of the charge depends on the geometry of the crystal.

When shear stress is applied to the crystal, the surface of crystal will produce a current. This phenomenon is called the shear effect (Fig.3.3c). The shear effect depends on the geometry and size of the crystal element, and the charge distribution. Due to these effects, current is generated, transmitted to an amplifier to convert into voltage which can be detected by a recording system.

3.4 Flow Visualization

High speed filming enables us to visualize the instantaneous behaviour of jets. By changing flow parameters, a high speed camera together with laser back light illumination can give qualitative information about jet structures.

Chapter IV

EXPERIMENTAL SETUP AND TEST PROCEDURE

General

The present study is primarily concerned with the experimental investigation of the velocity field, force field and the structure of waterjets and abrasive waterjets. The investigation was divided into three parts. The first experiment involved the LTA measurements of water and abrasive particle velocities along and across the jet.

The second experiment consisted of an investigation of forces developed in the jet- workpiece interface using the piezoelectric force transducer.

The third experiment involved the visual observation of WJs and AWJs by high speed filming.

The tests were carried out in Waterjet Machining Laboratory of the Mechanical Engineering Department of NJIT.

The waterjet cell was manufactured by Ingersoll Rand. It has a 5 axis robotic manipulator controlled with an Allen Bradley 200 robot controller. It consists of a water preparation unit, a nozzle assembly, an abrasive feeder, a work place with a traversing mechanism (CNC or robot controller) and a catcher (Fig. 4.1). The jet formation is shown in Fig. 4.2.

4.2 Waterjet Machine

The Ingersoll-Rand waterjet system provides three-

dimensional cutting with cutting speeds up to 2400 in/min with positioning accuracy 0.005 in. The work cell components include

-a gantry which is driven with a precision rack and pinion with a dual sided drive accomplished through a large diameter drive shaft to avoid the problem of a "walking gantry"

-stainless steel Thompson rods to enable operation in the most adverse conditions

-hardened and ground ball screws for Y and Z axis movement

-the Allen Bradley 8200 robot controller which provides the following feature:

-programable acceleration/decelleration ramps

-teach pendant programming

-feedback failure detection

-bubble memory

-on line edit capability.

4.3 Water Preparation Unit

The main function of this unit is to continuously feed pure water and to pressurize the water at the required high pressures. The major components of this unit are a booster pump, a filter, a water softener, a prime mover, an intensifer, an accumulator, and control and safety instruments.

4.3.1 Booster Pump

This pumps the water into the low pressure water circuit (1.25 MPa) in order to ensure continuous flow into

the high pressure cylinder, where it is charged into the system. Low pressure filters (1-10 microns) and the softener are used to soften the water and to remove the iron and calcium dissolved solids.

4.3.2 Intensifier

A hydraulic driven 40 hp oil intensifier is an essential part of the system. It develops pressure up to 345 MPa in the water from booster pump. There are two separate circuits for oil and water. The oil circuit is a closed circuit and the water circuit is an open one. The oil pressure of about 20 MPa developed by the rotary pump is used to drive the intensifier. The intensifier is a double-acting reciprocating type pump, of 152.4 mm diameter.

4.3.3 Control and Safety Instruments

The high pressure water from both sides of the intensifier is discharged to an accumulator where the pressure stabilizes. Since the water at 345 MPa is 12 percent compressed, the water is not discharged uniformly from the intensifier to all piston positions. Thus the accumulator provides the uniform discharge pressure and flow. A rupture disk is provided as a safety device for the intensifier. For recording oil and water pressure, two pressure gauges are mounted in the oil and water lines respectively.

4.3.4 High Pressure Water Distribution System

The high pressure water output of the accumulator, is conveyed to the work station through a series of pipes,

swivels, flexible joints and fittings. Up to pressure of 20 ksi, hose can be used to eliminate the need for swivels, which greatly simplifies the plumbing. The line pressure drop can be readily calculated on the basis of the number of joints, elbows and the total pipe length.

4.4 Work Station

This is the place where the actual experiment is performed. It consists of the following major components:

-a nozzle assembly

-an abrasive feeder

-a work place with traversing mechanism and

-a catcher

4.4.1 Nozzle Assembly

The pressure head of water is converted into kinetic energy in the nozzle assembly. There are two nozzles housed in the main body. A separate port for the abrasive entrance is provided (Fig. 4.2). The high pressure water supplied from the water distribution line passes through sapphire nozzle and accelerates to a velocity of 600-800 m/sec (Fig. 4.3). In the case of AWJs, abrasive enters from the side port, after the sapphire nozzle. Water from the sapphire nozzle and abrasive are mixed in a nozzle made from tungsten carbide (Fig. 4.4). Here abrasive particles are accelerated and the final energy transformation takes place. The performance of sapphire and carbide nozzles depends on the diameter, length, angle of convergence and weight. Also the entry angle of the abrasive, the diameter

of port, the vertical and horizontal distances between abrasive inlet and the sapphire nozzle are typical variables which affect the nozzle design. In this experiment, Ingersoll-Rand made 3 different sizes of sapphire (0.1778mm, 0.2540mm, 0.3048 mm) and three different sizes of carbide (0.762mm, 1.0922mm, 1.6002 mm) nozzles. Schematics of typical carbide and sapphire nozzles are shown in Figs. 4.3-4.4.

4.4.2 Abrasive Feeder

This unit continuously delivers abrasive into the nozzle assembly at a controlled rate. A feed hopper stores 10-180 kg of abrasive and an electromagnetic vibratory tray regulates the flow of abrasive from the hopper. The flow is regulated by changing the applied voltage which in turn changes the frequency of vibration. The suction created in the nozzle assembly draws abrasive from the vibratory tray. For different sizes of abrasive, the abrasive flow is then calibrated. For the entire experiment, abrasive 50 HP with flow rate 76 g/min is used.

4.4.3 Robots and CNC Controlled X-Y Positioning Table

There is a computer to load NC program to control water and abrasive flow as well as robot movement. CNS machine codes are used to write the program.

4.4.4 Entrapment, Separation and Drainage

There is an open tank type catcher used to store ejecting high energy jet which contains particles of used abrasive and cut materials. Vacuum tanks are used

intermittently to collect the water and the particulate slurry and subsequently to dispose of it. Noise reduction can be achieved by covering the cutting cell with a sound proof material such as stryofoam.

4.5 Instrumentation and Apparatus

The instruments used in this experiment are described below in a sequential order.

4.5.1 Laser Transit Anemometer (LTA)

a) Optics

A Dantec LTA (Fig. 4.5) was used to conduct the experiment. The He-Ne laser is used as the light source. The two polarizers P1 and P2 make it possible to rotate the internal parts of the system which is the beam plane, and so the direction of the measurement, can also be rotated. The beam splitter BS1 creates two beams either of the same, or of different, colors. Both beams are focused by the lens system to form a measuring volume as indicated in Fig. 4.6. The distance between the two focus points is 449 um. The image of the two points is received by the same lens system, and transmitted, via the mirrors M1 and M2, to the beam splitter BS2 which combines the two images. The beamsplitter BS2 is rotated together with BS1 to maintain alignment. The signal is analyzed by one photo multiplier (PM) tube.

b) Mechanics

The built-in traversing mechanism is compatible with other Dantec traversing mechanisms. The calibration factor

for the optical encoder is 150 pulses per degree.

c) Alignment

In operation only, bench alignment and pinhole adjustment are performed.

i) Bench Alignment

Vertical and horizontal bench position are adjusted to obtain transmitted beams of uniform intensity over the exit aperture.

ii) Pinhole Alignment

A pinhole with a black, non-diffuse surface, which is positioned in measuring volume, is adjusted.

d) Signal Processing Counter

The 55L90A counter was used as a signal processor for the LTA. Its fuction is to measure the time between two successive events. The calibration factor is selected from the 55L90A instruction manual, depending on the jet velocity. The thumb wheel switch, introduced on the front panel, functions as the transit time range limit control.

4.5.2 Piezoelectric Force Transducer

a) Transducer

Two identical, Kistler, three-component force measurement, platforms 9257A are used in this study (Fig. 4.7). Each multi-component transducer is assembled from stacked quartz disks, loaded mechanically in series with electrode interlayers. The force to be measured acts on the work-piece so that each quartz disk produces the same amount of charge in the same direction at the same time.

b) Work-piece

A steel plate measuring 356 X 102 X 19 mm is shown in Fig. 4.8. It contains 20 holes each of diameter 0.953 mm. This plate is attached to the insulation wood and transducers by means of screws. The bottom surface of the work-piece is fine machined to prevent possible vibration of the work-piece and the insulation wood.

c) Charge Amplifier

A Kistler three-component charge amplifier, model #5007, is used as an electrometer to enable the charge alteration at the quartz transducers to be measured. The measuring range scale and sensitivity switch of each component of the charge amplifier are adjusted to suit the experiment being conducted.

4.5.3 Read-out Devices

To measure the voltage output and signal for the LTA and the piezoelectric transducer two different read-out devices were used.

a) Multimeter

A Fluke Model # 8101A digital multimeter was connected in parallel to the charge amplifier.

b) Oscilloscope

A Nicolct 2-channel oscilloscope was used for both force and velocity measurement. It can store the voltage signal as a function of time. Time per point, AC, DC voltage and DC voltage offset were then adjusted to the measurement being made.

4.5.4 Optical Microscope

A portable, battery driven optical toolmakers microscope from Mitutoyo, was used to measure the piercing diameter in order to analyze the jet core diameter. The measured values are displayed on an 8 digit LCD. Different vertical and horizontal magnifications can be made. The range is 0-50mm and positioning accuracy is 0-.001 mm.

4.5.5 High Speed Camera

A Photec 16 mm rotating prism camera with a speed of 10,000 frames/sec is used with a laser beam (copper vapor) to film the jet. The exposure time is 30 nano seconds. A ground mirror was used for illumination.

4.5.6 Projector

An analytic 16mm sound projector, model# SC 210 from Hokushin Precision Co. Ltd., was used to study the high speed film. There are two auto speed controls for the frames of movie. Hand control is there to run frame by frame and to select frames for taking pictures.

4.6 Measurement Procedure

In this experiment, velocity and force were measured. High speed filming was also performed to study the jet structure. Piercing of aluminum plate was also performed to obtain information about jet core.

4.6.1 Alignment of the Nozzle Body

Before starting the experiment, alignment of the sapphire and carbide nozzles was checked as follows:

a) the new nozzles were first checked for manufacturing defects.

b) the nozzle body was removed from the robot and then cleaned

c) a new sapphire was placed in the nozzle body

d) by turning on the intensifier at low pressure, 25-35 MPa, and using the booster pump the jet stream was examined by turning the nozzle switch on. The coherence of the jet was observed visually and controlled by set screws, which determined the position of the carbide nozzle axis.

e) intensifier was set to AUTO and run at high pressure to observe the alignment by turning on nozzle switch on. If the jet coherence was not found acceptable then steps (a) to (d) were repeated

f) for the same nozzle combination and abrasive type, the experiments were conducted under the same alignment conditions to obtain consistant results.

4.6.2 Velocity Measurement

Water and abrasive particle velocities were measured by the use of the Laser Transit Anemometer. A new technique was developed to conduct the experiment. Both axial and transverse jet velocities were measured. Three different sapphire nozzles and three different carbide nozzles together with a 50 HP garnet abrasive (flow 76 g/min) were used.

a) Axial water velocity measurement for sapphire nozzles

Sapphire nozzles of diameters 0.1778, 0.2540 and 0.3048 mm were used for 12 stand off distances, 0.127, 3.81, 6.35, 12.7, 25.4, 38.1, 50.8, 63.5, 76.2, 88.9, 101.6 and 114.3 mm respectively (Table 4.1).

(i) First a defect-free sapphire nozzle, 0.1778 mm in diameter was attached to the nozzle body and a concentrated jet at low pressure was checked.

(ii) The foci of the two concentrated laser beam were focused on the low pressure jet, and a 10X magnifying glass was maintained behind the jet in order to observe the location of the laser light and the jet. Using the teach pendant, the jet is aligned right at the center with the two parallel laser beams (Fig. 4.9).

(iii) the LTA was then connected with the signal processing counter, the main computer and oscilloscope (Fig. 3.2).

(iv) The counter was set to operating mode. The mode selector was maintained in the transit position. Computer accuracy was set off. The digital high pass was turned on. The maximum time was first selected high enough to allow particles at the lowest expected velocity to be accepted. By selecting the maximum time as short as possible, the counter can better reject most of the false events caused by different particles during starting and stopping. The low-pass frequency was reduced until a pulse height reduction and pulse broadening was observed. The high-pass was increased until an overshoot of 30-60% was obtained. This overshoot makes the actual start/stop time less sensitive to pulse height variations and noise.

For low pass, 16 mHz, and for high pass 1 mHz, give excellent results. The scale factor selected from the manual is equal to 8396. The ensemble width was kept at 1

and thumb wheel position at 1 give the desired velocity range. Threshold window, amplifier gain and voltage reduction buttons were all released. Voltage gain was controlled in such a way as to subsidize noise level and to obtain a good signal.

(v) The counter output was connected with the oscilloscope to observe the response of the voltage signals. Channel A was made active. DC offset voltage was reset to zero. Time per point was selected as 500 ns and channel voltage was set to 300 mv. The AC signal was stored by selecting the normal operating mode.

(vi) After setting the LTA counter and oscilloscope, a NC program was loaded into the WJ machine for water flow at a pressure of 334.6 MPa for 2000 sec without robot movement.

(vii) While the program is starting, the counter and the oscilloscope are receiving signals. These signals are recorded instantly.

(viii) When two peaks are above 150 mv and all other peaks are below +/- 50 mv, then oscilloscope is receiving a satisfactory signal. This signal is stored and an instantaneous picture is taken using a polaroid camera. At this moment about 200 data points are recorded from the counter. Later these data points are analyzed using statistically to give the average centerline velocity at that station.

(ix) Then using the teach pendant, nozzle was moved to the next stand off distance and the above steps (ii) through (viii), were repeated. The experiments for the other stand

off distance were conducted in a similar manner.

b) Axial Water Velocity Measurement for the Sapphire-Carbide Nozzle

The velocities of the jets formed by 3 sapphire nozzles of diameters 0.1778, 0.2540, 0.3048 mm and 3 carbide nozzles of diameters 0.7620, 1.0922, 1.6002 mm were measured for stand off distances of 0.127, 3.81, 6.35, 12.7, 25.4 and 38.1 mm respectively (Table 4.2). The stand-off is the distance between the plane in question and the carbide nozzle tip. The sapphire-carbide nozzle combinations were arranged in such a way that three sets had common sapphire nozzle but different carbide nozzles and another three sets had a common carbide nozzle but different sapphire nozzles. After fixing the sapphire-carbide nozzle combination to the nozzle body of the WJ machine, alignment was checked as discussed above. Then steps (ii)-(ix) (Art. 4.6.2 (a)) were repeated.

c) Axial Abrasive Velocity Measurement

The experiments at Art. 4.6.2 were repeated for the water/abrasive particle mixture. Abrasive (50 HP) with a flow rate 76 g/min was used. The voltage was very carefully adjusted to maintain the noise level between +/- 50 mv on the oscilloscope.

d) Velocity Distribution Across the Jet

The velocity distribution across the jet was measured for a single combination of sapphire-carbide nozzle (d=0.1778 mm, D=1.6002 mm) with an abrasive particle size

of 50 mesh and an abrasive particle flow rate of 76 g/min. To measure the velocity distribution across jet at a selected stand-off distance, two parallel beams of laser light were first focused at the center of the jet, and then the jet was moved towards the left by a step of 0.1270 mm. At each position, the velocity was measured in the same way as in Art. 4.6.2 (a) . This movement of the jet and the measuring of the velocity were continued until the noise level remains within +/- 50 mv and no random velocity responses were occurring.

For the sapphire nozzle at 0.1270, 6.635, 25.4, 50.8, 76.2, 127, 177.8, 228.6 and 279.4 mm stand off distances (Table 4.3), and for the sapphire-carbide nozzle and water/abrasive flow at stand off distances 0.1270, 25.4, 50.8, 76.2, 127, 177.8, 228.6 mm (from carbide nozzle tip) (Table 4.4) the velocity distribution across jet was measured. The measurement procedure is the same given in Art. 4.6.2 (a)- (c).

4.6.3 Force Measurement

The piezoelectric force transducer was used to measure the water and abrasive particle forces. Two transducers were installed on a flat surface. The work-piece was post-machined flat and fixed on the top surface of the transducers. Between the work-piece and the transducers, a thin wooden plate was placed as insulation, in order to reduce the signal disturbance of the transducers caused by thermal effects. Both work-piece and the wood plate were fixed on the transducer surfaces by screws.

The outputs of the transducers were connected to the charge amplifier where the signal was converted into voltages proportional to the forces acting on the work-piece. The charge amplifier was then connected parallel to the read-out equipment- the multimeter and the oscilloscope. The outputs were used to compare the results.

In order to determine the correlation between force and velocity, both variables are determined under similar experimental conditions (Table 4.1-4.2). During the experiments the nozzle was held vertical and normal to the target plate. Transducer sensitivity was set according to the manufacturer's calibration. In the charge amplifier, the charge was converted to voltage by a range switch. Correct setting of these switches is essential to conduct the experiments. The time constant switch was on "long", representing the high frequency of the jet. After each individual measurement the amplifier was reset. Resetting discharges the voltage in the transducer allowing it to read the correct signals in the following experiments.

This signal was stored in the oscilloscope and the voltage was calculated from the sign change of the signal. The equivalent force was then measured from the amplifier control position.

4.6.4 Jet Core Diameter Measurement

In this experiment, the aluminum plate was drilled to create holes at conditions similar to those used in Art. 4.6.2. An aluminum plate of 455mm X 305mm X 2mm was

installed horizontally on the grate of the WJ machine using a spirit level. The jet was allowed for 10, 20, 30 and 40 seconds respectively to pierce the plate. The experiment was repeated 3 times for each setting. Comparing the hole diameters, it was found that the 30 sec and 40 sec piercing times gave almost the same hole diameter. Because of that the piercing was carried out for 30 sec duration for all of the combinations of nozzle settings. The diameters of the holes were measured using an optical microscope. It was assumed that the hole diameters were equal to the diameters of the jet core at the impinging plane. Thus the measurements of the hole diameters enables determination of the diameters of the jet core at different stand-off distances, and different conditions of jet formation.

4.6.5 High Speed Filming

A Photec high speed camera (10,000 frames/sec), with a 16 mm rotating prism was used for filming 20 different conditions of jet formation (Table 4.5) at the nozzle exit. A copper-vapor laser was used as a light source. The exposure time was 30 nano secods. The laser source and ground mirror were placed in line to illuminate the jet. The camera was placed 710 mm from the jet axis. The laser beam diameter was maintained as 50 mm, of which 6.5 mm was focused on the nozzle and 43.5 mm on the jet. A schematic of the experimental setup is shown in Fig. 4.10.

Chapter V

RESULTS AND DISCUSSION

5.1 General

Velocity and force distributions for waterjets and abrasive waterjets were determined experimentally under different conditions of jet formation. To visualize the instantaneous behaviour of jet and its structure, high speed filming was performed. A qualitative study on jet core was also conducted. All these experimental data have been analyzed to obtain information regarding waterjet and abrasive waterjet dynamics. This chapter also includes some correlations between velocities and forces of the waterjets and the abrasive waterjets. Software, "Statistical Analysis for Engineers" was used to process the raw data of velocity obtained from LTA.

5.2 Experimental Results

Two different kinds of experiments were performed- one with the LTA to determine velocities and one with the piezoelectric force transducer to determine forces. Three different jets- a waterjet from a sapphire nozzle, a waterjet from a sapphire-carbide nozzle and an abrasive waterjet were utilized.

The calibration of the waterjet flow was performed by collecting the water and abrasive particle/water (Tables. 5.1-5.5). Velocity was determined on the basis of sapphire nozzle diameter. Table. 5.1 shows that the increase of the

sapphire nozzle diameter causes a decrease in velocity but an increase in the flow rate. It also shows that increasing the carbide nozzle diameter significantly increases the flow rate (Tables 5.2-5.5).

5.2.1 Velocity Distribution

Velocity measurements along and across the jet were conducted for both waterjets and abrasive waterjets by LTA as described in Art. 4.6.2. About 200 data points were recored for each station. These data were processed by using "statistical Analysis for Engineers" package.

Figs. 5.1-5.9 show the percentage of occurrences of velocities at the axis of the jet at two terminal stand off distances. The mean occurrence range gives the velocity at that station. It was noticed that there are few occurrences of velocities remote from the highest occurrence zone because of noise and deviant signals. These were below 2% and do not affect the determination of the actual velocity at that position. The peaks occur at lower velocity at remote stations than at nearer stations which was due to the velocity decrement. Figs. 5.1-5.3 for sapphire nozzle, Figs. 5.4-5.8 for sapphire-carbide nozzle and water flow and Fig. 5.9 for abrasive flow are presented here. Fig. 5.9 shows 5 cases of the velocity measurements for abrasive flow where noise and deviant signals occured within a 3.5 % level and hence do not affect the results. Similar results are present in other graphs.

Velocities obtained from the percentage occurrence at

each stand off distance are presented in Figs. 5.10-5.15. All these graphs indicate that velocity decreases in the axial direction. The velocity of pure water (Fig. 5.10) substantially depends on the sapphire diameter, but there is no practical correlation between the water velocity and the carbide diameter (Fig. 5.11). At the same time, the velocity of the abrasive flow is affected by both diameters (Figs. 5.14-5.15).

Axial and peripheral velocities of the jet are determined for the maximum available stand off distance for a single sapphire and a sapphire-carbide nozzle combination. Results are plotted in Figs. 5.16-5.18. The velocity decay for the abrasive flow is much faster than for the waterflow. These results confirm the theoretical data given in [42].

Figs. 5.19-5.21 show radial velocity distributions at different stand off distances. It is not possible to measure velocity near the perimeter of the jet at large stand off distances since the velocity received by LTA at perimeter does not conform for a single particle motion and hence the velocity recorded shows random values. These distributions (Figs. 5.19-5.21) are recorded in the region where the LTA confirms single particle motion. From these figures, it is clear that the velocity decrement in the radial direction corresponds to the Gaussian velocity distribution.

Figs. 5.22 - 5.24 show the normalized velocity distributions across the jet at different stand off

distances. These figures demonstrate the domain of of the jet core and are in agreement with Hishida [18].

5.2.2 Piezoelectric Force Measurement

Prior to taking measurements, the calibration of the transducer was verified (Figs. 5.25-5.26). It was noticed that the water and the abrasive-water force remain constant within the range of the test coordinates (X,Y).

Force measurements were recorded in two different parallel connected readout devices. These measurements, for same nozzle combinations, are presented in Figs. 5-27-5.33. It was found that no nozzle combinations caused substantial difference in the two readings which additionally validates the two techniques. The average of these two readings are taken to plot all of the other graphs.

The measured force distributions at various stand off distances are presented in Figs. 5.34-5.39. Fig. 5.34 shows that an increase in the sapphire nozzle diameter causes an increase in force. The force appears to remain constant up to 8 mm, and then there is a sharp increase. In the downstream direction, the force decreases at a slower rate with little fluctuation.

Comparing the carbide and sapphire nozzles (Figs. 5.35-5.37,) it is noticed that the carbide nozzle decreases the force but its effect is much weaker than that of the sapphire nozzle. Addition of abrasive also decreases the force (Figs. 5.38-5.39).

Dimensionless force is defined as the ratio between an

actual force and the force as determined from Bernoullis' equation [7]. The results are shown in Figs. 5.40-5.43 for water flow. They confirm Edwards [7] results. For the variable carbide diameter (Fig. 5.41) it was found that points almost collapse on each other while the opposite nature is found in Figs. 5.42-5.43 where the sapphire diameter variable. This confirms that the sapphire diameter has a substantial effect on the force.

5.2.3 Jet Core

Figs. 5.44-5.49 show how the jet core diameters vary with stand off distance for different nozzle combinations. The core diameter was found to be almost the same for sapphire 10 and 12 (Fig. 5.44). The use of the carbide nozzle and abrasive causes jet diversion. It was noticed that the core diameter just at the carbide tip is less than the carbide nozzle diameter (Figs. 5.45-5.49). From these figures it is also noticed that the core diameter increases sharply within 10 mm after exit and than the curve is almost linear. It is further noticed that the sapphire nozzle has a dominant effect on the jet diameter.

5.2.4 Correlation between Flow Properties

Correlations between central and average velocities of the water in the jet at different stand off distances are presented in Figs. 5.50-5.52. These measurements depend on the material, its physical properties and thickness on which the piercing is performed and also on the piercing

duration time. As mentioned in Art. 4.6.4, 30 seconds time was selected for piercing 2 mm thick aluminum plate. However, these figures demonstrate the qualitative aspects of the average velocity distribution in the axial direction.

Average velocity determined by the use of measured force and jet diameter sharply drops within 0.005 mm from the nozzle exit because of air drag and jet diversion but remains almost same below this level.

In Figs. 5.53-5.60, dimensionless force and velocity are plotted against the stand off distances. From these figures it follows that the rate of force decrease is higher than that of velocity. Force curves show fluctuations whereas velocity curves are almost linear.

The effect of the sapphire area on the velocity and force are demonstrated in Figs. 5.61-5.63. With an increase of sapphire area, the velocity decreases but force increases. It is also noted that the force has a direct, almost linear, relation with sapphire area which concludes with the results of other investigators [12,24].

The correlations between force and velocity are presented in Figs. 5.64-5.68. It is noticed that with increase of velocity, the force increases and the larger diameter of sapphire causes greater forces. This result shows good agreement with Amano's numerical results [1].

5.3 Flow Visualization

High speed filming was used to visualize the

instantaneous behaviour of the jet. Table 4.5 shows 20 different conditions of filming. The entire study is presented in tabular form in Table 5.6. Some still pictures were taken to demonstrate the jet behaviour.

From case A and B, it is found that in the water flow through the sapphire nozzle or a combination of sapphire and carbide nozzles, three distinct zones occur- a core, a mist and a droplet can be identified (Fig. 5.69). The jet acts in a pulsating manner and there is a tendency to form ring vortices at the boundaries near the developing zone of the jet (Fig. 5.70).

From case C, it is observed that the abrasive particle size has a strong effect on the jet structure. Larger particles cause larger cavities inside the jet body but the jet diameter increases with a decrease in abrasive particle size as shown in Fig. 5.71. For abrasive size 50 mesh (HP), particles and particles clusters are distinct (Fig. 5.72). The jet pulsations have an approximate period of 0.001 sec (Fig. 5.72-5.73).

In case D, jet diameter changes significantly with the abrasive flow rate and it is found that the increase in flow causes an increase of jet diameter (Fig. 5.74). At lower flow rates, clusters of particles are distinguishable (Fig. 5.75) but at higher flow rates the abrasive are concentrated like a solid core (Fig. 5.76). Flow discontinuities cause particle accumulation, and as a result, sudden enlargement and contraction inside the jet body are observed (Fig. 5.77-78).

In this experiment, it is not possible to find the particle velocity because the same particles cannot be identified in two successive frames.

5.4 Plate Study

During the LTA and force transducer measurements, polaroid pictures were taken from oscilloscope screen. These demonstrate the velocity and force at that station. For velocity (Figs. 5.79-5.89), it is found the noise level is within +/- 15 mv. Time is calculated from the horizontal displacement and the velocity is determined from the distance between two spots $449X10^{-6}$ m. Measured velocities as shown in the figures are quite similar to those obtained by LTA.

Force is calculated from the sign change of voltages in the pictures. Results presented in Figs. 5.90-5.96 are quite similar to the multimeter and transducer readings.

Chapter VI

CONCLUSIONS

Velocity and force measurements for waterjets and abrasive waterjets by laser transit anemometer and piezoelectric force transducer measurements respectively have been established. A qualititive analysis of the jet structure, the instantaneous behaviour of jet and the core diameter has been performed. The effects of the operating parameters of the jet generating system have been studied. The following conclusions can be drawn from the acquired data:

(1) At constant pressure, the sapphire nozzle diameter is the principal variable determining the jet dynamics.

(2) An increase of the sapphire nozzle diameter causes an increase of the force and a decrease of the velocity. Velocity range 400-780 m/sec and force range 8-32 N are observed for the experimental conditions.

(3) Flow rate increases with the increase of sapphire and carbide diameters.

(4) The velocity decrement across jet is found to be large in the downstream rather than the upstream direction.

(5) Force and velocity are found to be proportional to the sapphire nozzle diameter.

(6) Addition of abrasive decreases the force and the velocity.

(7) There is a jump in the magnitude of force within 5-25 mm (critical distance) into the jet.

(8) After the critical distance from the nozzle exit, the rate of velocity decrease becomes substantial.

(9) The jet core diameter increases rapidly within 5-30 mm. Sapphire 10 and sapphire 12 generate almost same jet core diameter i.e., they have geometrically similar shapes. Jet inside the carbide nozzle does not envelope the whole clearence area and, consequently, the core diameter at the exit is smaller than the carbide nozzle diameter.

(10) The average velocity in the vicinity (1 mm) of the nozzle tip is high but then it drops to 300-450 m/sec and then remains closely constant in downstream direction.This average velocity depends on material properties, the physical dimensions and also the piercing time. However, it demonstrates the qualititive nature of average velocity distribution.

(11) In the axial direction, the rate of force decrease exceeds that of the rate of velocity decrease.

(12) From high speed filming,

(a) The jet is like a pulsating body. It is substantial in the case of the abrasive waterjet. The average period of pulsation is observed to be 0.001 sec from the waterjet exiting from sapphire 10 and sapphire 14.

(b) Ring vortices are present at the boundary of the waterjet but they break away with the main stream for AWJ.

(c) Flow discontinuity causes particle accumulation. As a result, sudden enlargement and contraction inside the jet are observed.

(d) Abrasive particles cause cavities inside the jet and this phenomenon is prominent for larger size particles in the flow.

(e) Increasing the carbide nozzle diameter, or for abrasive flow decreasing the abrasive particle size causes increase of the overall jet diameter.

Finally, the present work acquired the information which will be used to construct an expert system for waterjet machining.

Appendix - A

LASER TRANSIT ANEMOMETRY (LTA) SIGNAL SIMULATION

A.1 There are two independent electronic systems in LTA, each taking one focus as its detector for the first pulses. One of these two systems always secures the incorrect stop pulse, while the other can receive 'correct' and 'incorrect' stop pulses. The relation between the counts and the probability of a particle traveling directly from the first focal point to the second is analyzed statistically for these two systems.

There are five possible cases regarding the travel of particles as shown in Fig. A.1.

(i) A particle travels directly from the first focus A to the second focus B within T. The probability of this event is P_s.

(ii) After a particle passes through focus A, no other particle crosses focus B during time T. The probability of this event is denoted by P_{ao}.

(iii) After a particle passes focus A, another particle crosses focus B during time T. The probability of this event is denoted by P_{ab}.

(iv) After a particle passes focus B, no other particle crosses focus A during time T. This probability is P_{bo}.

(v) After a particle passes focus B, another particle crosses the focus A during T. The probability of this event is P_{ba}.

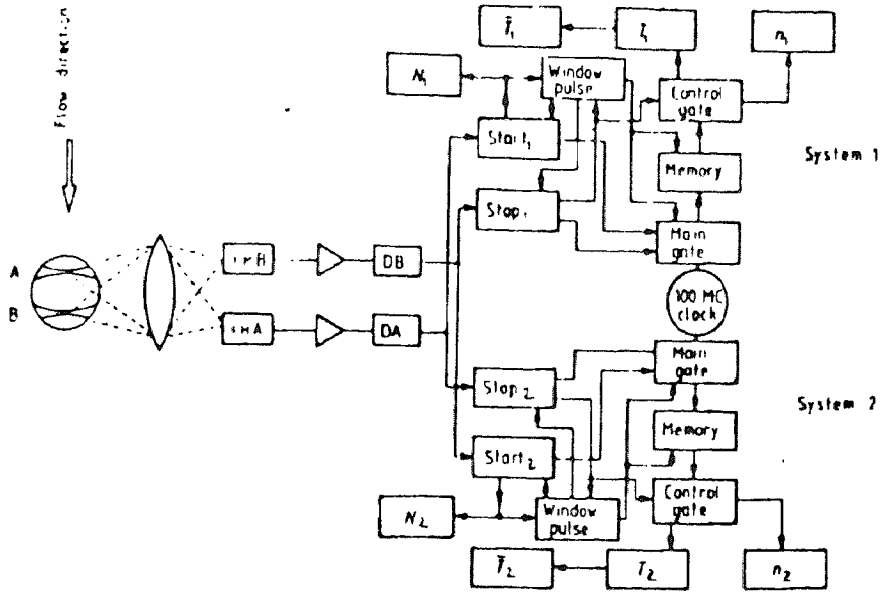

(a)

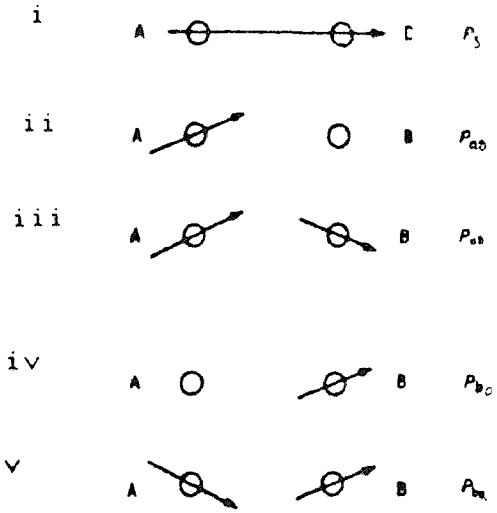

(b)

Fig. A. 1 LTA (a) electronic system (b) the five possible cases relating to the travel of particles

For homogeneous turbulence, if the distance between the two foci is small enough, the turbulence parameter can be considered constant. Then events (iii) and (v), 'start' and 'stop' are independent which gives,

Then $P_{ab} = P_{ba}$ ---------- A.1.1

For system 1, event (i) or event (iii) can both increase the counts of n1.

Hence $P_+ = P_s + P_{ab}$ ---------- A.1.2

For system 2, only event (v) can increase the counts of n2.

Hence $P_- = P_{ba}$ ---------- A.1.3

From the above equations,

$P_s = P_+ - P_-$ ---------- A.1.4

P_s/P_+ is the percentage of 'correct stop' signals in the measurements by system 1. By using eqn. A.1.4, we can measure the probability of a particle traveling directly from the first focal point to the second by making use of the counts. If the particle distribution is random, the time average will be homogeneous for steady flow within the measuring time.

The average of T_2 should be equal to the half width 0.5T. T'_1 is the arithematic average of T_1. The true average value of particle flight time between the two foci t can be determined from,

$$T'_1 = t\ P_s\ /\ P + T\ (P_+ - P_s)/\ 2\ P_+ \qquad \text{A.1.5}$$

For a stable flow we can carefully adjust the width to reach this point.

Appendix - B

EQUATIONS RELATED TO PIEZOELECTRIC EFFECTS

B.1 Cady [3] derived two sets of equations for both direct and converse piezoelectrical effects.

$$P_x = e_{11}x_x + e_{12}y_y + e_{13}z_z + e_{14}y_z + e_{15}z_x + e_{16}x_y$$
$$P_y = e_{21}x_x + e_{22}y_y + e_{23}z_z + e_{24}y_z + e_{25}z_x + e_{26}x_y$$
$$P_z = e_{31}x_x + e_{32}y_y + e_{33}z_z + e_{34}y_z + e_{35}z_x + e_{36}x_y$$

$$P_x = d_{11}X_x + d_{12}Y_y + d_{13}Z_z + d_{14}Y_z + d_{15}Z_x + d_{16}X_y$$
$$P_y = d_{21}X_x + d_{22}Y_y + d_{23}Z_z + d_{24}Y_z + d_{25}Z_x + d_{26}X_y$$
$$P_z = d_{31}X_x + d_{32}Y_y + d_{33}Z_z + d_{34}Y_z + d_{35}Z_x + d_{36}X_y$$

$$X_x = e_{11}E_x + e_{21}E_y + e_{31}E_y$$
$$Y_y = e_{12}E_x + e_{22}E_y + e_{32}E_y$$
$$Z_z = e_{13}E_x + e_{23}E_y + e_{33}E_y$$
$$Y_z = e_{14}E_x + e_{24}E_y + e_{34}E_y$$
$$Z_x = e_{15}E_x + e_{25}E_y + e_{35}E_y$$
$$X_y = e_{16}E_x + e_{26}E_y + e_{36}E_y$$

Where E = electric field strength

X, Y, Z = related stresses

x, y, z = related strains

P = electric polarization

e_{ij} = piezoelectric stress coefficients

d_{ij} = piezoelectric strain coefficients

i, j = notation of different constants.

In these equations, all coefficients are constant and

determined by the kind of a crystal.

The following two values of the piezoelectric coefficients are used in the Kistler Force Transducer at 20^0 C.

$$d_{11} = 2.3 \times 10^{-12} \quad C/N$$

$$d_{14} = 0.67 \times 10^{-12} \quad C/N$$

Table 4.1 Stand off distances and sapphire nozzles used for force and axial velocity measurements

Sapphire d*	7, 10, 12
Stand off dist. x (mm)	0.127, 3.81, 6.35, 12.7, 25.4, 38.1, 50.8, 63.5, 76.2, 88.9, 101.6, 114.3

Table 4.2 Stand off distances and Sap-Carb Nozzles used for the measurements of Force and Axial Velocity of WJ and AWJ

Nozzle Sap-Carb*	7-30, 7-43, 7-63, 10-63, 12-63, 10-30, 12-30
Stand off dist. X (mm)	0.127, 3.81, 6.35, 12.7, 25.4, 38.1

Table 4.3 Stand off distances and sapphire nozzle used for velocity measurement across jet (step across jet is 0.128 mm)

Sapphire d*	7
Stand off dist. x (mm)	0.127, 6.35, 25.4, 50.8, 76.2, 127, 177.8, 228.6, 279.4

Table 4.4 Stand off distances and Sap-Carb nozzle used for water and abrasive velocity measurement across jet (step across jet is 0.128 mm)

Nozzle Sap-Carb*	7-63
Stand off dist. X (mm)	0.127, 25.4, 50.8, 76.2, 127, 177.8, 228.6

* diameter in thousandth inch

Table 4.5 Various Conditions of High Speed Filming

No. of Filming	Abrasive Size HP #	Nozzle Combination Sapphire Carbide		Abrasive Flow Rate g/min
		d (mm)	D (mm)	
1	-	0.127	-	-
2	-	0.178	-	-
3	-	0.254	-	-
4	-	0.356	-	-
5-7	-	0.254	0.762	-
8	-	0.254	2.362	-
9	50	0.254	0.762	540.8
10	50*	0.254	0.762	540.8
11	50	0.254	2.362	540.8
12	80	0.254	0.762	102.5
13-15	80	0.254	0.762	299.3
16-17	80	0.254	0.762	370.0
18	220	0.254	0.762	191.5
19	220	0.254	0.762	318.5
20	220	0.254	2.362	318.5

* a demonstration for cutting steel plate

Table 5.1 Direct Measurement of Velocity and Flow for Sapphire Nozzle

Sapphire d (mm)	Velocity (m/sec)	Flow (g/min)
0.178	480	725
0.254	350	1055
0.305	334	1456

Direct Measurement of Water velocity and Flow for Sapphire-Carbide Nozzle

Table 5.2

Nozzle Sap-Carb	Vel (m/sec)	Flow (g/min)
*7-30W	429	648
7-43W	442	667
7-63W	463	699

Table 5.3

Nozzle Sap-Carb	Vel (m/sec)	Flow (g/min)
7-30W	429	648
10-30W	345	1041
12-30W	319	1391

Direct Measurement of Abrasive Water Mixture Flow

Table 5.4

Nozzle Sap-Carb	7-30A	7-43A	7-63A
Flow (g/min)	725	738	749

Table 5.5

Nozzle Sap-Carb	7-30A	10-30A	12-30A
Flow (g/min)	725	1100	1467

* thousandth inch diameter

Table 5.6 Comparing Parameters used in High Speed Filming

Case	Flow Media		Nozzle Consists of		Abrasive	
	Water	Water + Abrasive	Sapphire tube	Sapphire + Carbide tube	Size	Flow Rate
A	yes	-	variable	-	-	-
B	yes	-	-	variable	-	-
C	-	yes	-	constant	vari-able	cons-tant
D	-	yes	-	constant	cons-tant	vari-able
E	-	yes	constant	variable	cons-tant	cons-tant

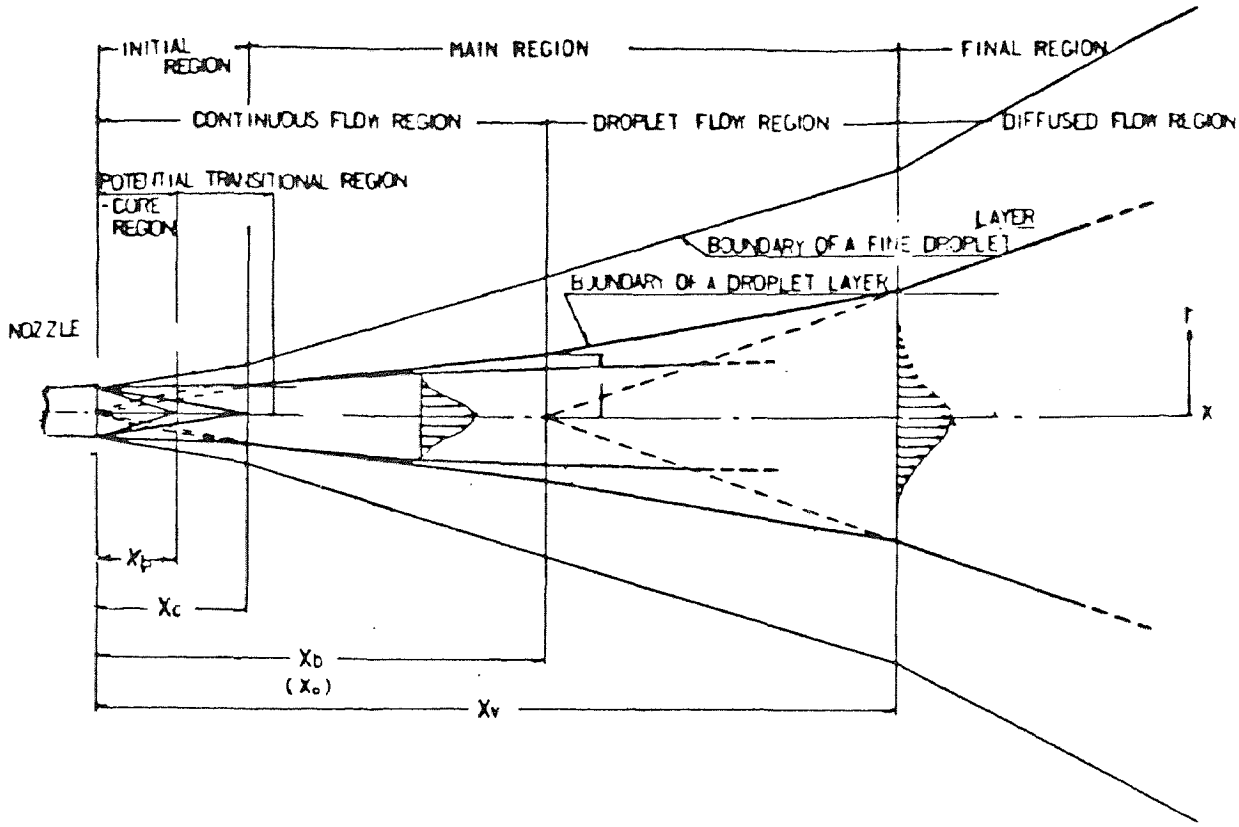

Fig. 3.1 Jet structure

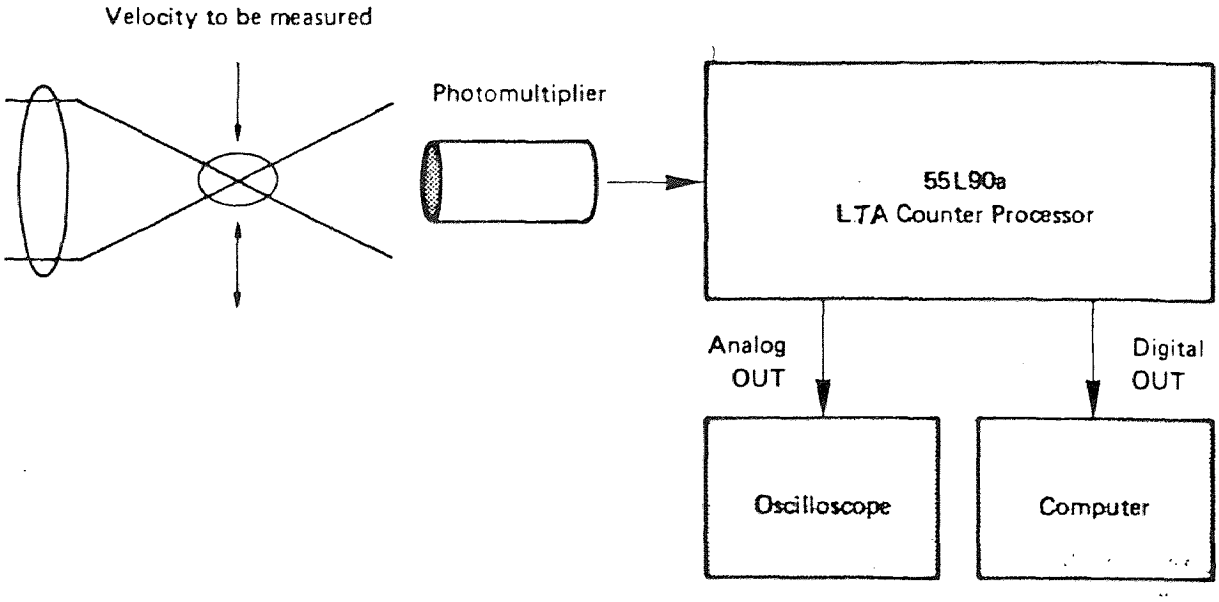

Fig. 3.2 LTA with counter processor

Crystal structure (simplified)
unloaded loaded

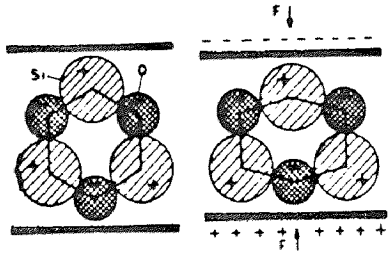

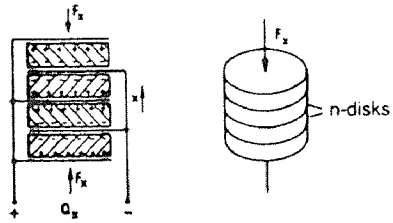

Fig. 3.3a
Principle of the longitudinal piezoelectric effect (top) and schematic assembly of transducer (bottom)

Crystal structure (simplified)
unloaded loaded

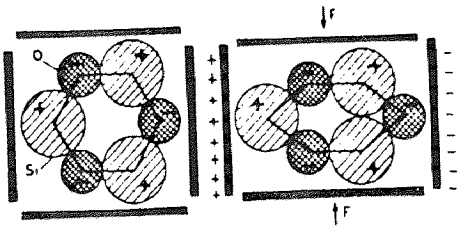

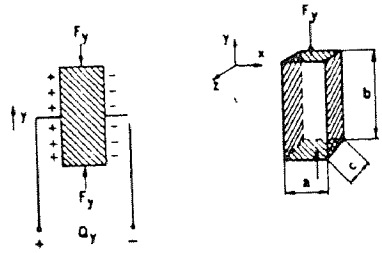

Fig. 3.3b
Principle of the transverse piezoelectric effect (top) and its practical utilization (bottom)

Crystal structure (simplified)
unloaded loaded

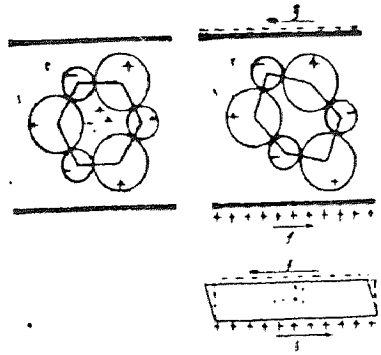

Fig. 3.3c
Principle of the shear effect (top) and mode of force application (bottom)

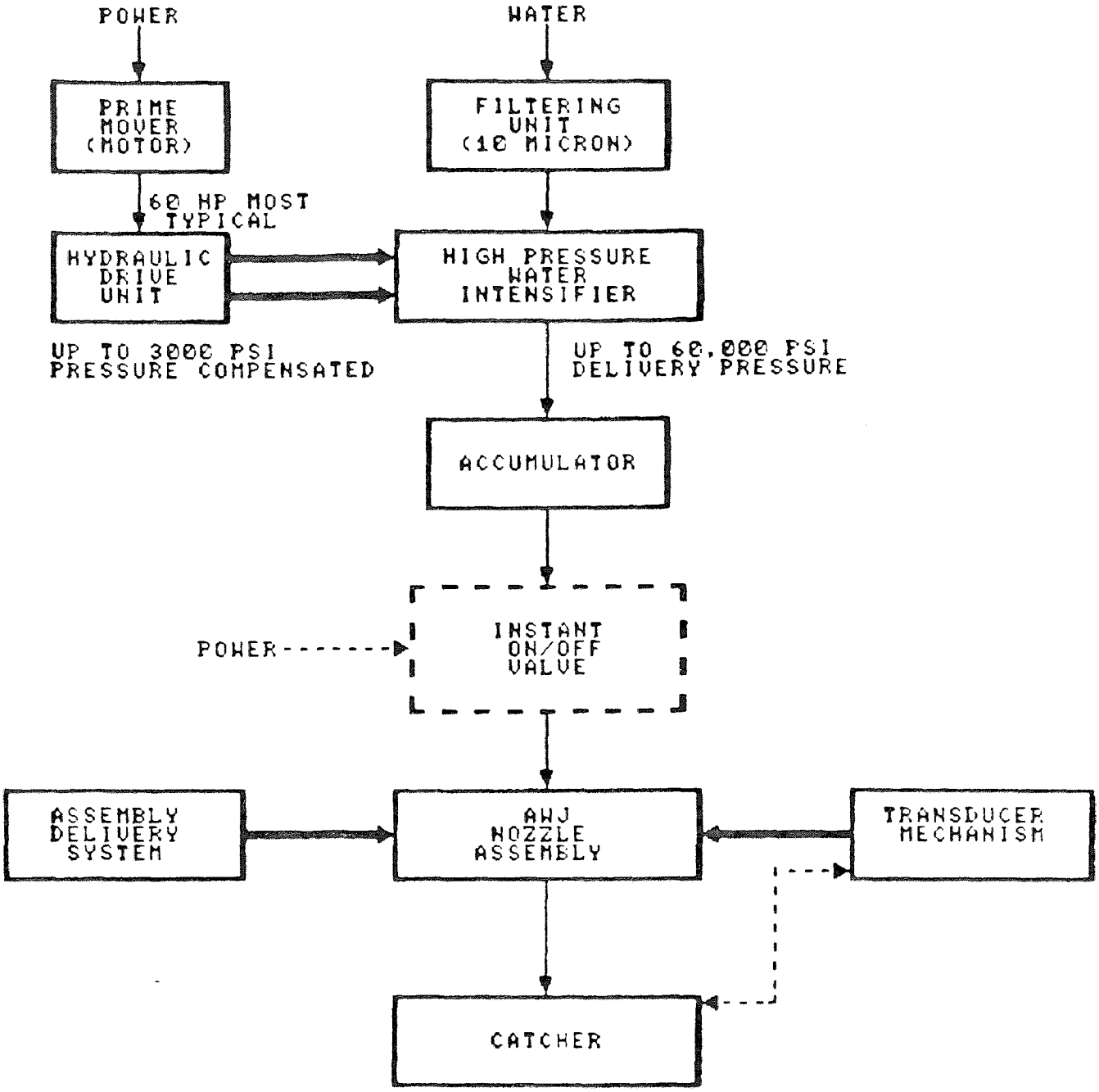

Fig. 4.1 Operation of WJ machine in block diagram

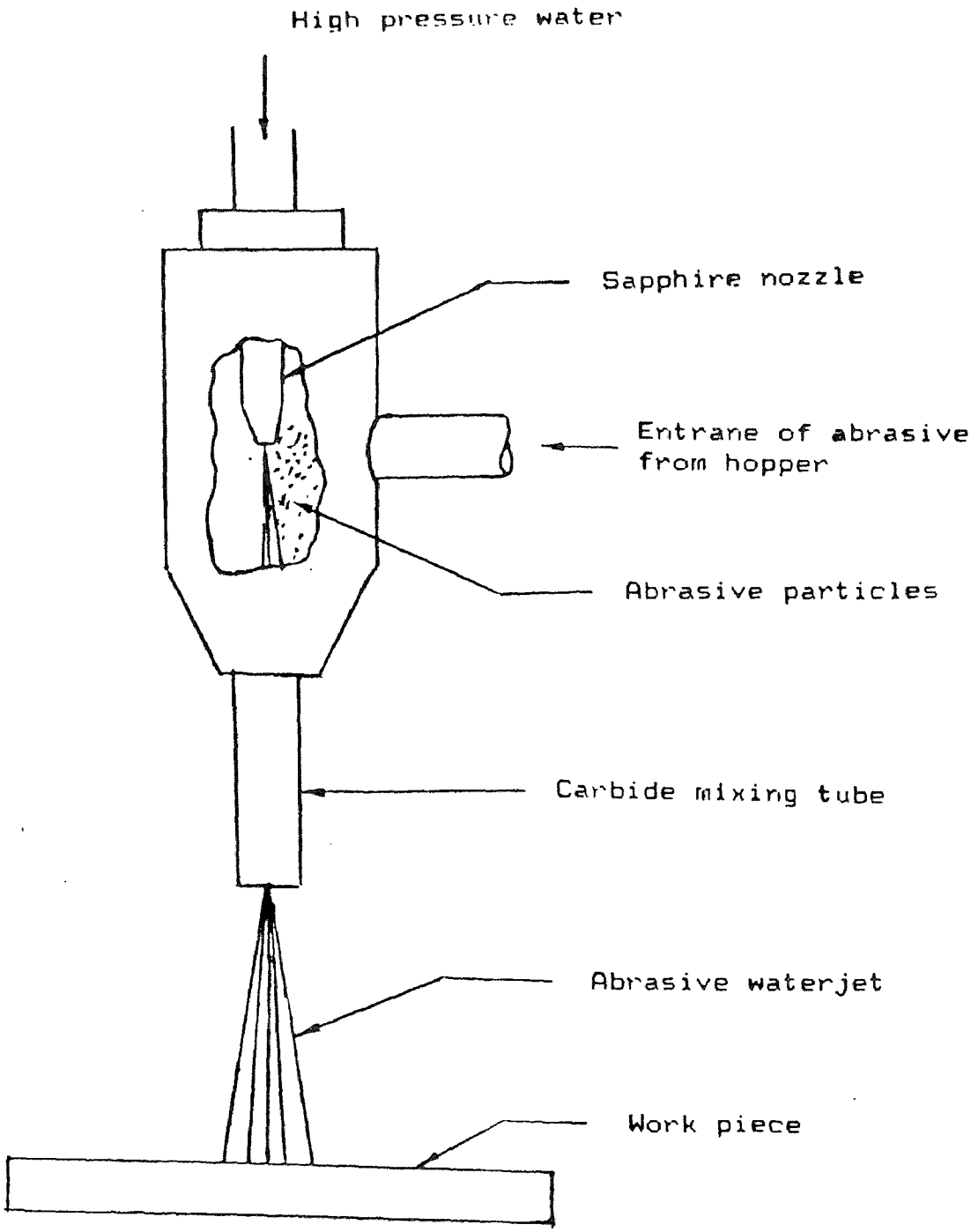

Fig. 4.2 Schematic of the jet formation and jet-work piece interaction.

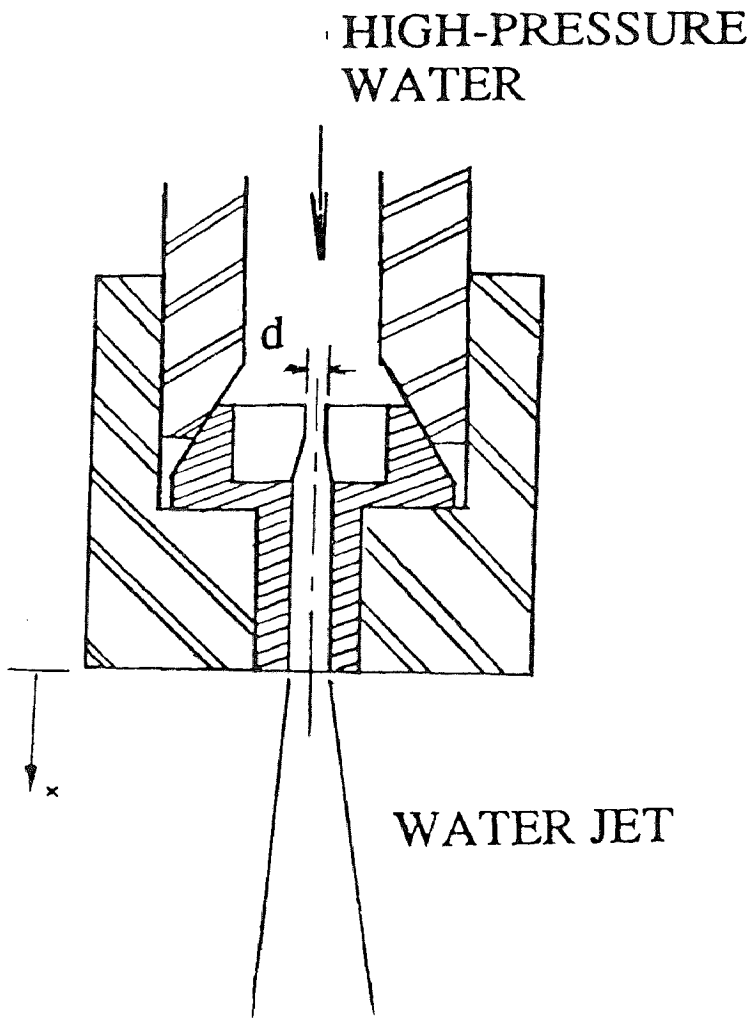

Fig. 4.3 Schematic of sapphire nozzle with water flow

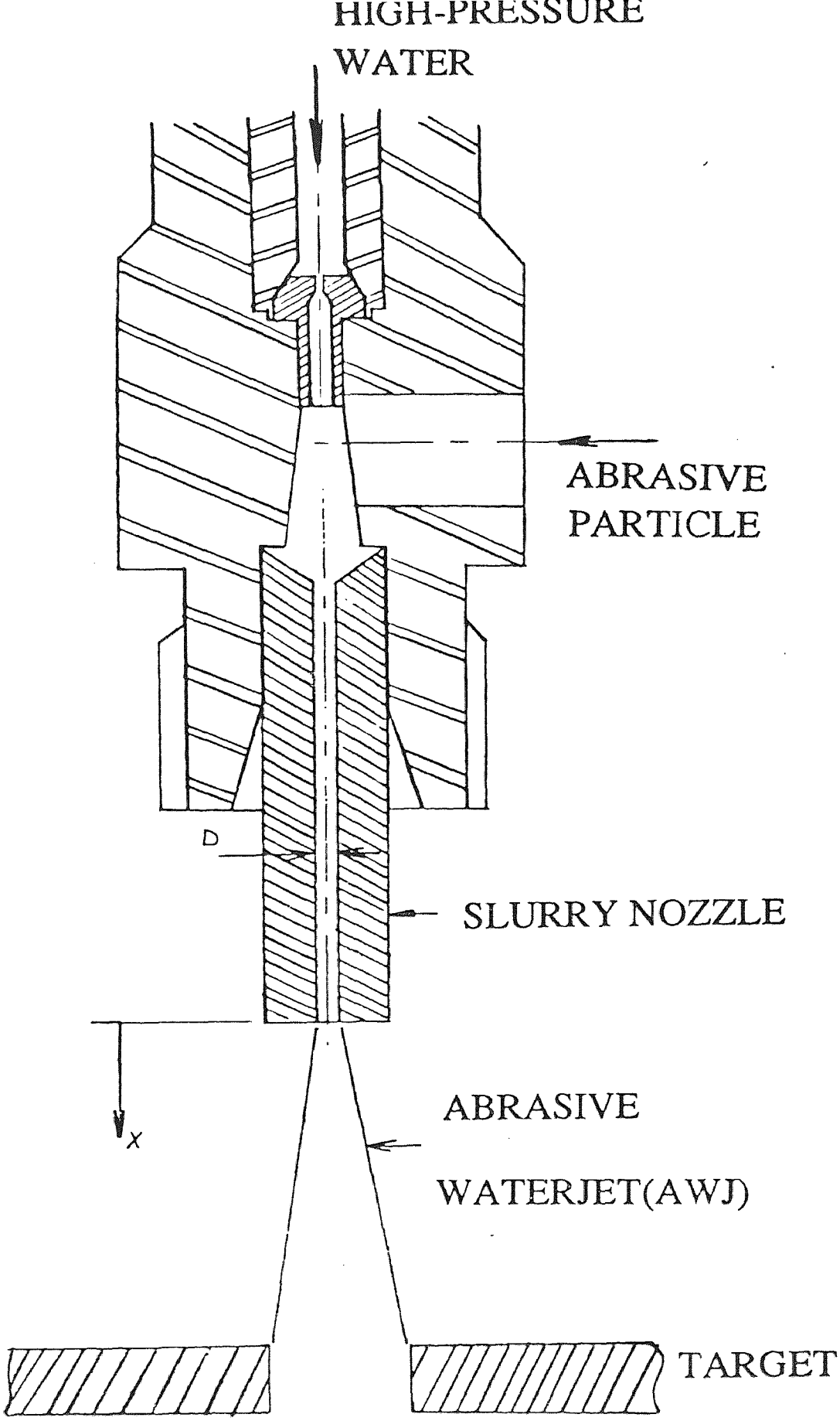

Fig. 4.4 Schematic of carbide nozzle with flow

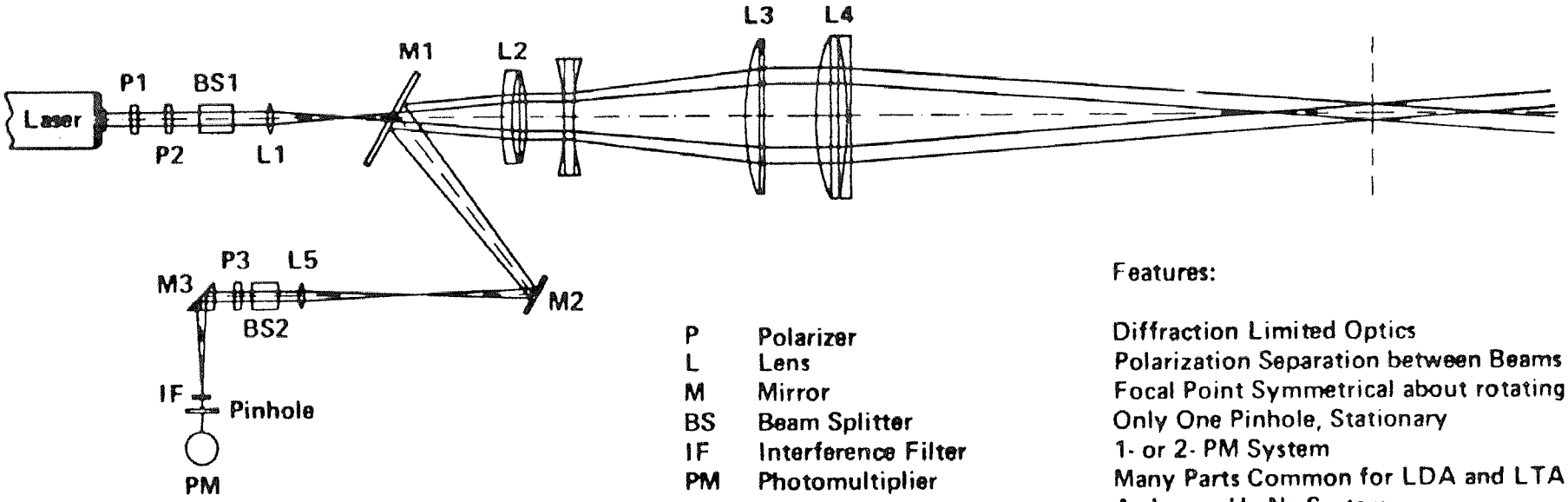

P	Polarizer
L	Lens
M	Mirror
BS	Beam Splitter
IF	Interference Filter
PM	Photomultiplier

Features:

Diffraction Limited Optics
Polarization Separation between Beams
Focal Point Symmetrical about rotating Axis
Only One Pinhole, Stationary
1- or 2- PM System
Many Parts Common for LDA and LTA
Ar-Ion or He-Ne System

Fig. 4.5 Schematic of LTA operation

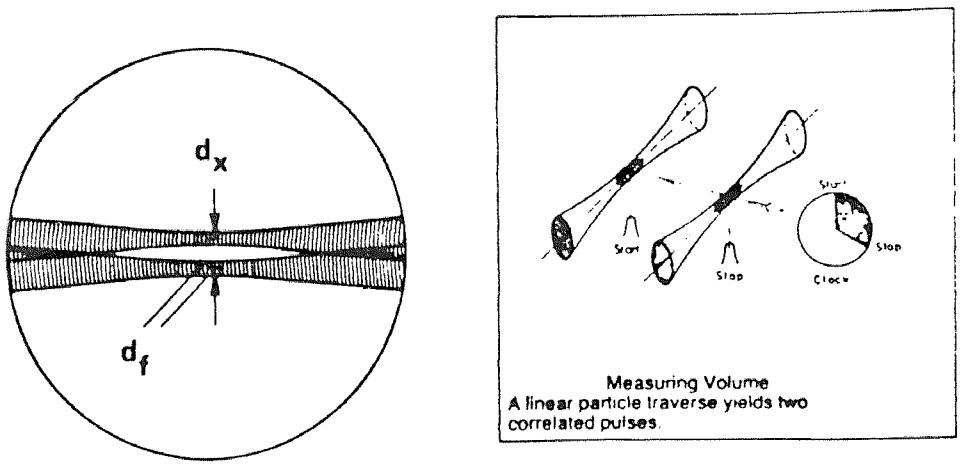

Fig. 4.6 Measuring volume of LTA

Mechanical Arrangement

S=1:30

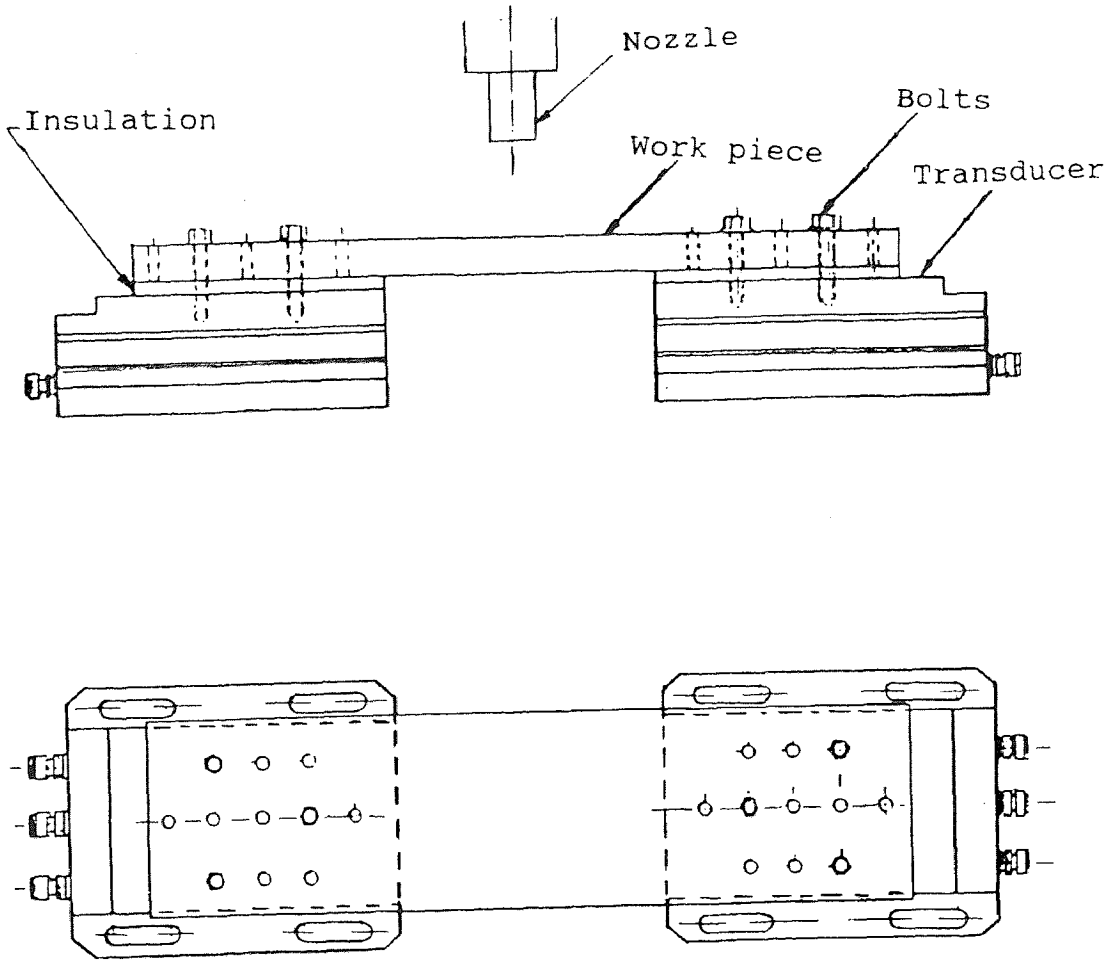

Fig. 4.7 Schematic of piezoelectric force transducer

Detail of work piece

s= 1:30
(scale in mm)

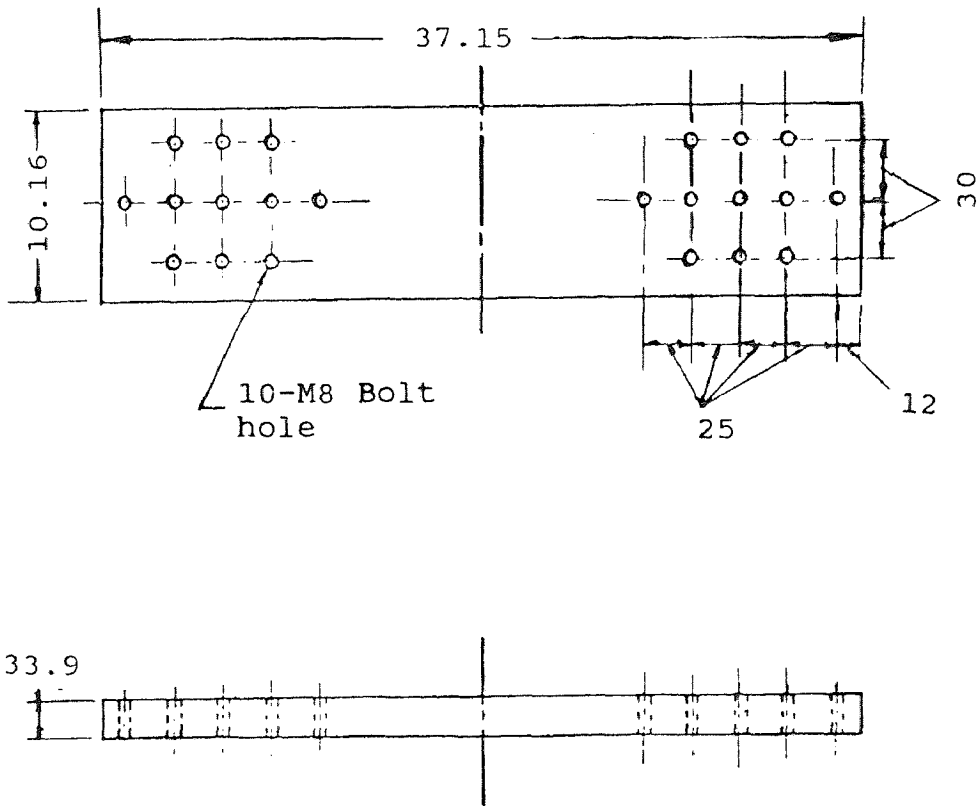

Fig. 4.8 Schematic of work piece

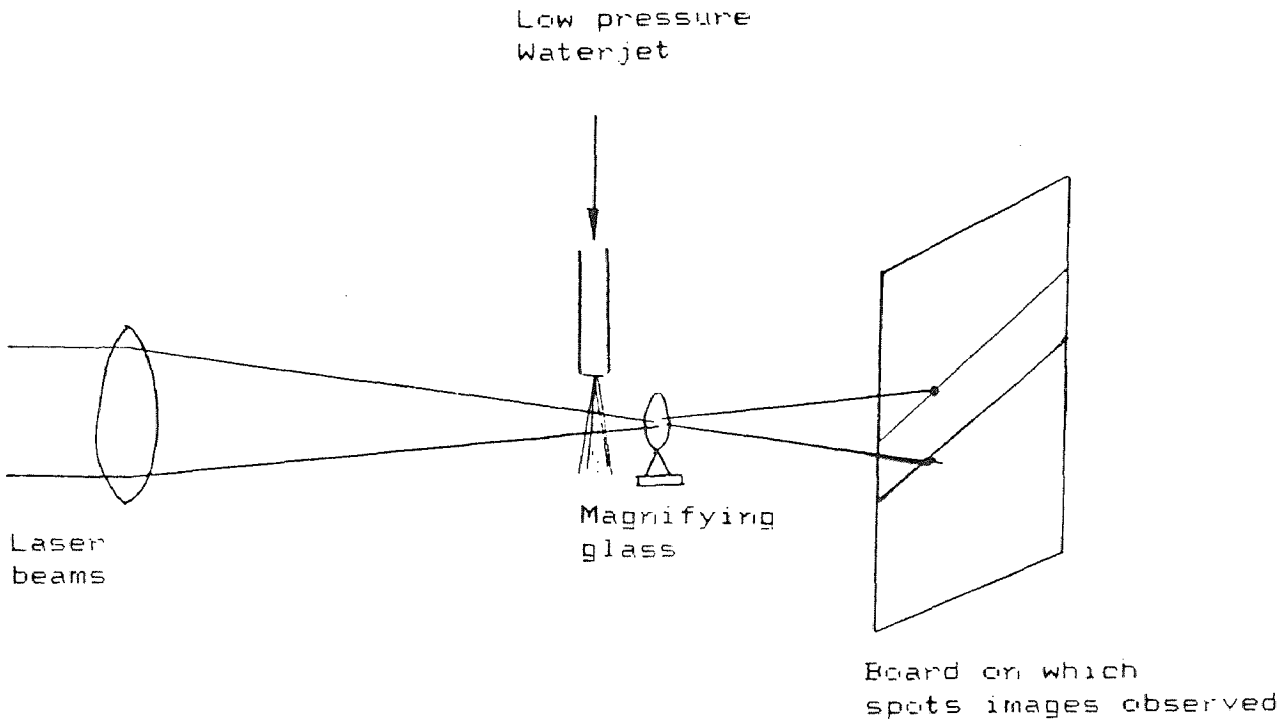

Fig. 4.9 Checking the jet alignment with focusing spots

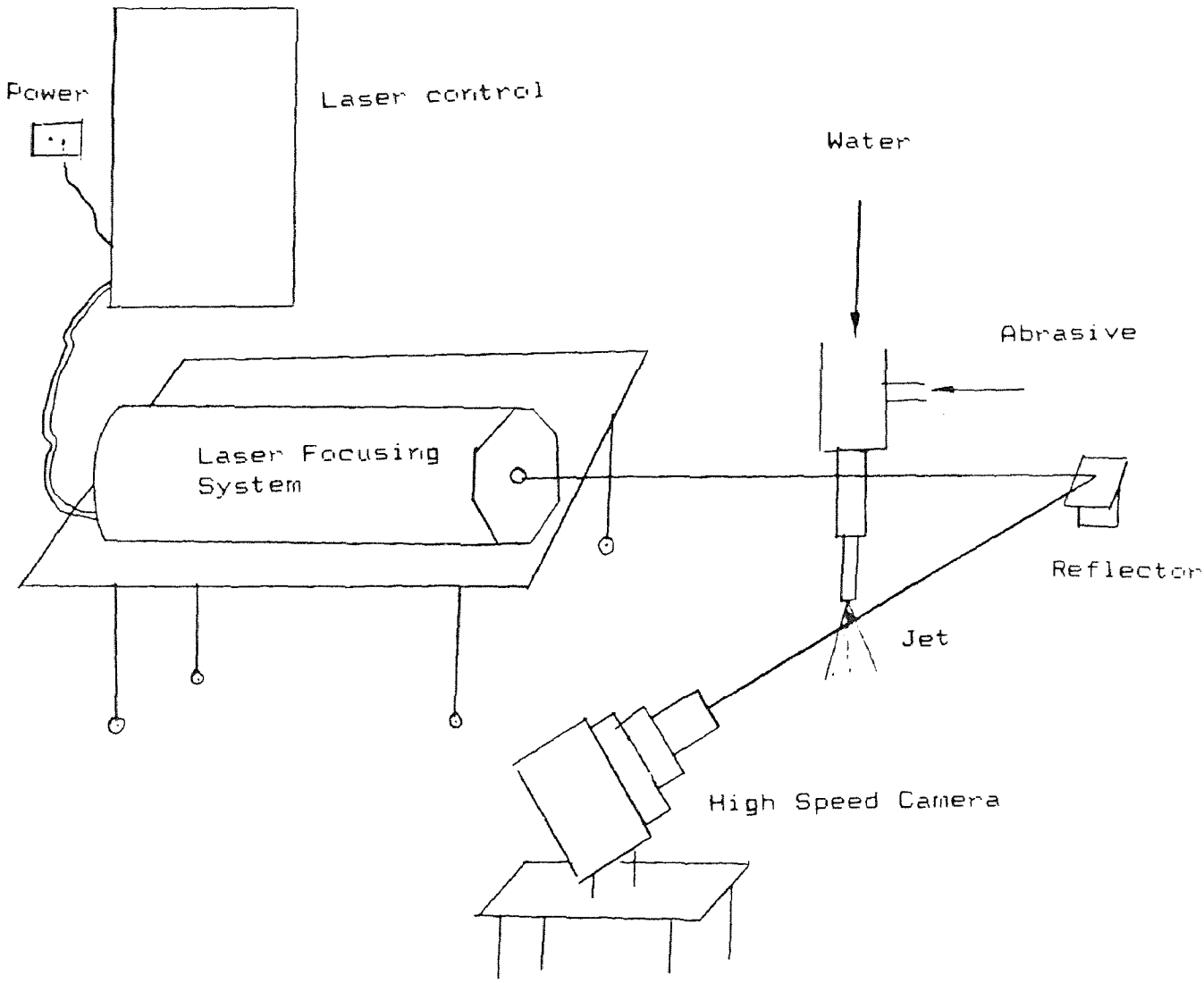

Fig. 4.10 Schematic of experimental set up for high speed filming

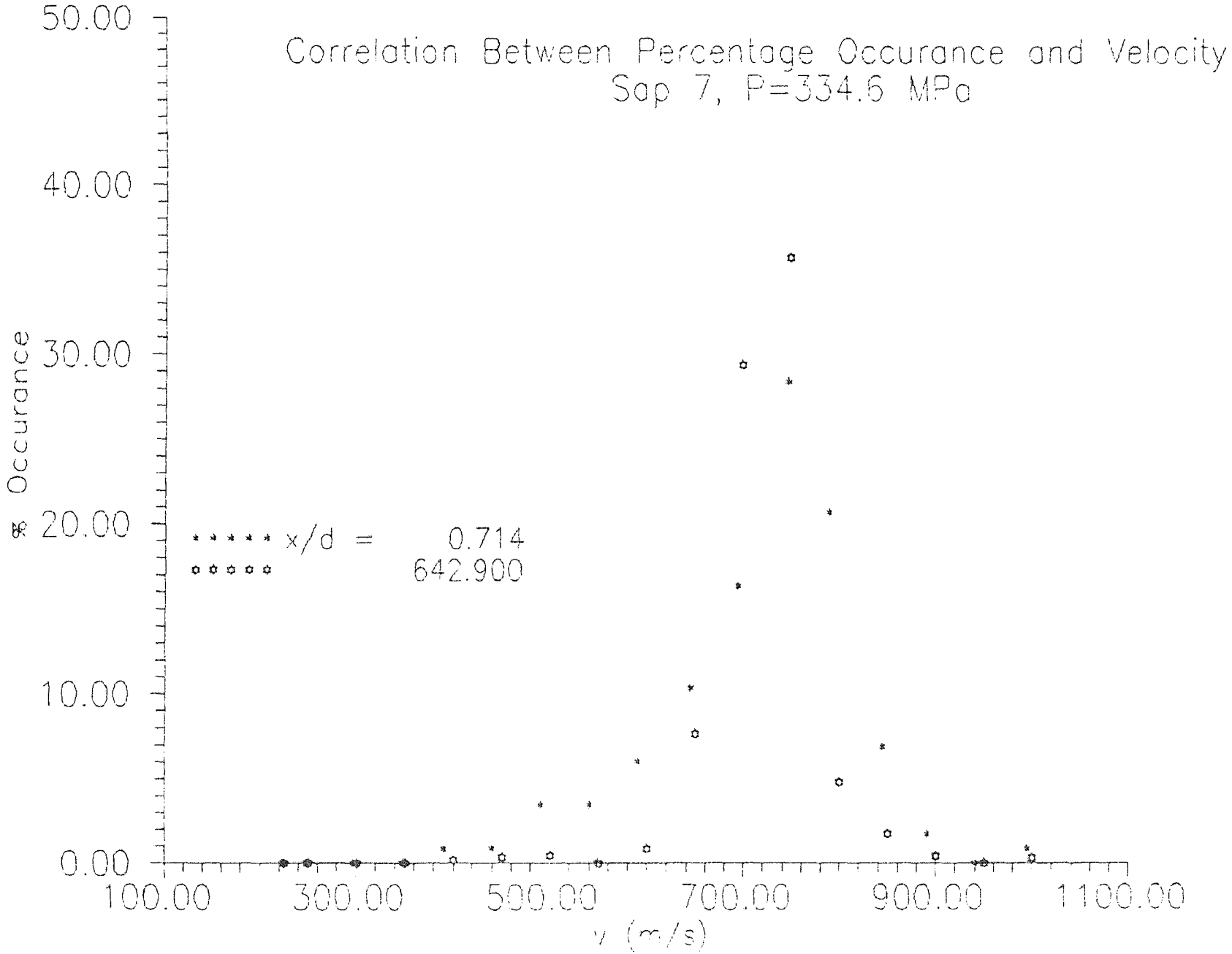

Fig. 5.1 Correlation between percentage occurance and velocity for Sap 7

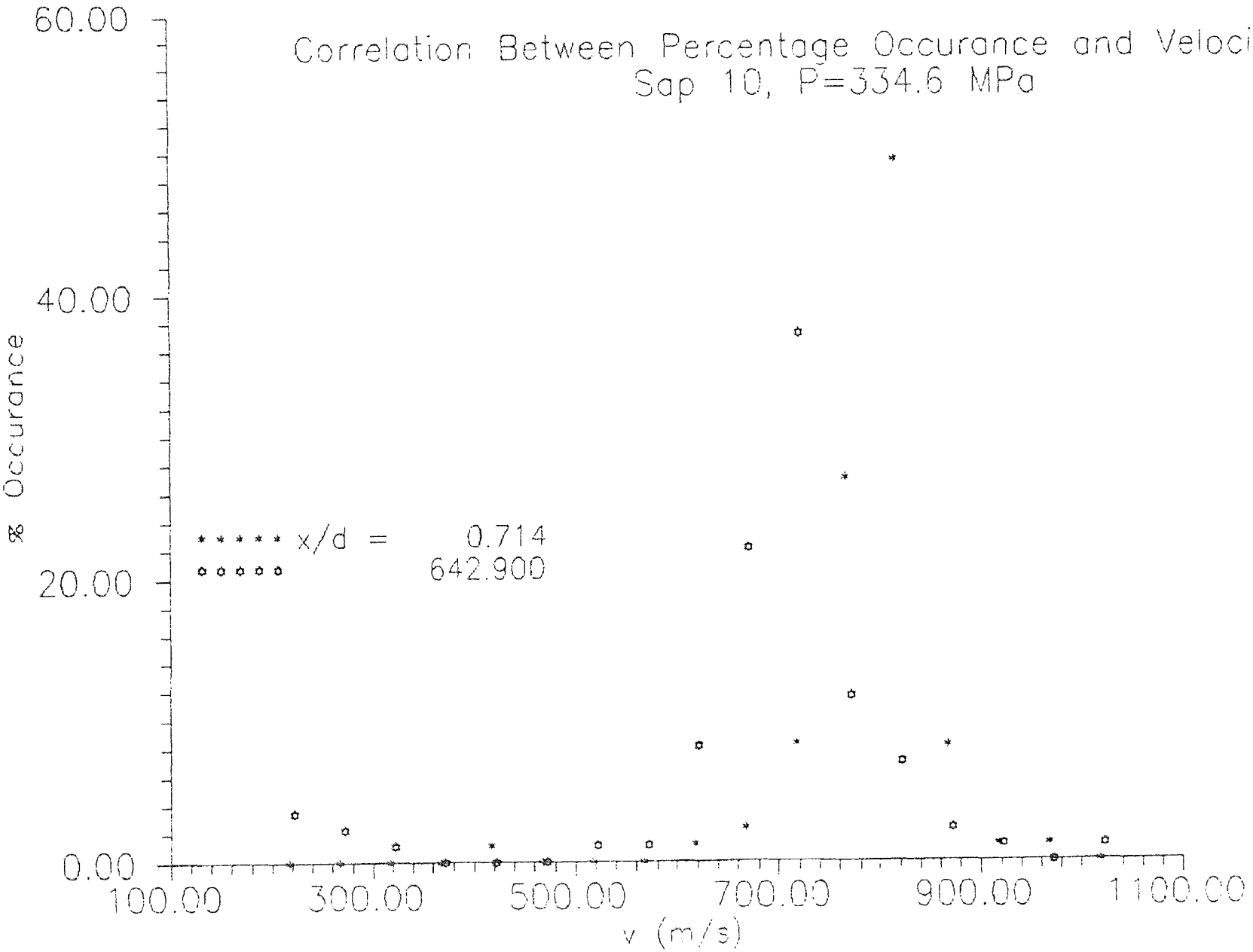

Fig. 5.2 Correlation between percentage occurance and velocity for Sap 10

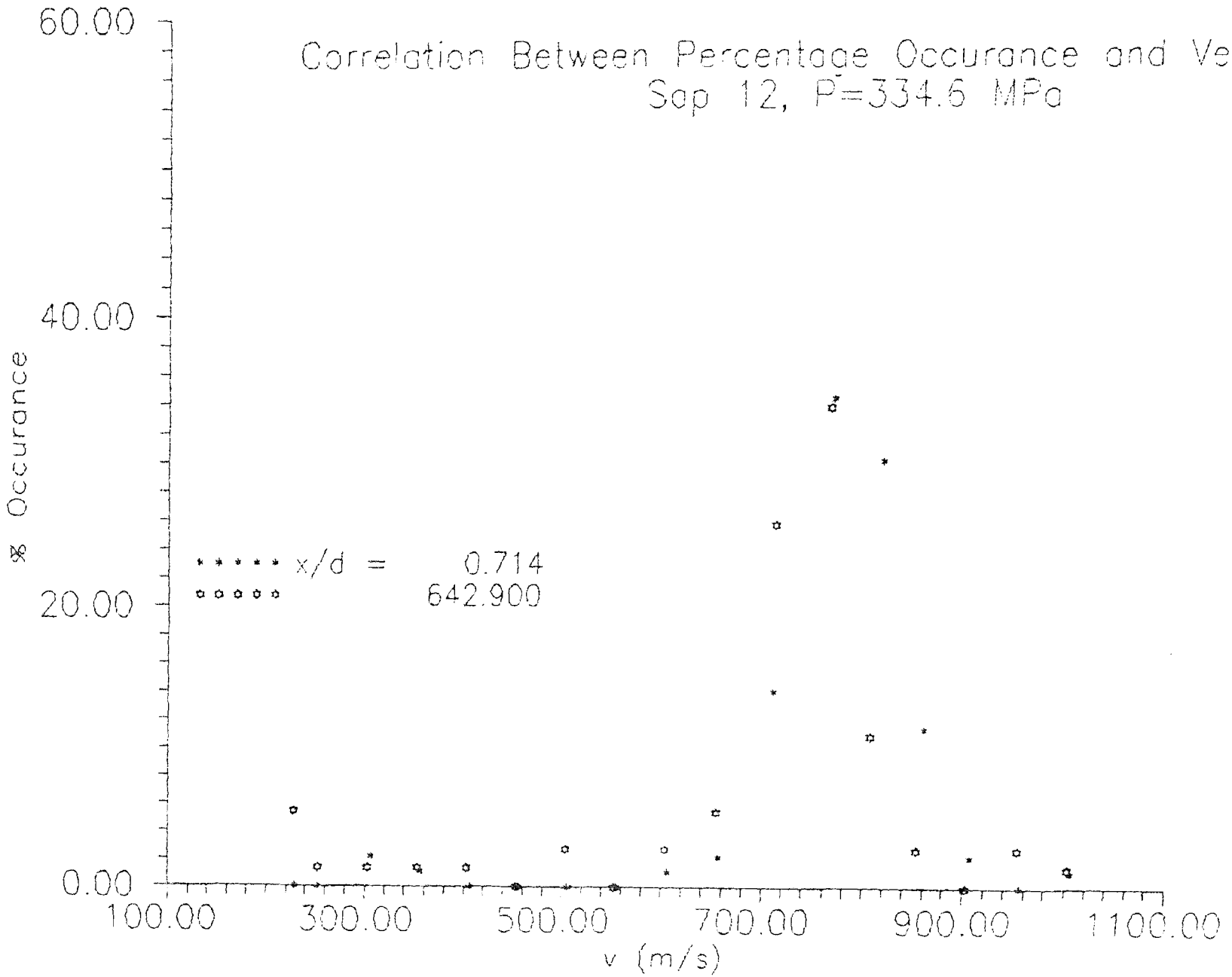

Fig. 5.3 Correlation between percentage occurance and velocity for Sap 12

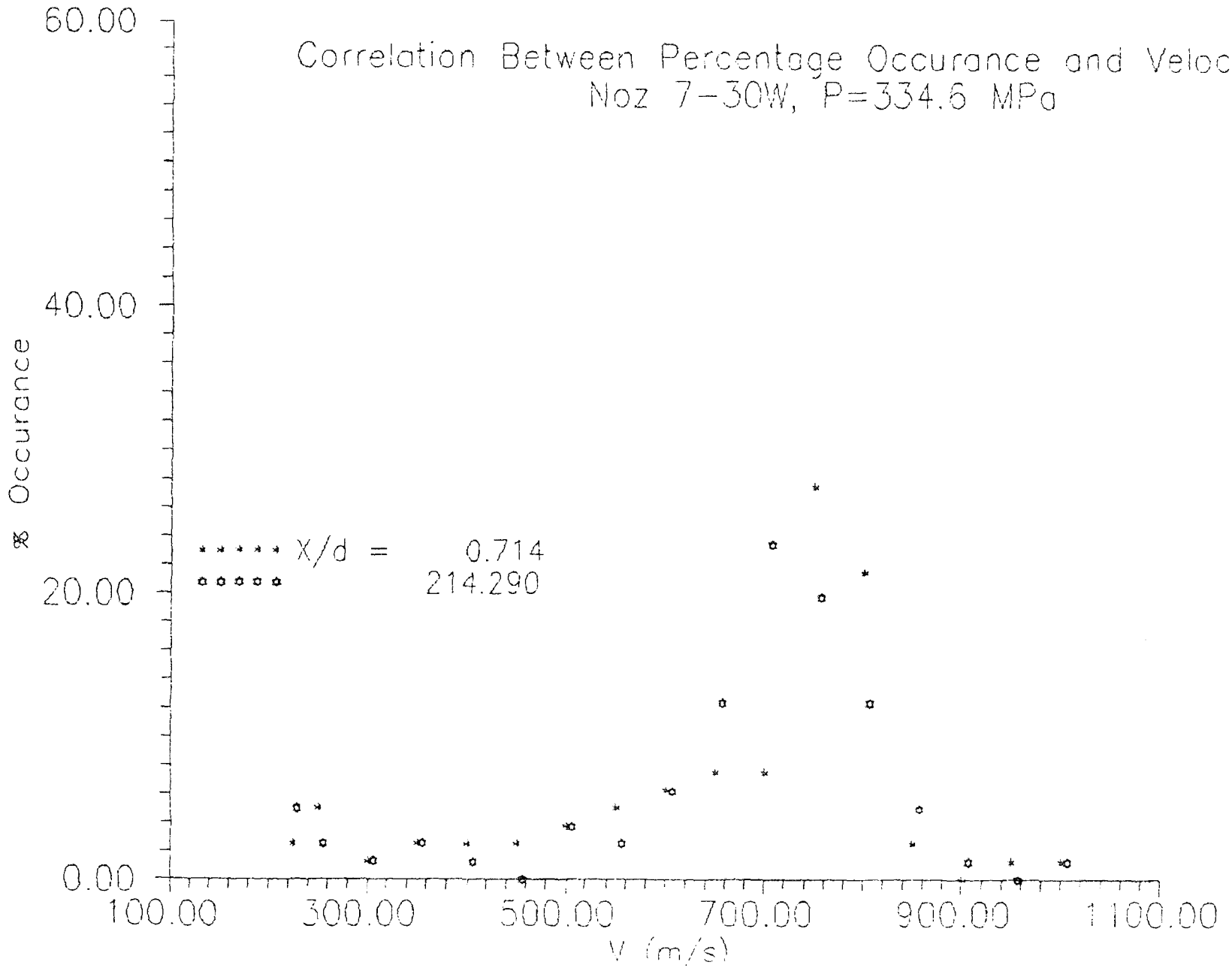

Fig. 5.4 Correlation between percentage occurance and velocity for Noz 7-30W

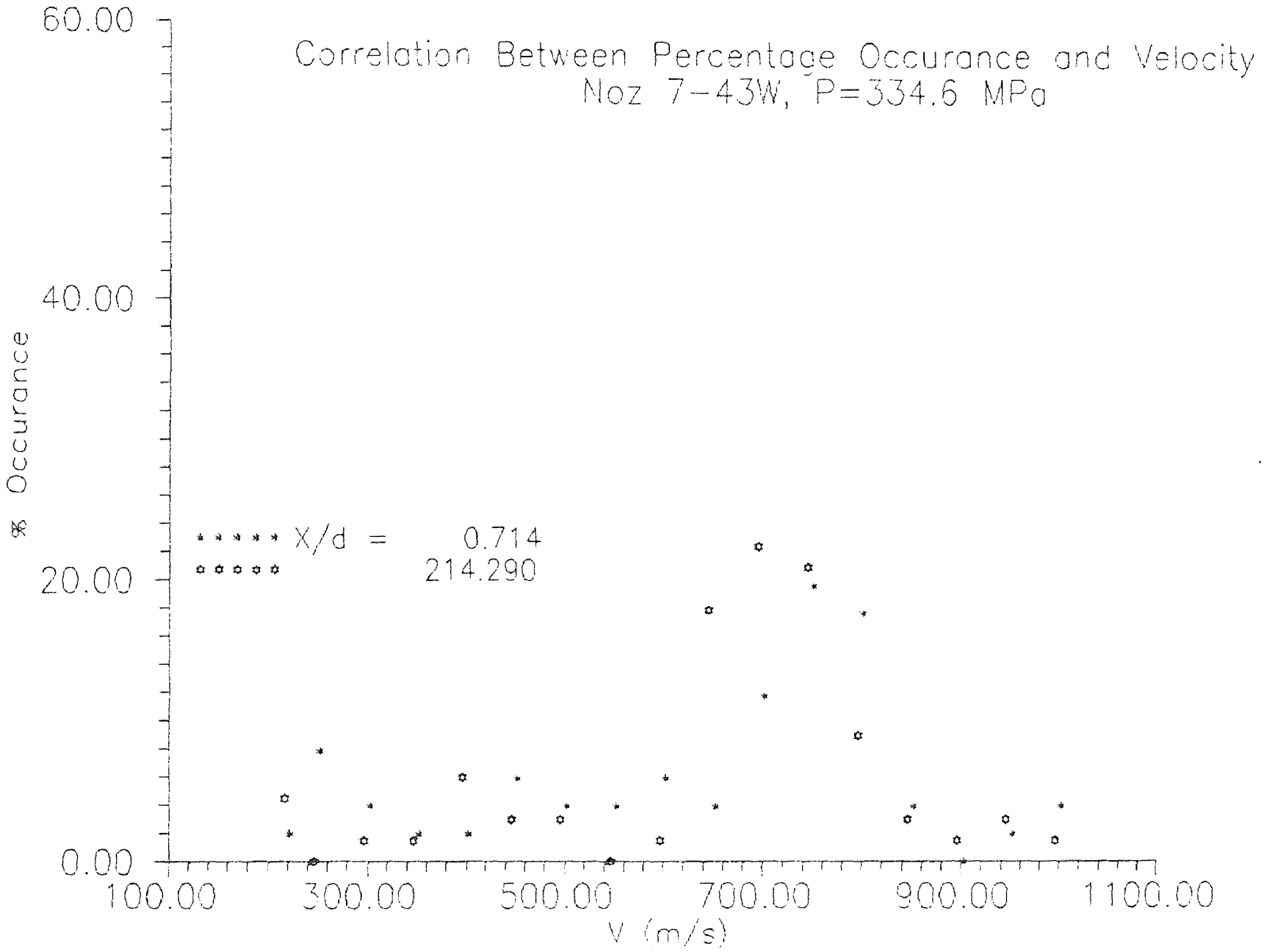

Fig. 5.5 Correlation between percentage occurance and velocity for Noz 7-43W

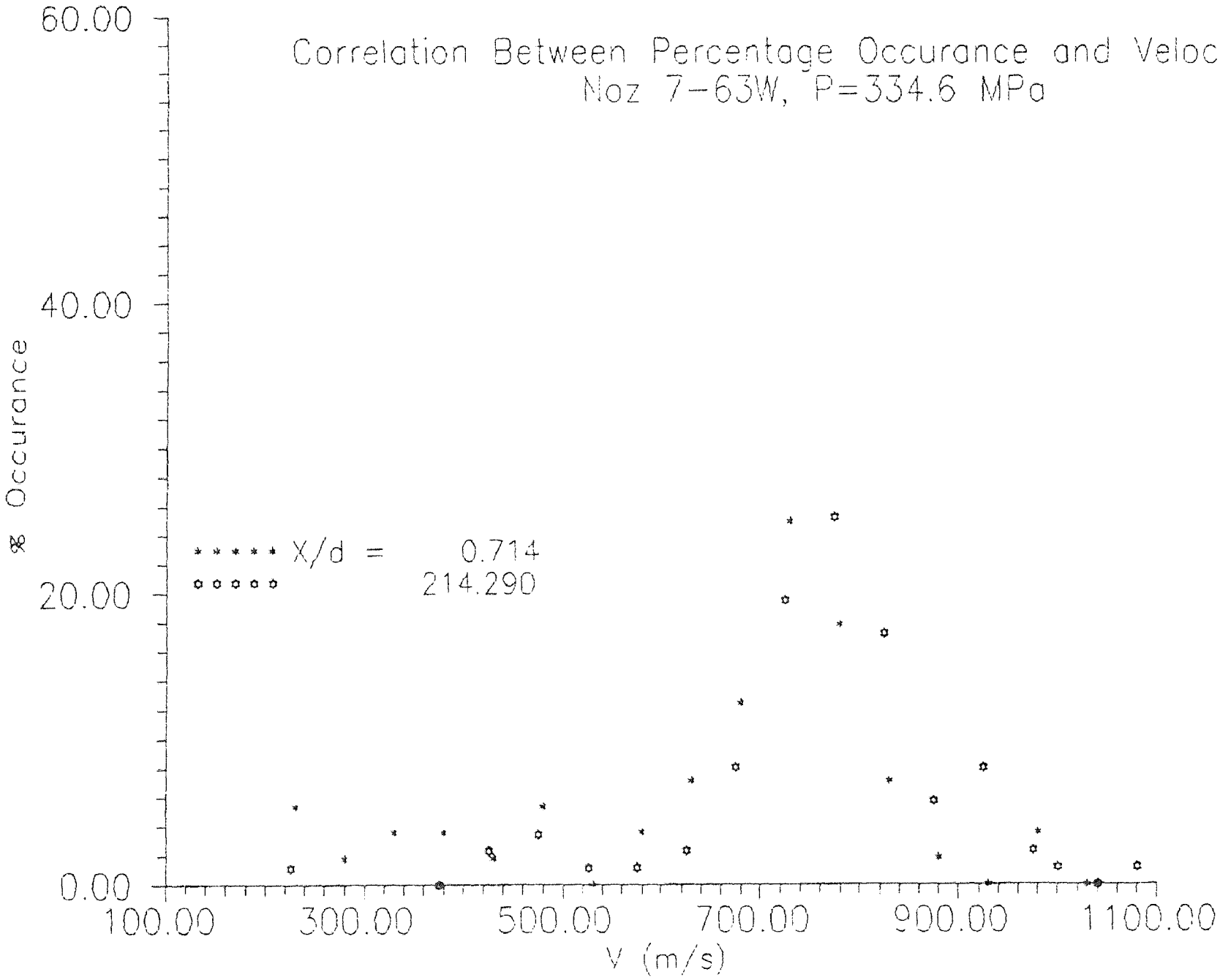

Fig. 5.6 Correlation between percentage occurance and velocity for Noz 7-63W

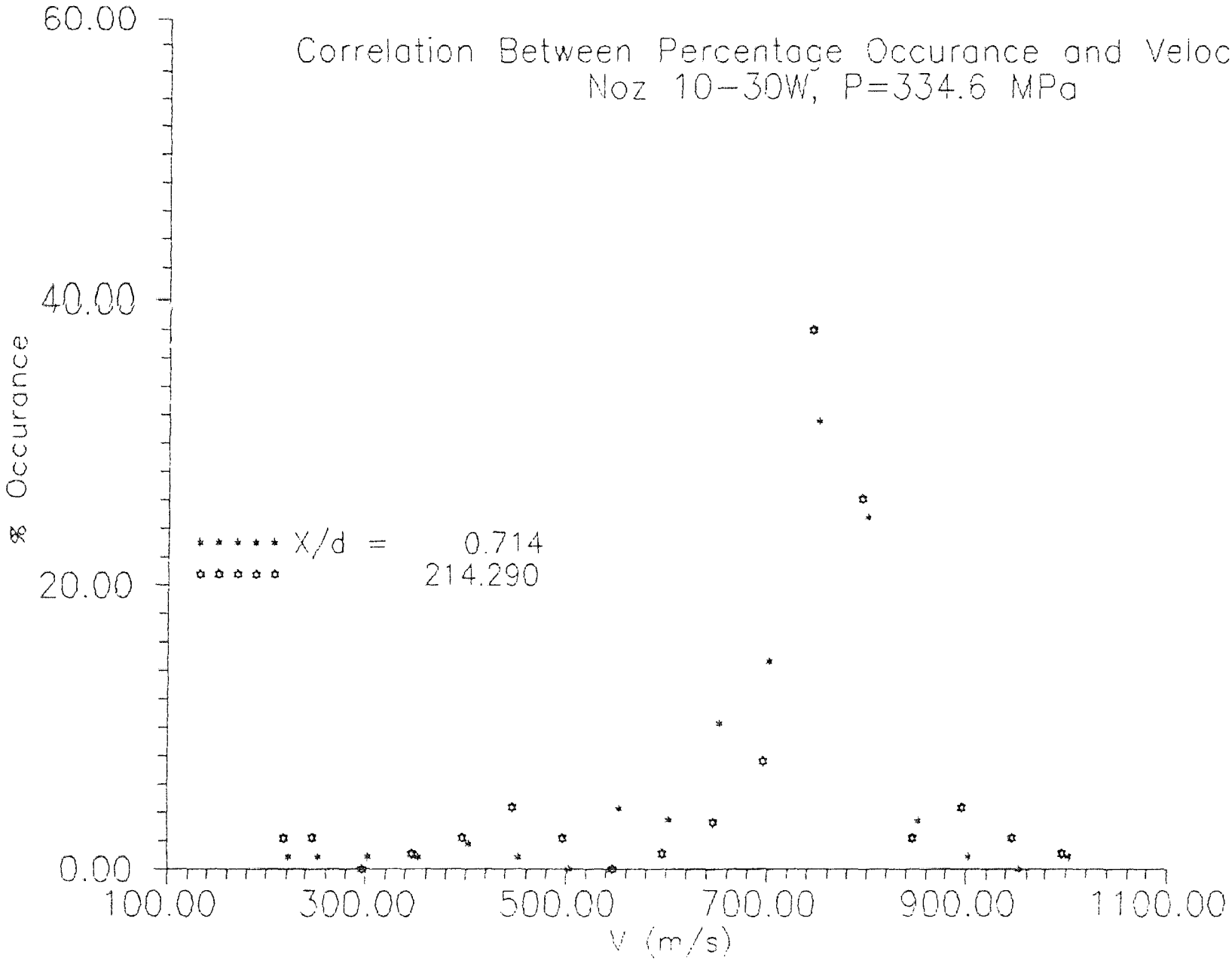

Fig. 5.7 Correlation between percentage occurance and velocity for Noz 10-30W

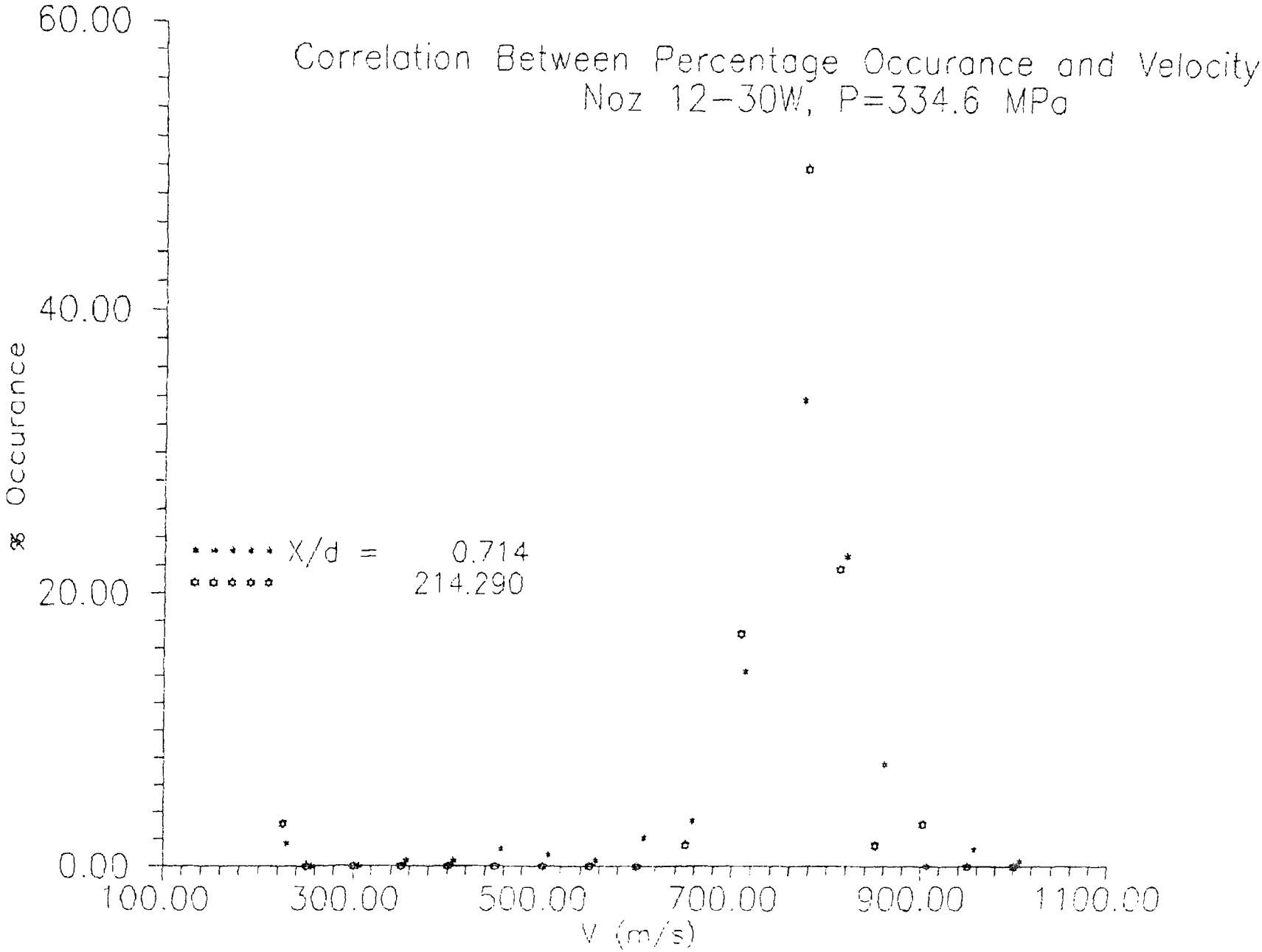

Fig. 5.8 Correlation between percentage occurance and velocity for Noz 12-30W

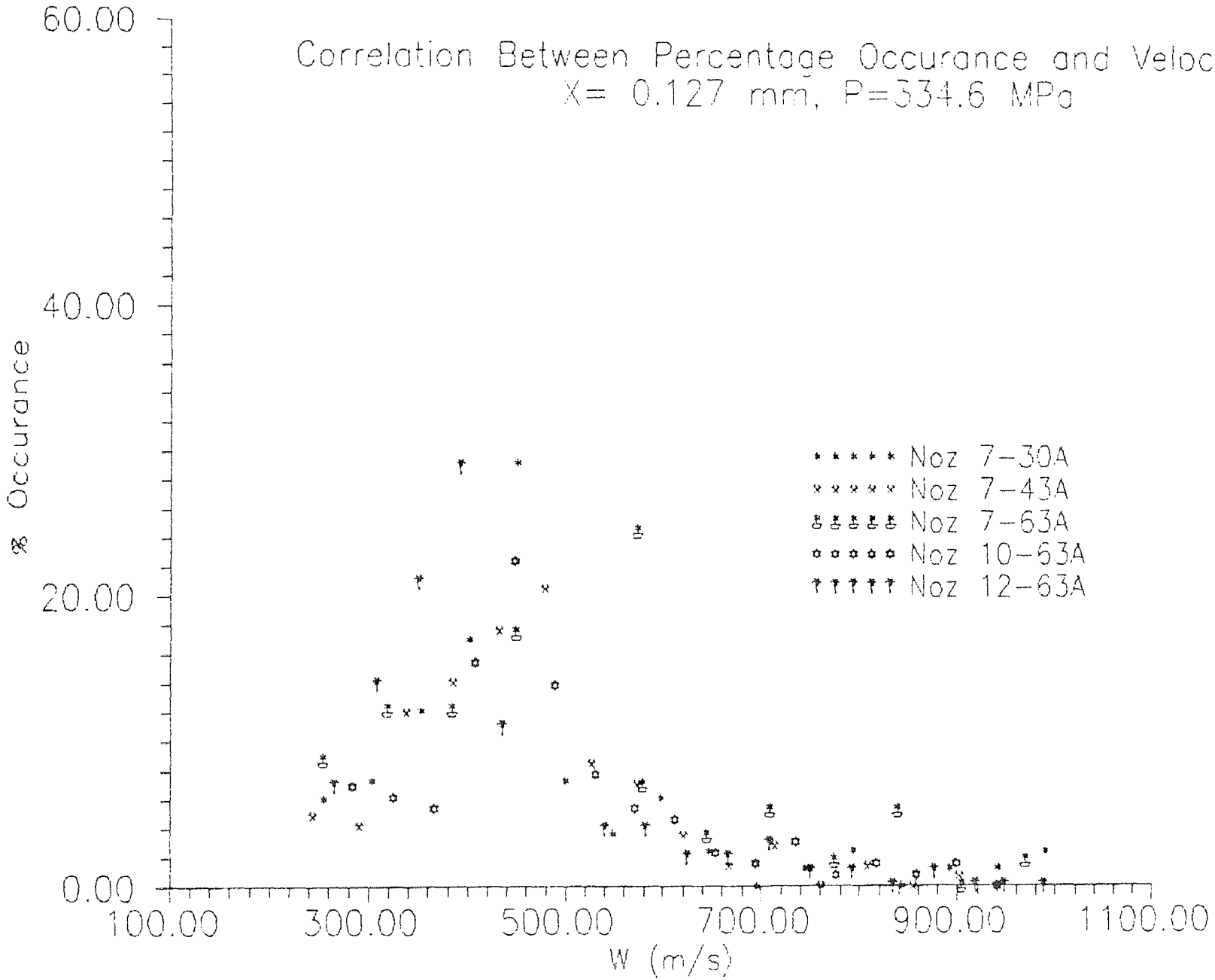

Fig. 5.9 Correlation between percentage occurance and abrasive velocity for different nozzle combinations

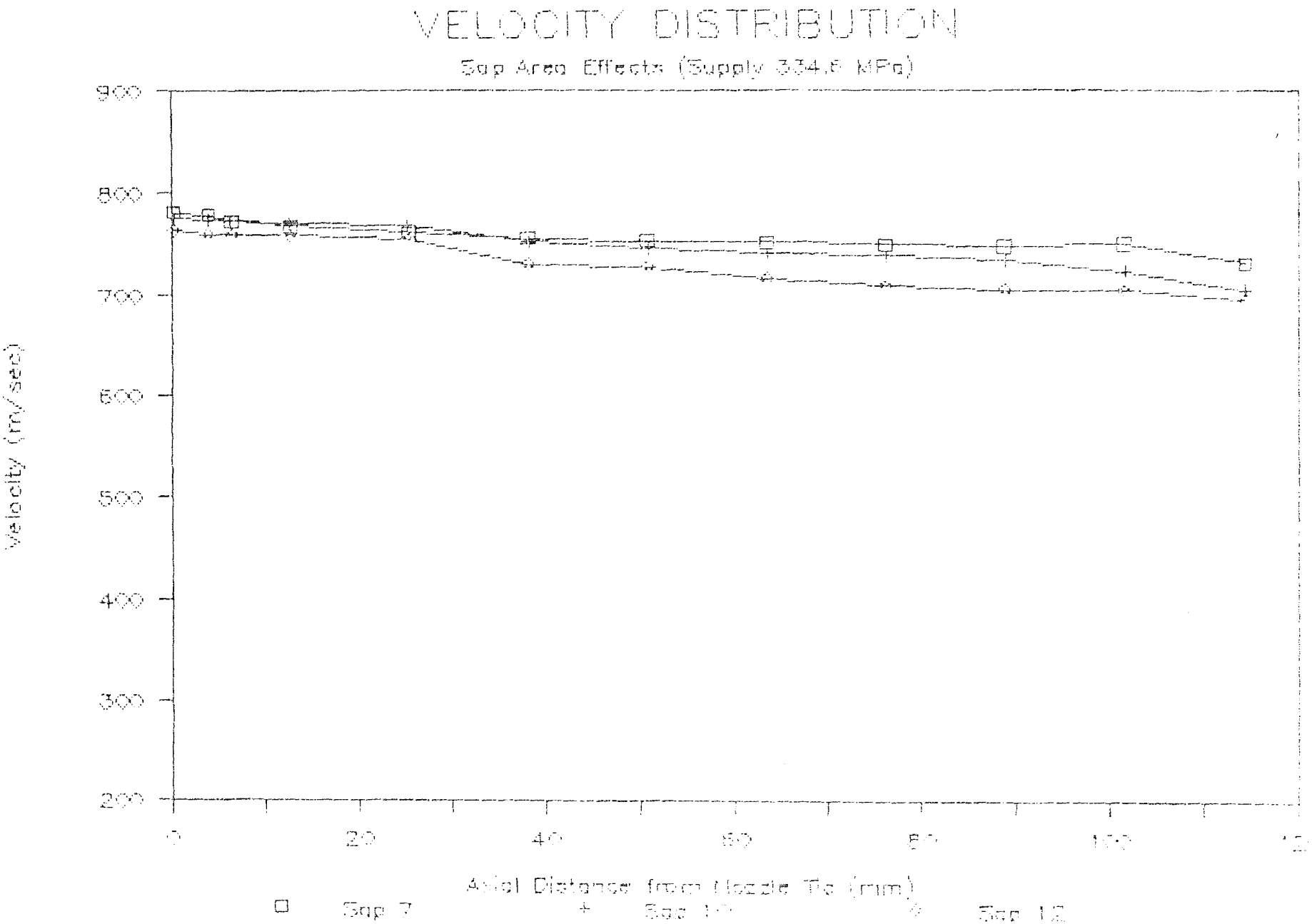

Fig. 5.10 Velocity distribution for different sapphire nozzles

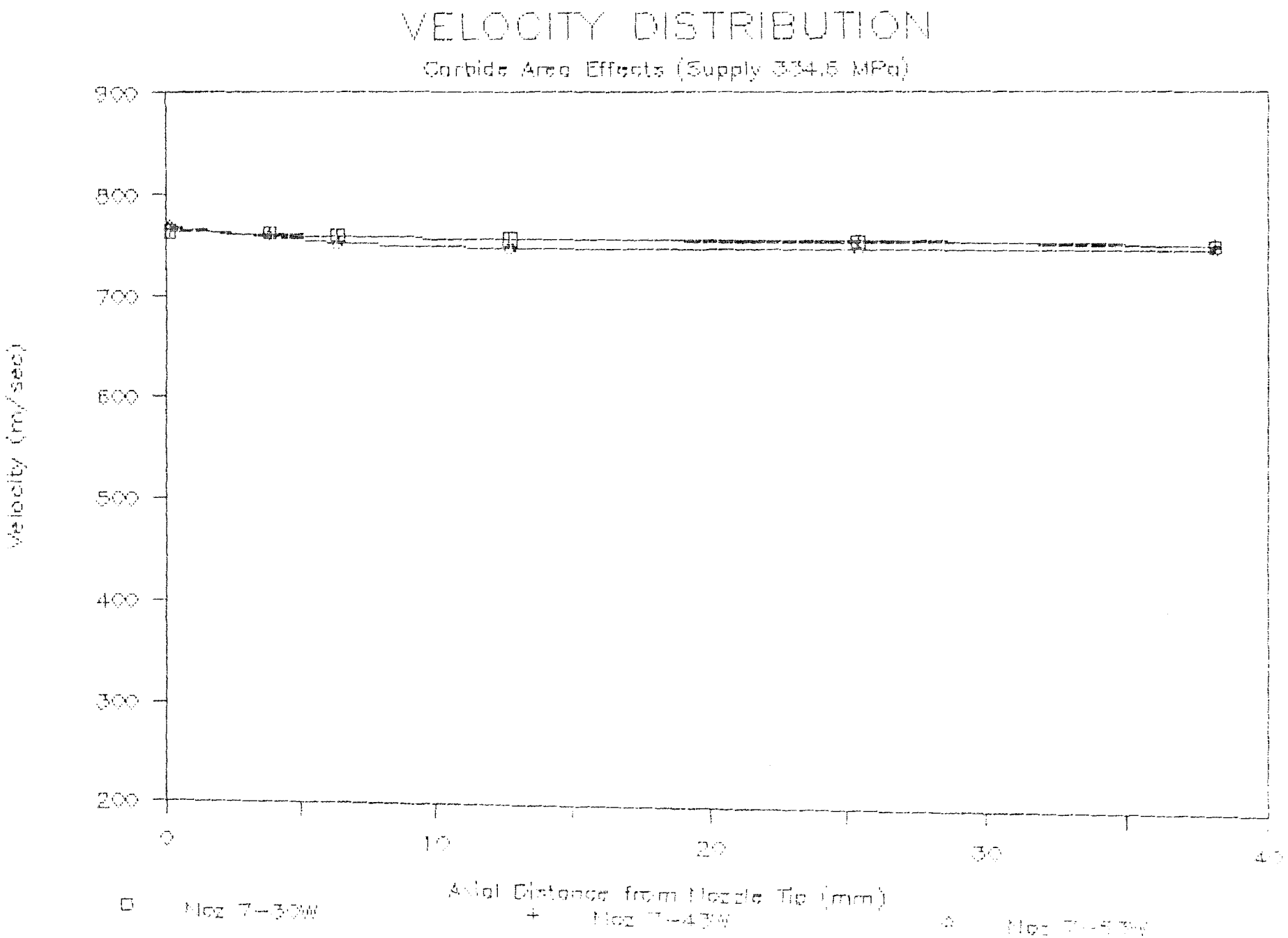

Fig. 5.11 Water velocity distribution showing carbide effects over sapphire

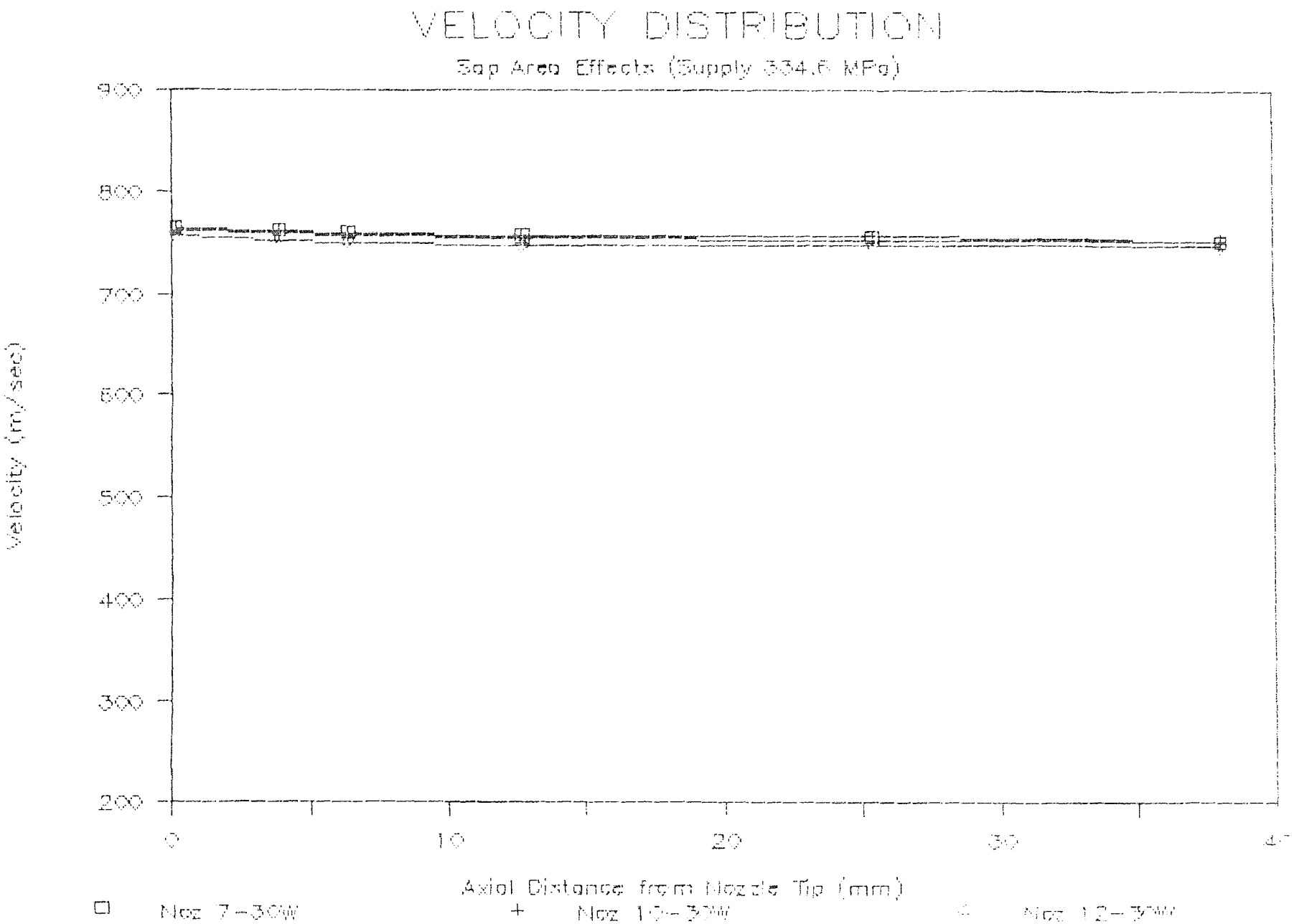

Fig. 5.12 Water velocity distribution showing sapphire effects over carbide

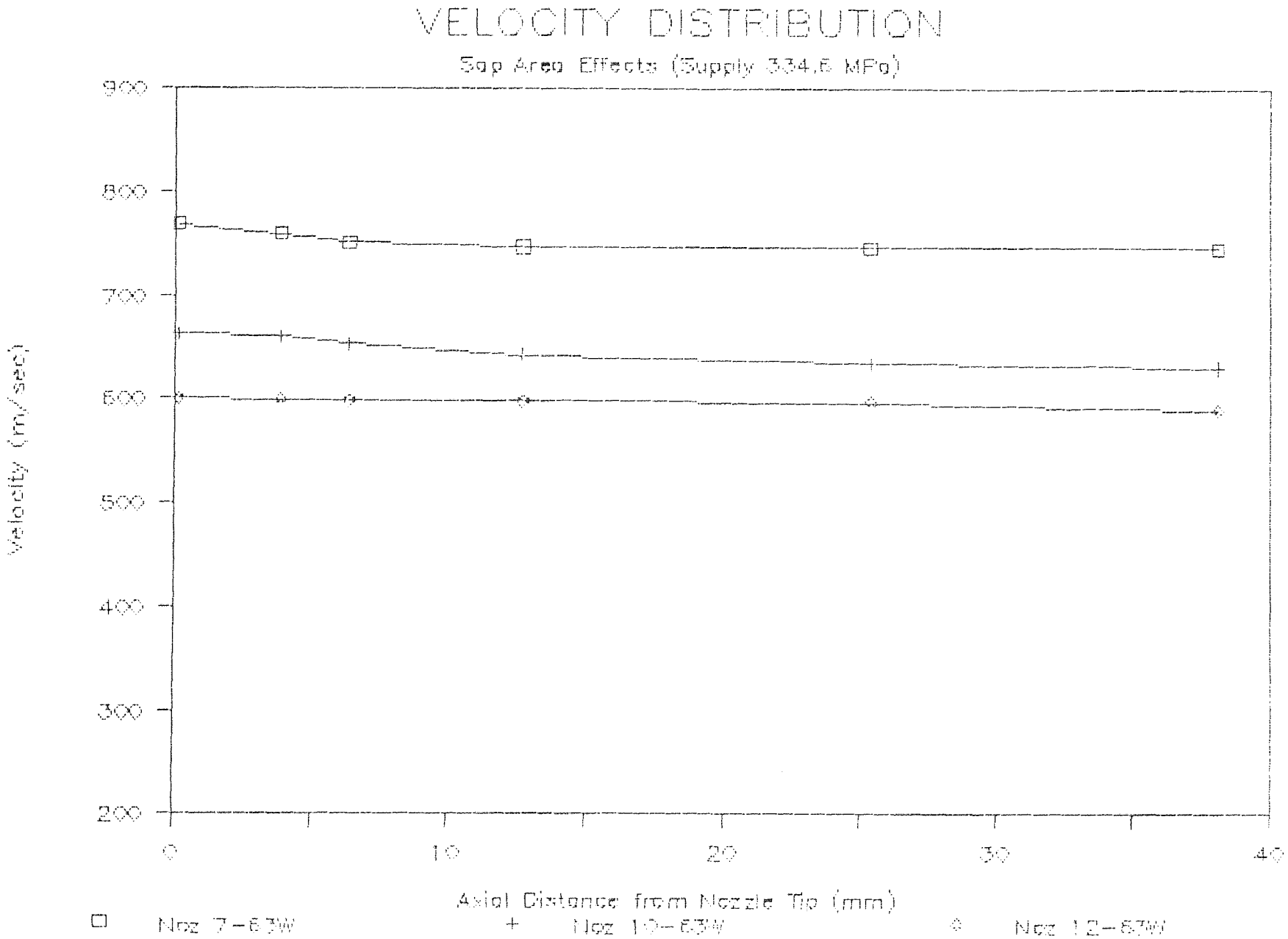

Fig. 5.13 Water velocity distribution showing sapphire effects over carbide

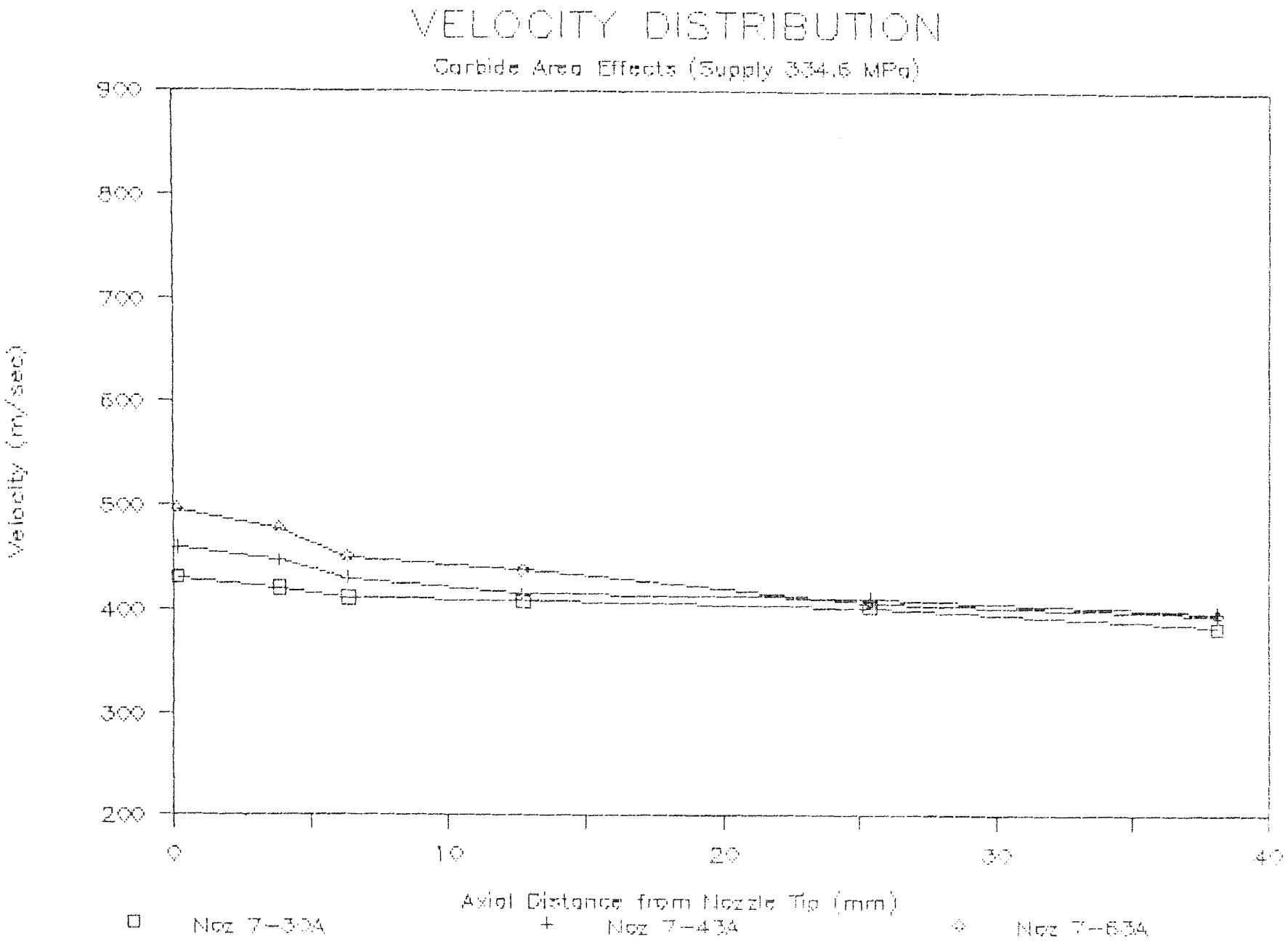

Fig. 5.14 Abrasive velocity distribution for different carbide nozzle

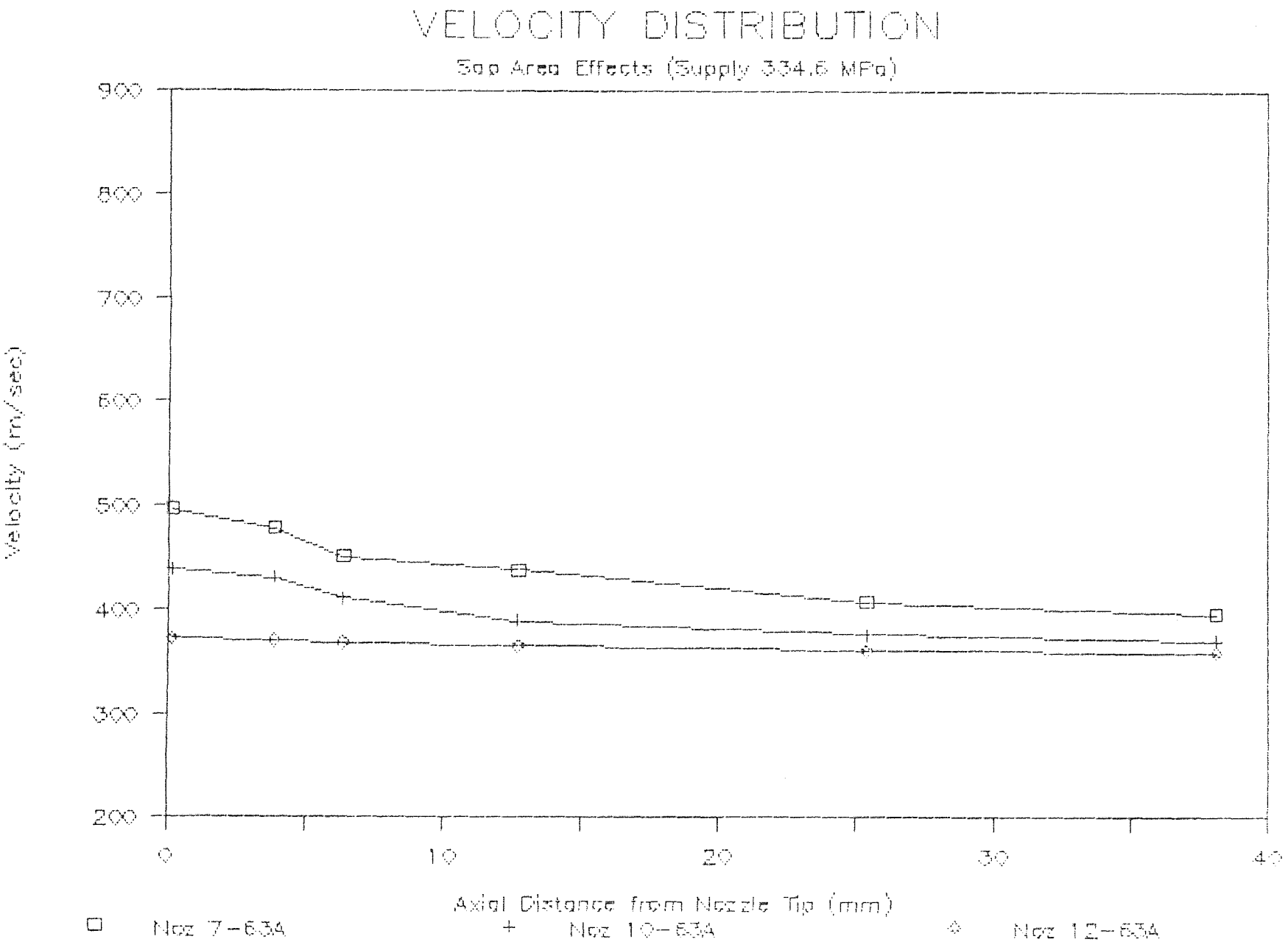

Fig. 5.15 Abrasive velocity distribution for different sapphire nozzle

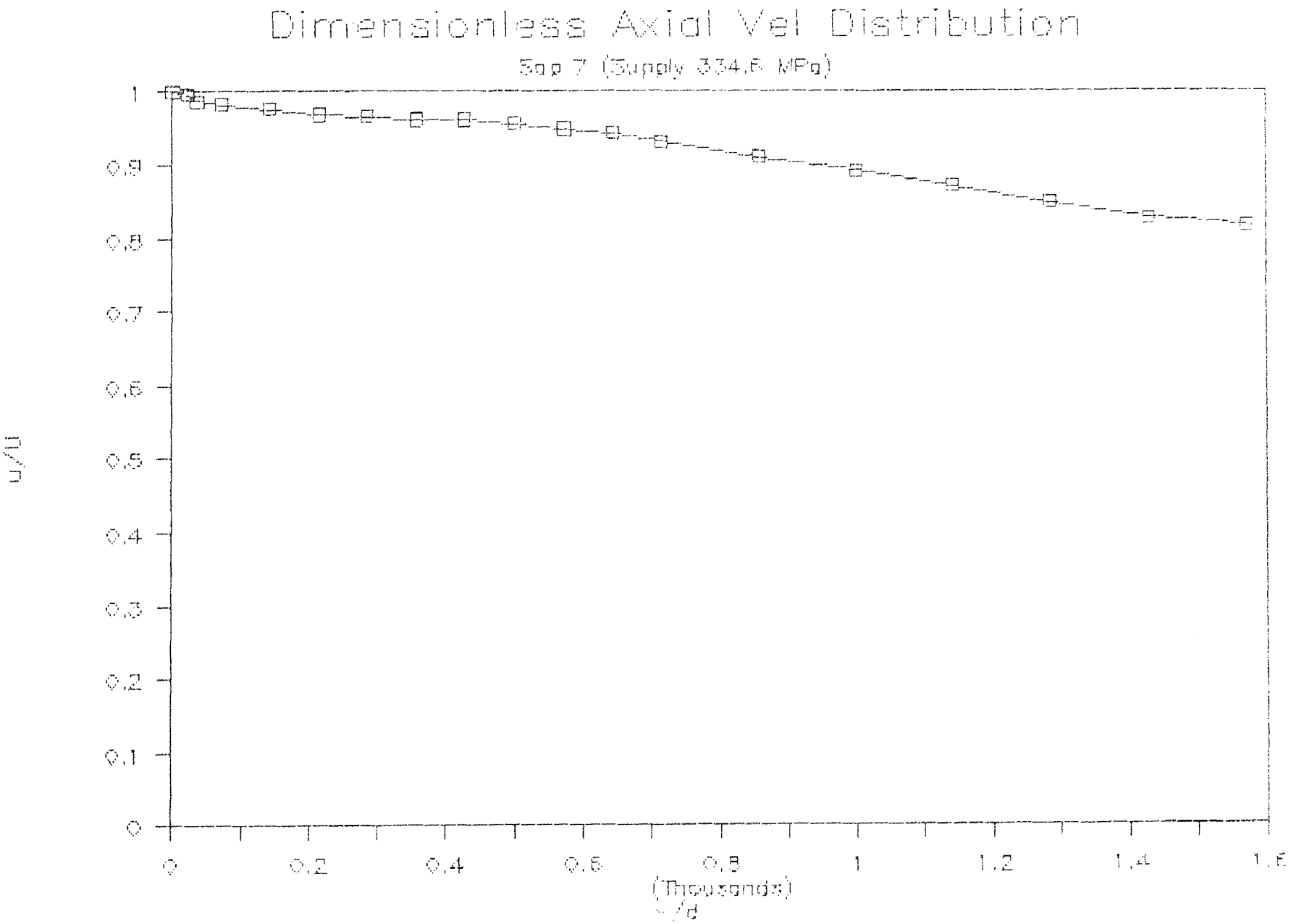

Fig. 5.16 Dimensionless axial velocity distribution for sap 7

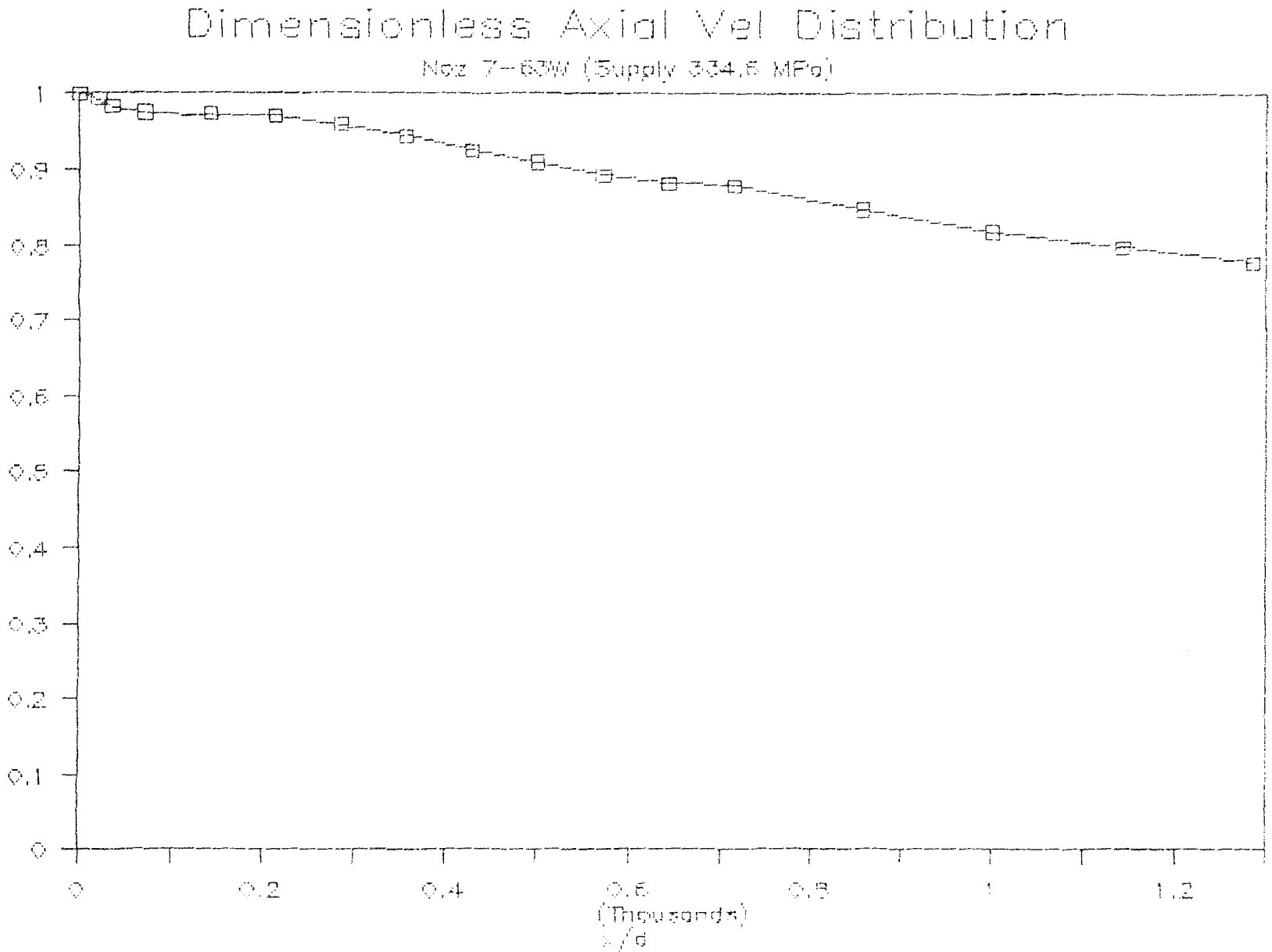

Fig. 5.17 Dimensionless axial water velocity distribution for Noz 7-63W

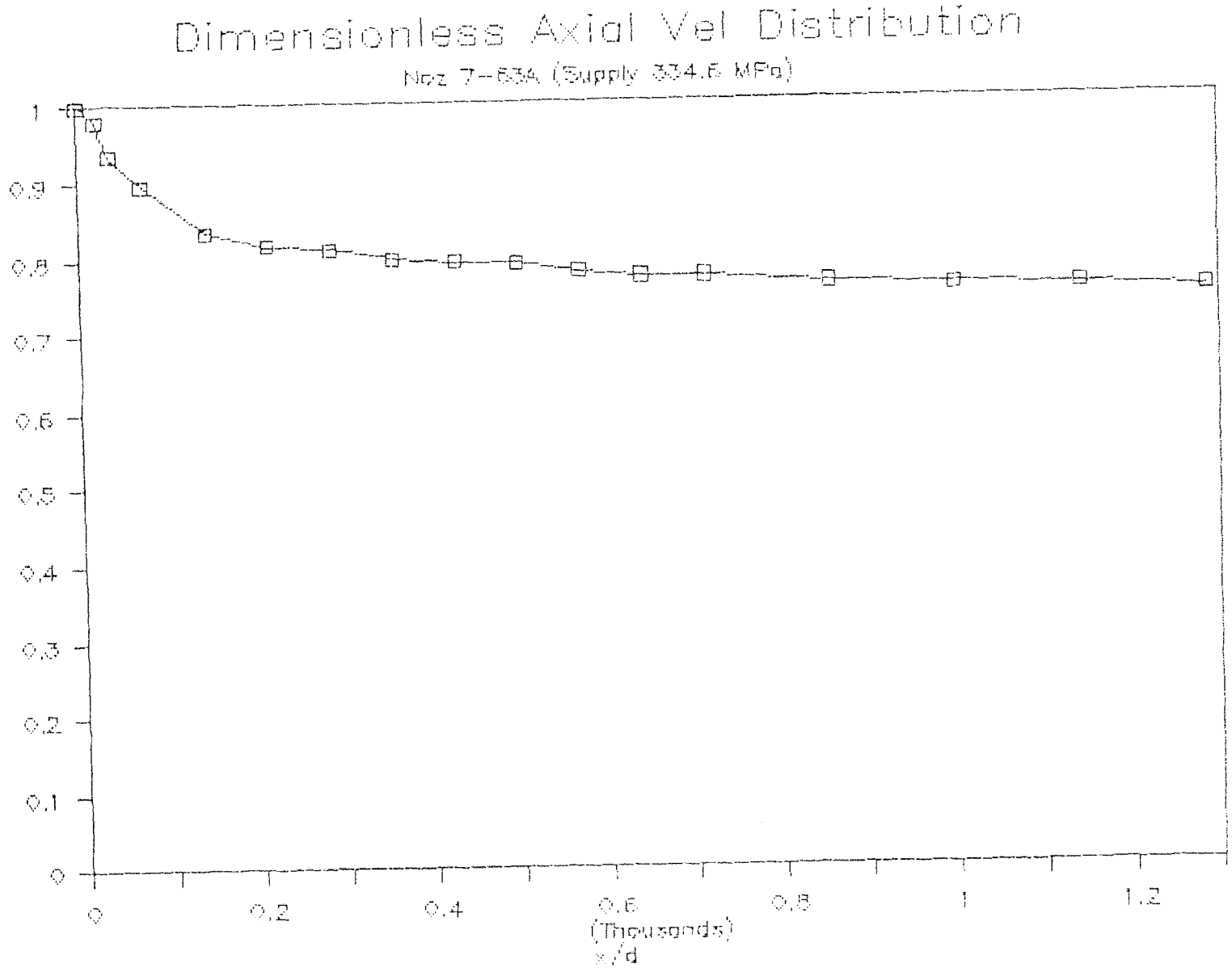

Fig. 5.18 Dimensionless axial abrasive velocity distribution for Noz 7-63A

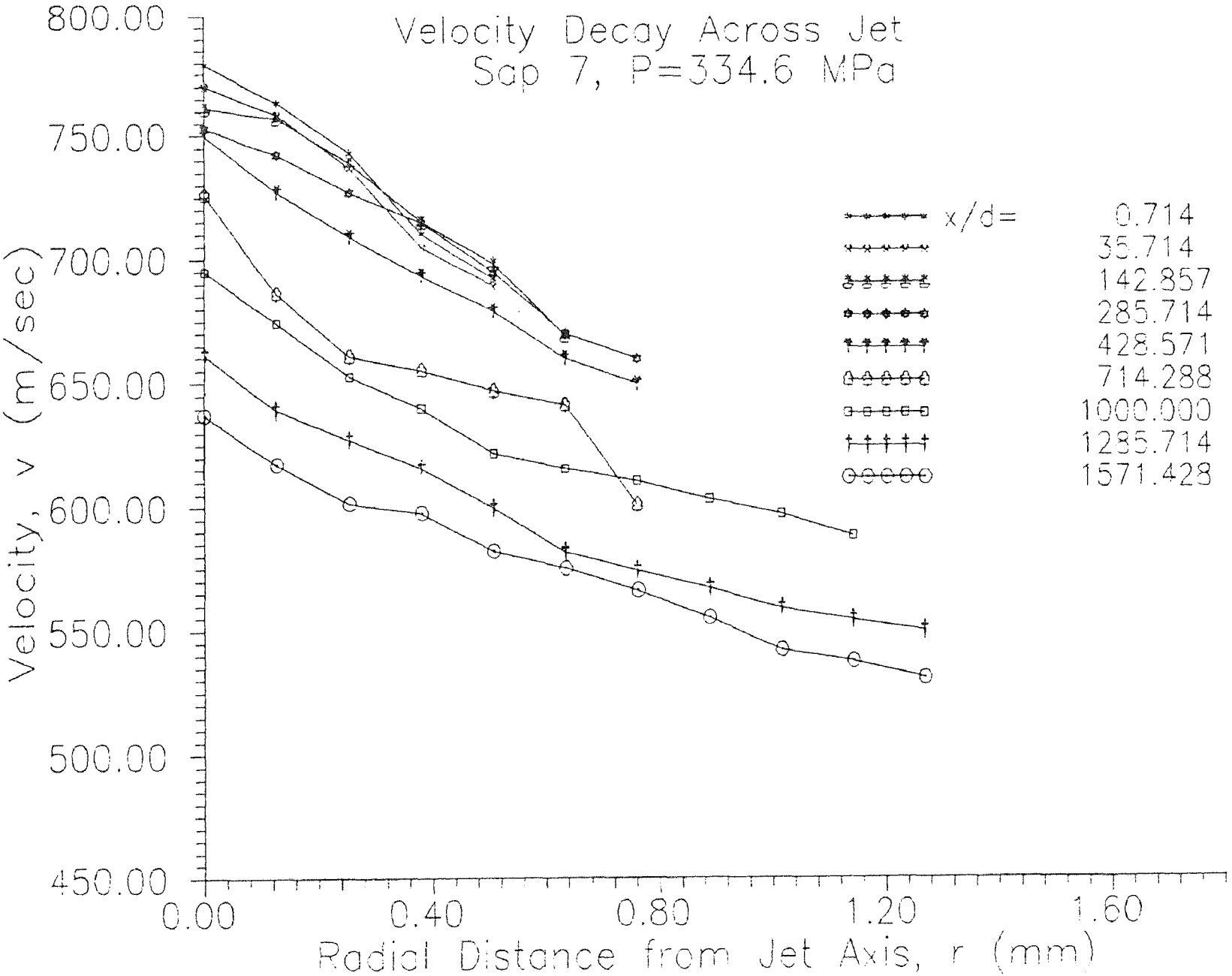

Fig. 5.19 Velocity distribution across jet for sap 7

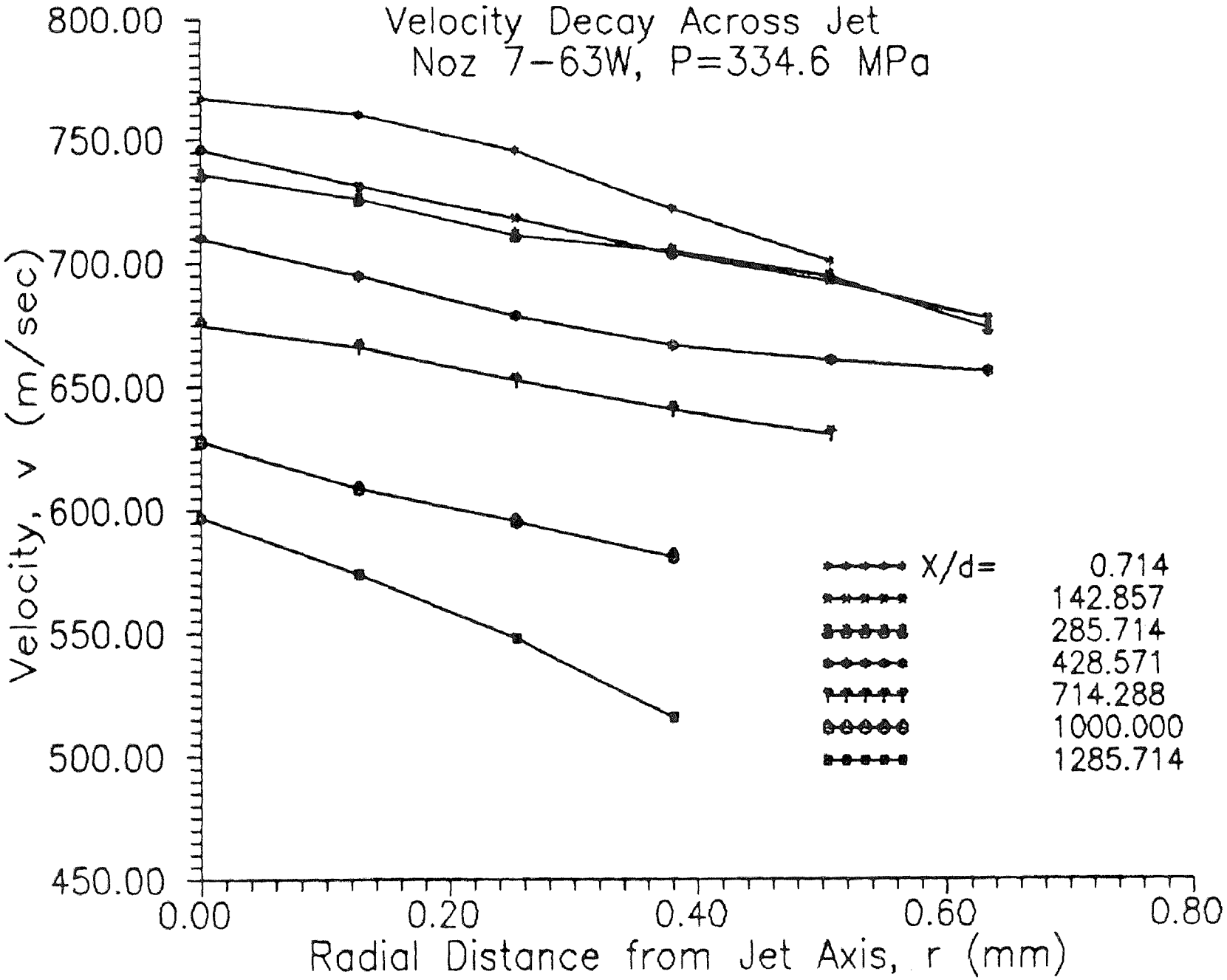

Fig. 5.20 Water velocity distribution across jet for Noz 7-63W

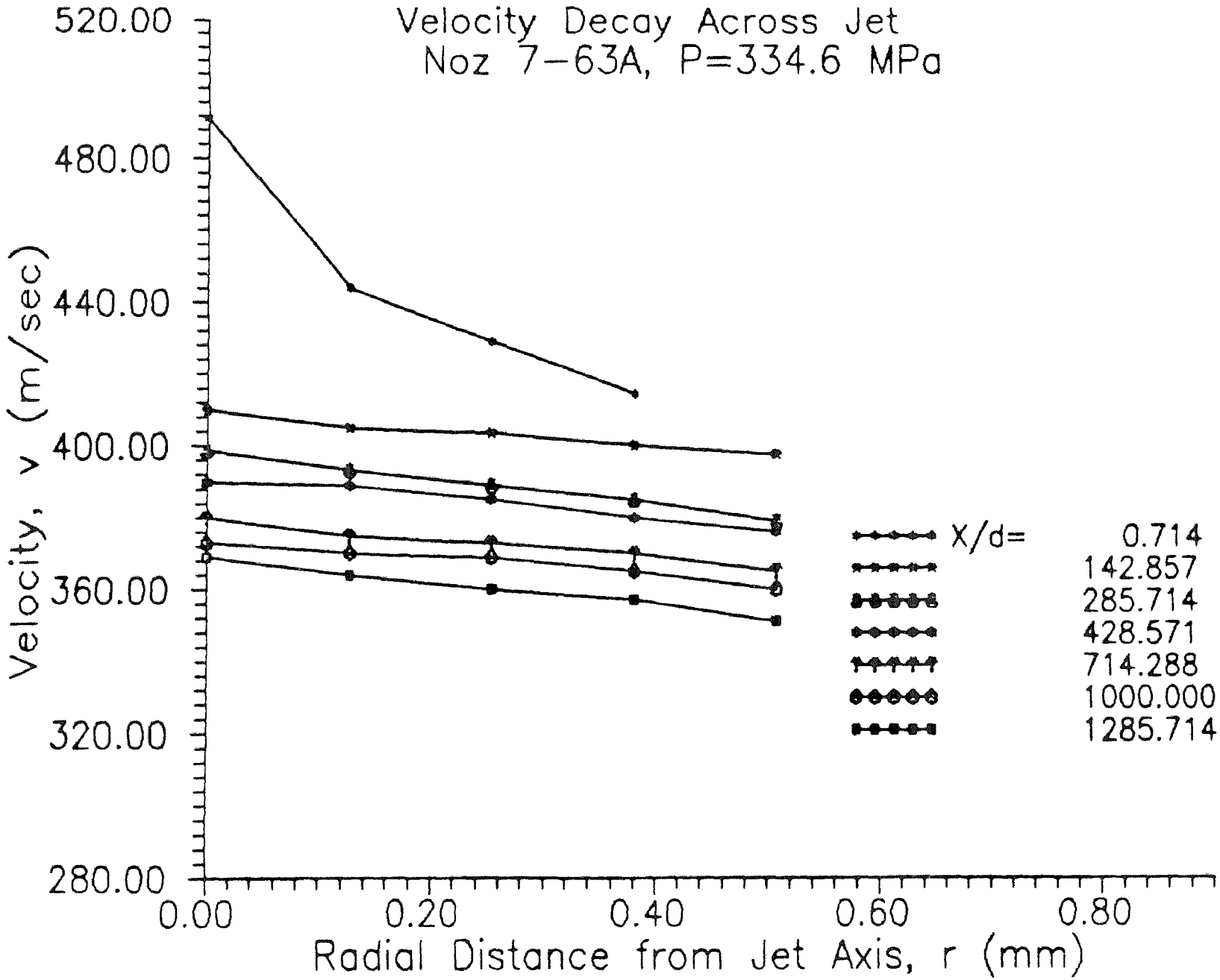

Fig. 5.21 Abrasive velocity distribution across jet for Noz 7-63A

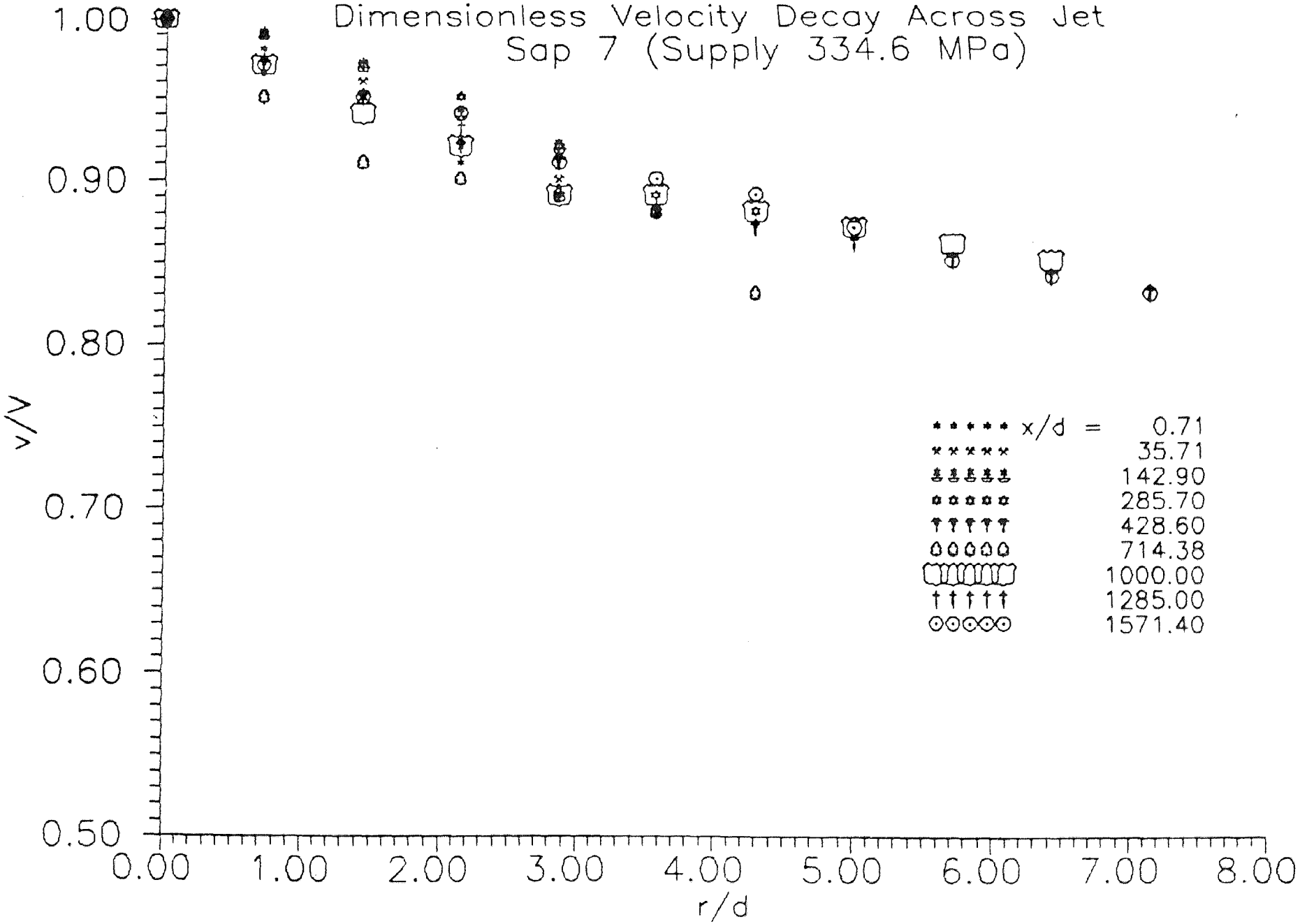

Fig. 5.22 Dimensionless velocity plot across jet for sap 7

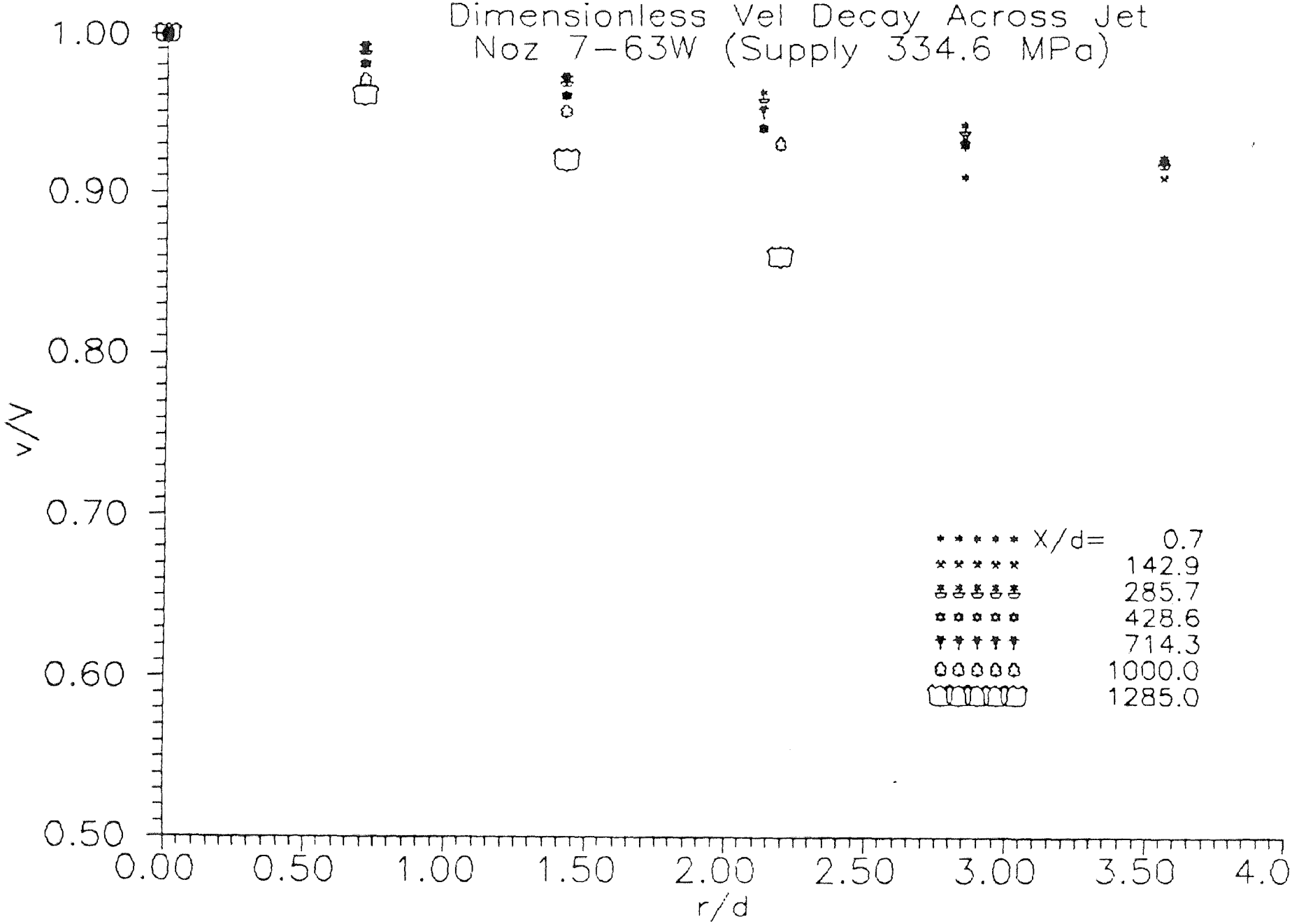

Fig. 5.23 Dimensionless water velocity plot across jet for Noz 7-63W

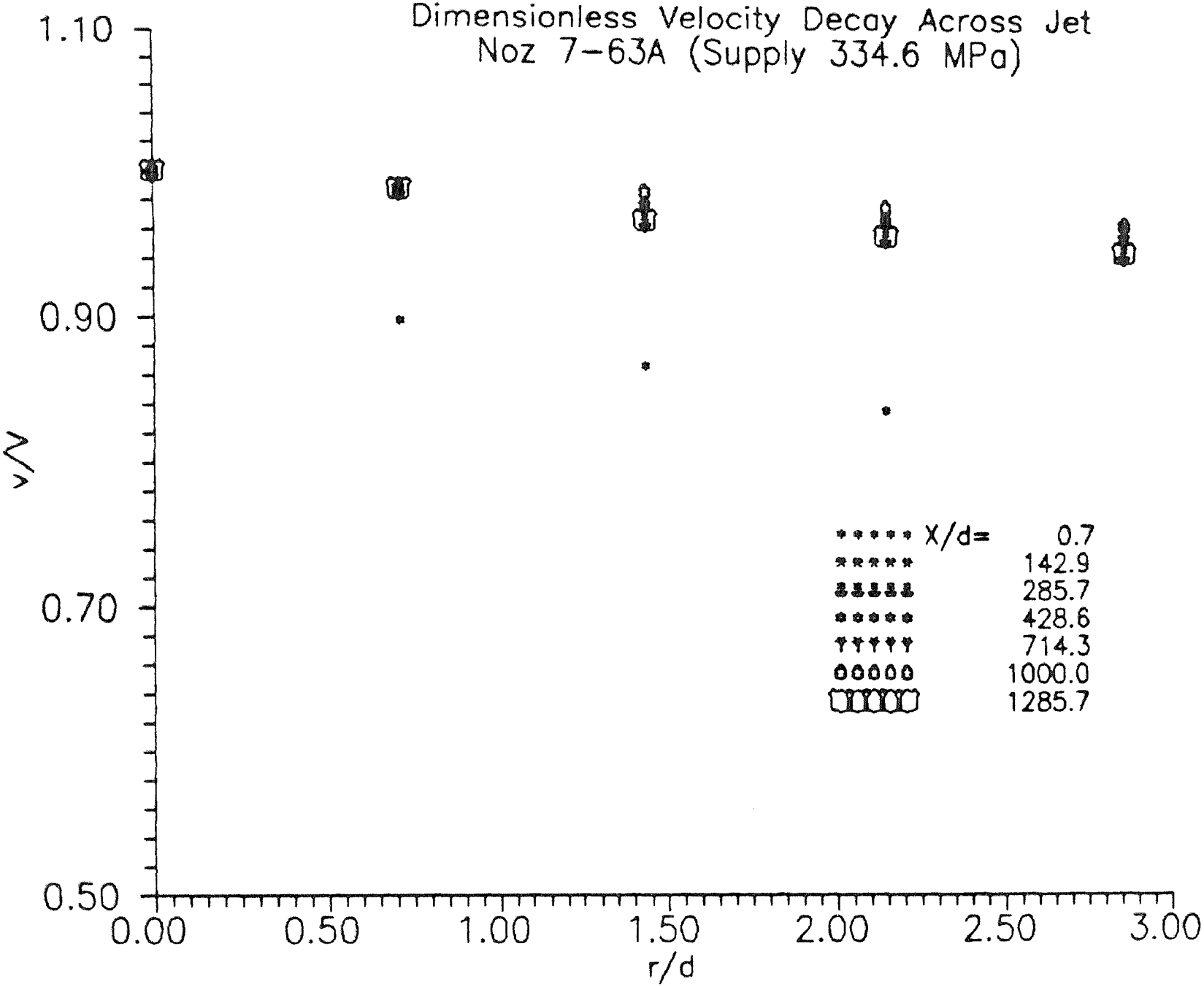

Fig. 5.24 Dimensionless abrasive velocity plot across jet for Noz 7-63A

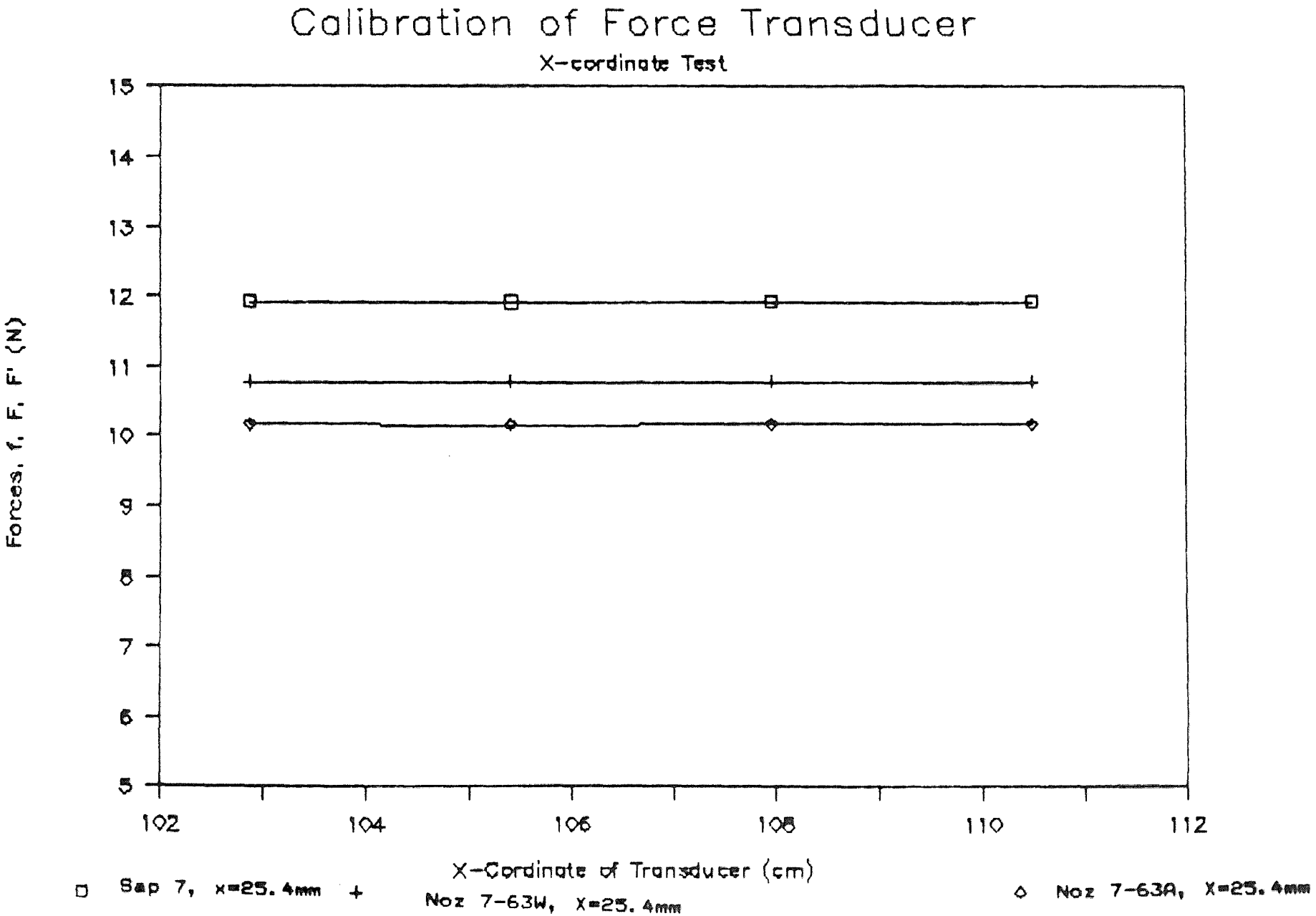

Fig. 5.25 Calibration of force transducer (X-cordinate test)

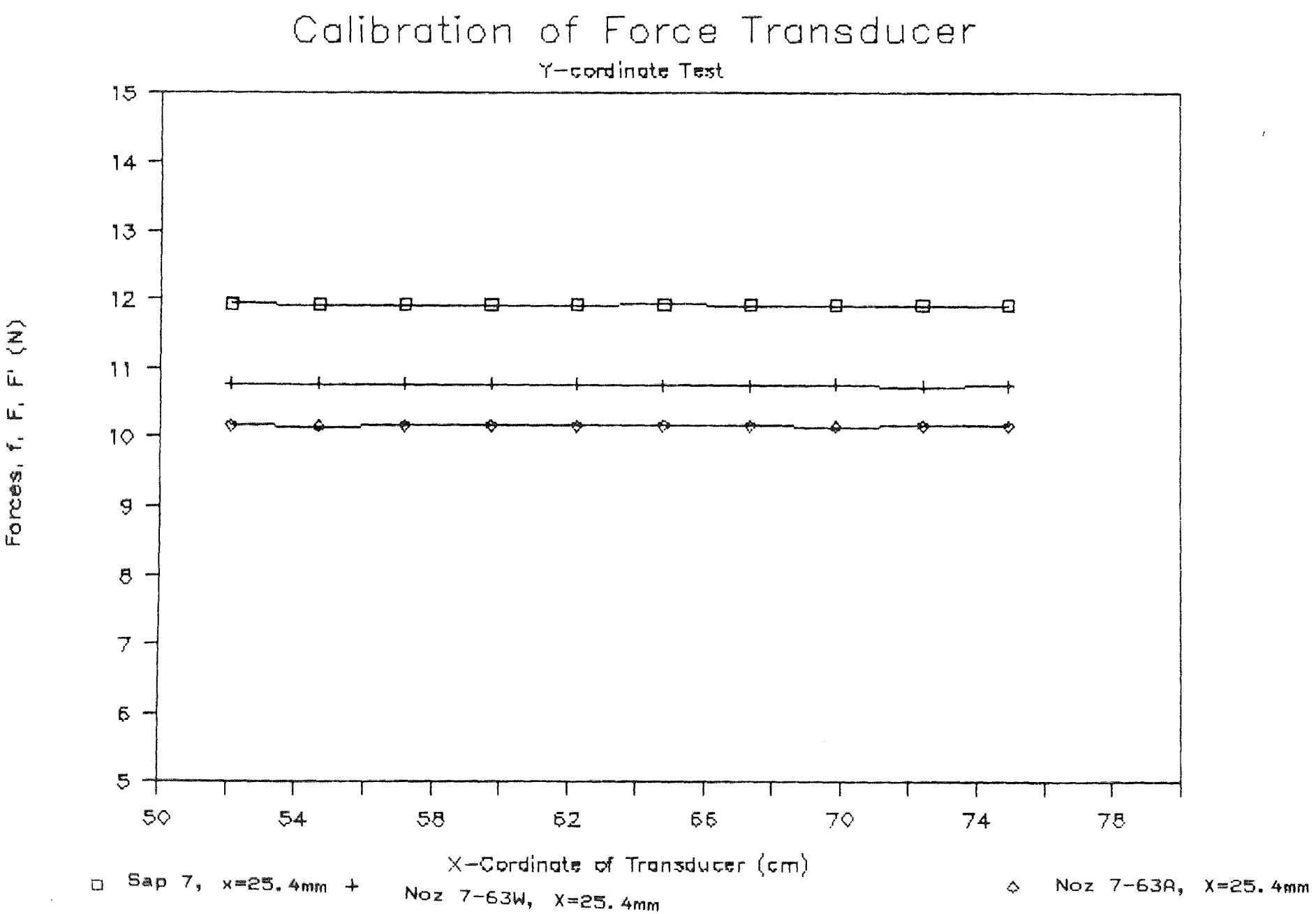

Fig. 5.26 Calibration of force transducer (Y-cordinate test)

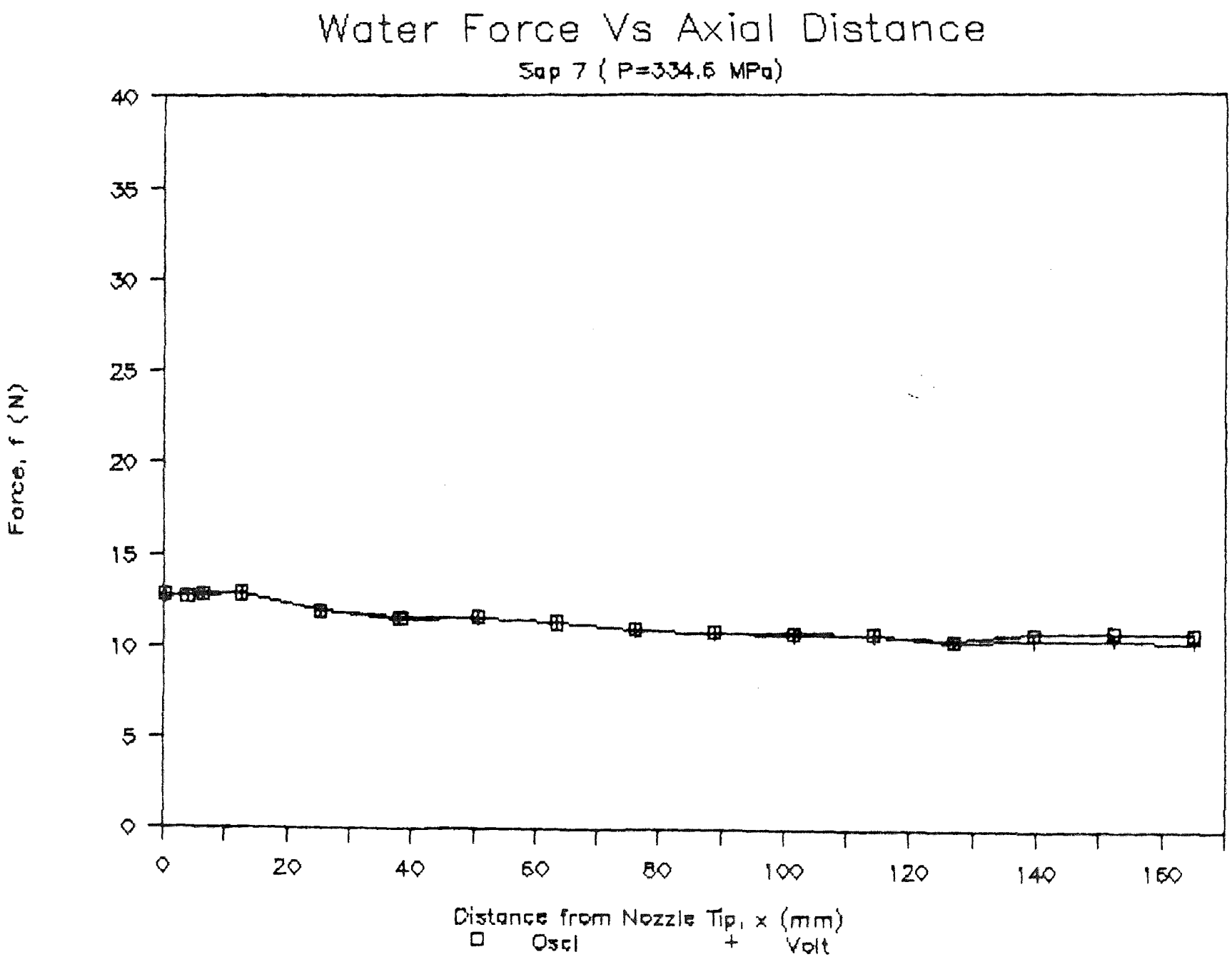

Fig. 5.27 Water force vs axial distance for Sap 7

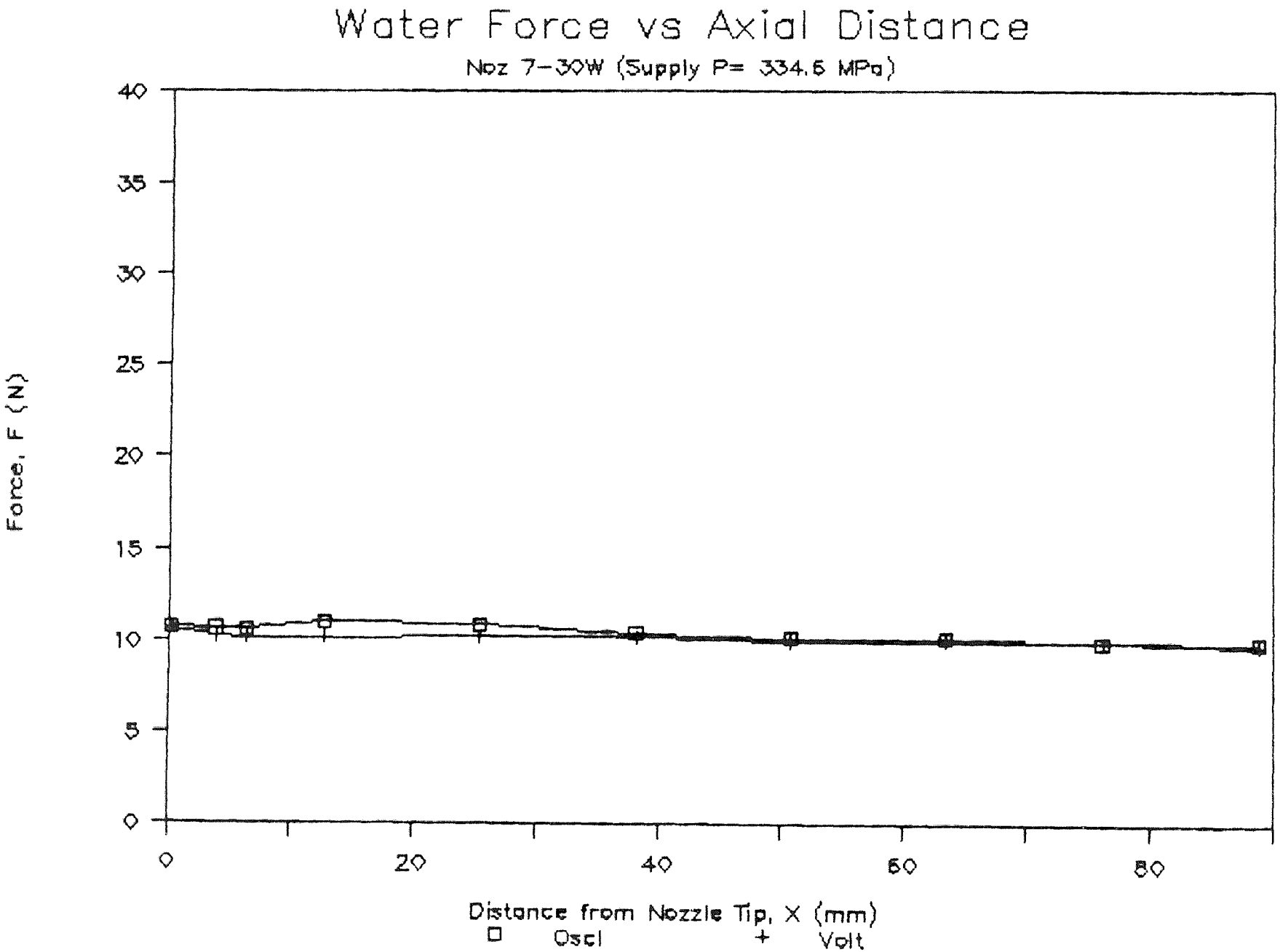

Fig. 5.28 Water force vs axial distance for Noz 7-30W

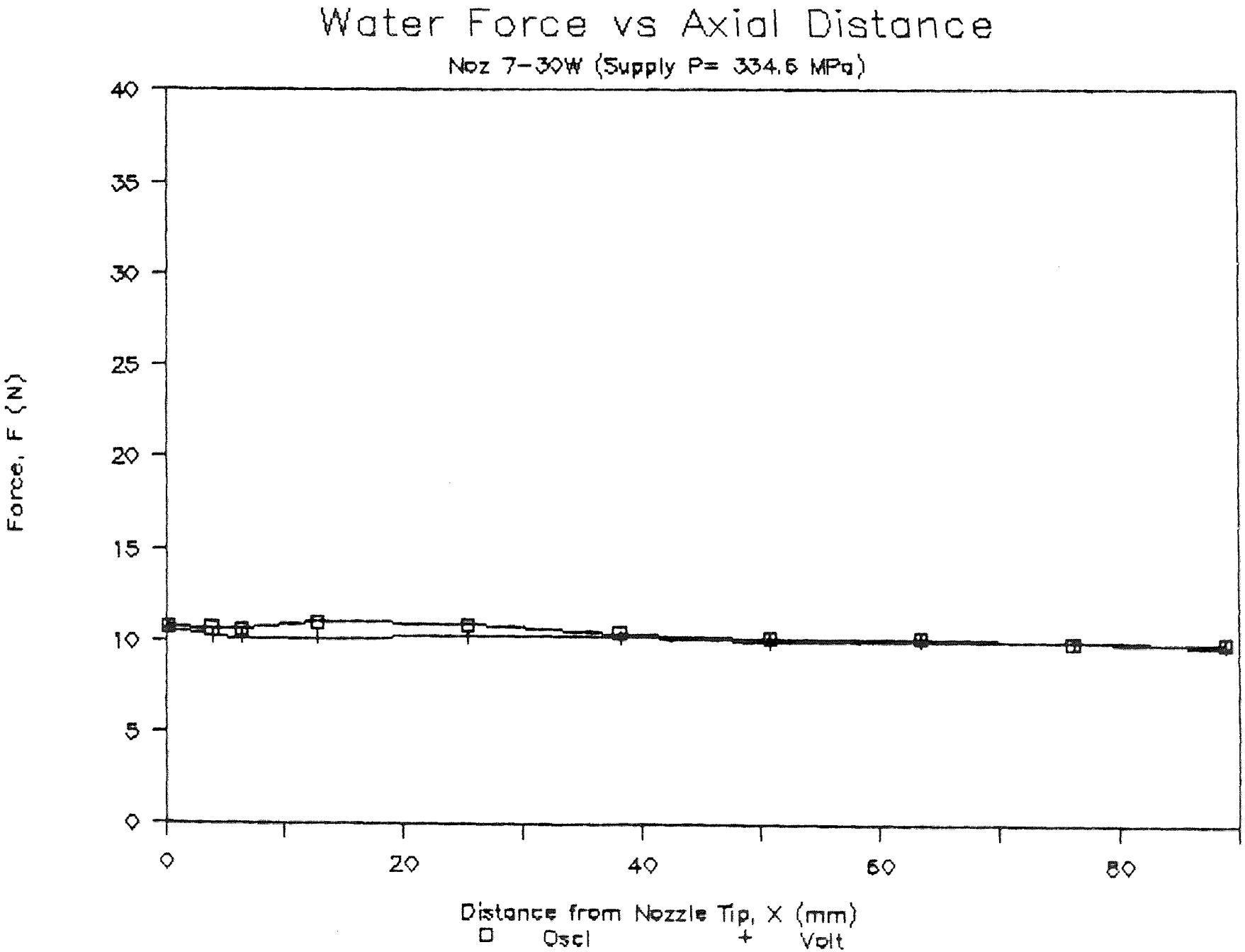

Fig. 5.28 Water force vs axial distance for Noz 7-30W

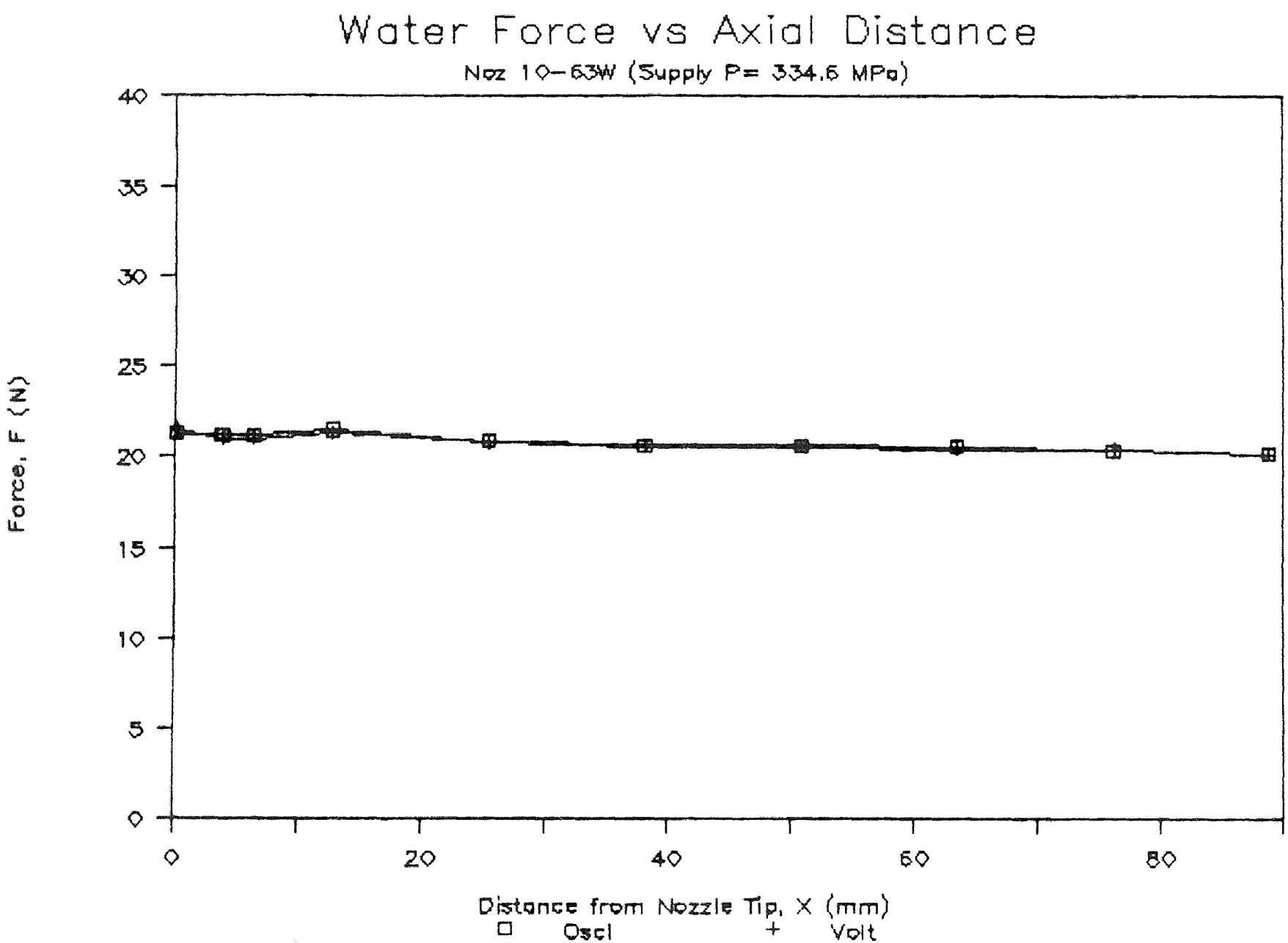

Fig. 5.30 Water force vs axial distance for Noz 10-63W

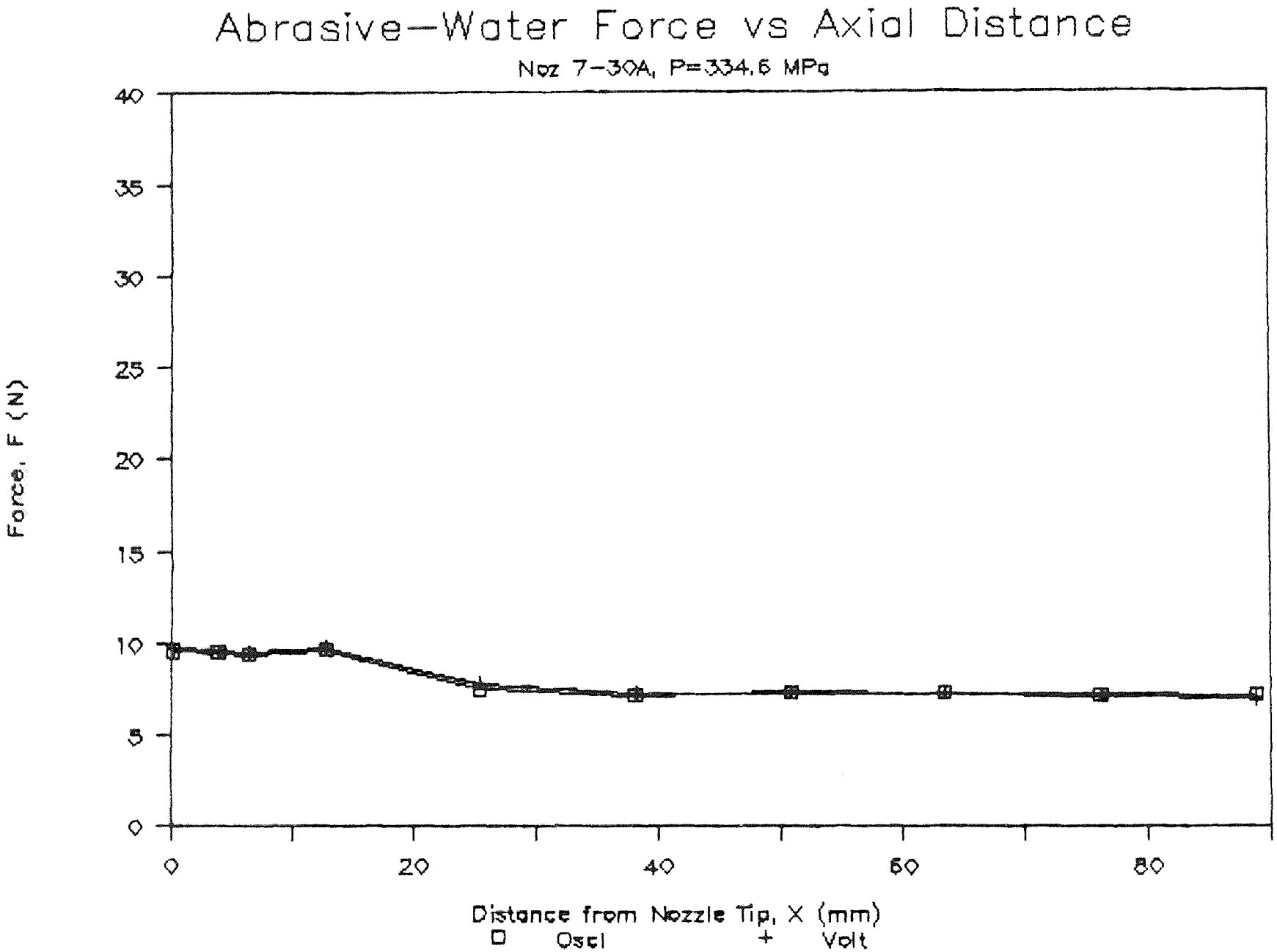

Fig. 5.31 AW force vs axial distance for Noz 7-30A

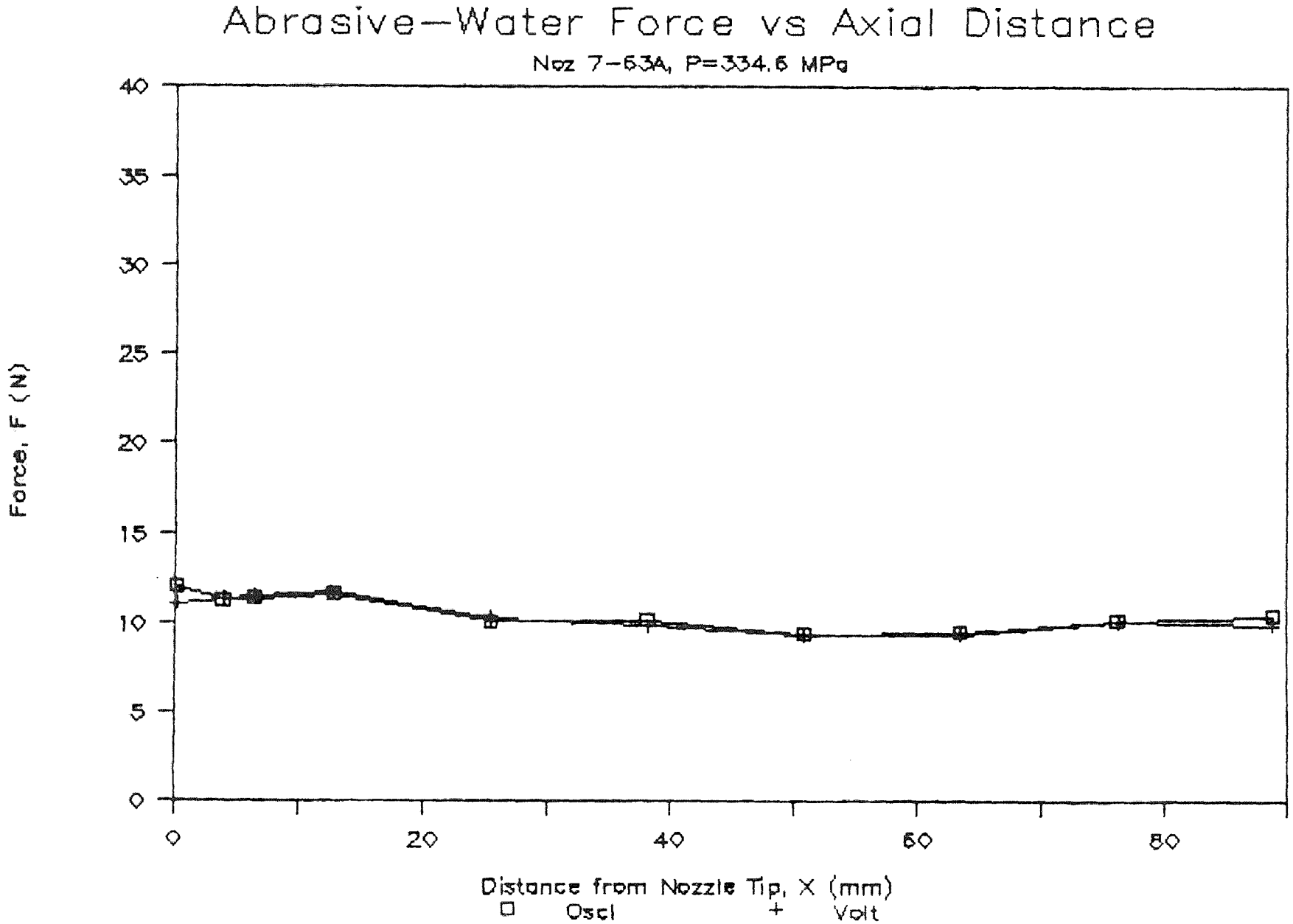

Fig. 5.32 AW force vs axial distance for Noz 7-63A

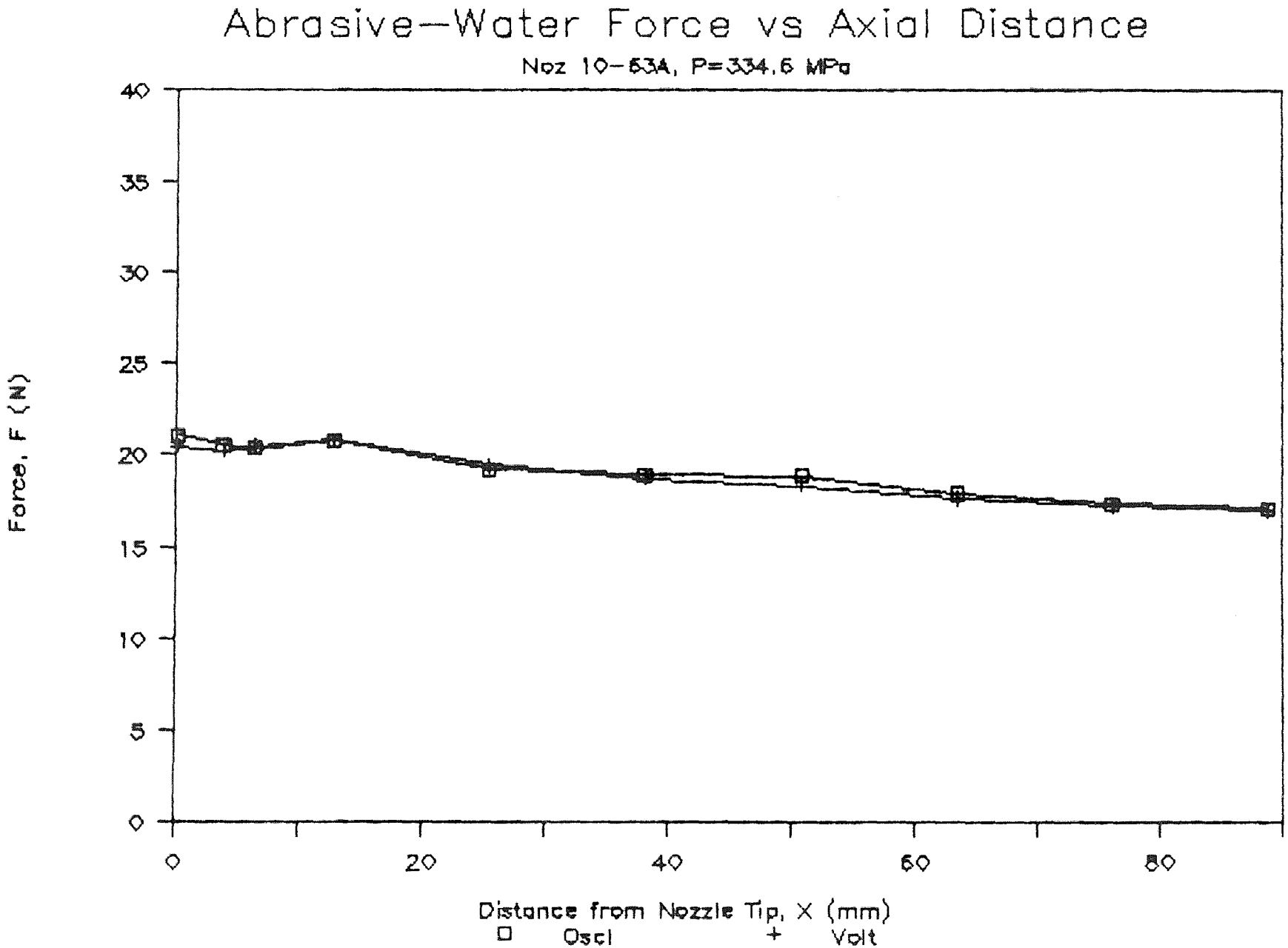

Fig. 5.33 AW force vs axial distance for Noz 10-63A

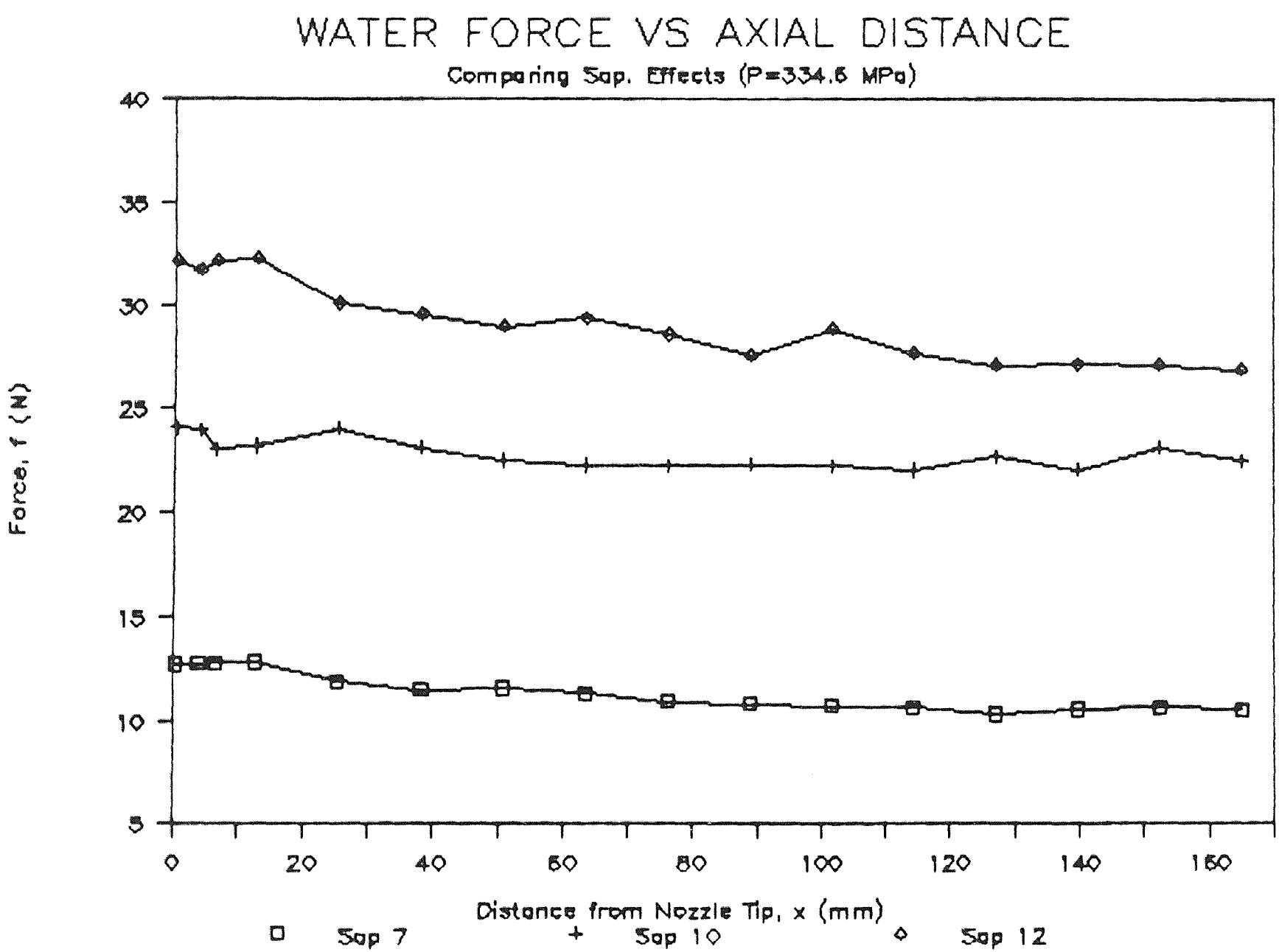

Fig. 5.34 Sapphire nozzle effects on force

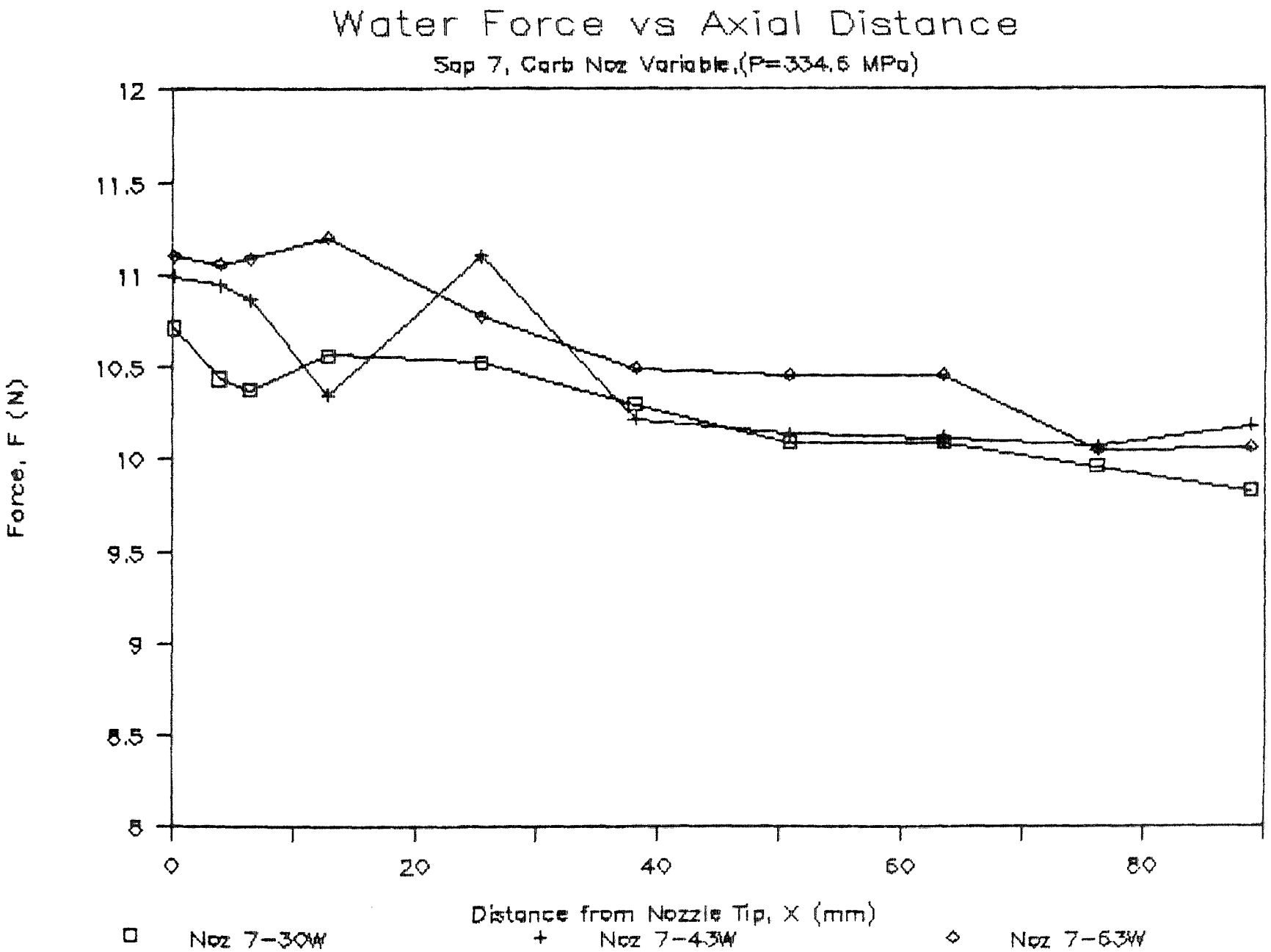

Fig. 5.35 Water force plot showing carbide effects on sapphire

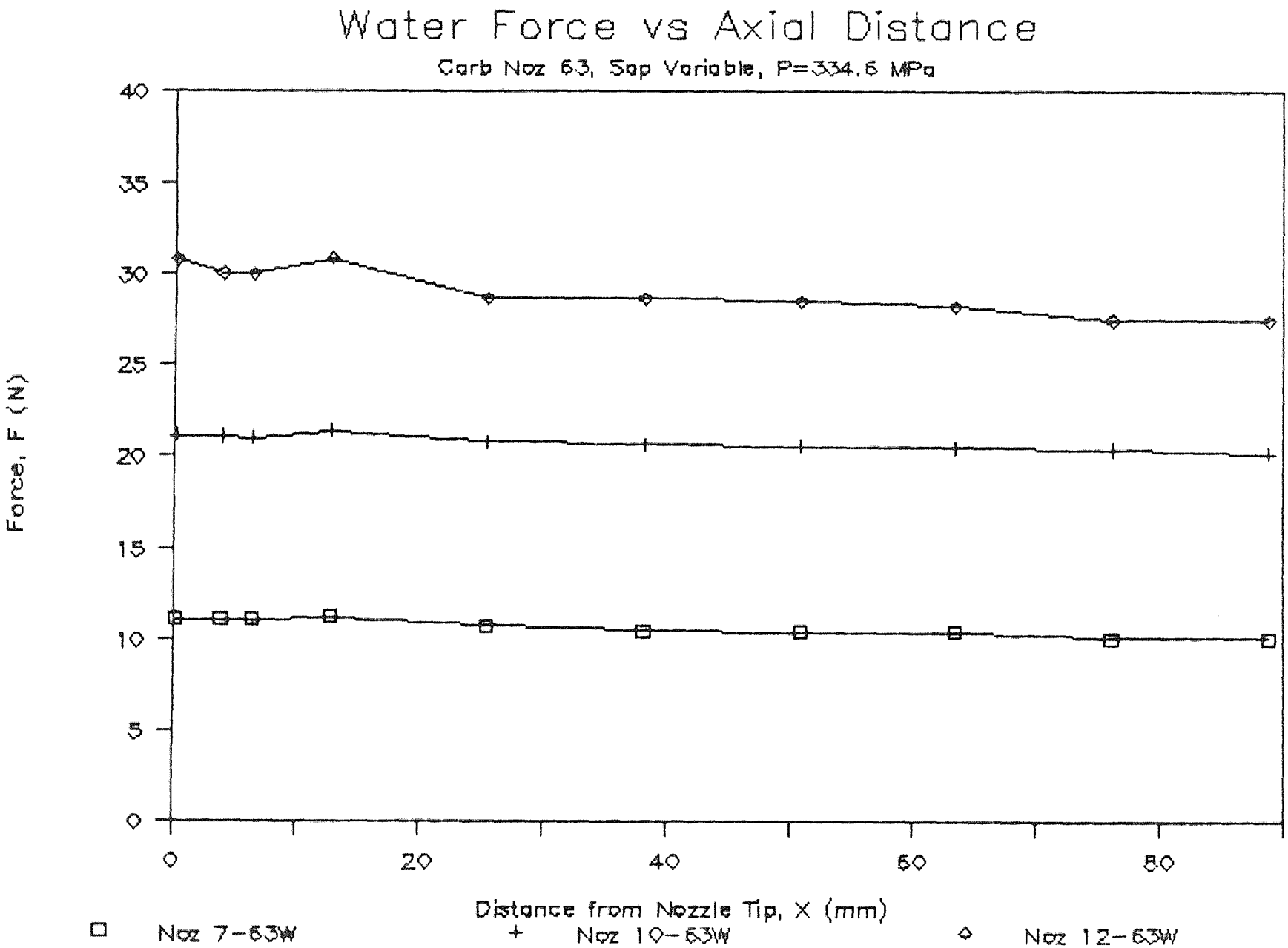

Fig. 5.36 Water force plot showing sapphire effects on carbide

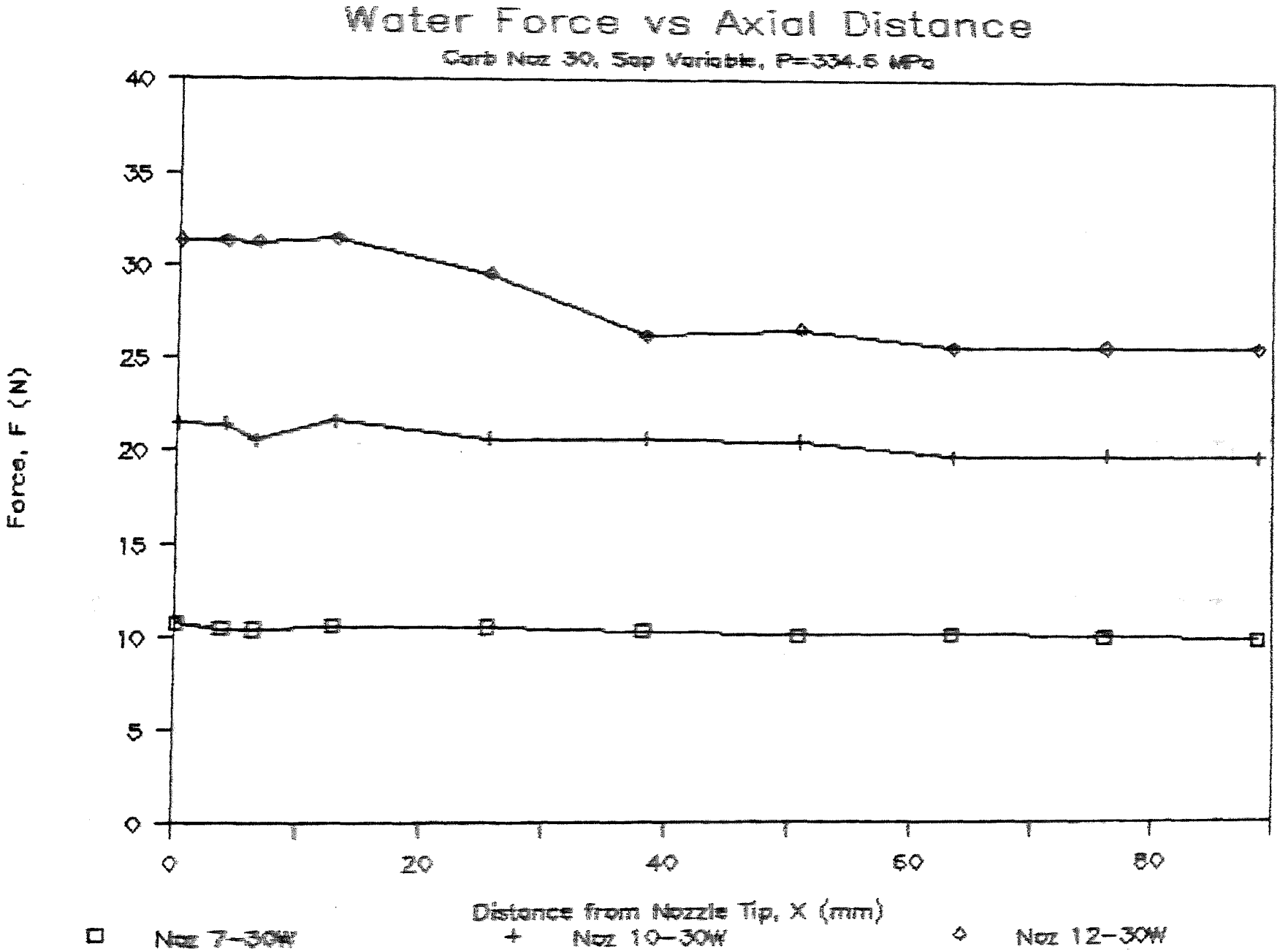

Fig. 5.37 Water force plot showing sapphire effects on carbide

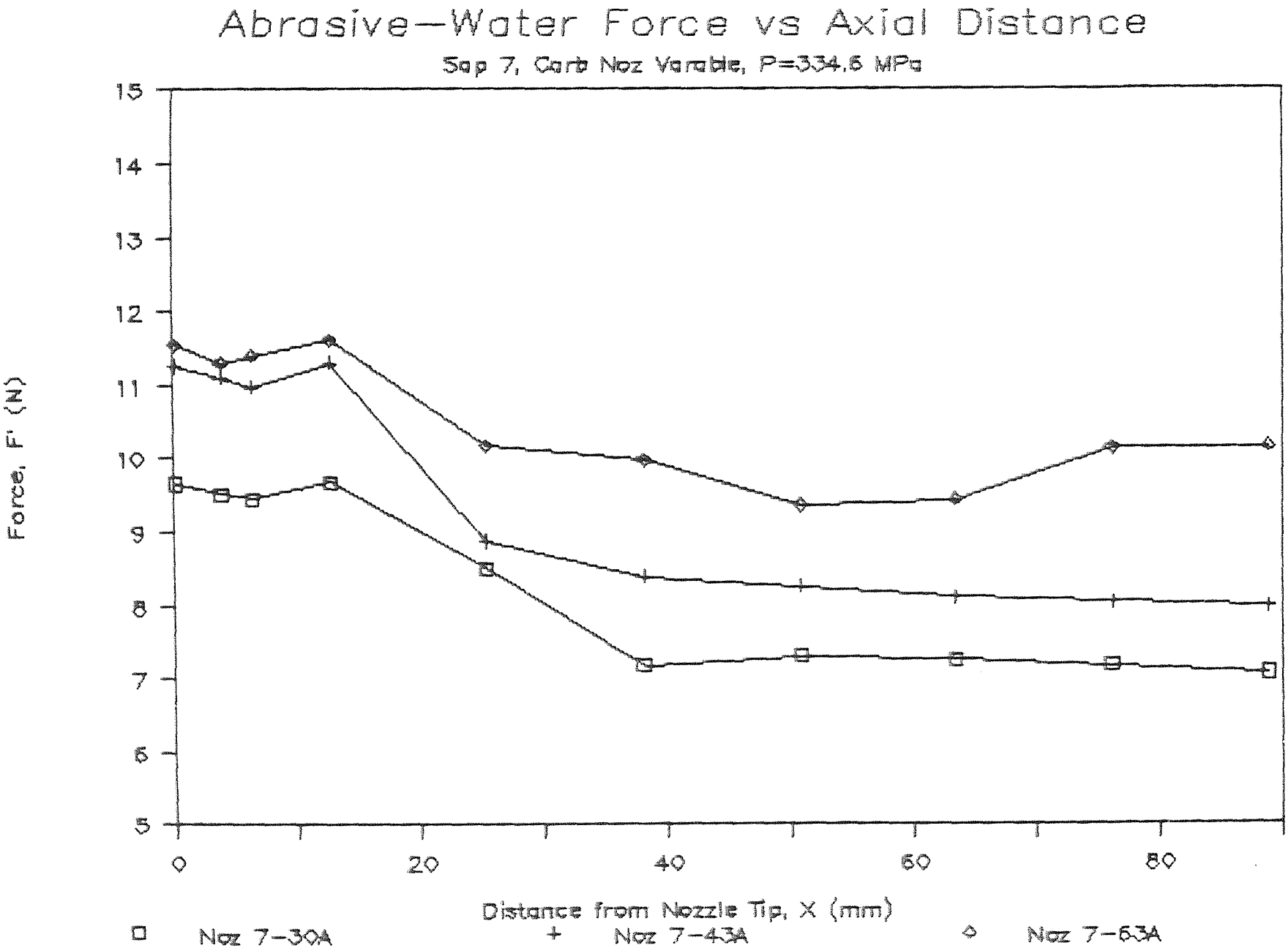

Fig. 5.38 AW force plot showing carbide effects on sapphire

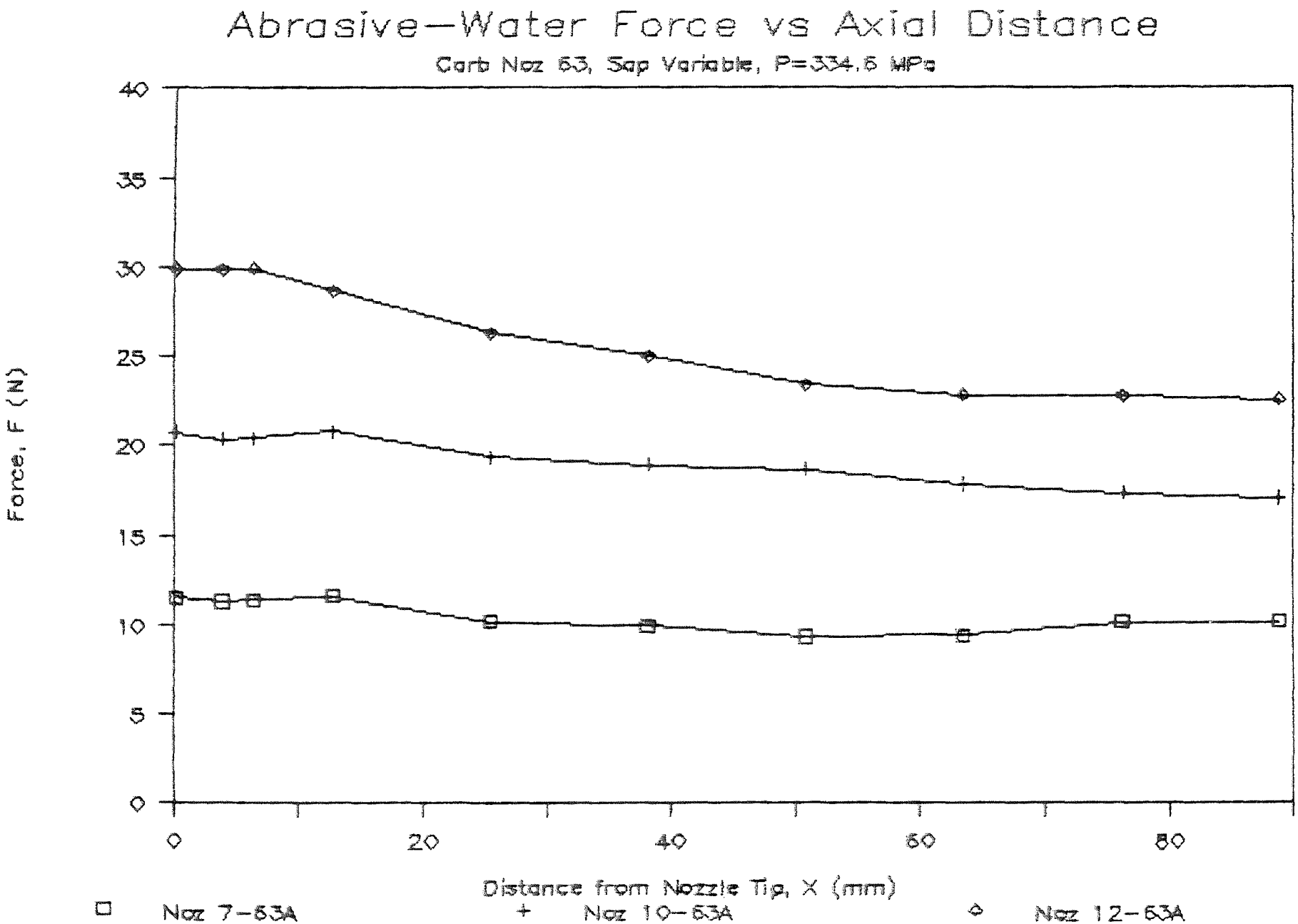

Fig. 5.39 AW force plot showing sapphire effects on carbide

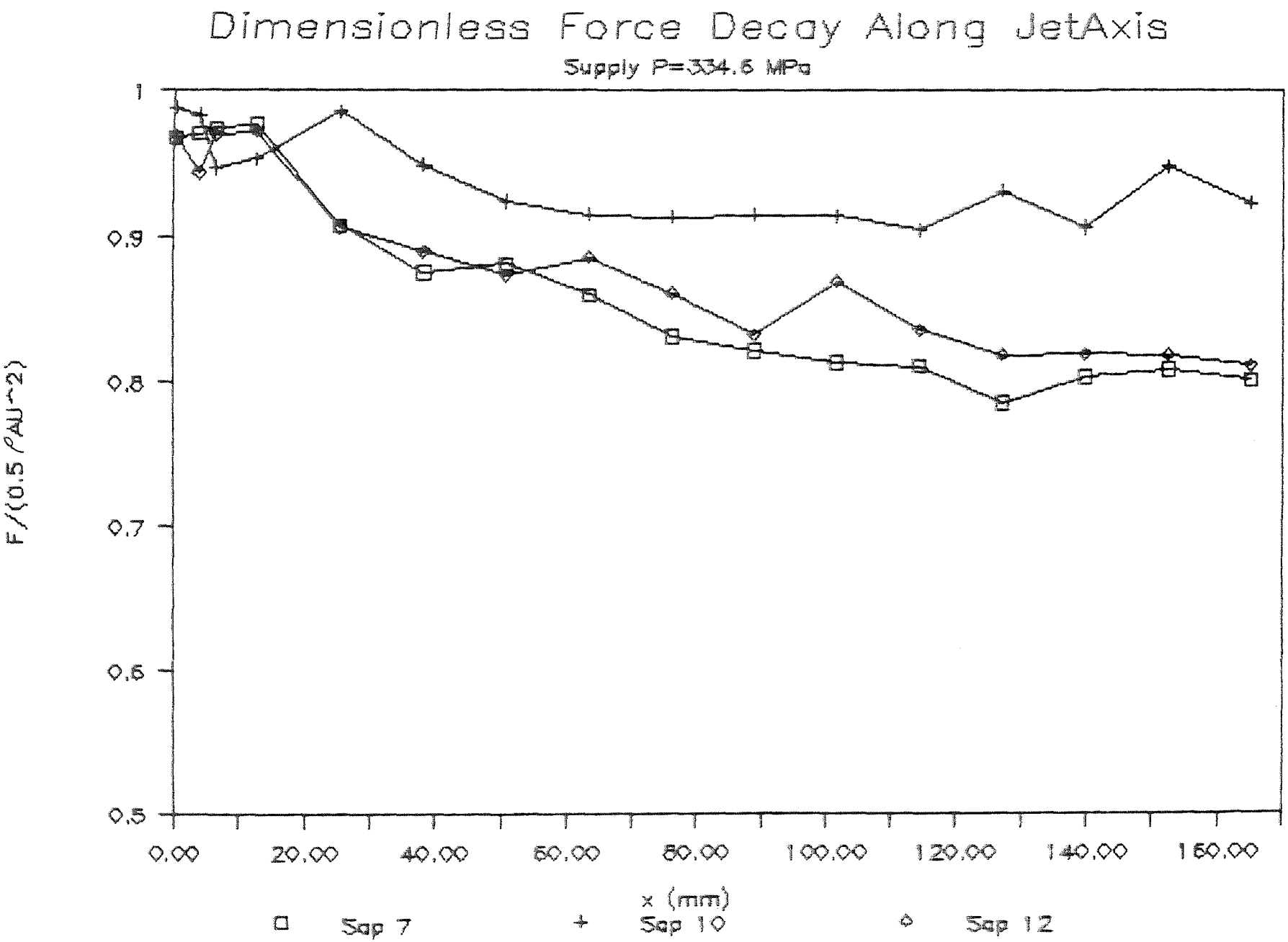

Fig. 5.40 Dimensionless water force vs stand off distance for different sapphire nozzles

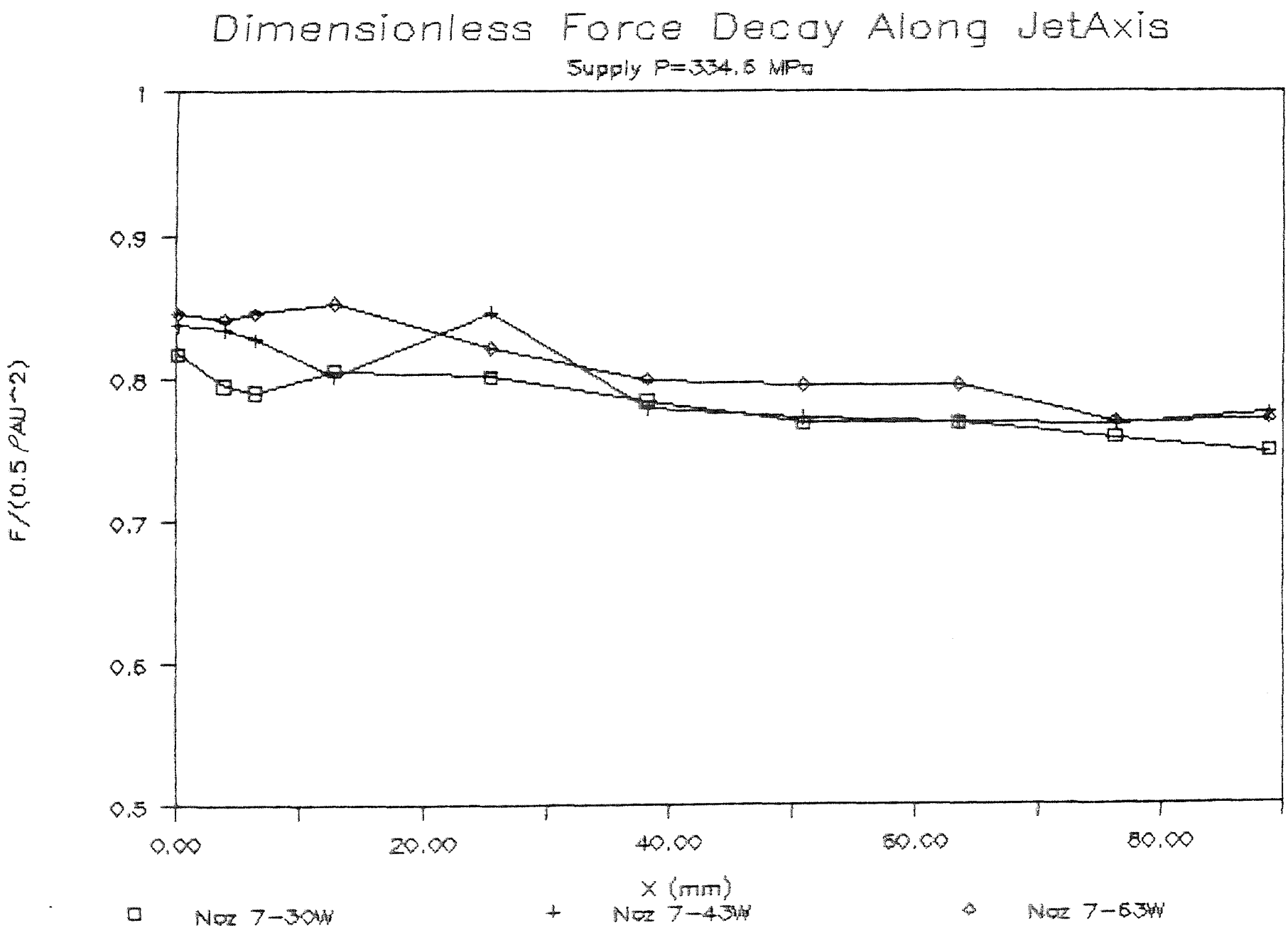

Fig. 5.41 Showing the carbide effects on dimensionless water force decay along jet axis

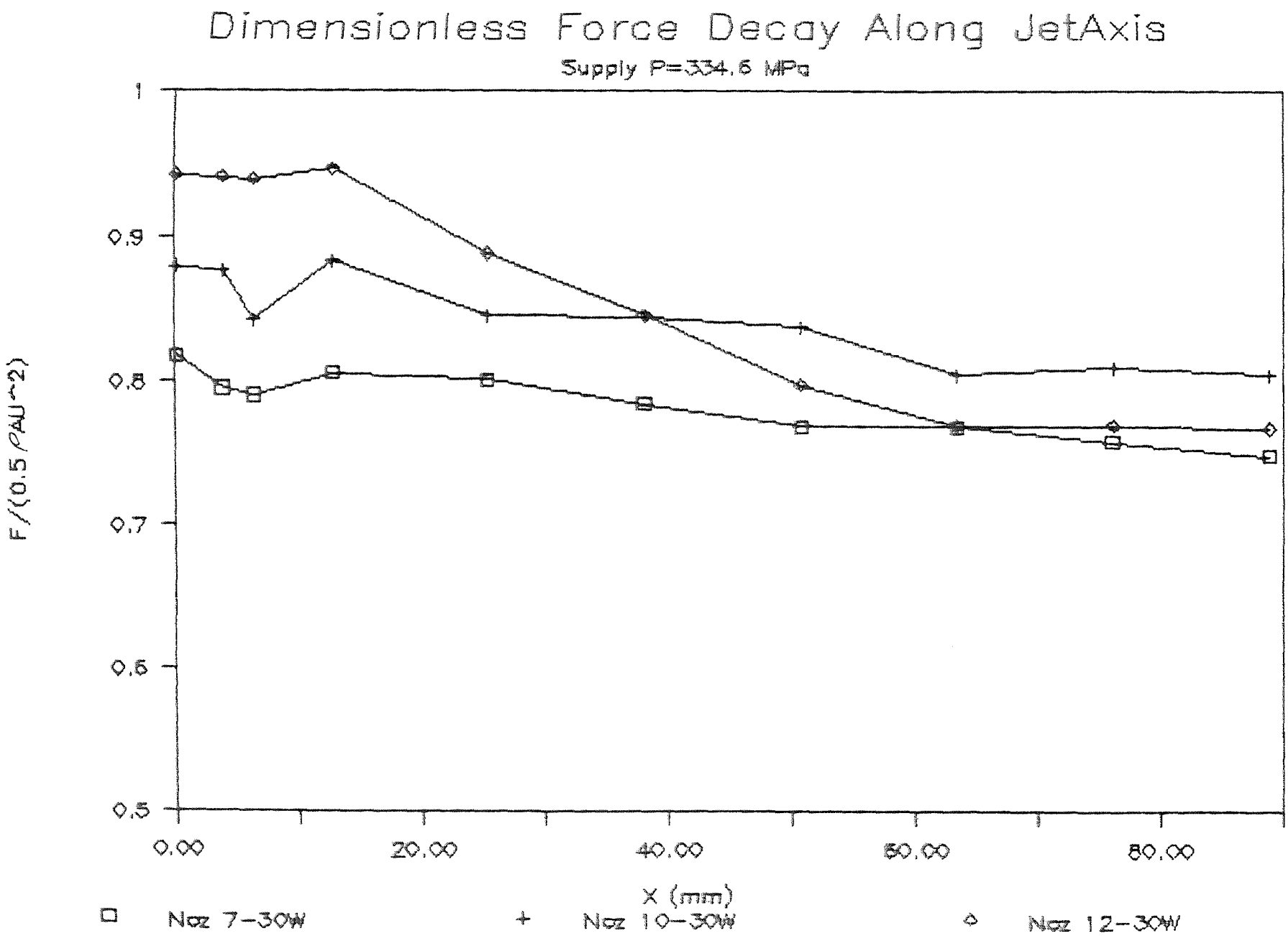

Fig. 5.42 Showing the sapphire effects on dimensionless water force decay along jet axis

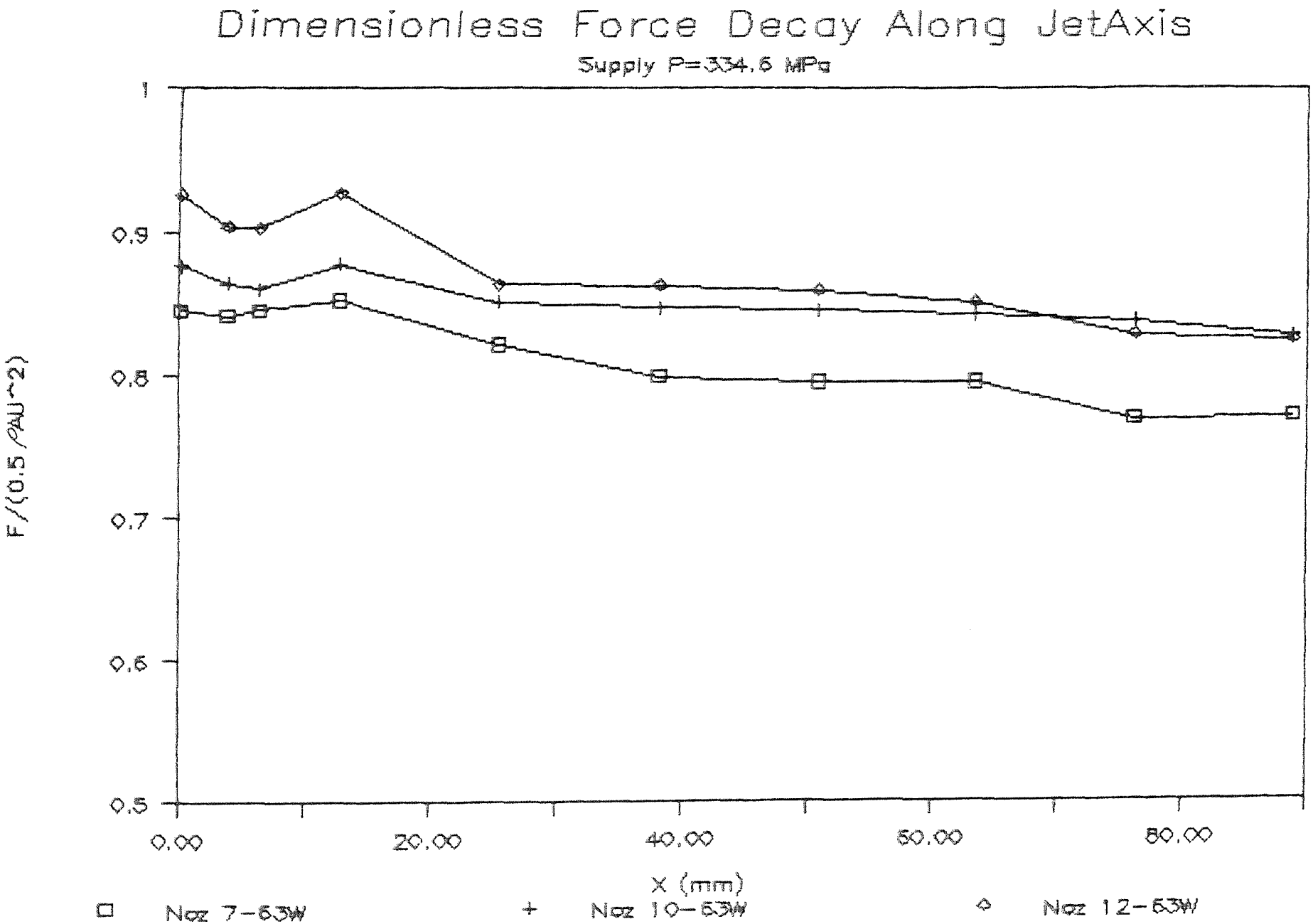

Fig. 5.43 Showing the sapphire effects on dimensionless water force decay along jet axis

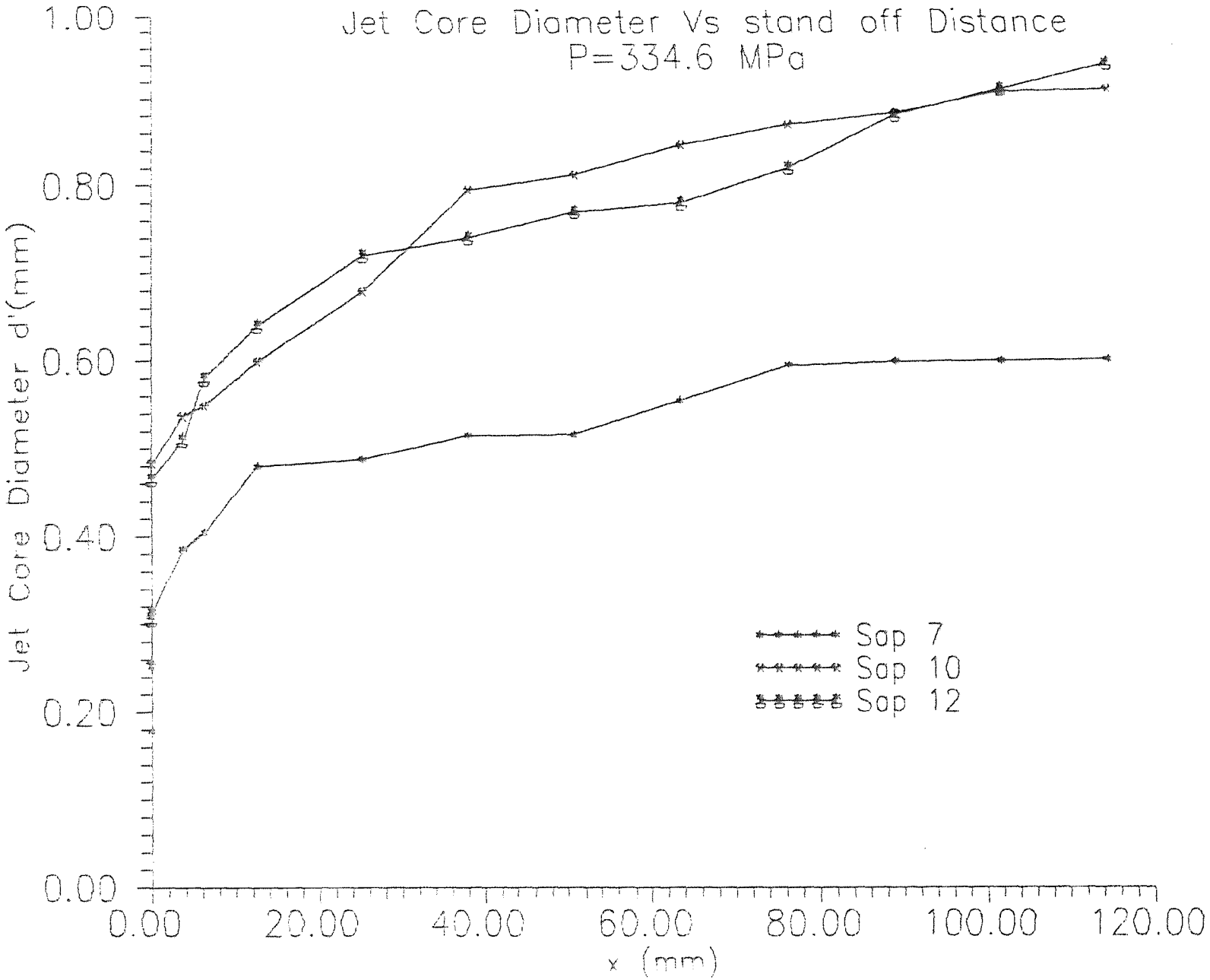

Fig. 5.44 Jet core diameter vs stand off distance for different sapphire nozzles

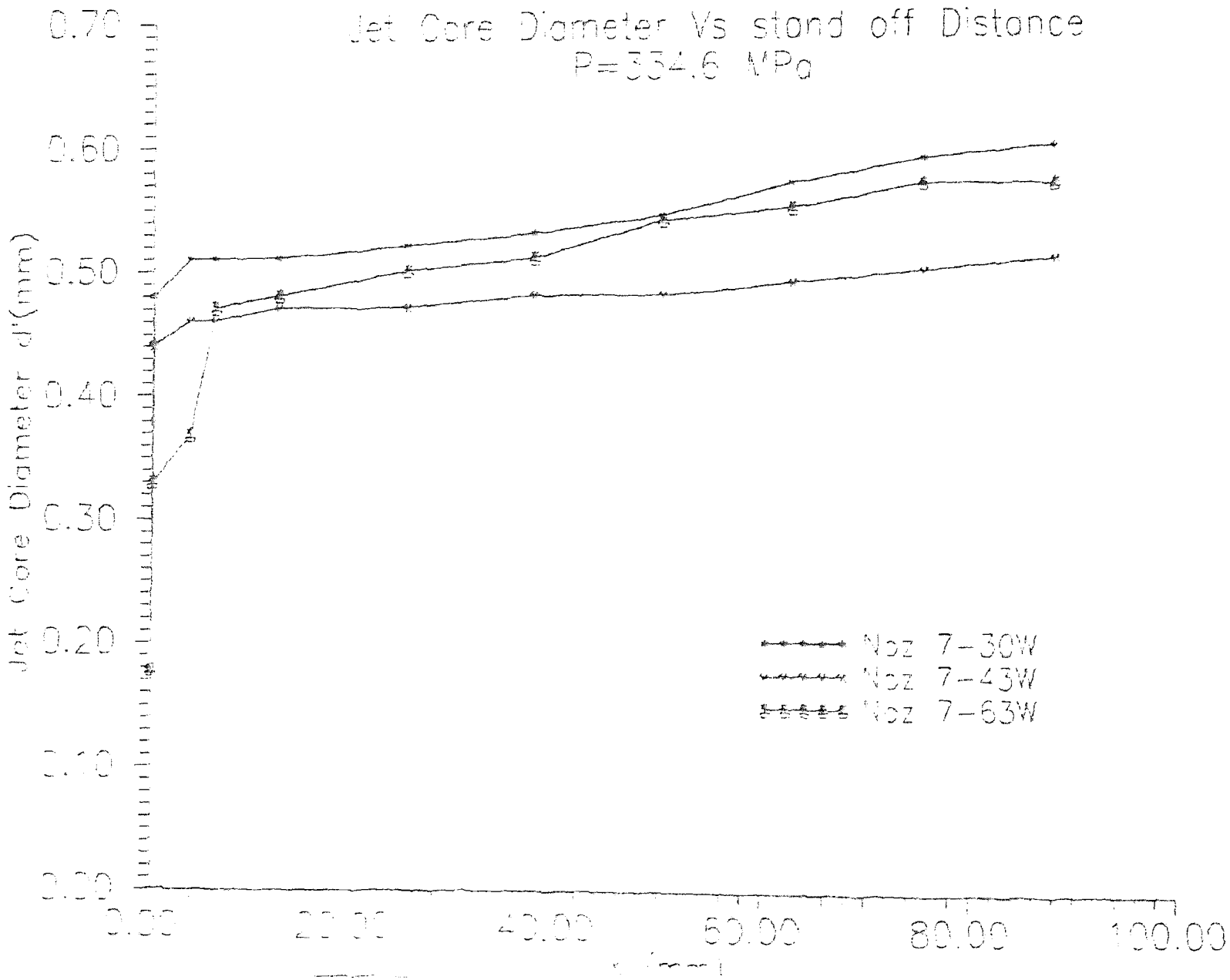

Fig. 5.45 Jet core diameter vs stand off distance showing carbide effects on water flow

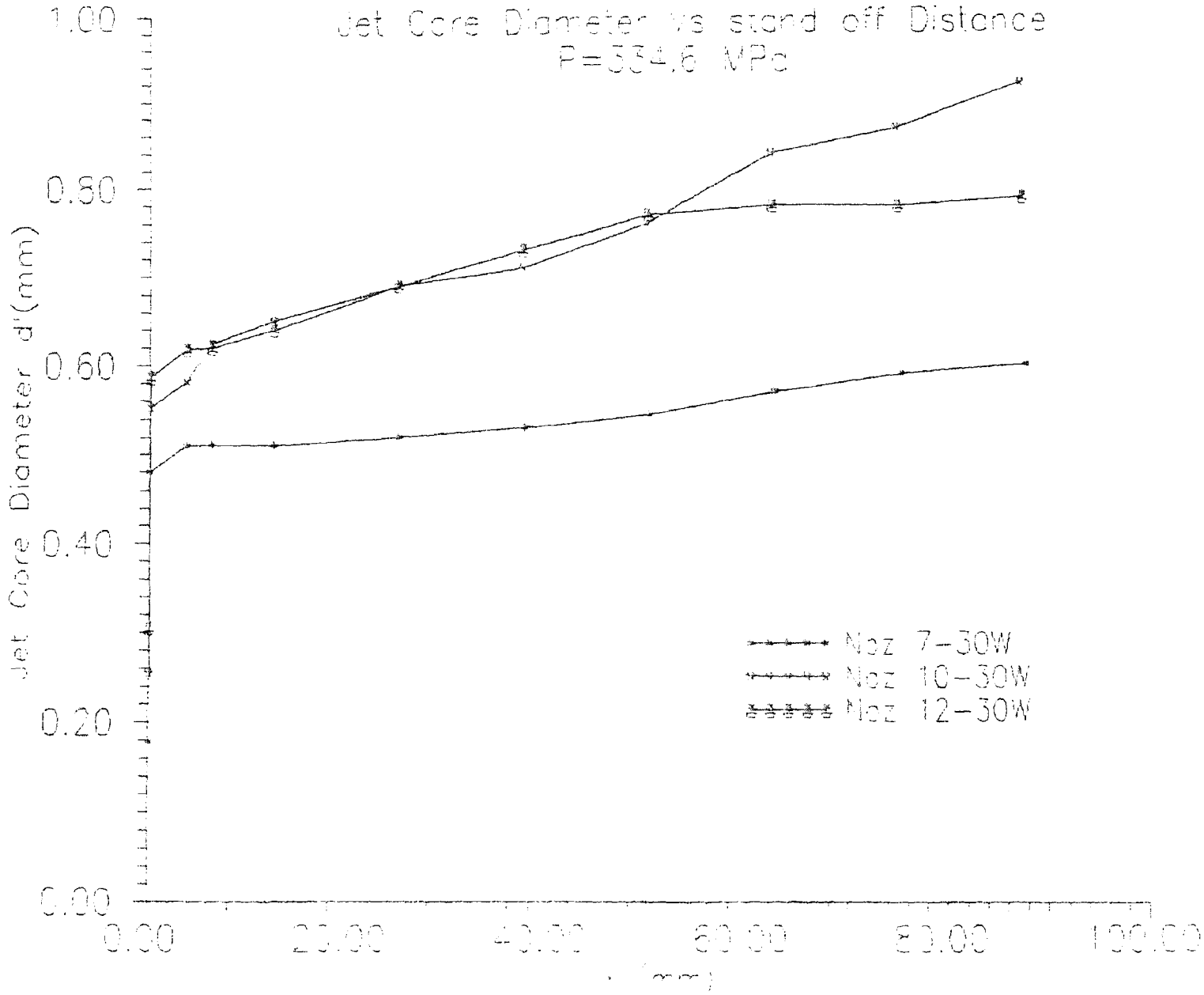

Fig. 5.46 Jet core diameter vs stand off distance showing sapphire effects on water flow

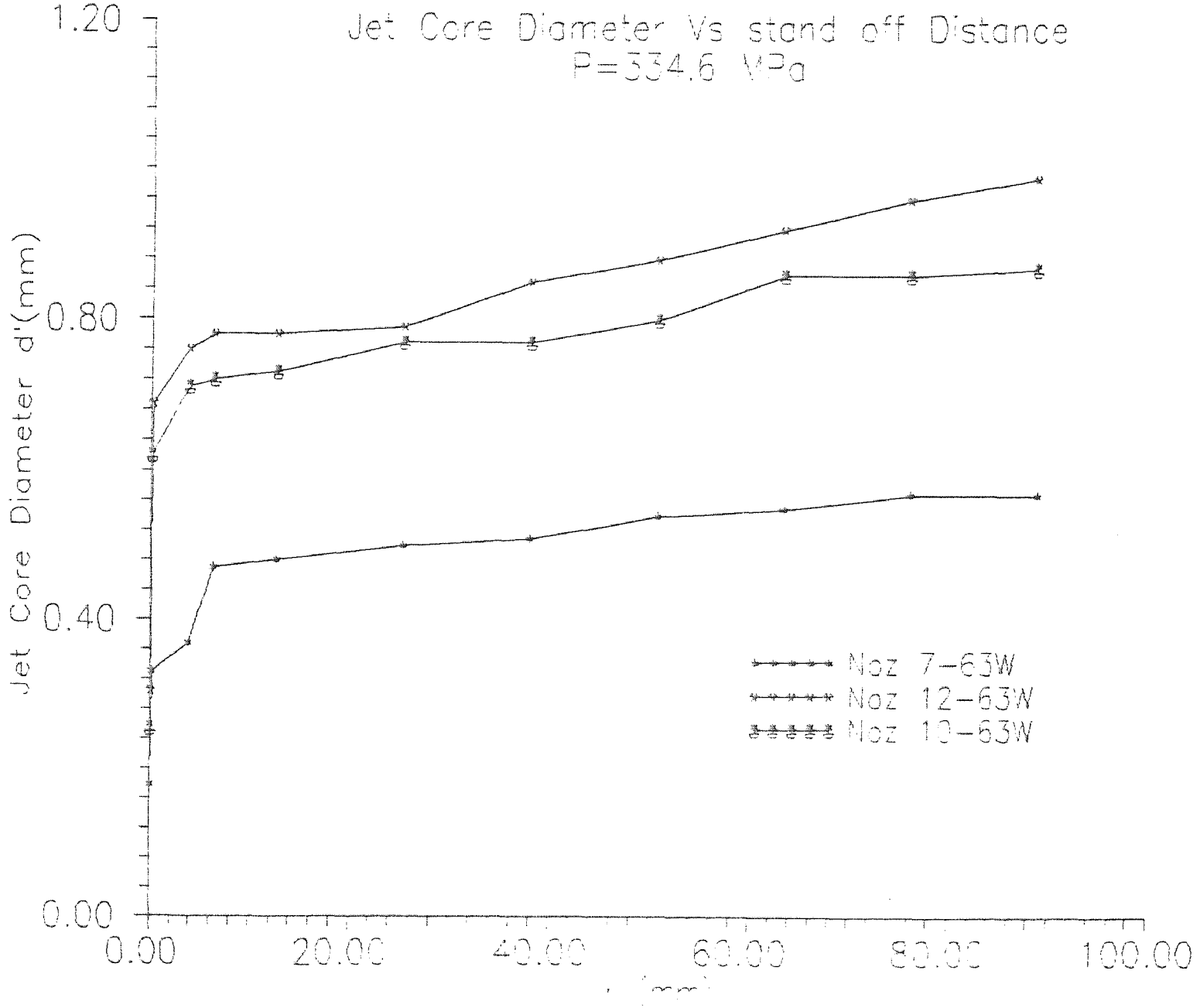

Fig. 5.47 Jet core diameter vs stand off distance showing sapphire effects on water flow

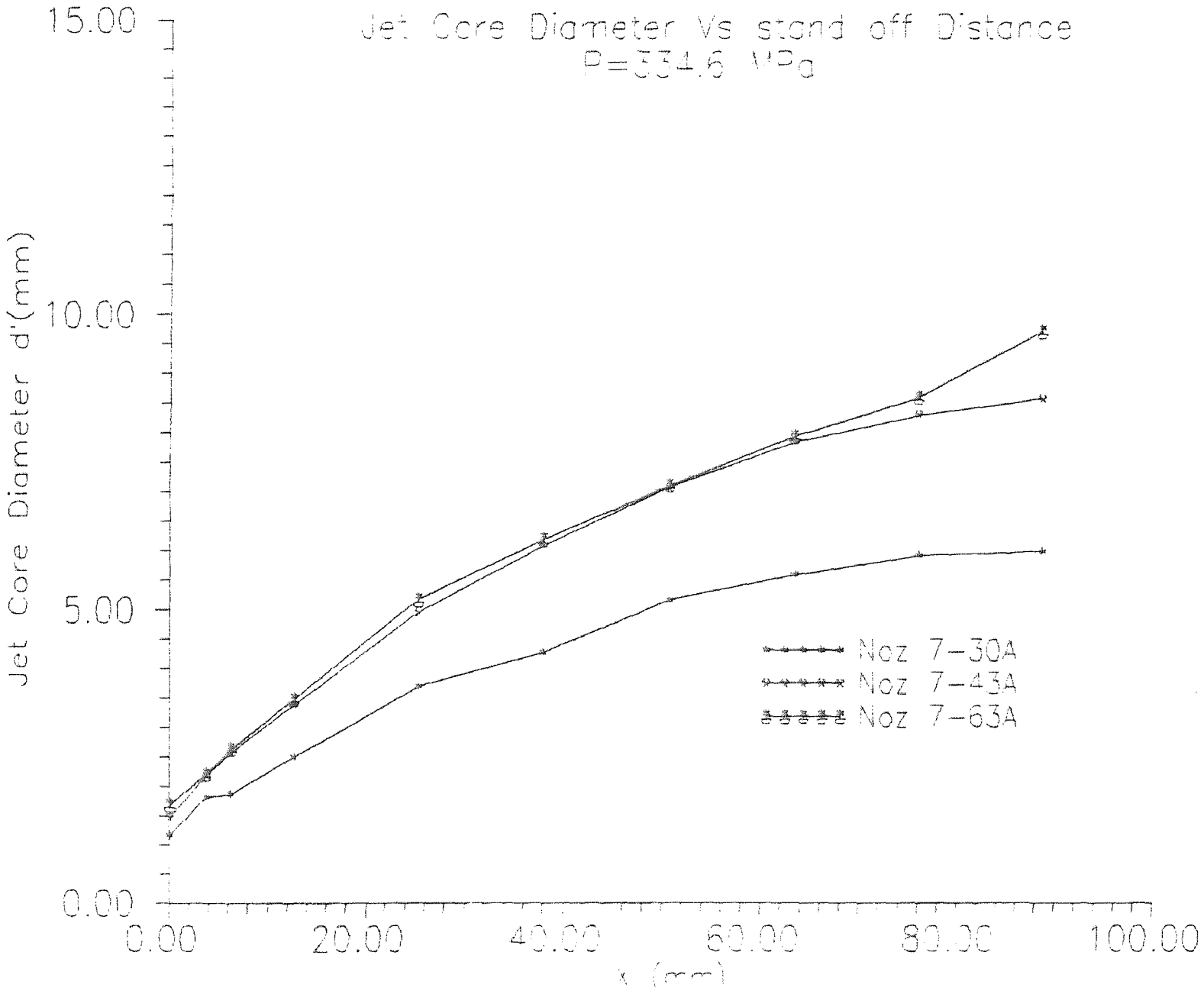

Fig. 5.48 Jet core diameter vs stand off distance showing carbide effects on water abrasive flow

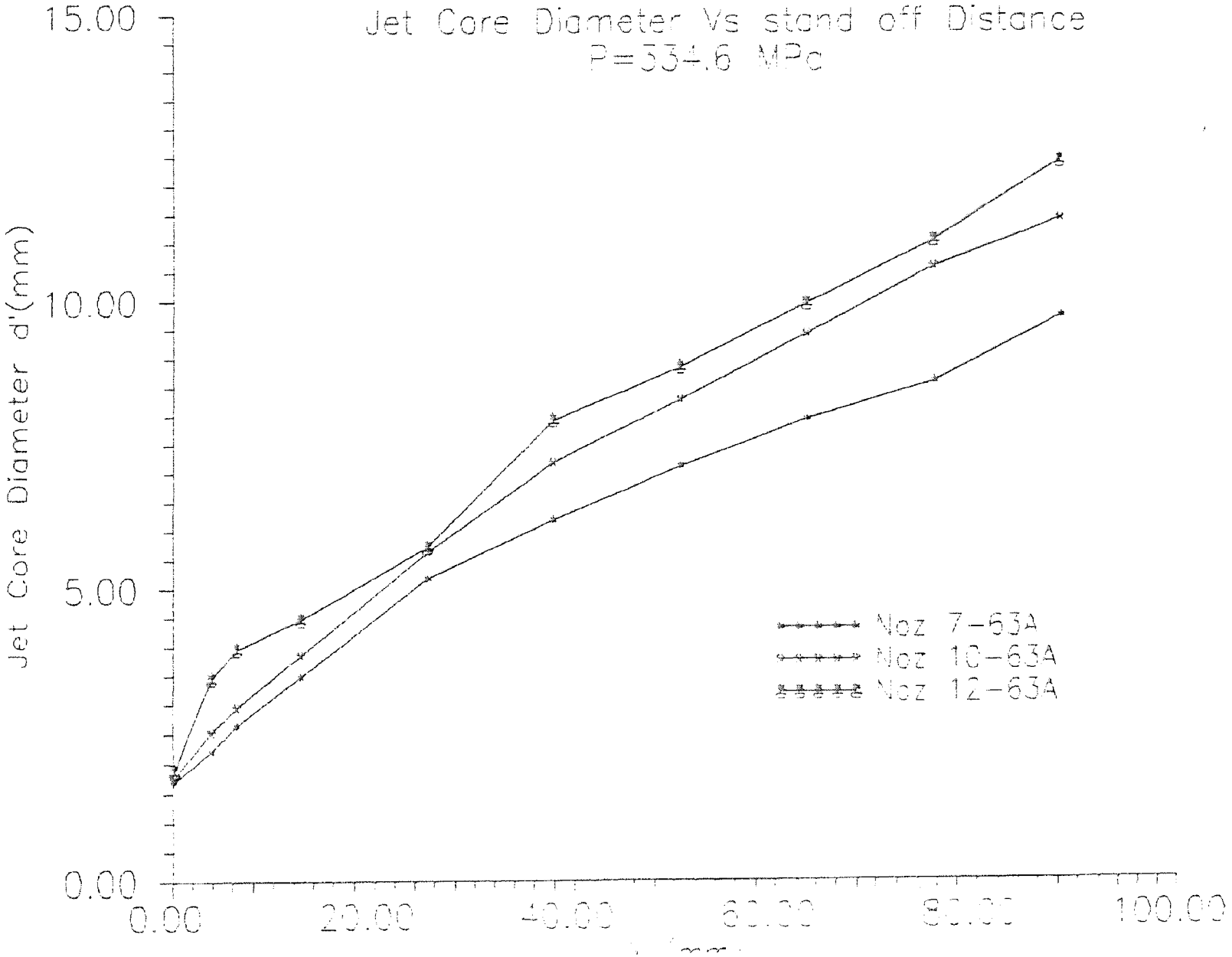

Fig. 5.49 Jet core diameter vs stand off distance showing sapphire effects on water abrasive flow

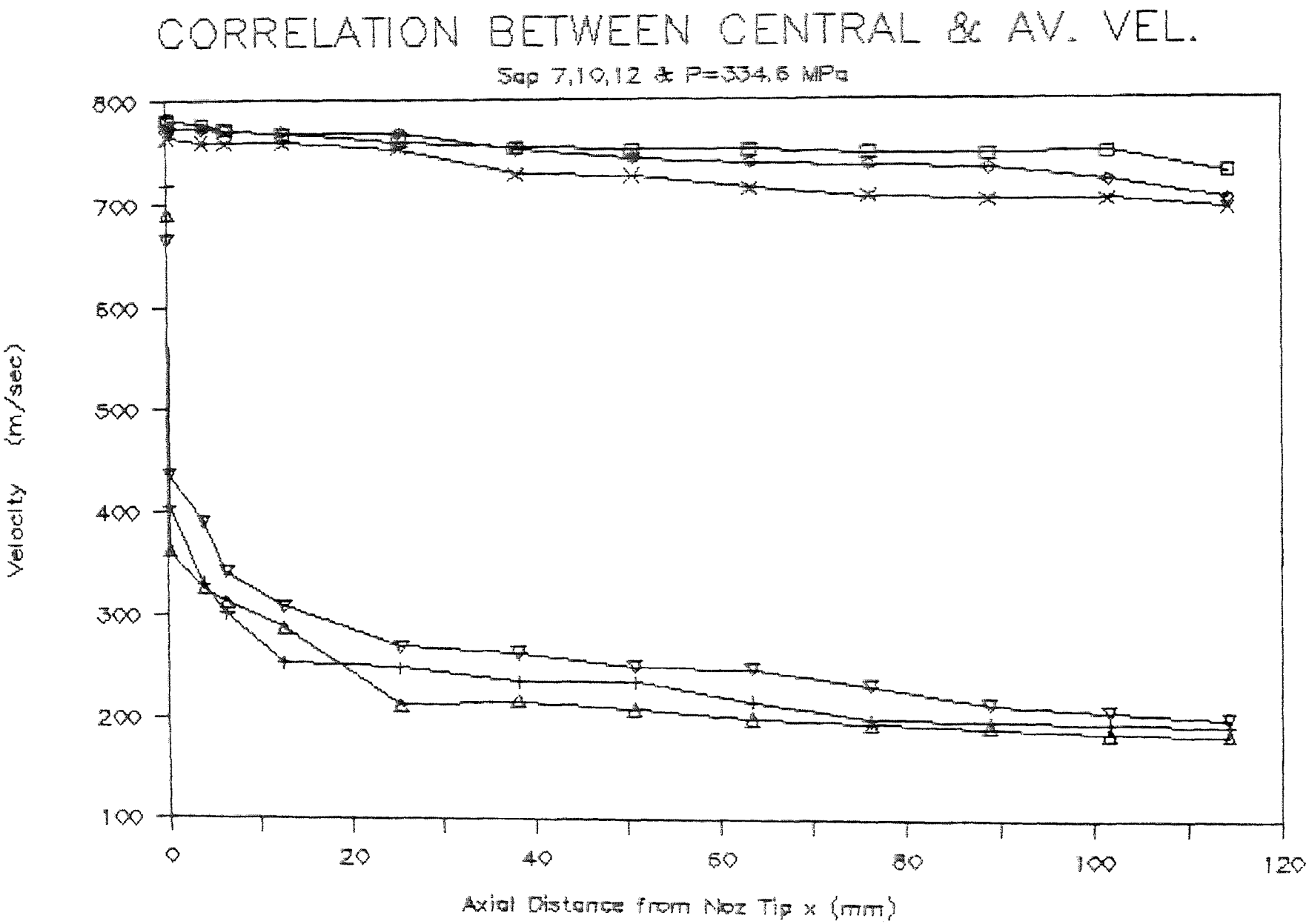

Fig. 5.50 Correlation between central and average velocity for different sapphire nozzles

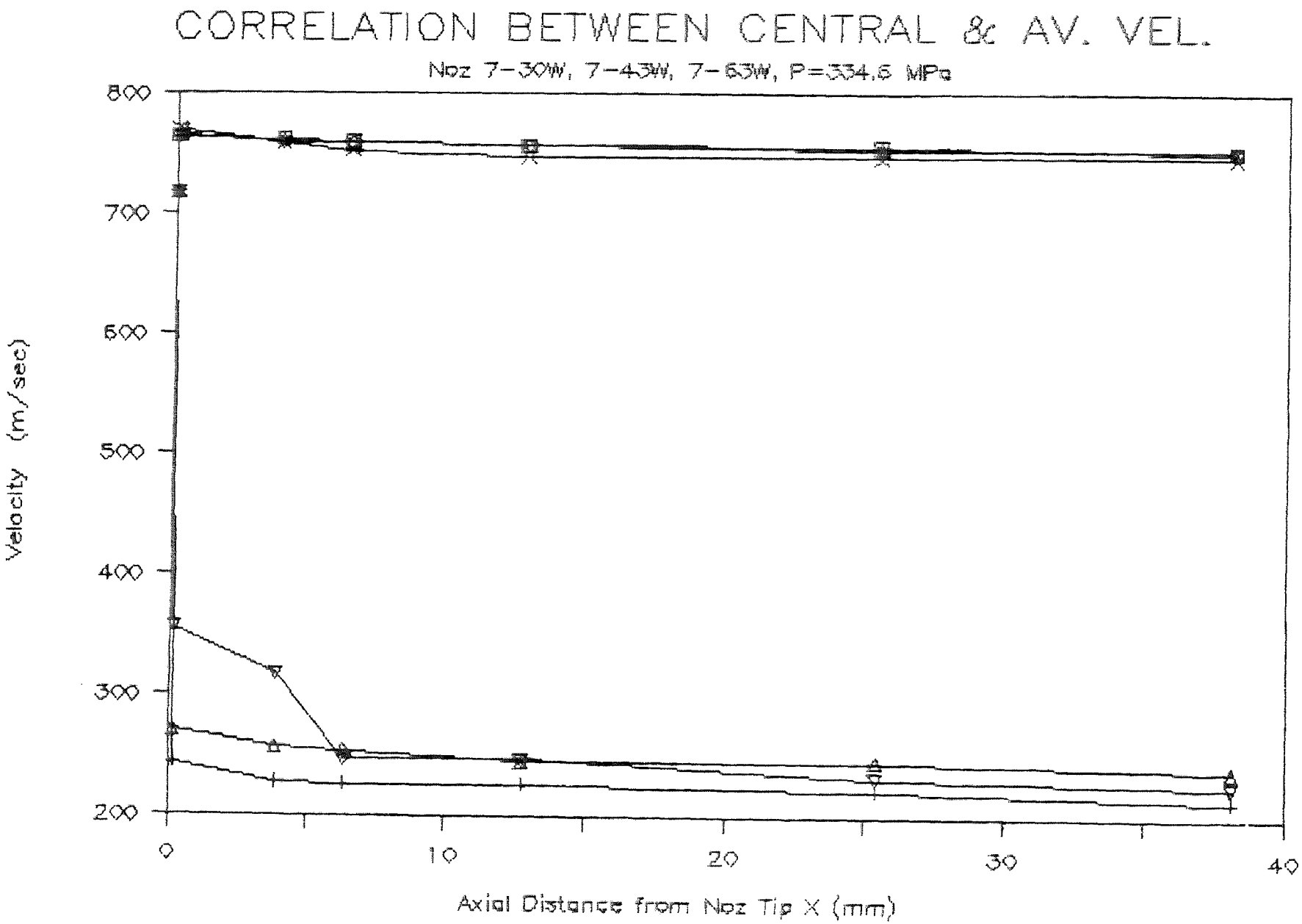

Fig. 5.51 Correlation between central and average velocity for water flow and showing the carbide effects

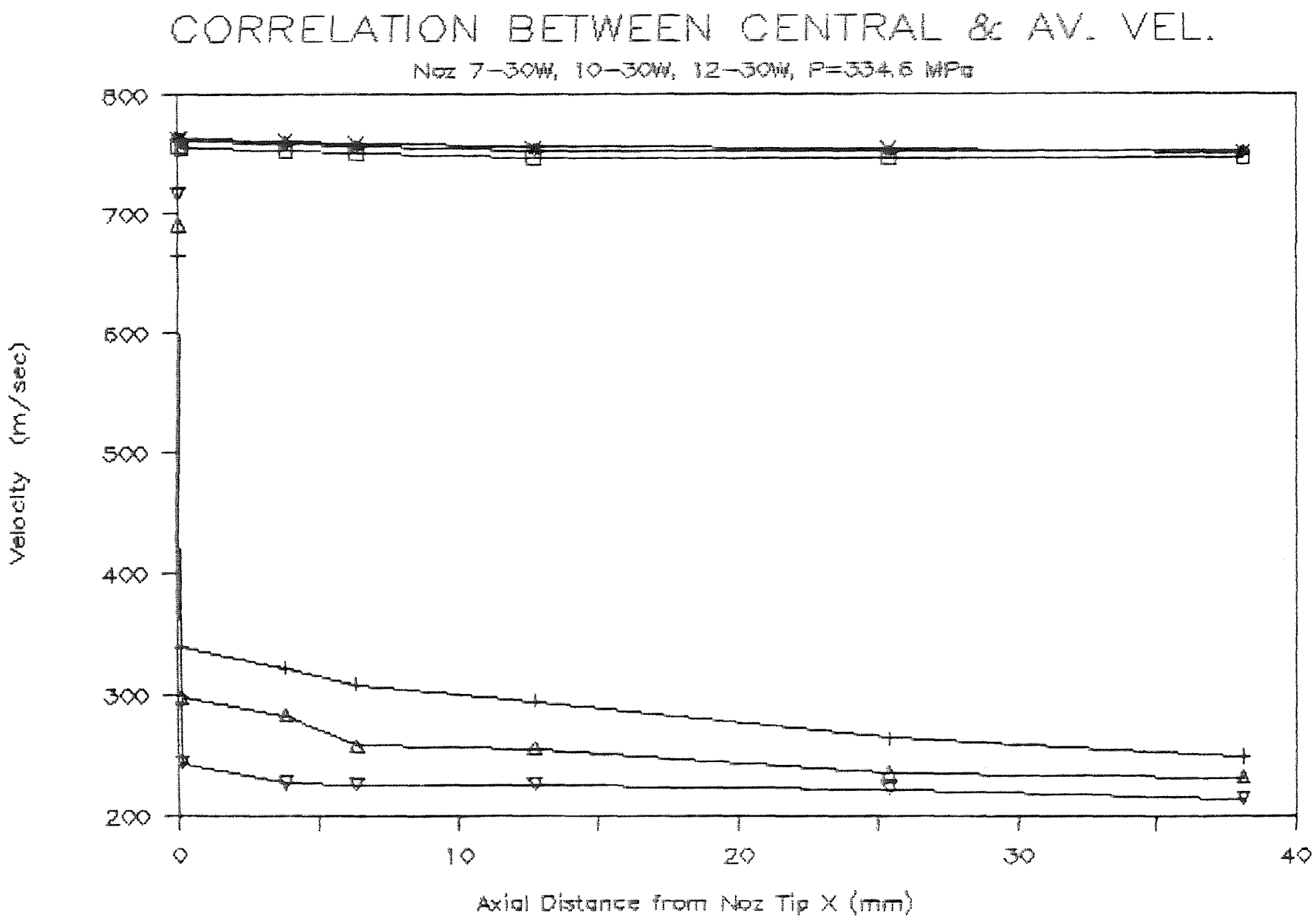

Fig. 5.52 Correlation between central and average velocity for water flow and showing the sapphire effects

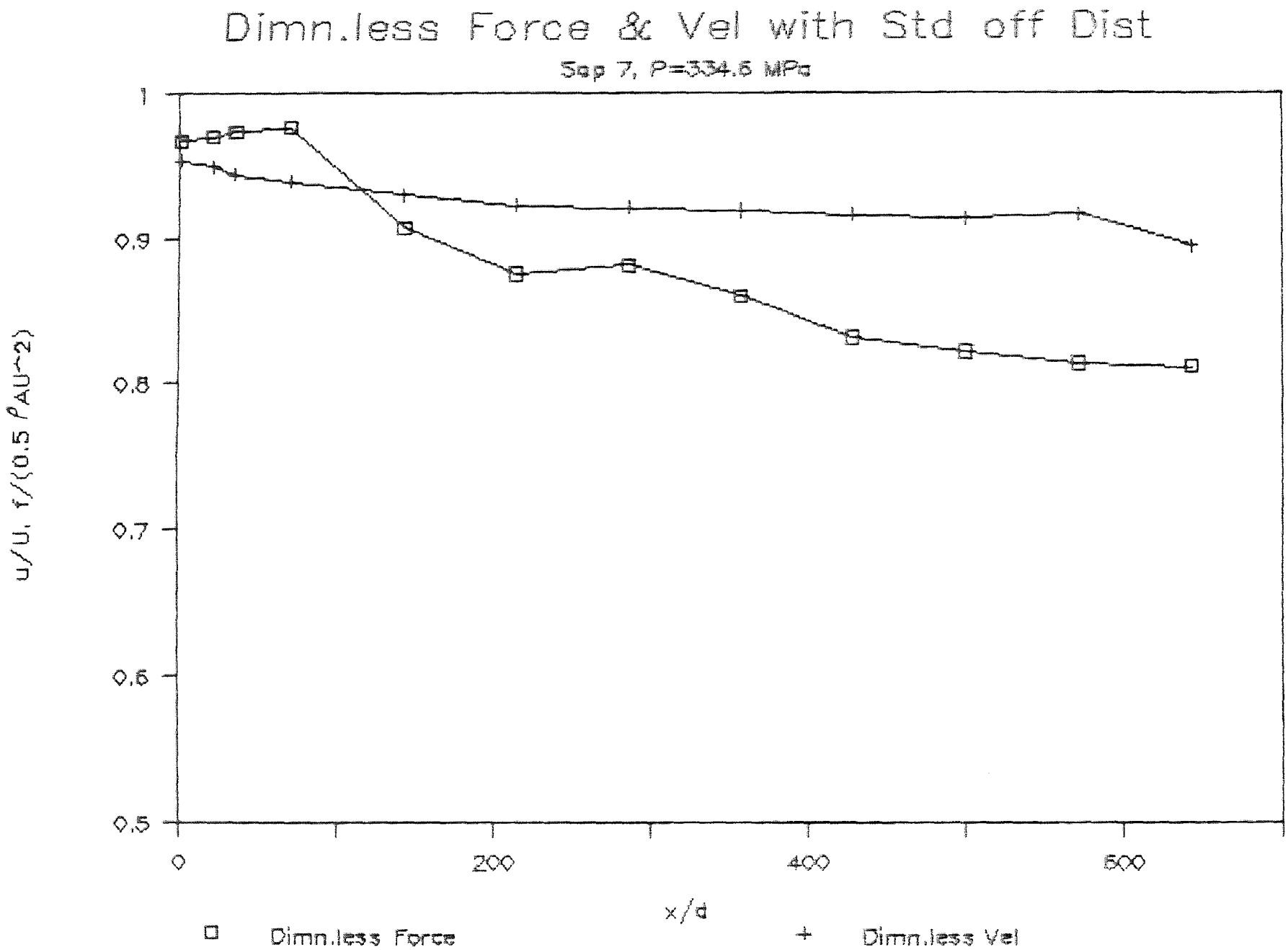

Fig. 5.53 Dimensionless force and velocity plot with stand off distance for sap 7

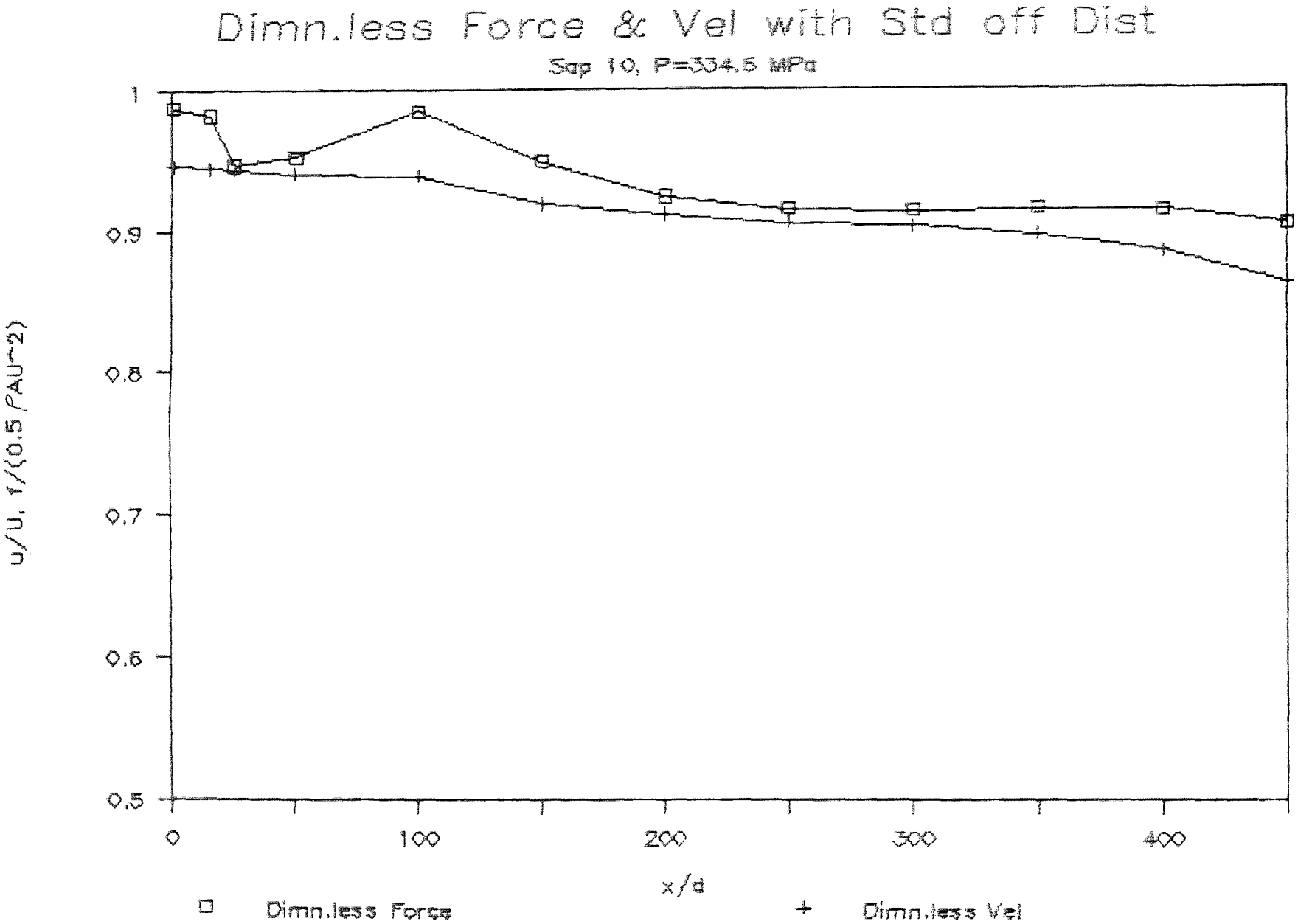

Fig. 5.54 Dimensionless force and velocity plot with stand off distance for sap 10

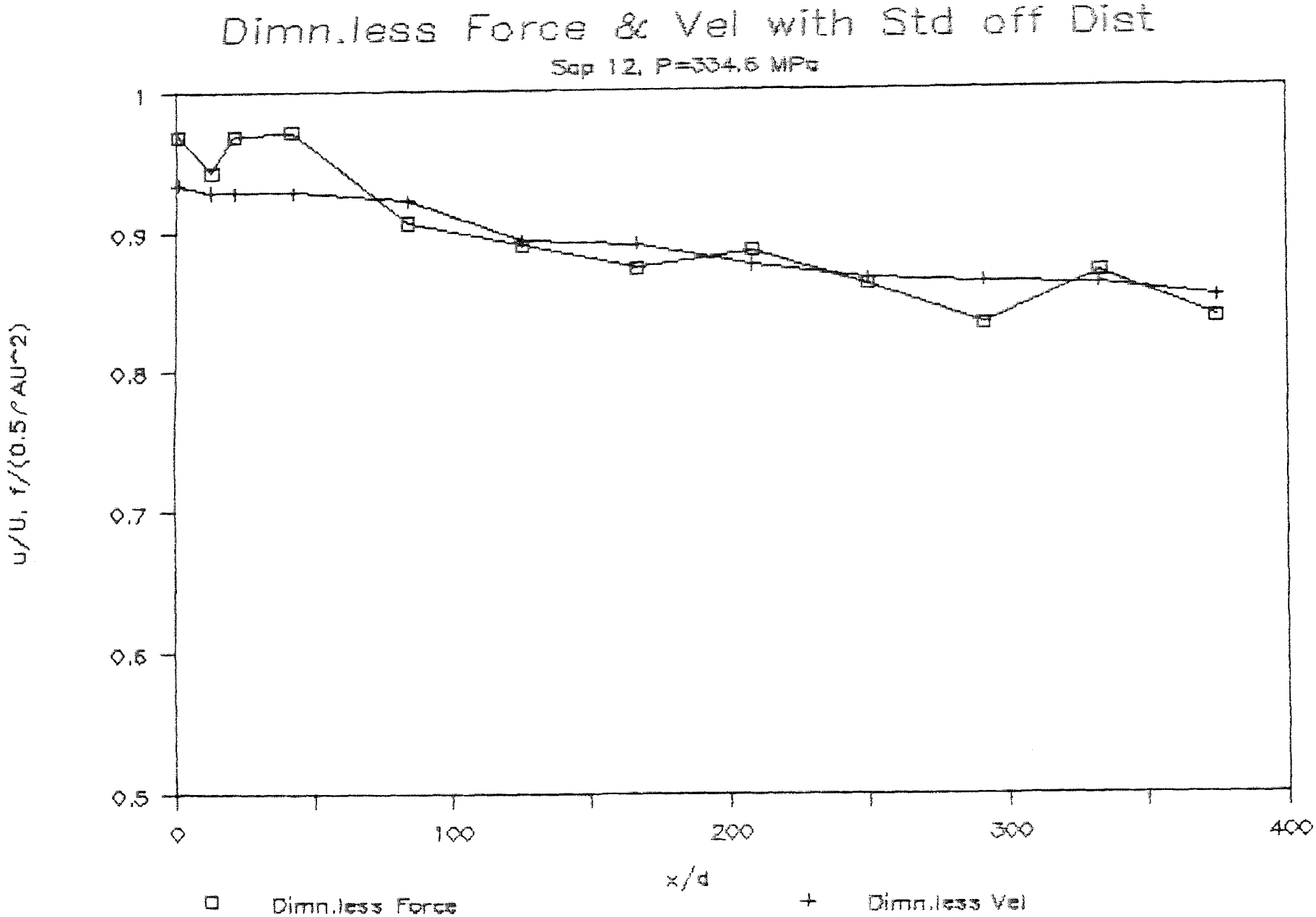

Fig. 5.55 Dimensionless force and velocity plot with stand off distance for sap 12

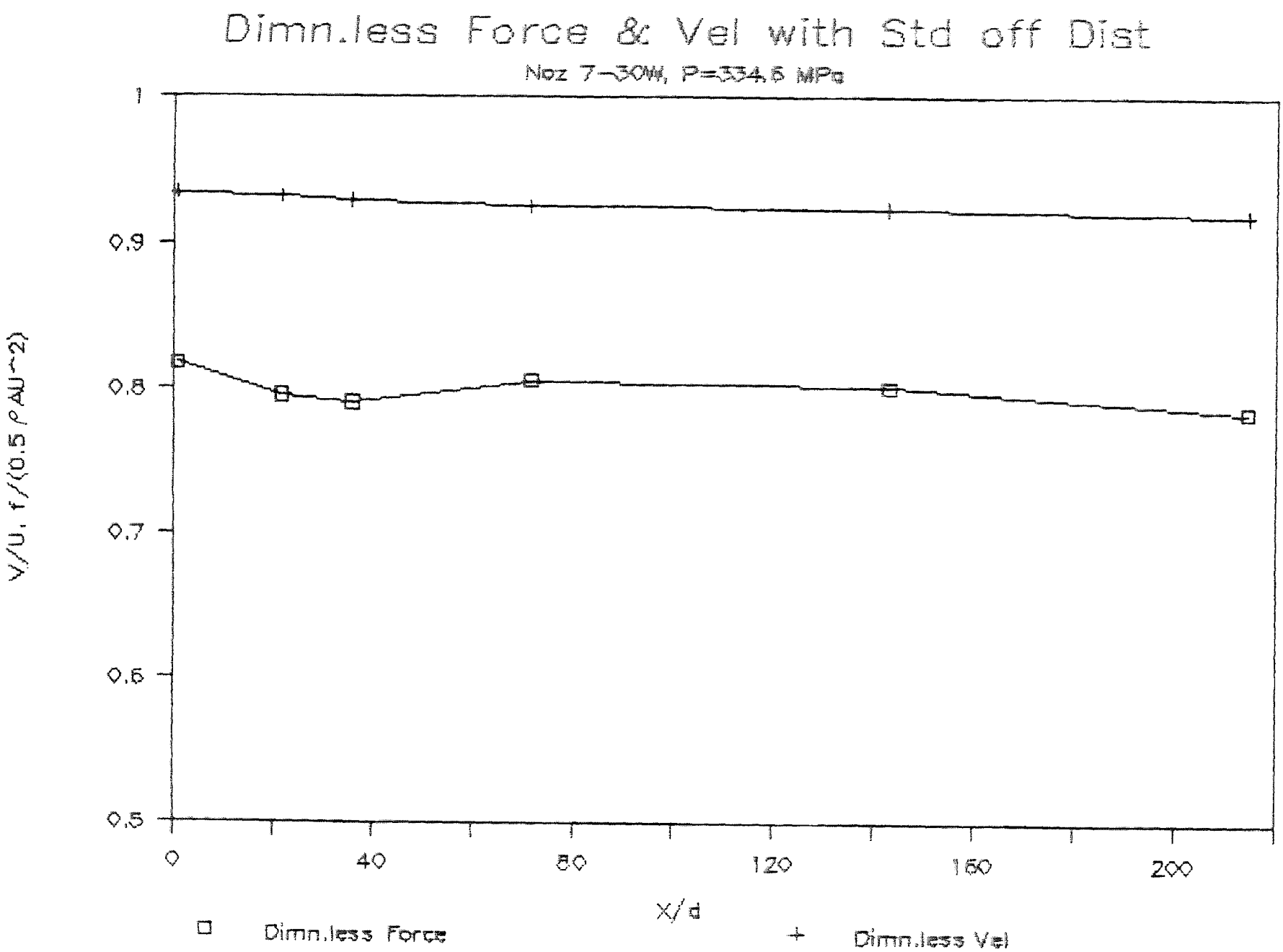

Fig. 5.56 Dimensionless force and velocity plot with stand off distance for Noz 7-30W

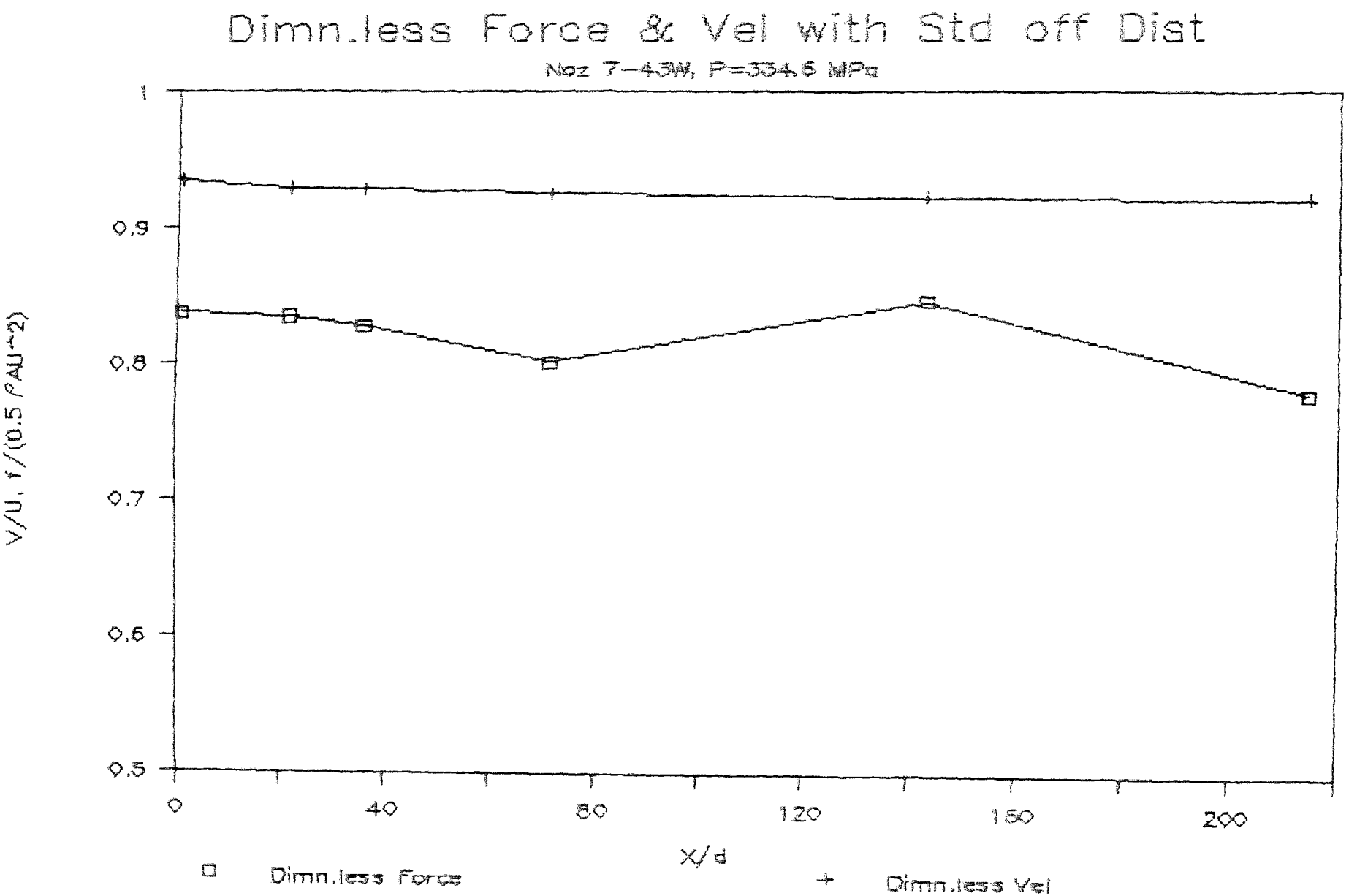

Fig. 5.57 Dimensionless force and velocity plot with stand off distance for Noz 7-43W

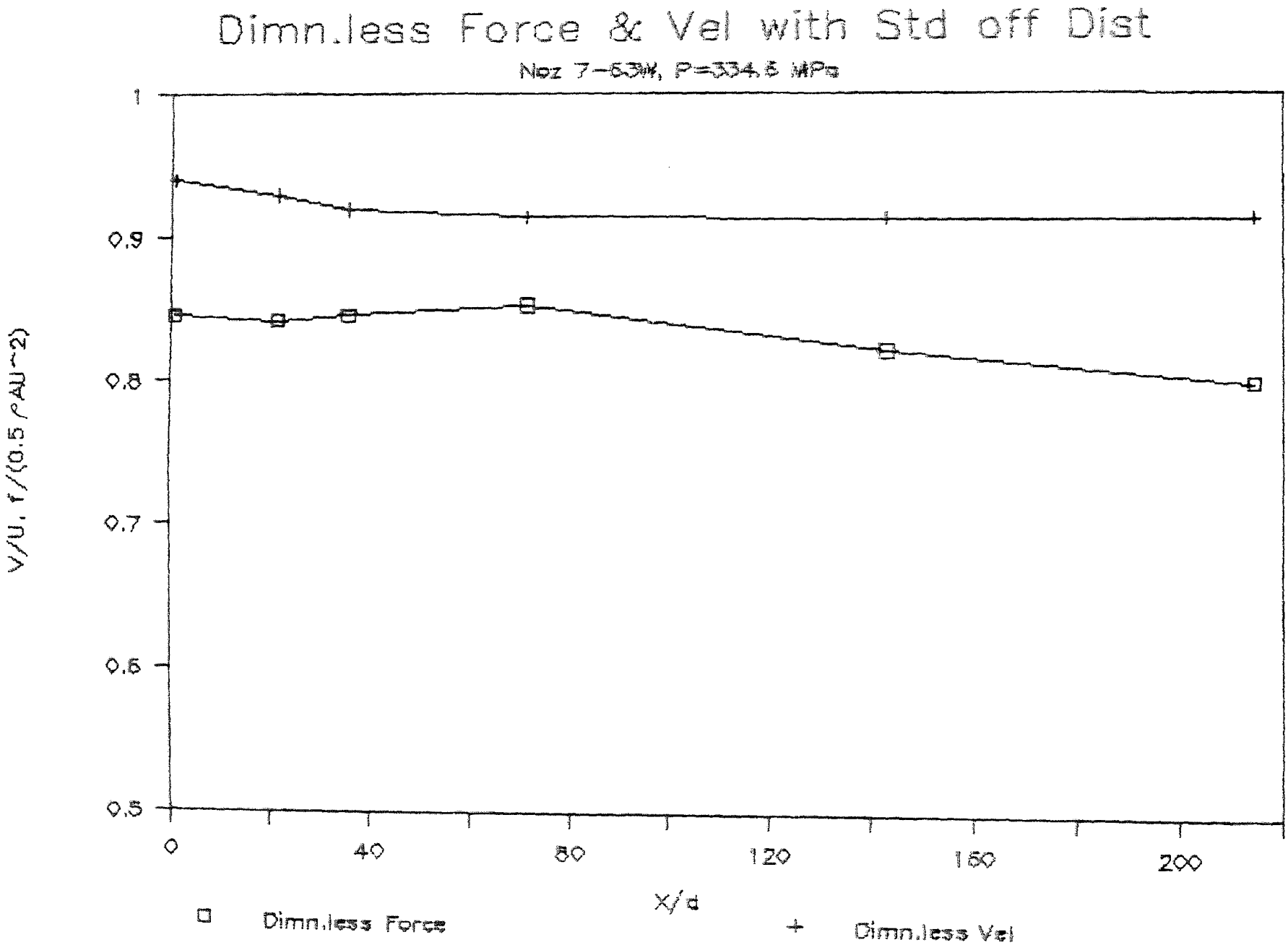

Fig. 5.58 Dimensionless force and velocity plot with stand off distance for Noz 7-63W

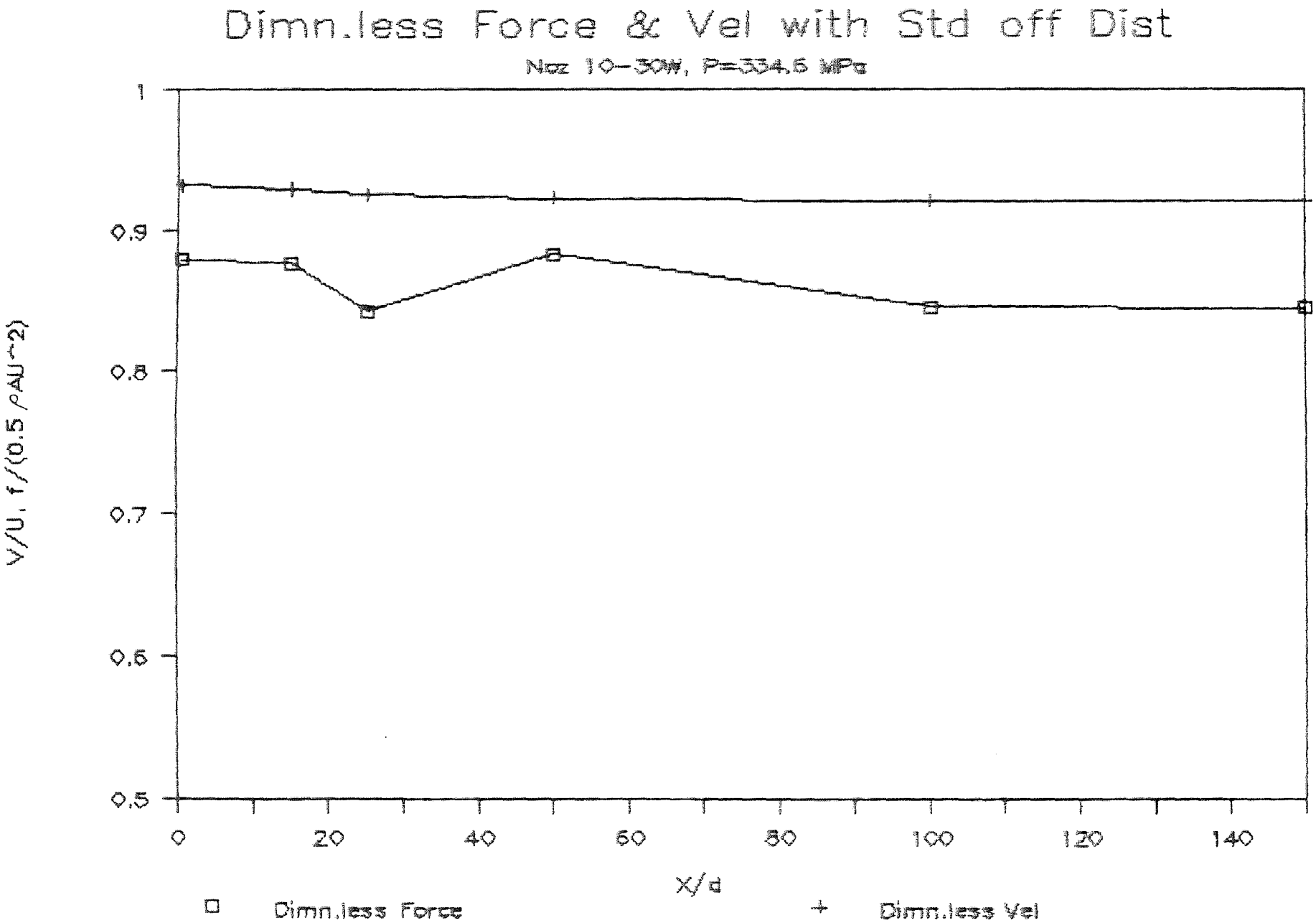

Fig. 5.59 Dimensionless force and velocity plot with stand off distance for Noz 10-30W

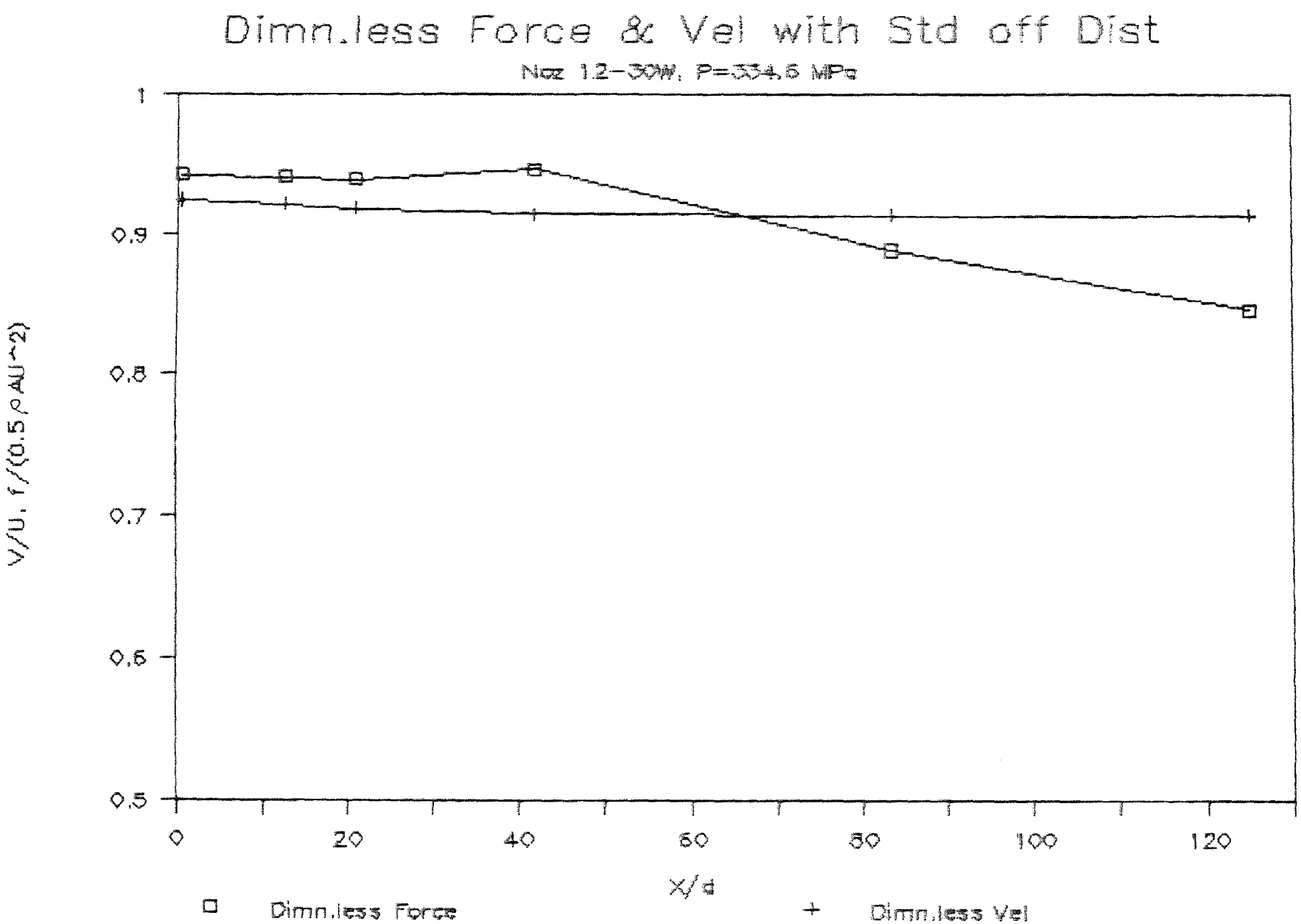

Fig. 5.60 Dimensionless force and velocity plot with stand off distance for Noz 12-30W

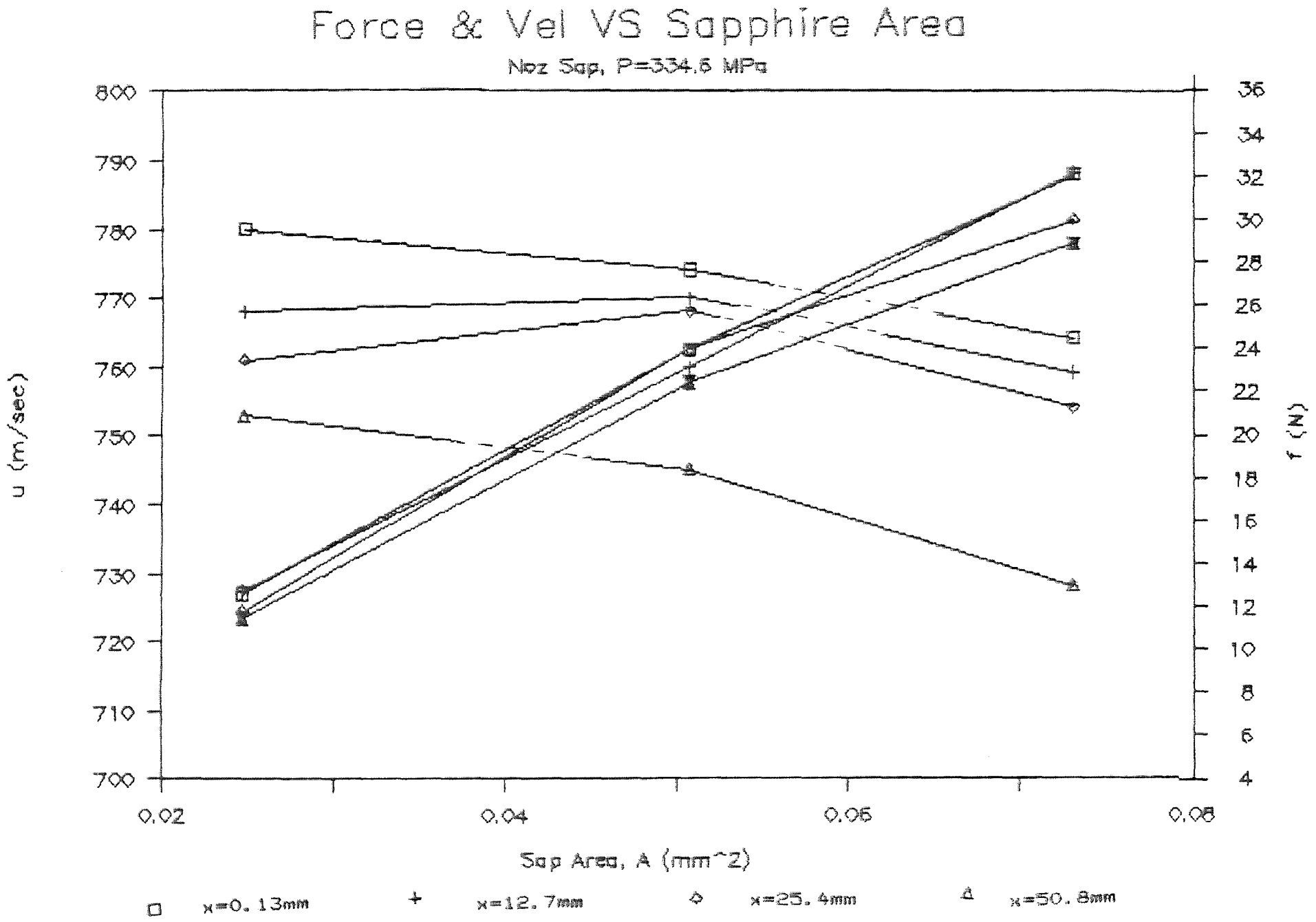

Fig. 5.61 Force and velocity plot with sapphire area for different sapphire nozzles

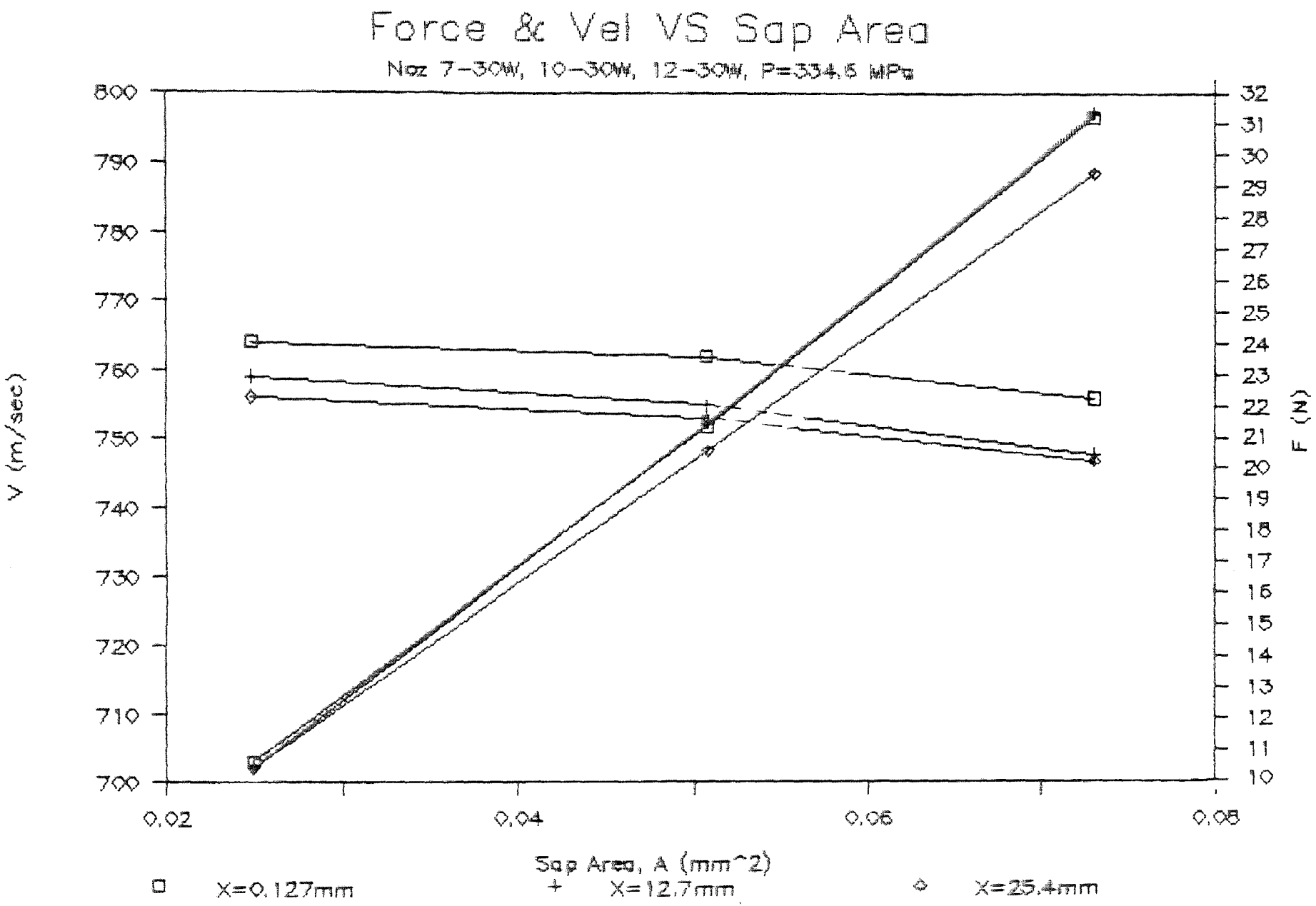

Fig. 5.62 Water force and velocity plot with sapphire area for different sap-carb nozzles

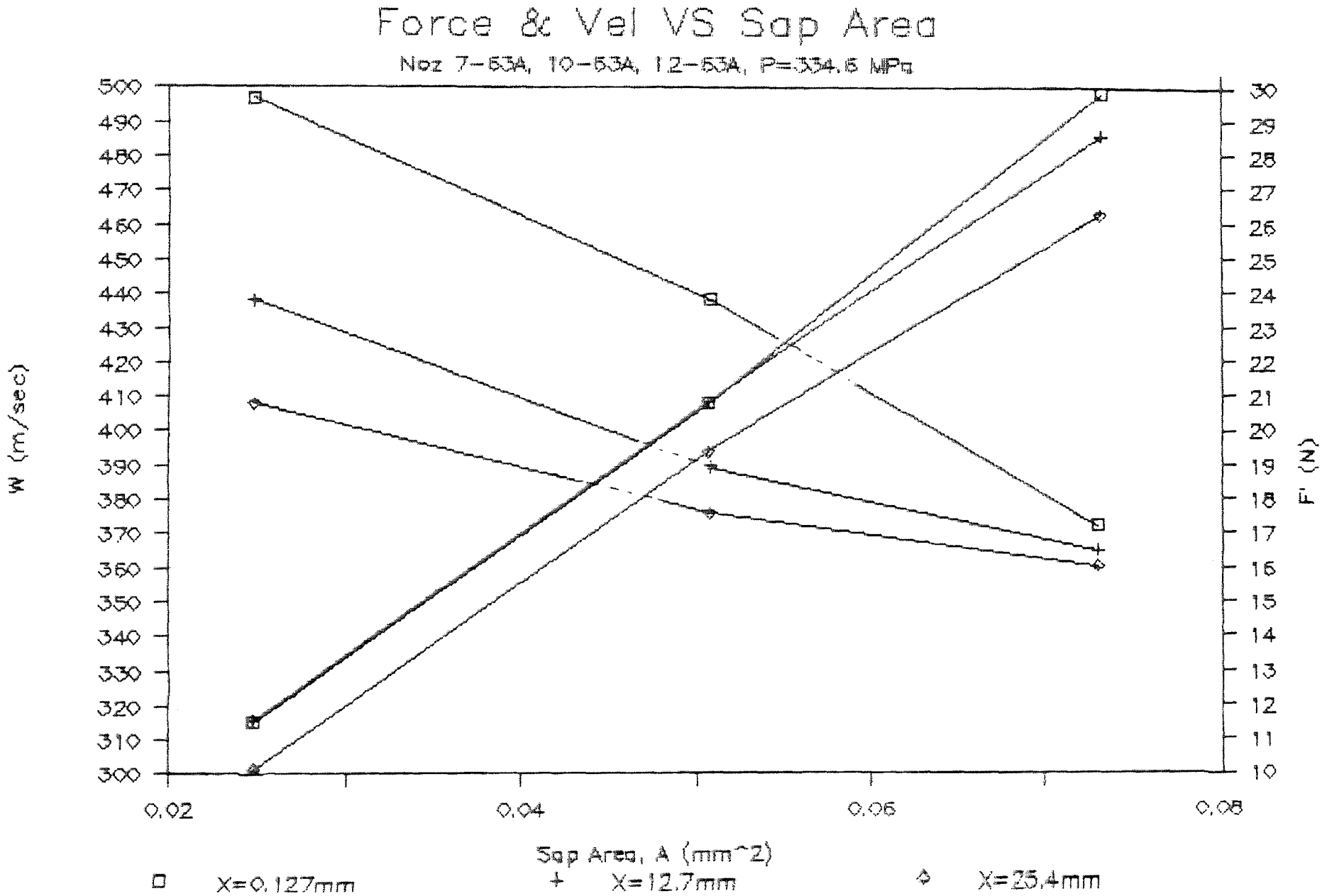

Fig. 5.63 Abrasive force and velocity plot with sapphire area for different sap-carb nozzles

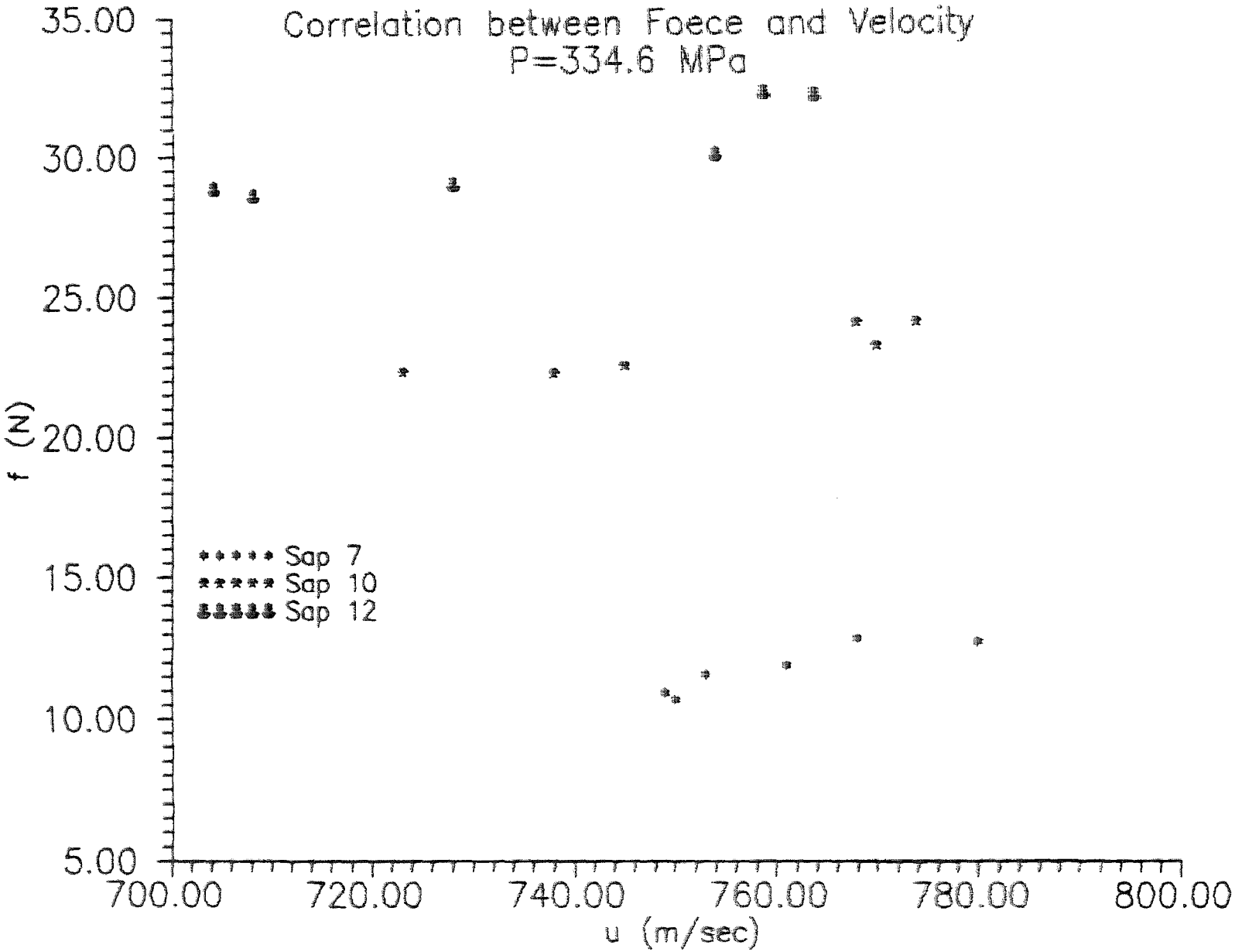

Fig. 5.64 Correlation between force and velocity for different sapphire nozzles

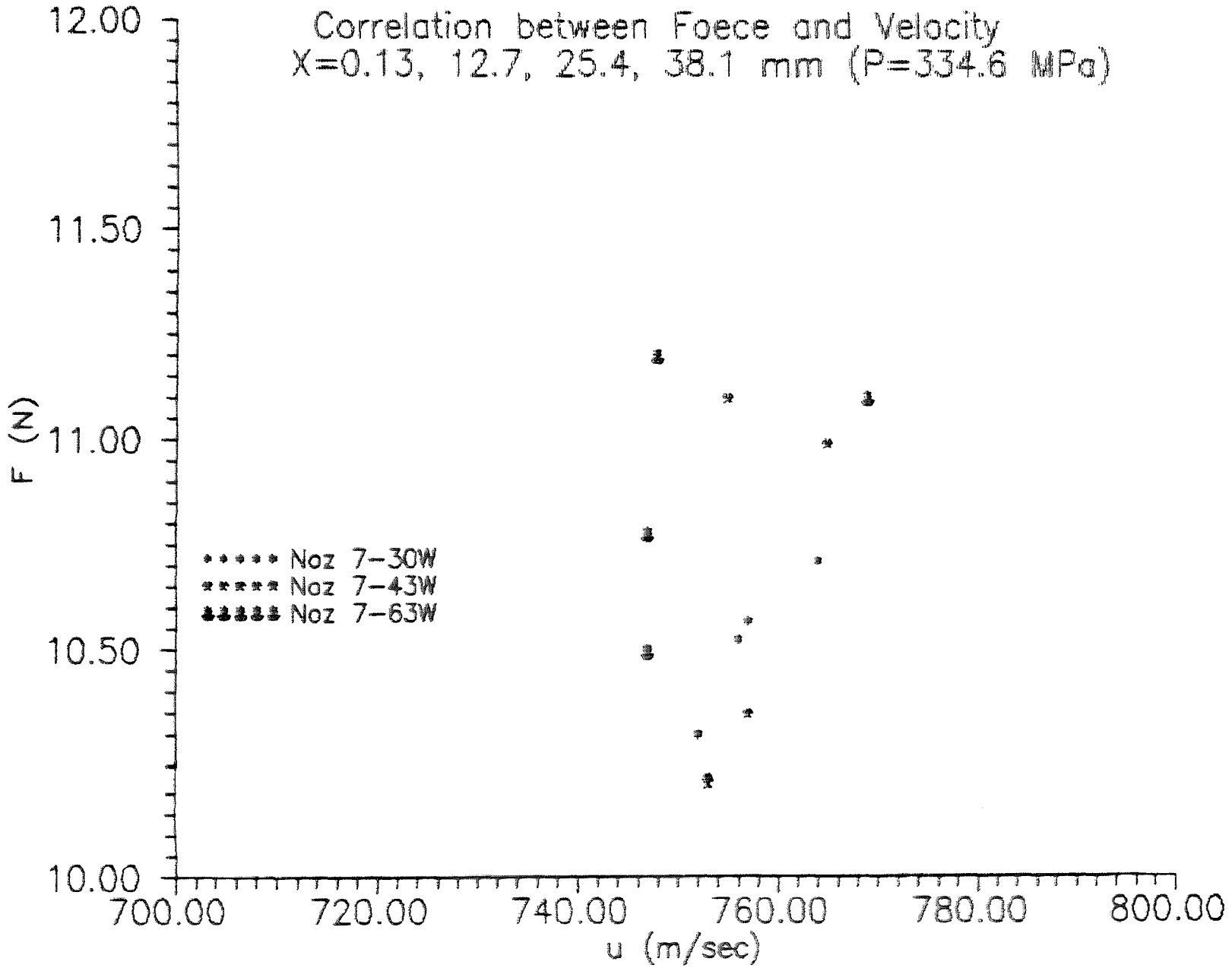

Fig. 5.65 Correlation between water force and velocity for different carbide nozzles

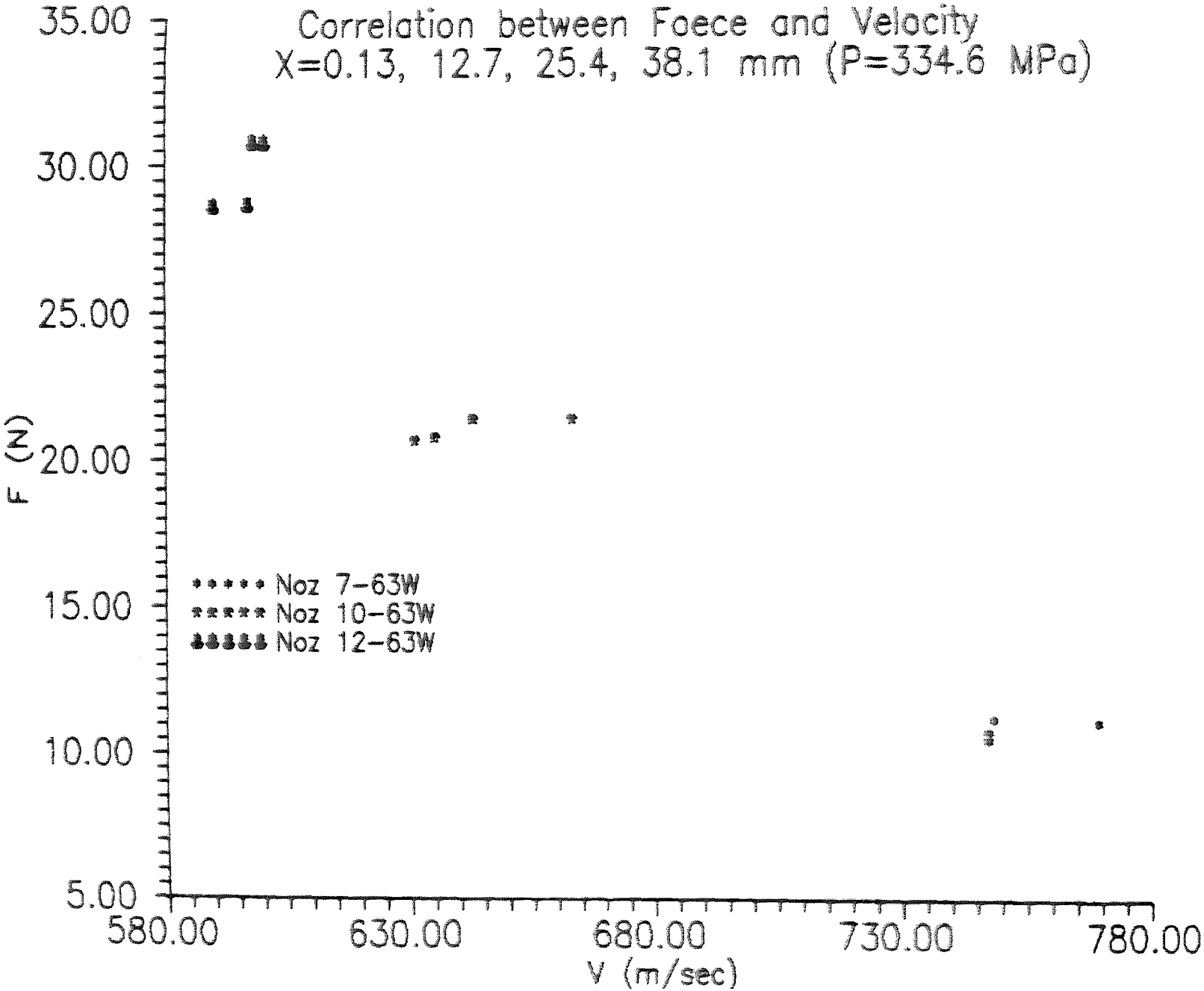

Fig. 5.66 Correlation between water force and velocity showing the sapphire effects

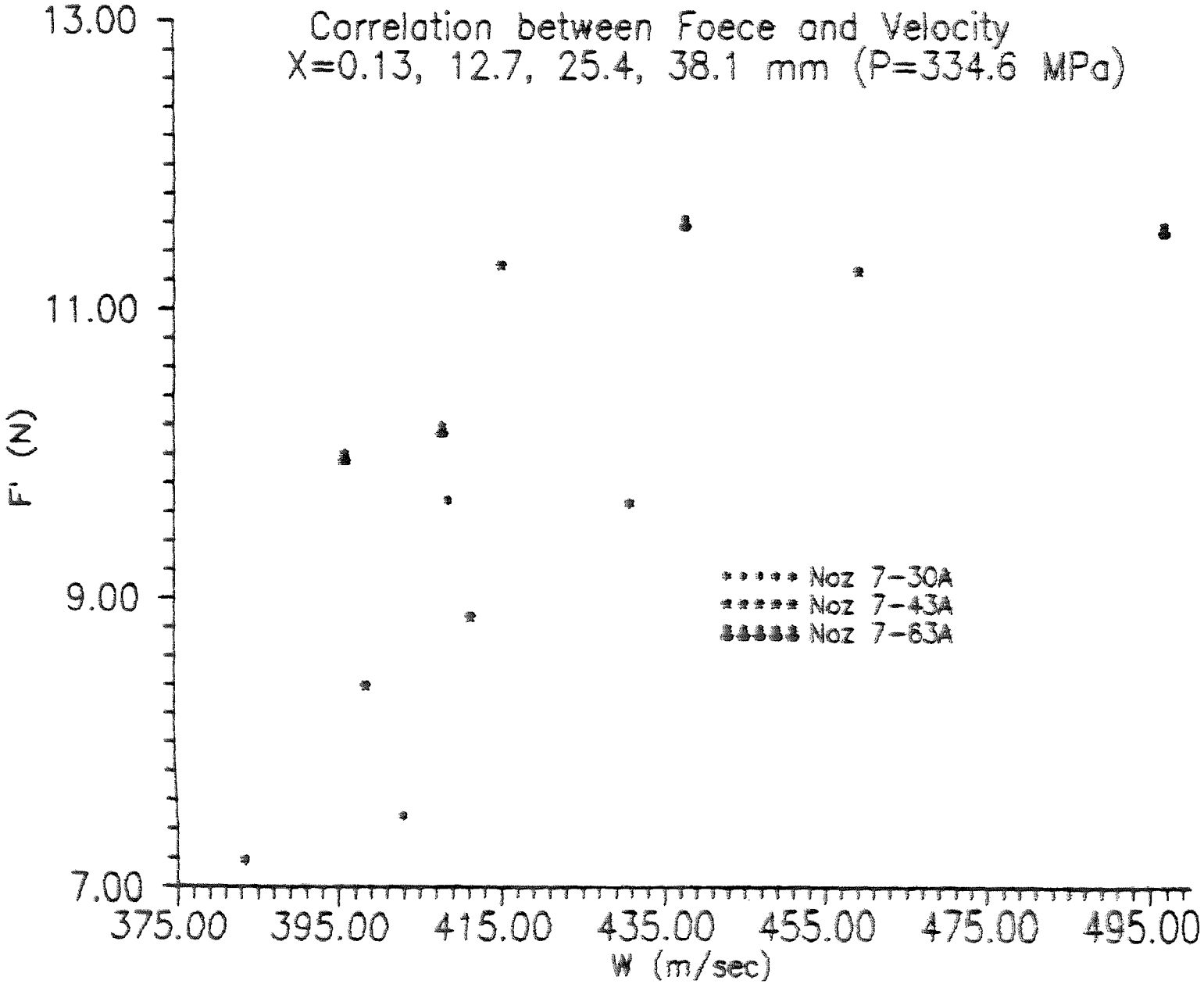

Fig. 5.67 Correlation between abrasive force and velocity showing the carbide effects

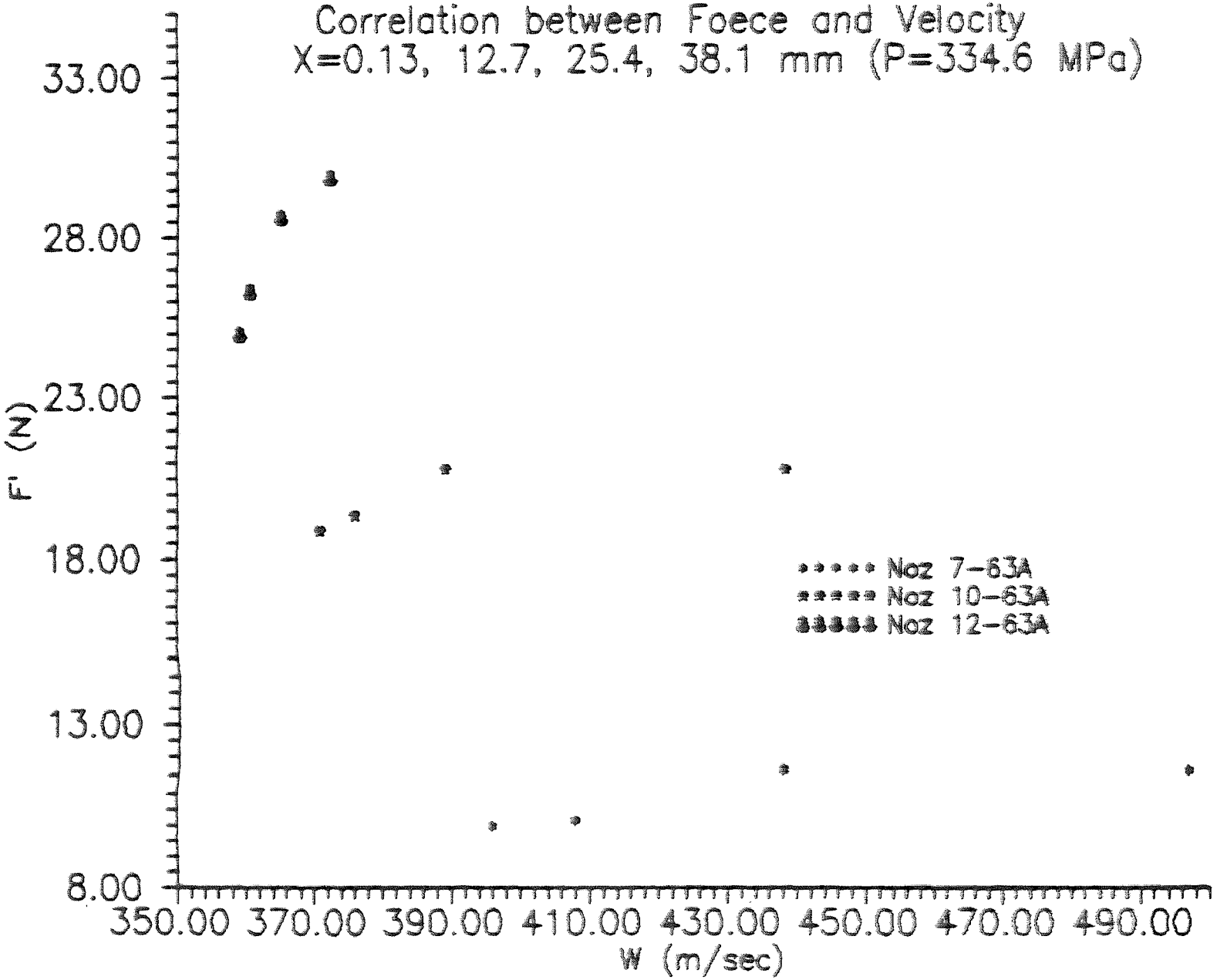

Fig. 5.68 Correlation between abrasive force and velocity showing the sapphire effects

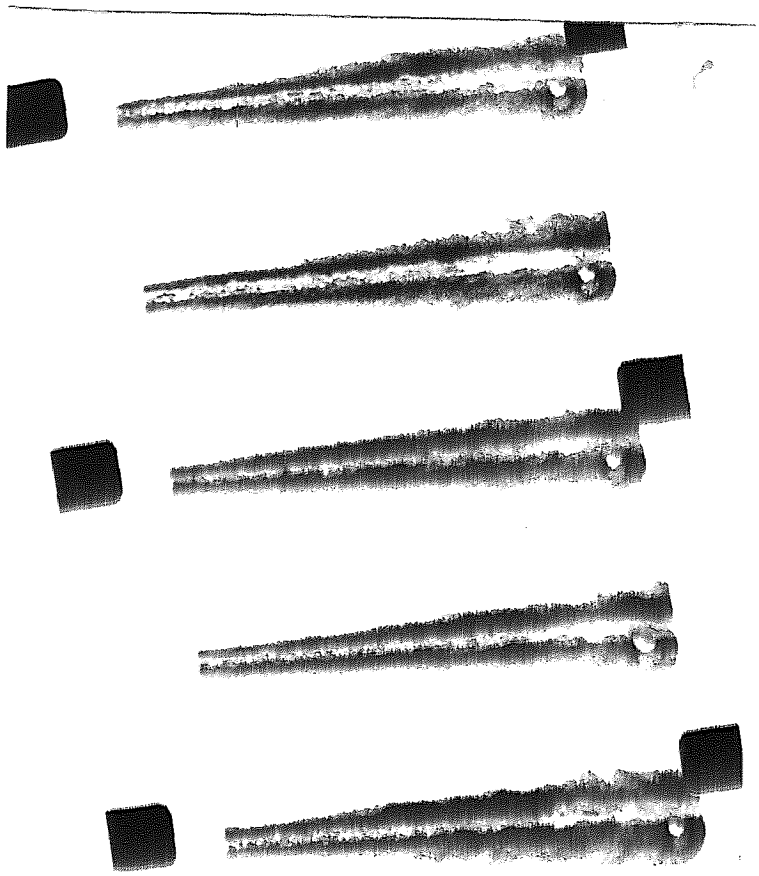

(a)

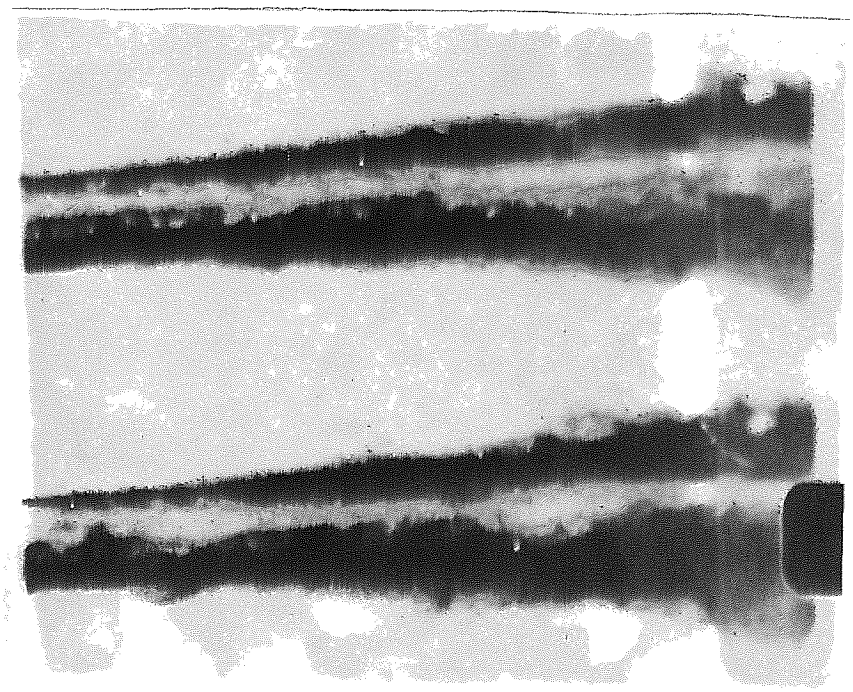

(b)

Fig. 5.69 Photograph showing core, mist and droplet for (a) film # 3 and (b) film # 20 of Table 4.5

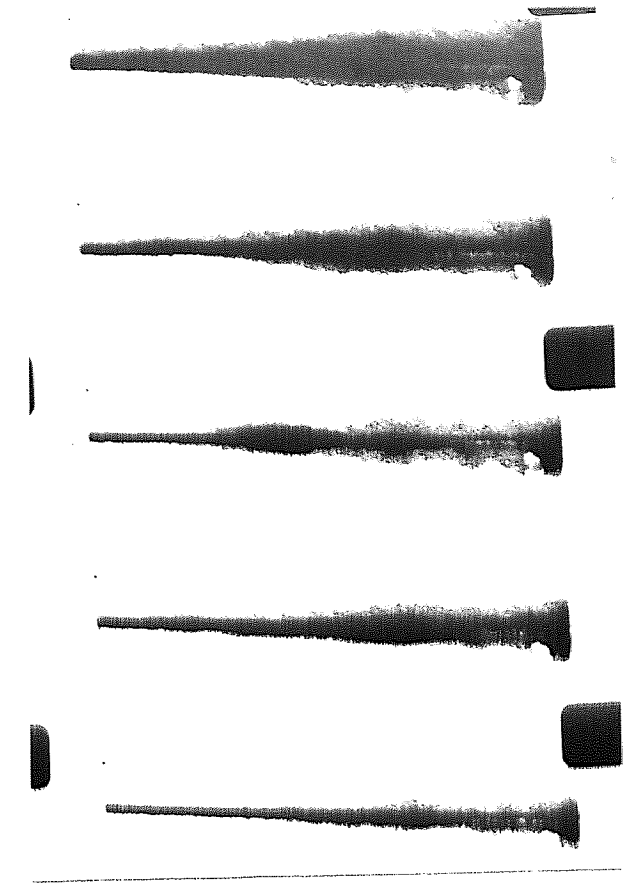

(a)

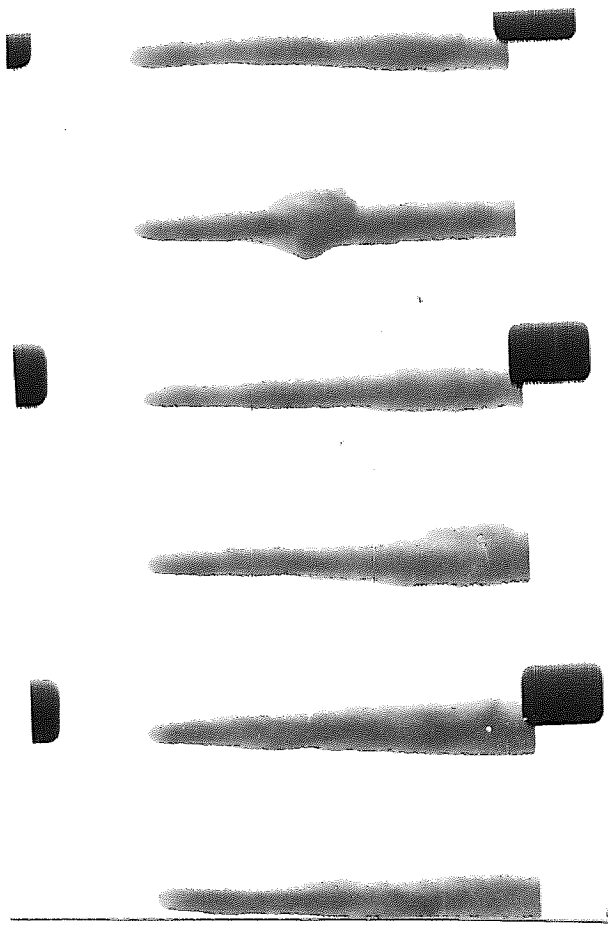

(b)

Fig. 5.70 Photograph showing pulsation for (a) film # 2 and (b) film #5 of Table 4.5

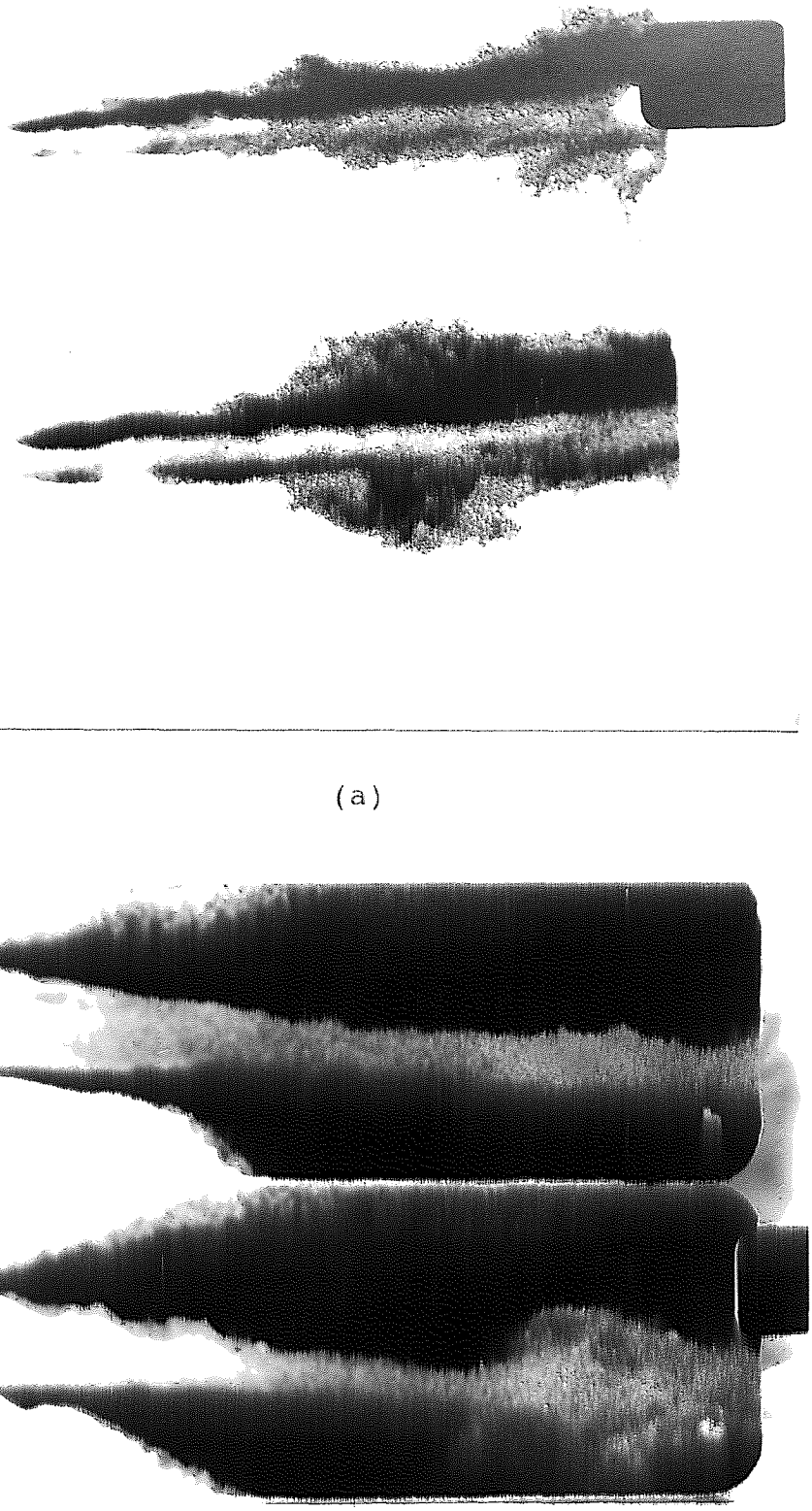

(a)

(b)

Fig. 5.71 Photograph showing the effects of abrasive on jet diameter for (a) film # 3 and (b) film #11 of Table 4.5

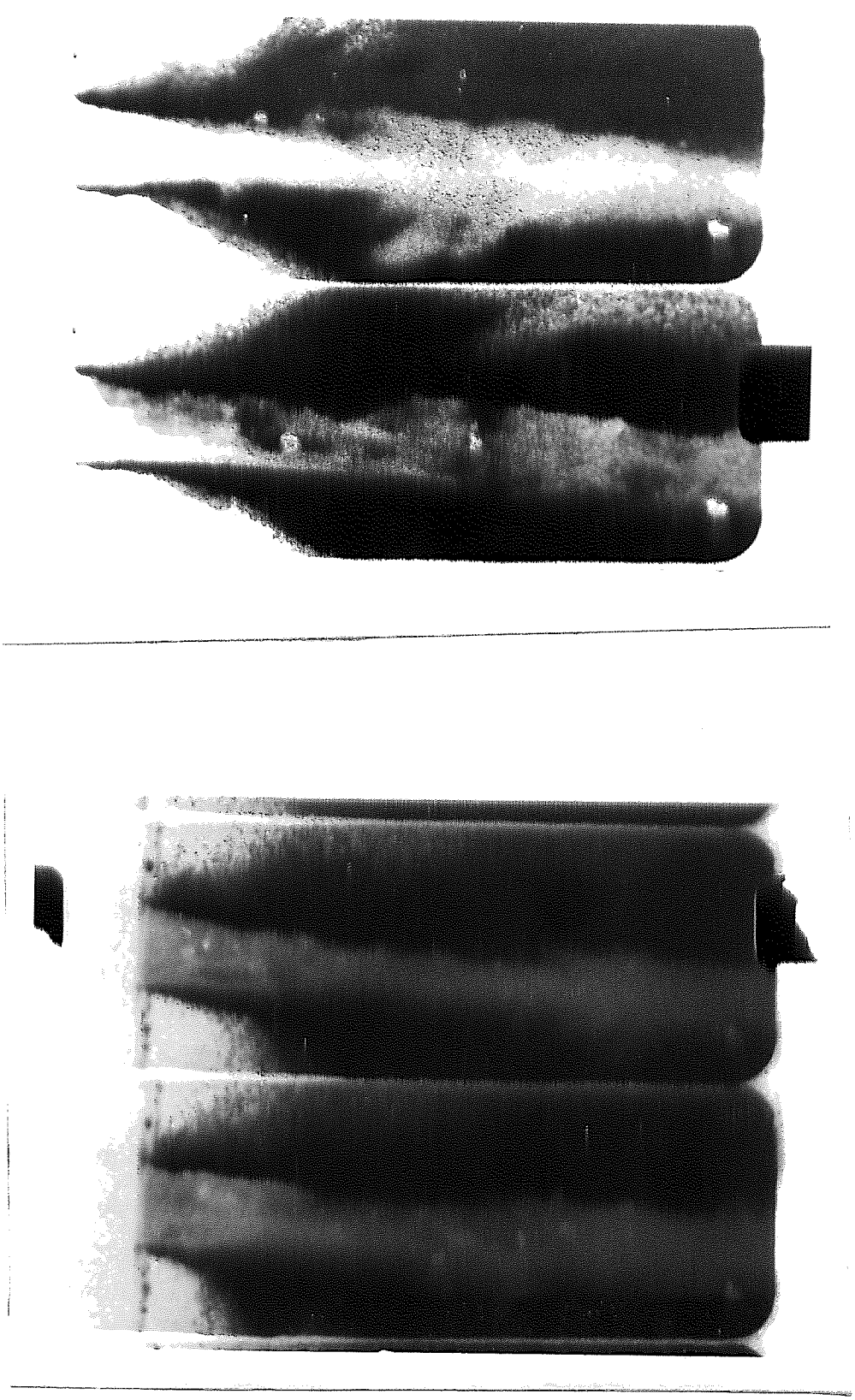

Fig. 5.72 Photograph showing cluster of particles for film #11 of Table 4.5

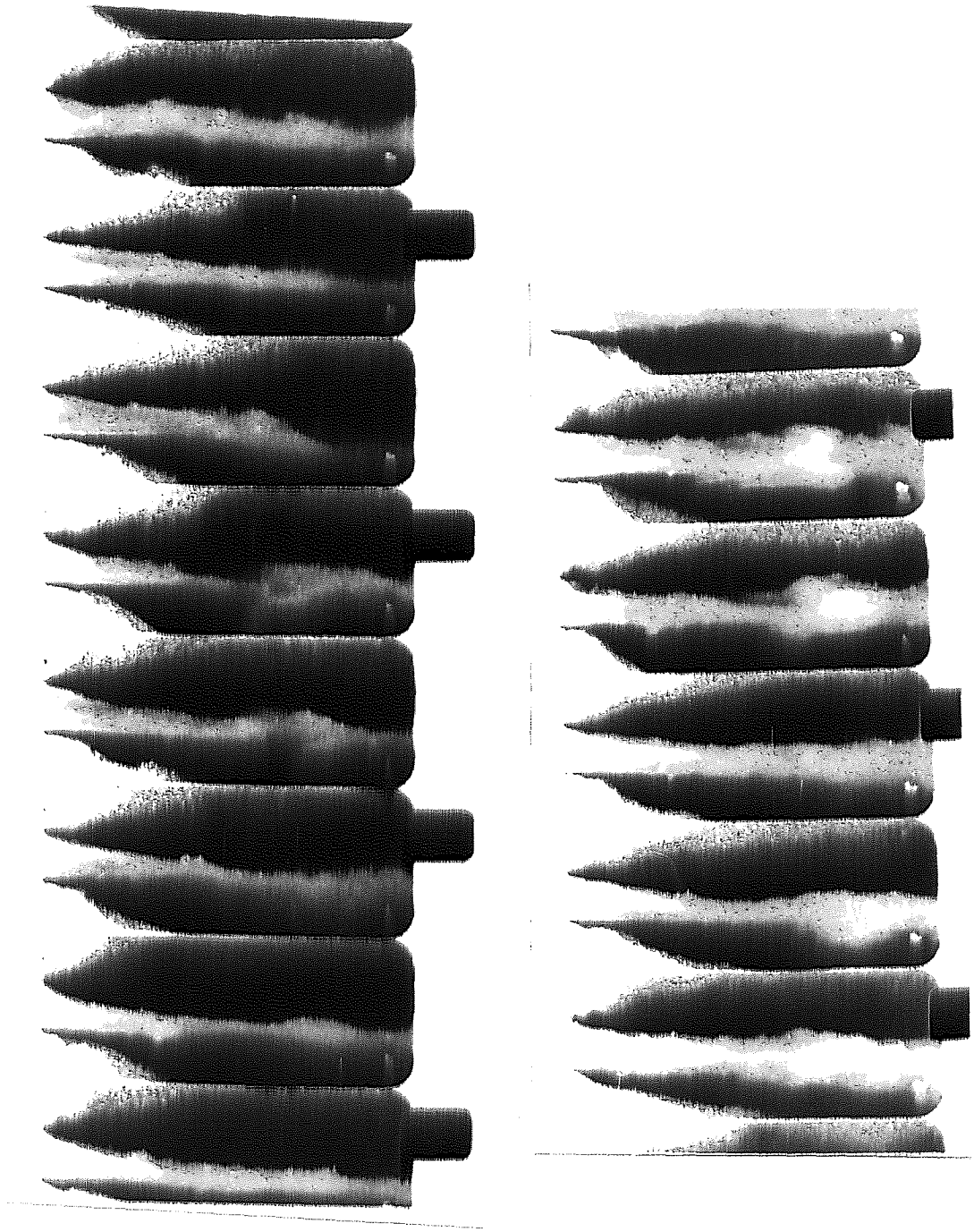

Fig.5.73 Photograph showing pulsation of AWJ for for film #11 of Table 4.5

(a)

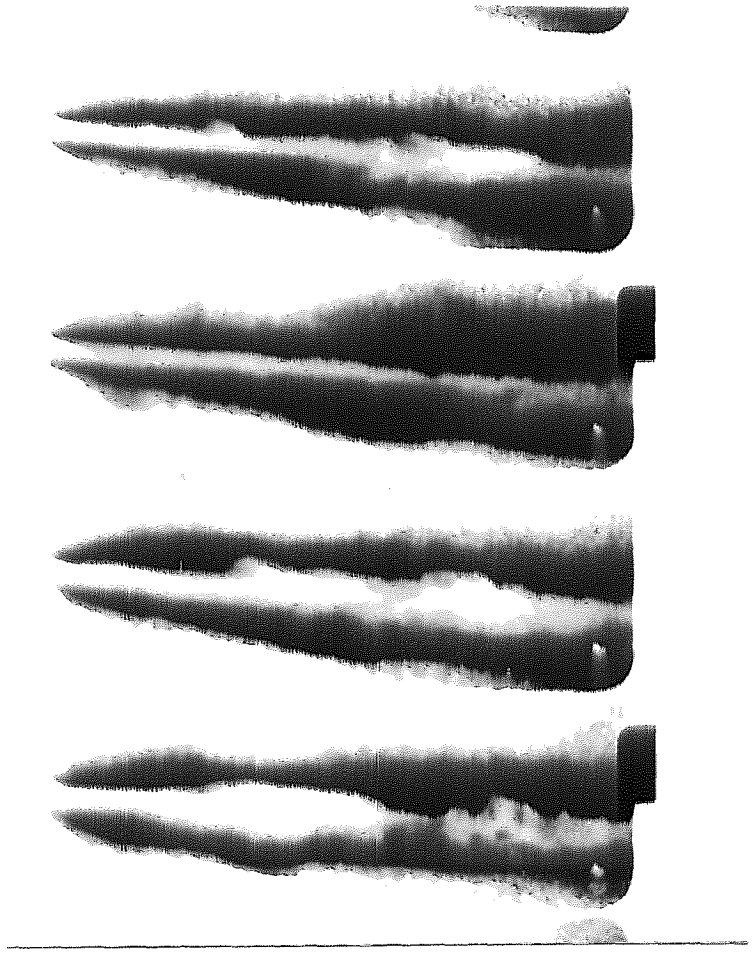

(b)

Fig. 5.74 Photograph showing the effects of abrasive flow rate on jet diameter for (a) film # 13 and (b) film #9 of Table 4.5

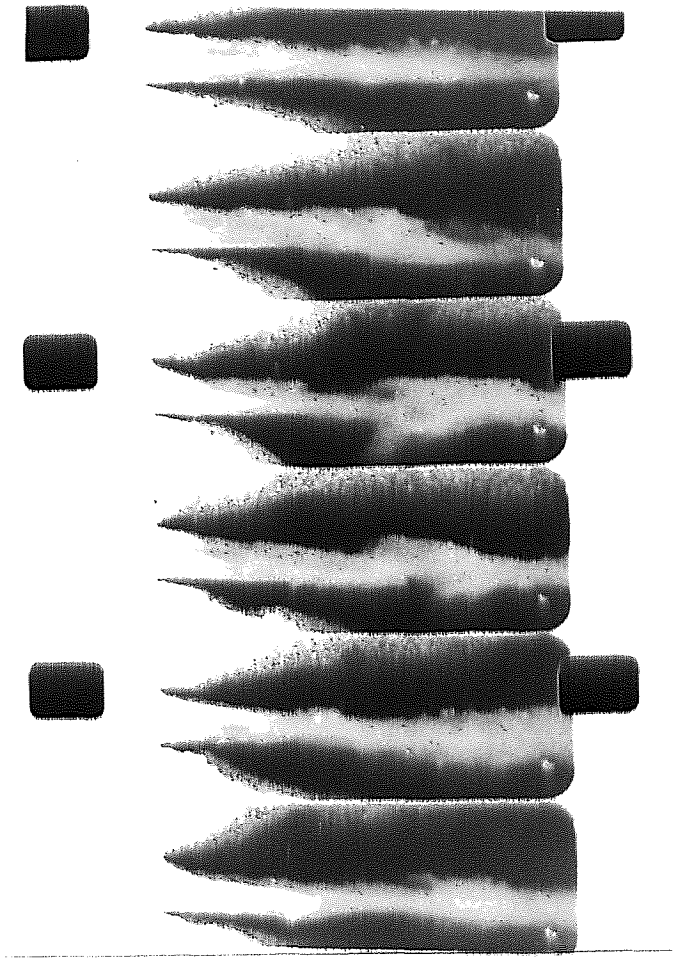

Fig. 5.75 Photograph showing cluster of particles for film # 11 of Table 4.5

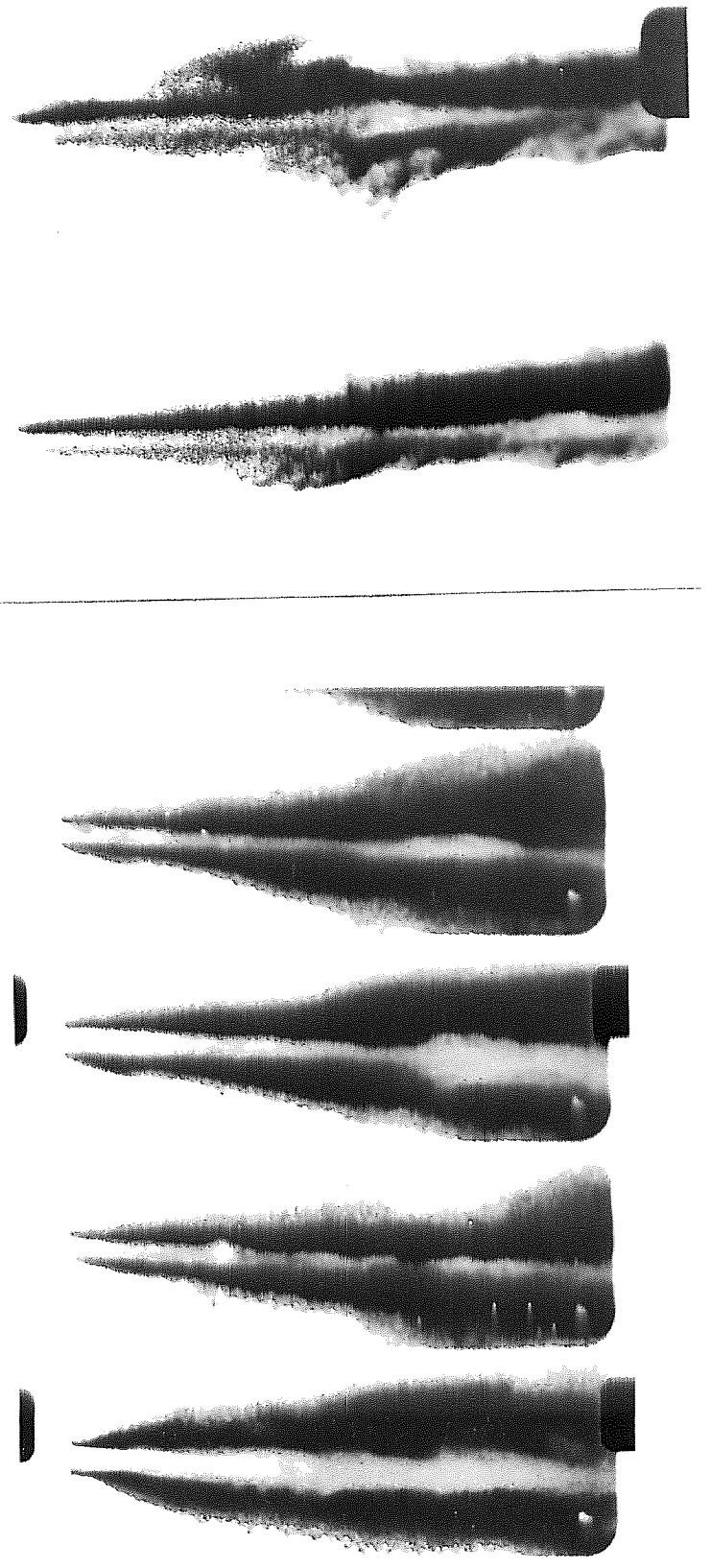

Fig. 5.76 Photograph showing abrsive flow path for film # 9 of Table 4.5

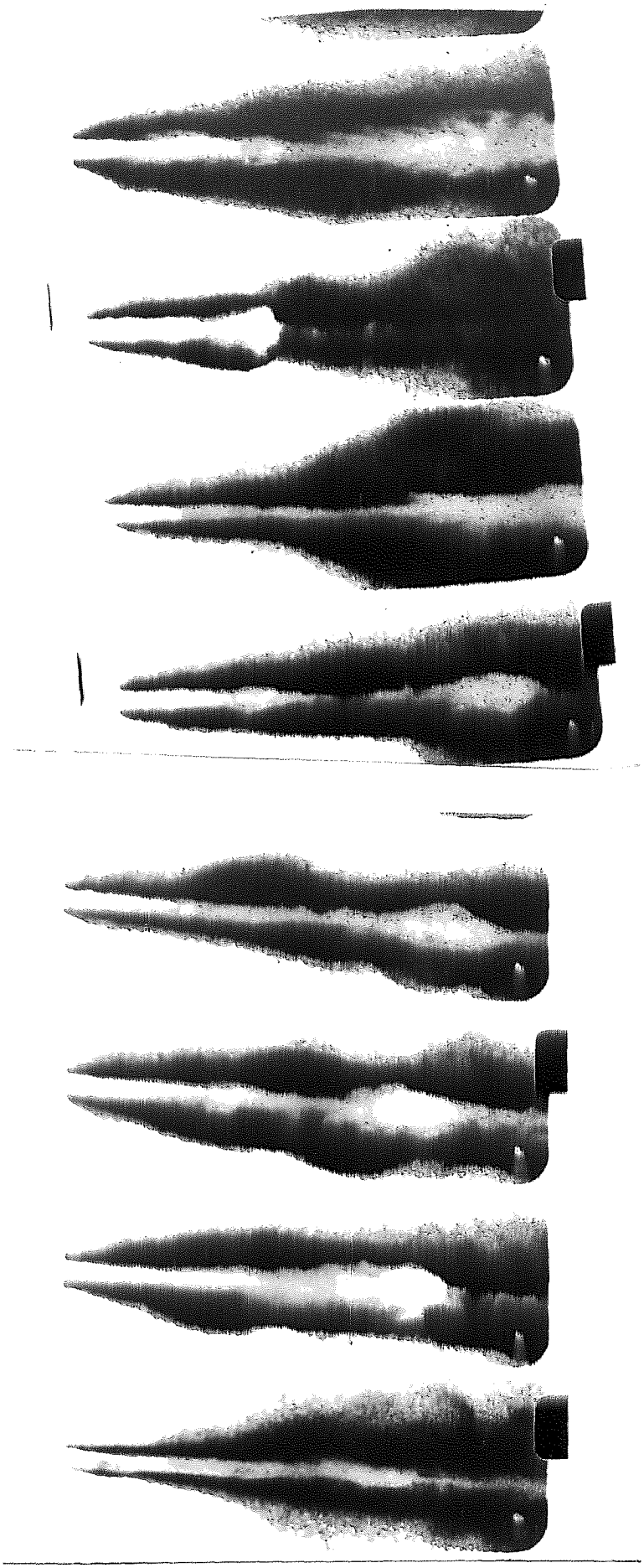

Fig. 5.77 Photograph showing jet enlargement and contraction for film #9 of Table 4.5

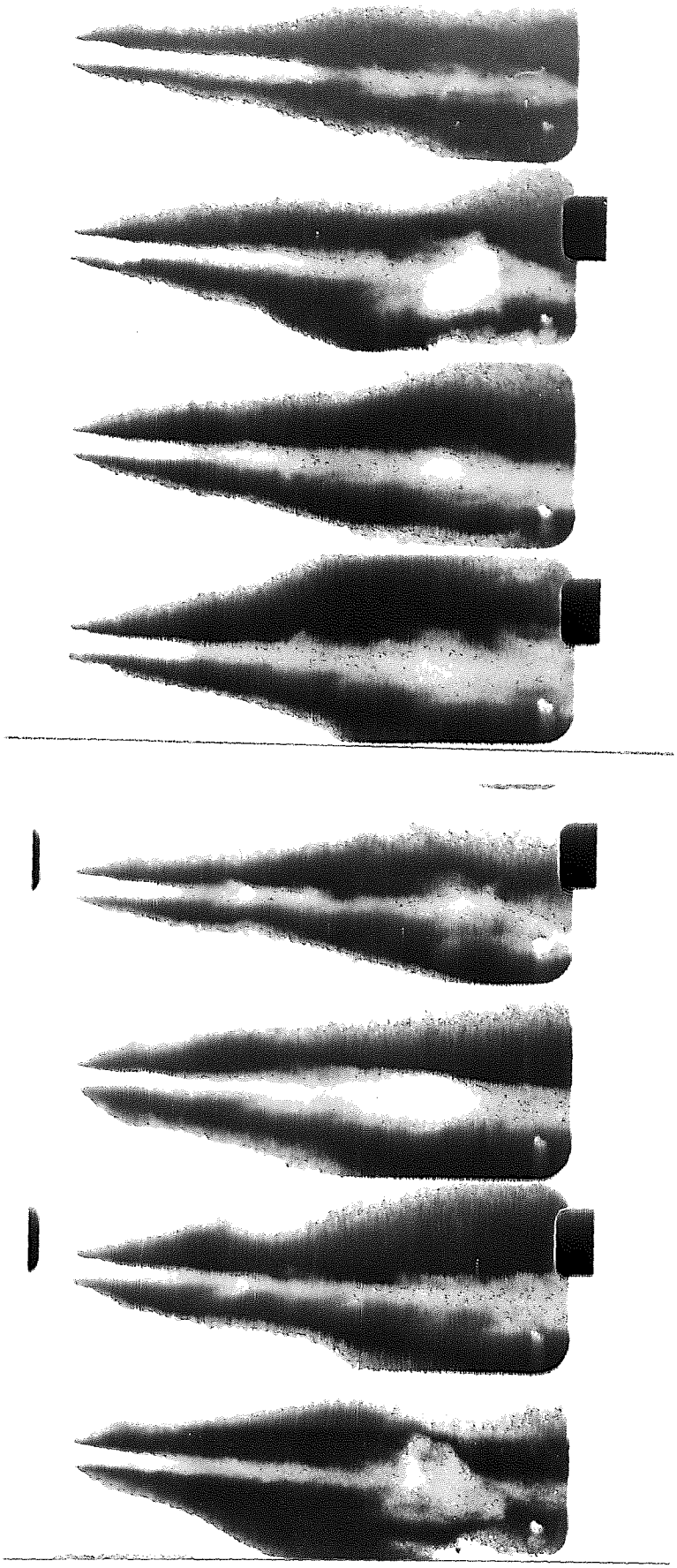

Fig. 5.78 Photograph showing jet enlargement and contraction for film #15 of Table 4.5

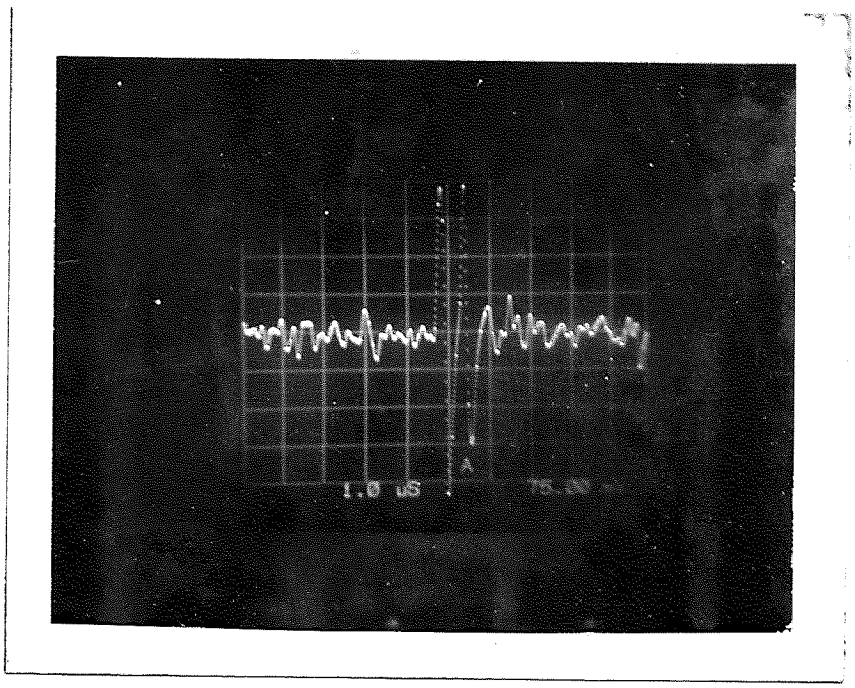

(a)

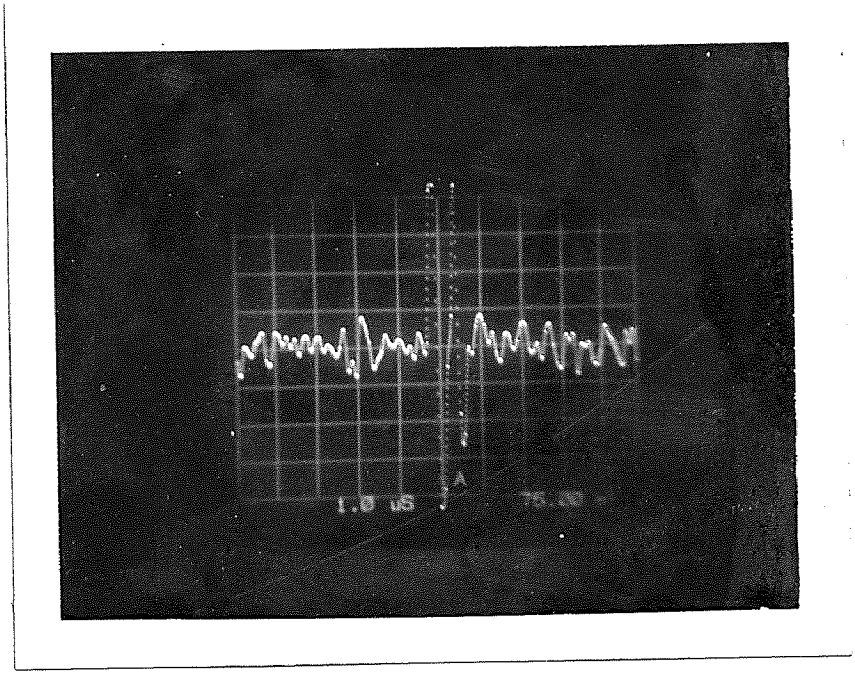

(b)

Fig. 5.79 Velocity plate for sap 7 at (a) x = 0.127 mm. u = 779 m/sec and (b) x = 114.3 mm, u = 739 m/sec

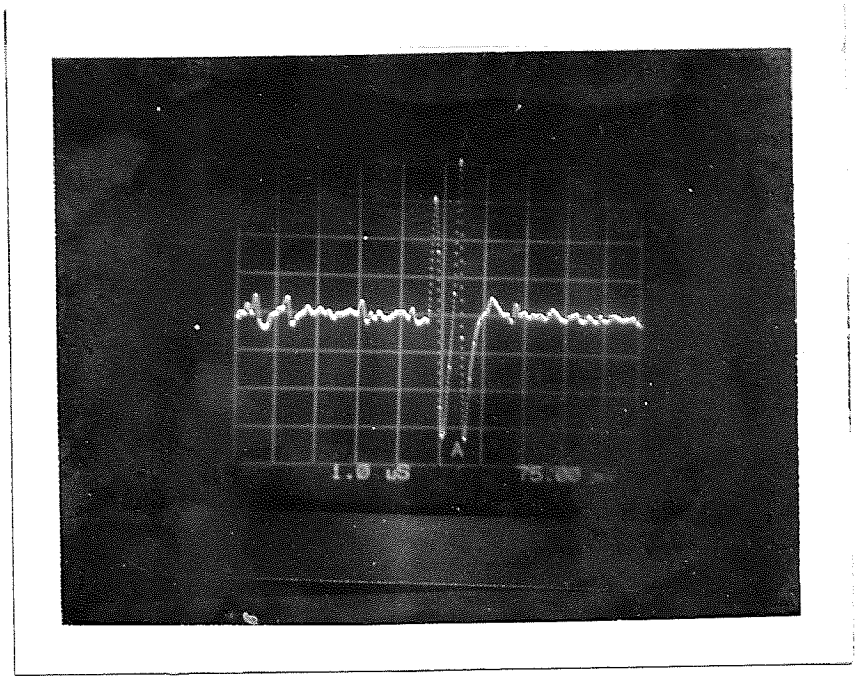

(a)

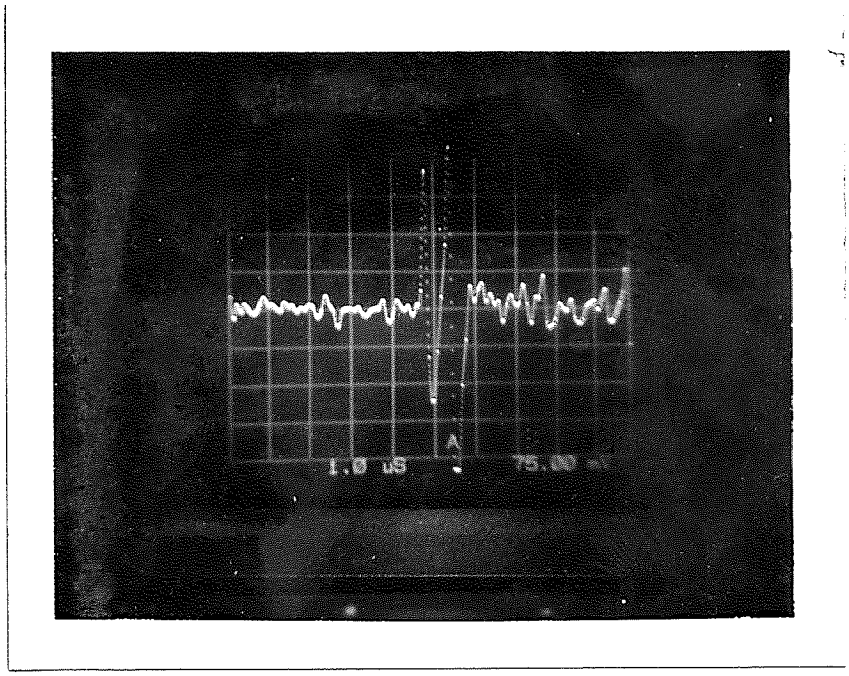

(b)

Fig. 5.80 Velocity plate for sap 10 at (a) x = 0.127 mm. u = 773 m/sec and (b) x= 114.3 mm, u=710 m/sec

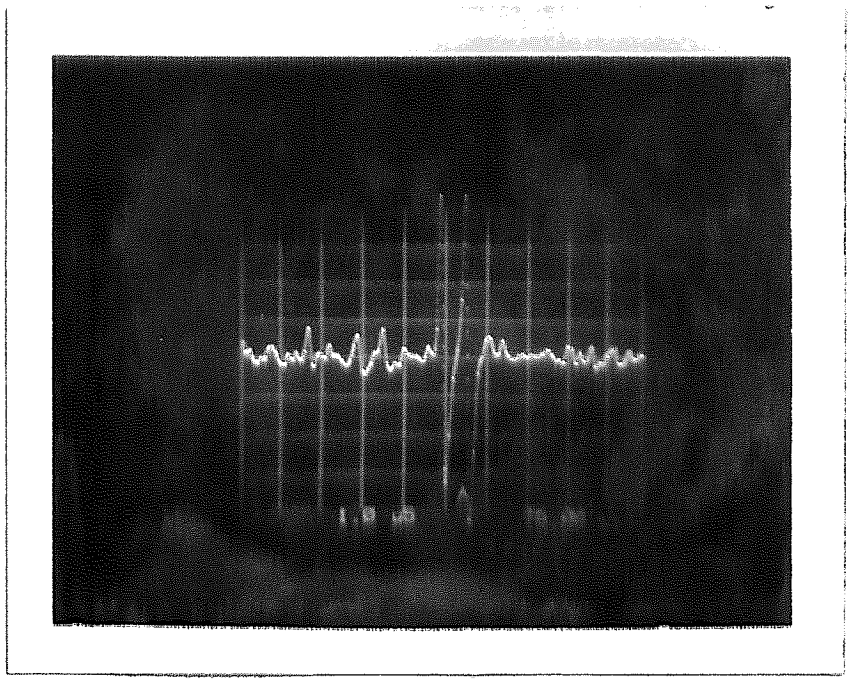

(a)

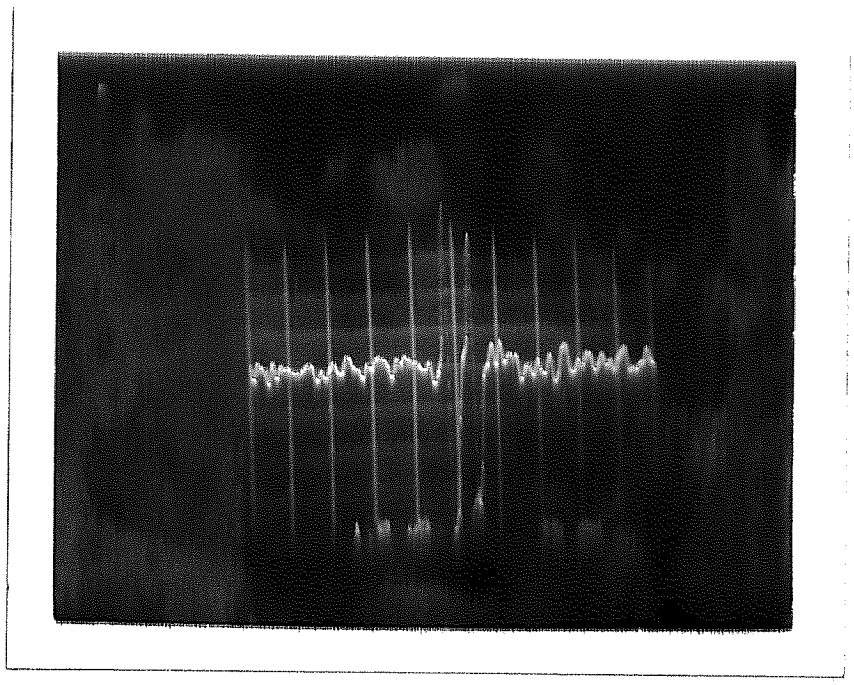

(b)

Fig. 5.81 Velocity plate for sap 12 at (a) x = 0.127 mm. u = 766 m/sec and (b) x=114.3 mm, u=701.2 m/sec

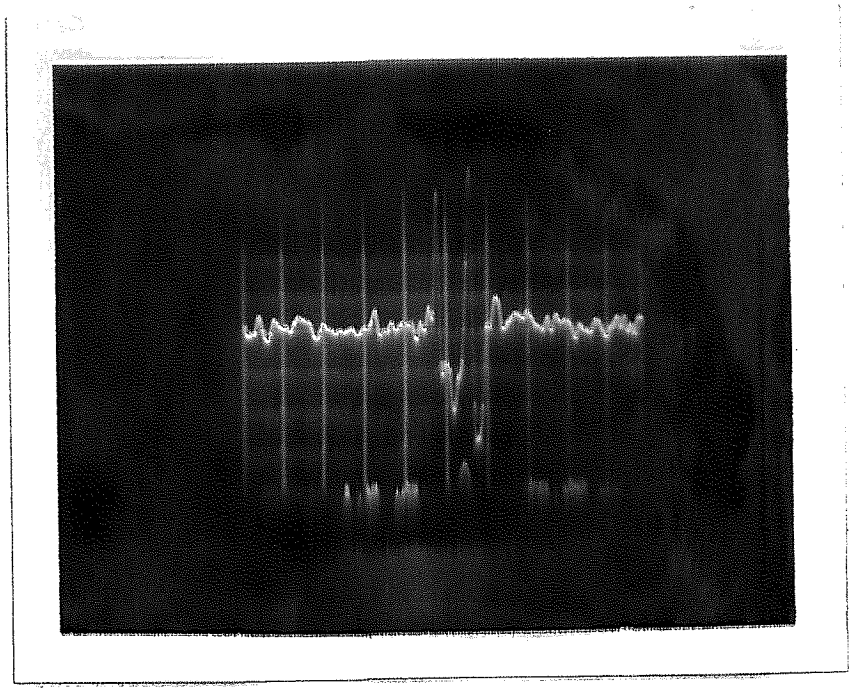

(a)

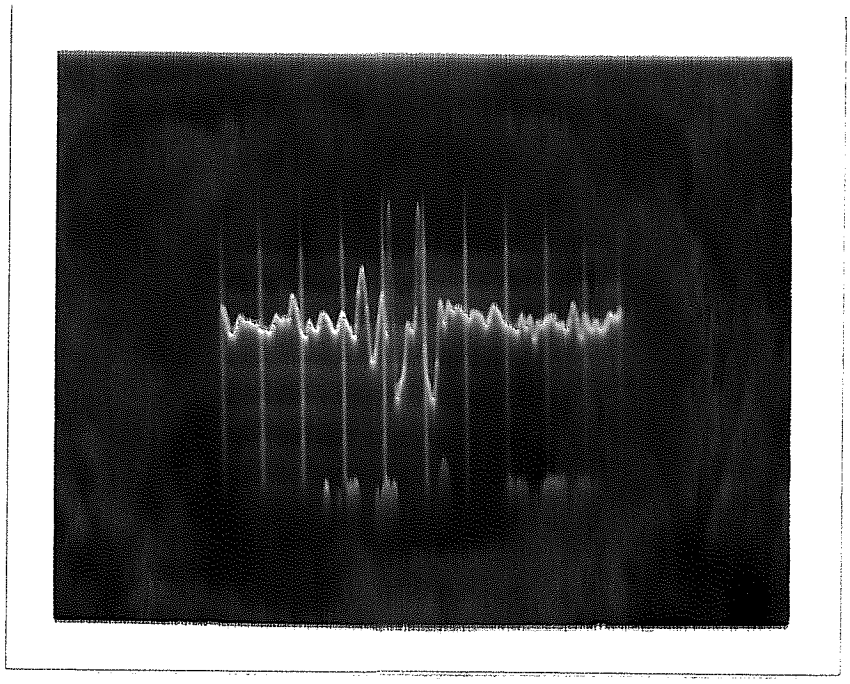

(b)

Fig. 5.82 Water velocity plate for Noz 7-30W at (a) X= 0.127mm, V = 763 m/sec and (b) X=38.1 mm, V=748 m/sec

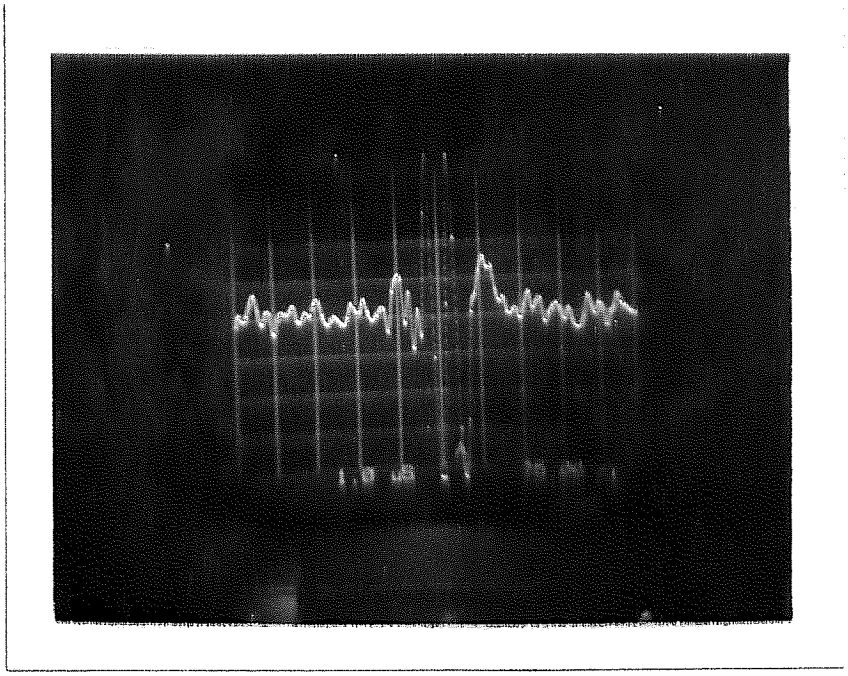

(a)

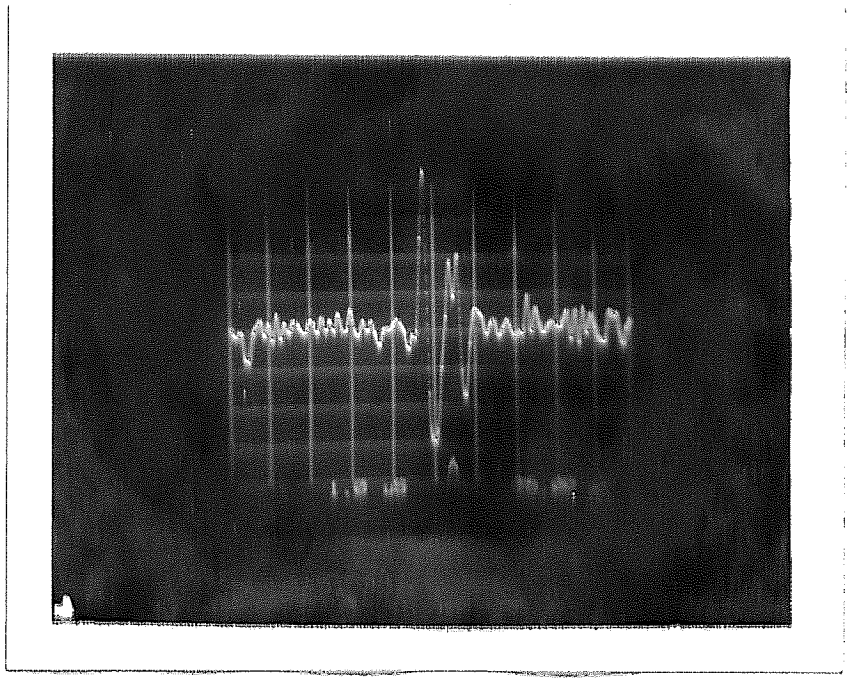

(b)

Fig. 5.83 Water velocity plate for Noz 7-43W at (a) X= 0.127mm, V = 768 m/sec and (b) X=38.1 mm, V=756 m/sec

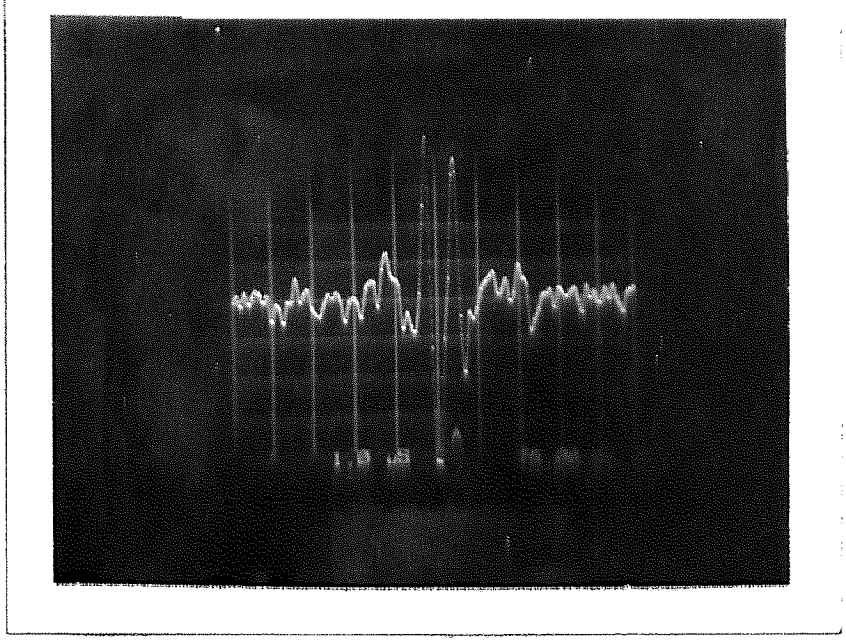

(a)

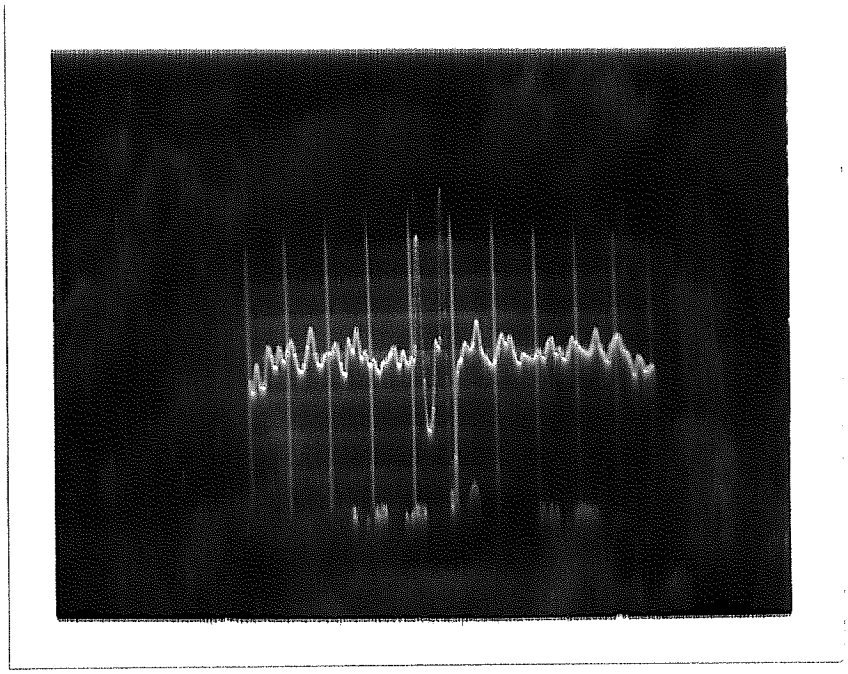

(b)

Fig. 5.84 Water velocity plate for Noz 7-63W at (a) X= 0.127mm, V = 770 m/sec and (b) X=38.1 mm, V=748 m/sec

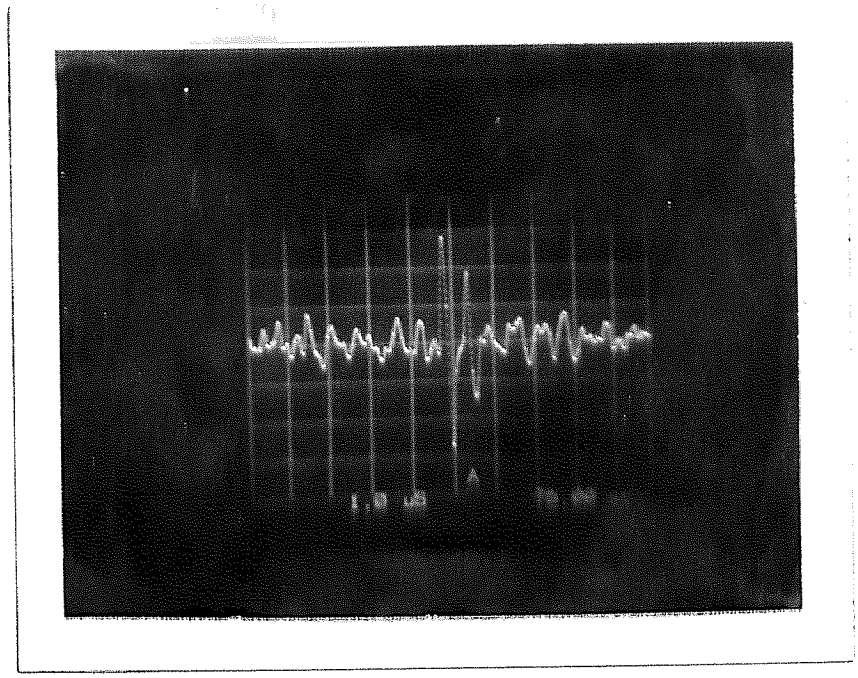

(a)

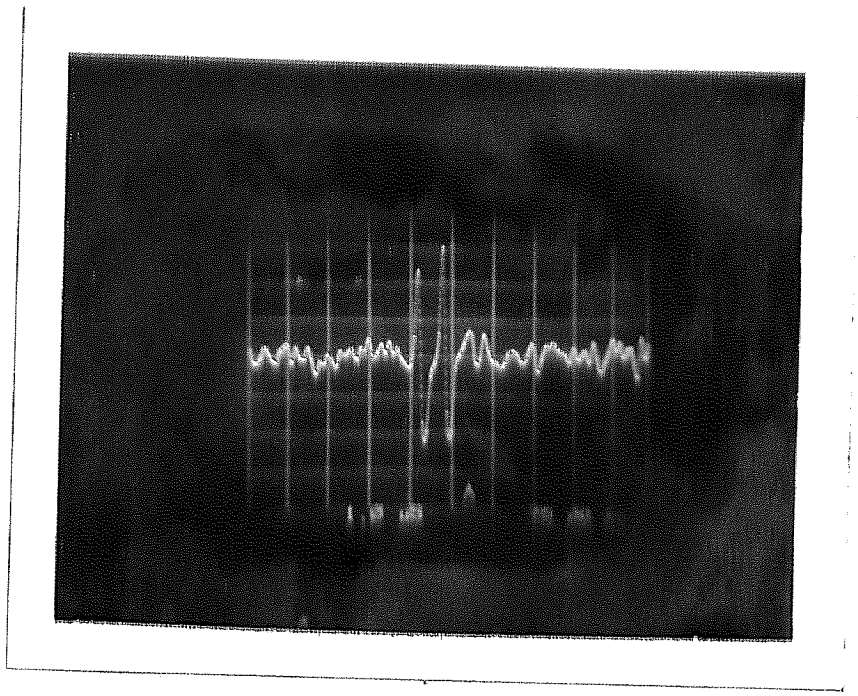

(b)

Fig. 5.85 Water velocity plate for Noz 10-30W at (a) X= 0.127mm, V = 759 m/sec and (b) for Noz 12-30W at X=0.127 mm, V= 756 m/sec

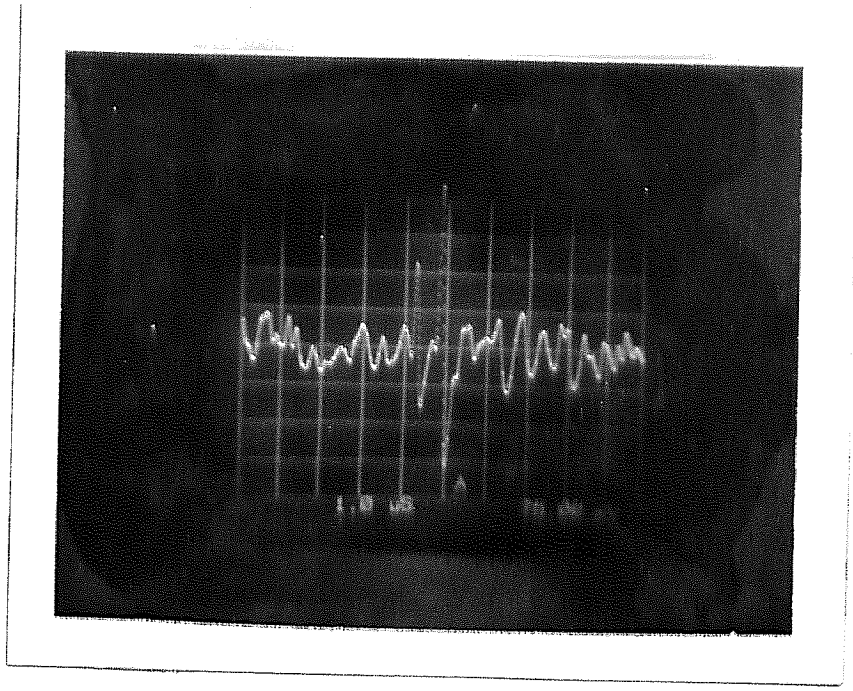

(a)

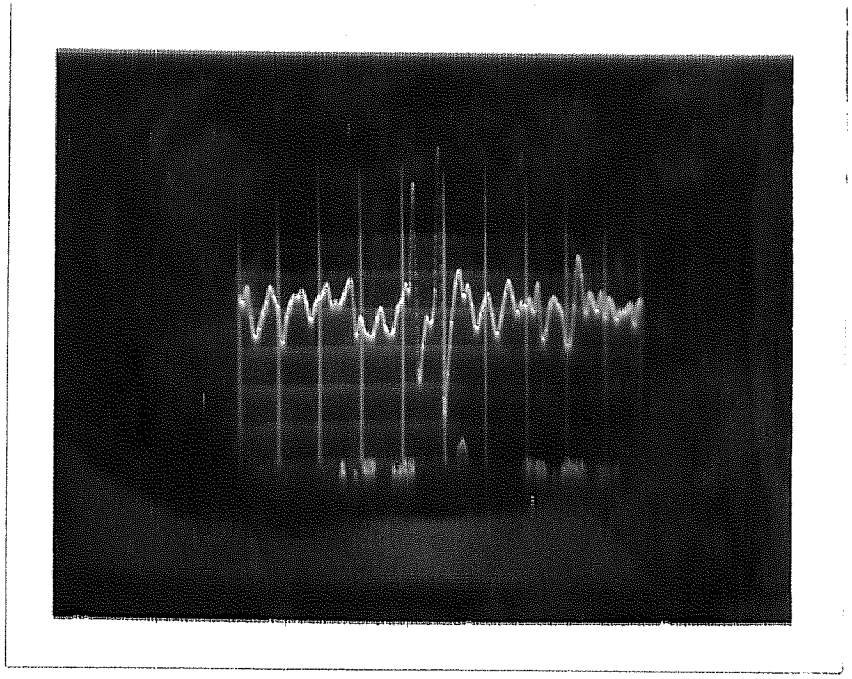

(b)

Fig. 5.86 Water velocity plate for Noz 10-63W at (a) X= 0.127mm, V = 660 m/sec and (b) for Noz 12-63W at X=0.127 mm, V= 608 m/sec

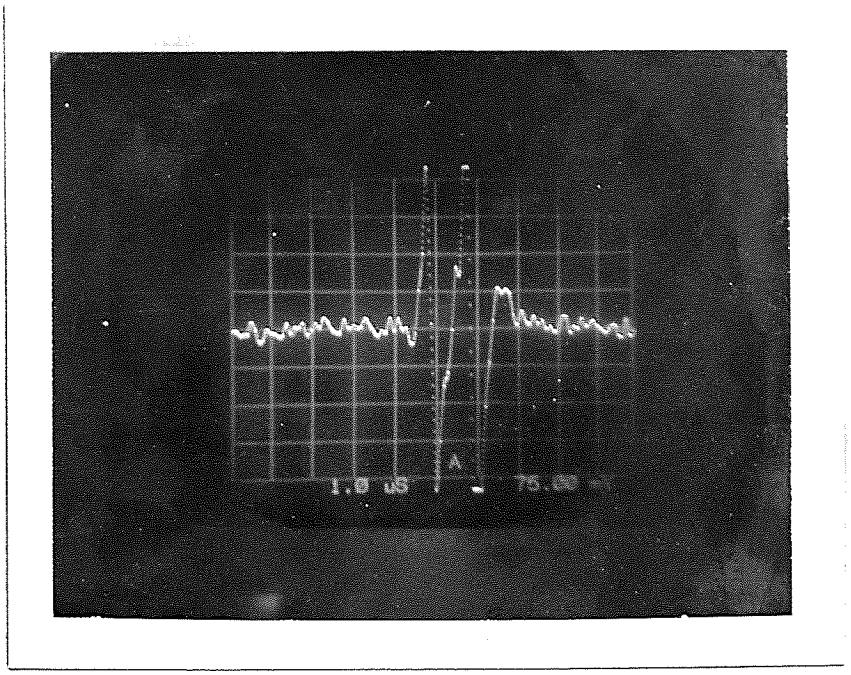

(a)

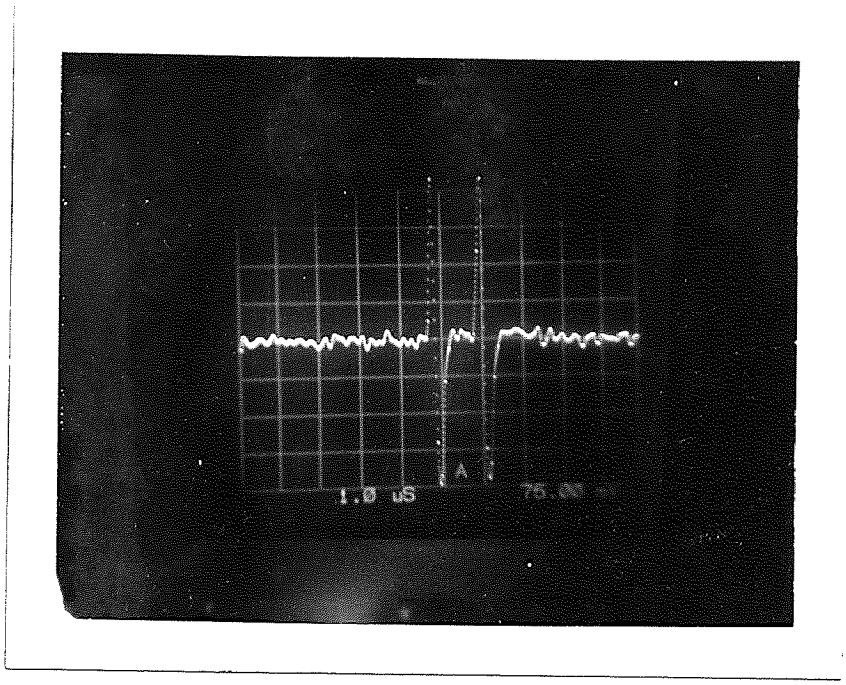

(b)

Fig. 5.87 Abrasive velocity plate for Noz 7-63A at (a) X= 0.127mm, W = 502 m/sec and (b) for Noz 7-43A at X=0.127 mm, W= 465 m/sec

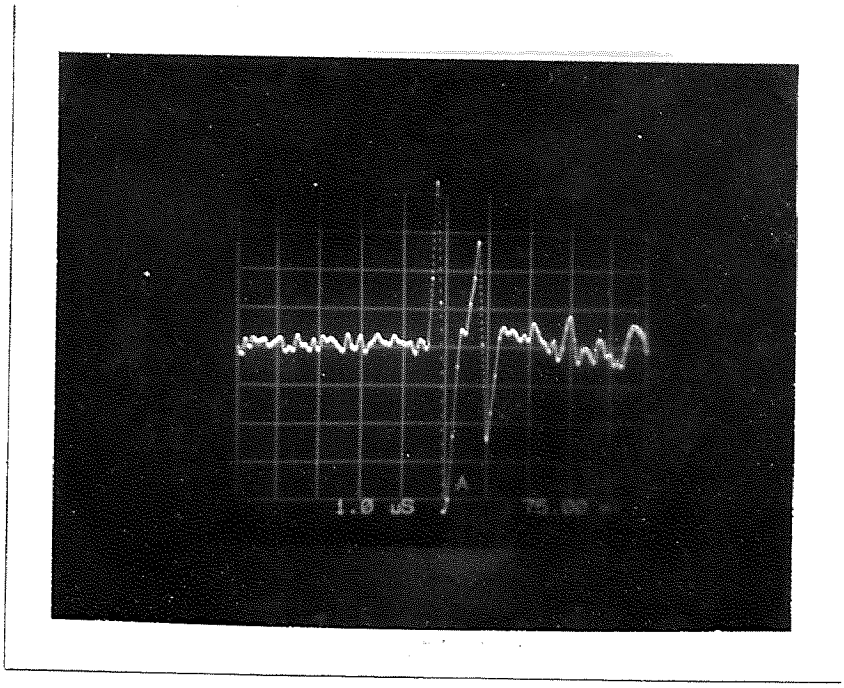

(a)

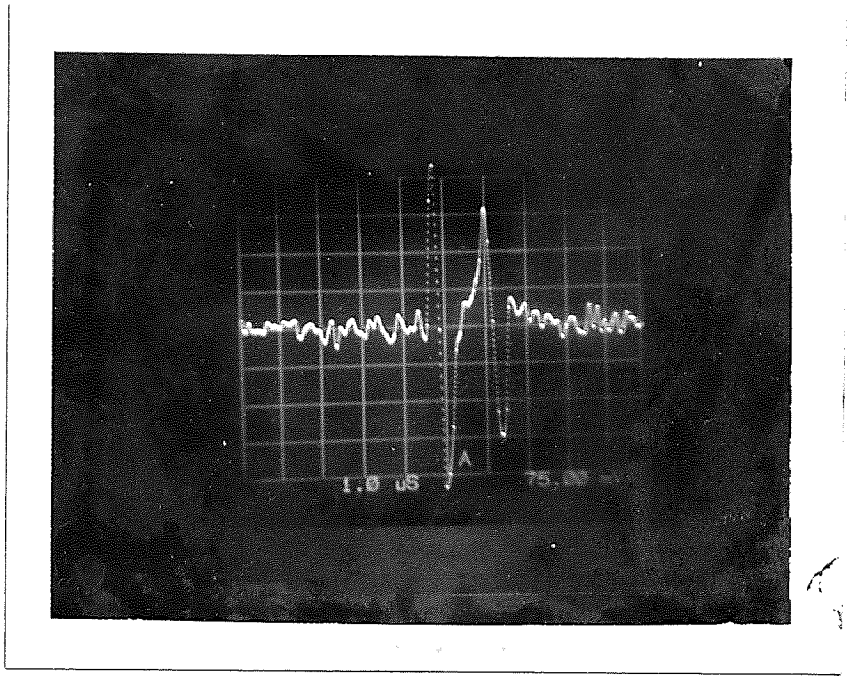

(b)

Fig. 5.88 Abrasive velocity plate for Noz 7-30A at (a) X= 0.127mm, W = 435 m/sec and (b) at X=38.1 mm, V= 395 m/sec

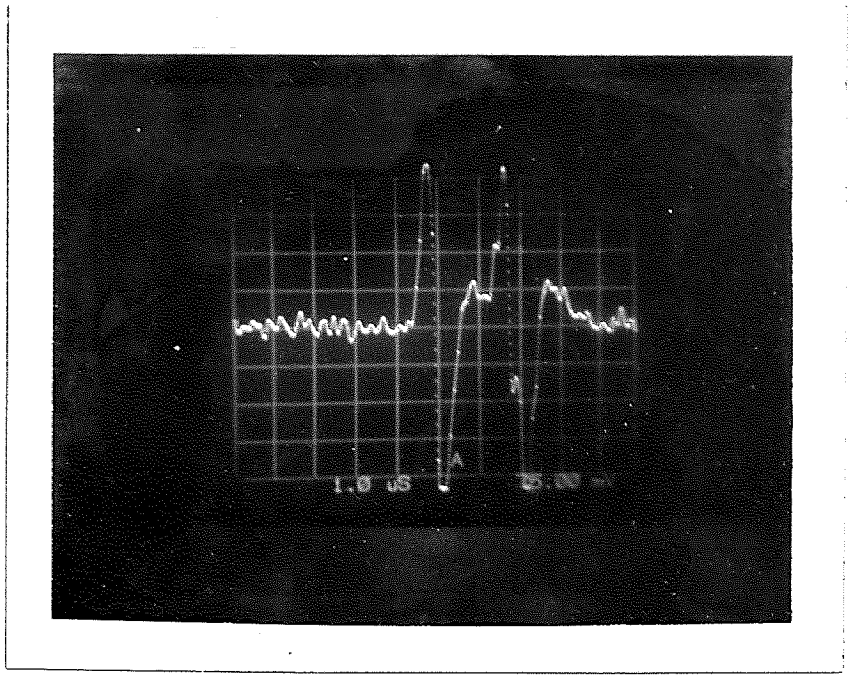

(a)

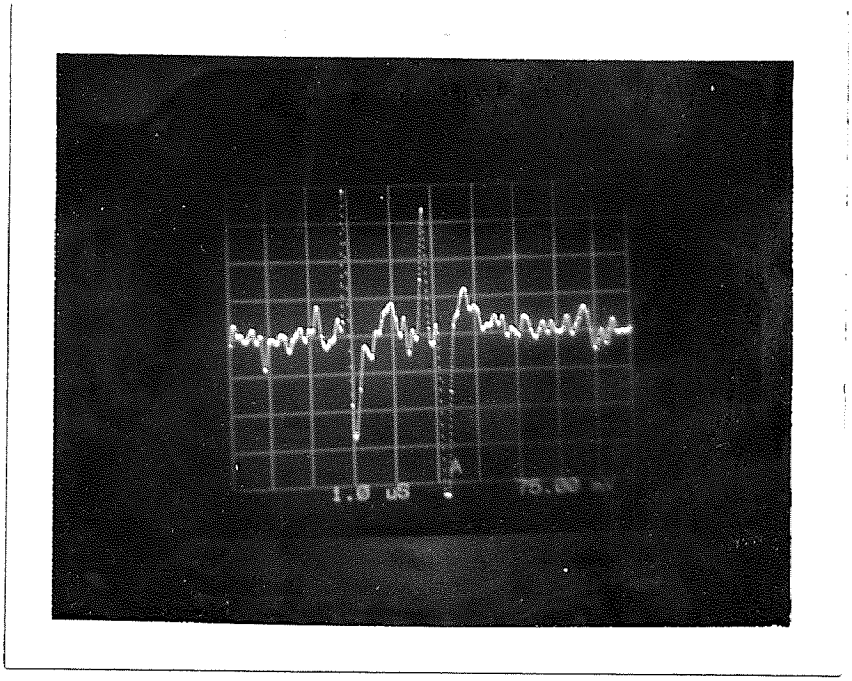

(b)

Fig. 5.89 Abrasive velocity plate for Noz 10-63A at (a) X= 0.127mm, W = 435 m/sec and (b) for Noz 12-63A at X=0.127 mm, W= 385 m/sec

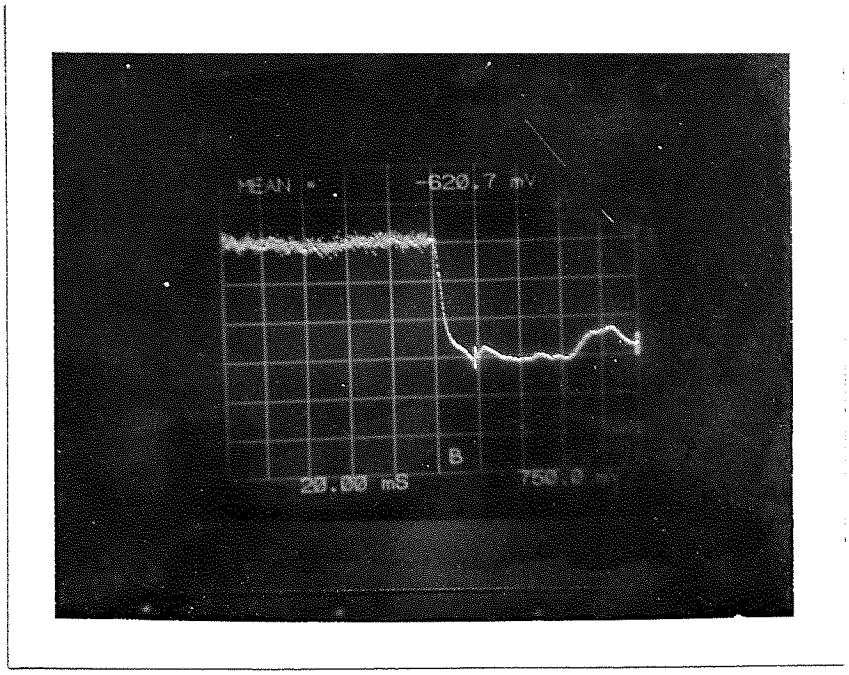

(a)

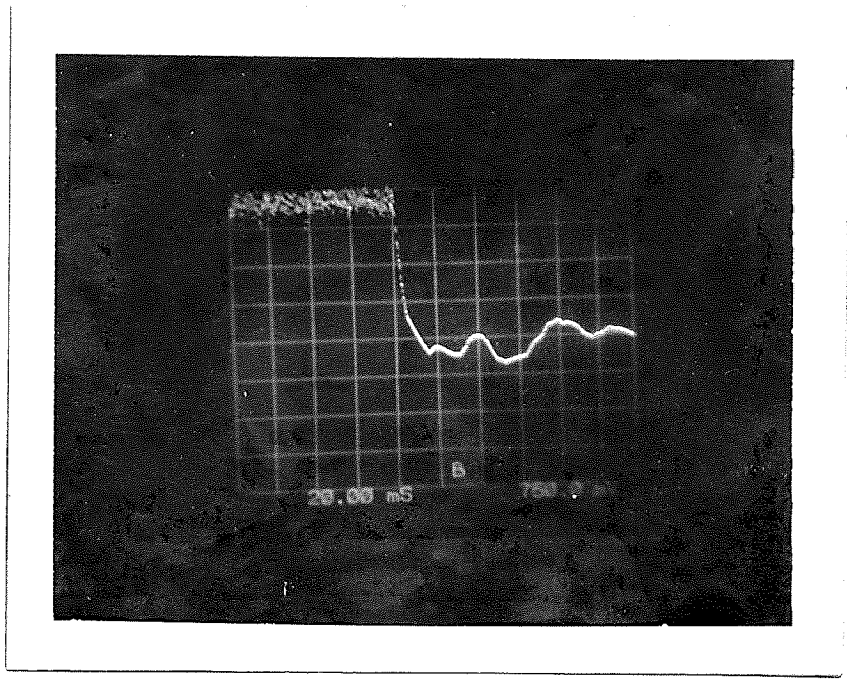

(b)

Fig. 5.90 Water force plate for (a) sap 7, f= 11.85 N and (b) sap 10, f=23.8 N at x= 25.4 mm.

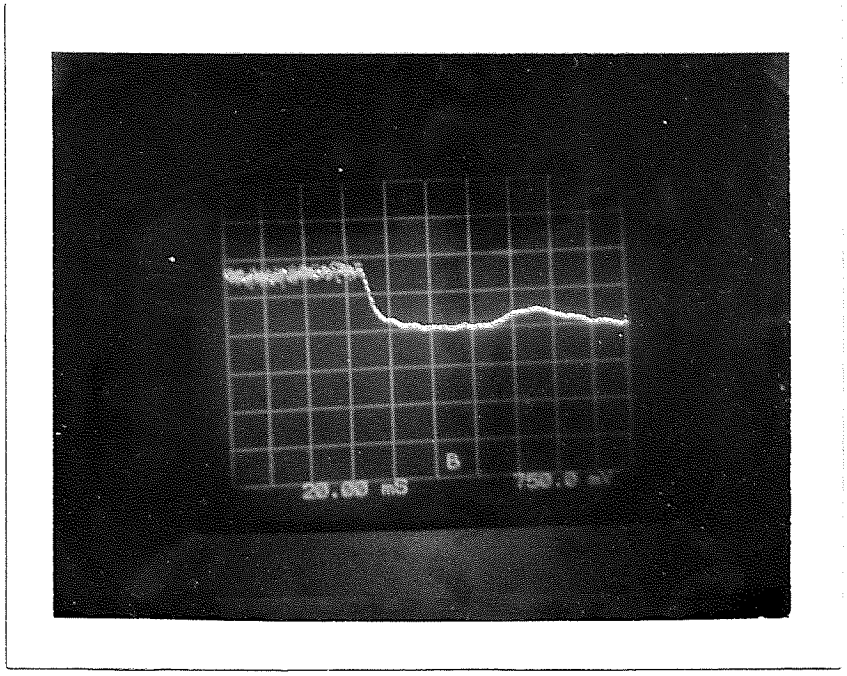

(a)

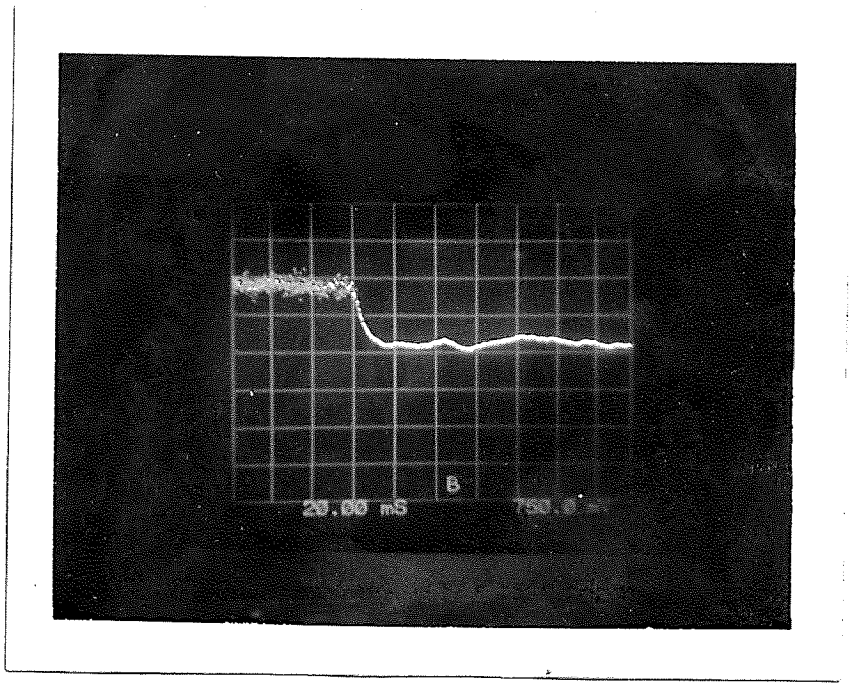

(b)

Fig. 5.91 Water force plate for (a) sap 12, f= 11.85 N at x= 25.4 mm(b) Noz 7-30W, F=10.83 N at X= 25.4 mm.

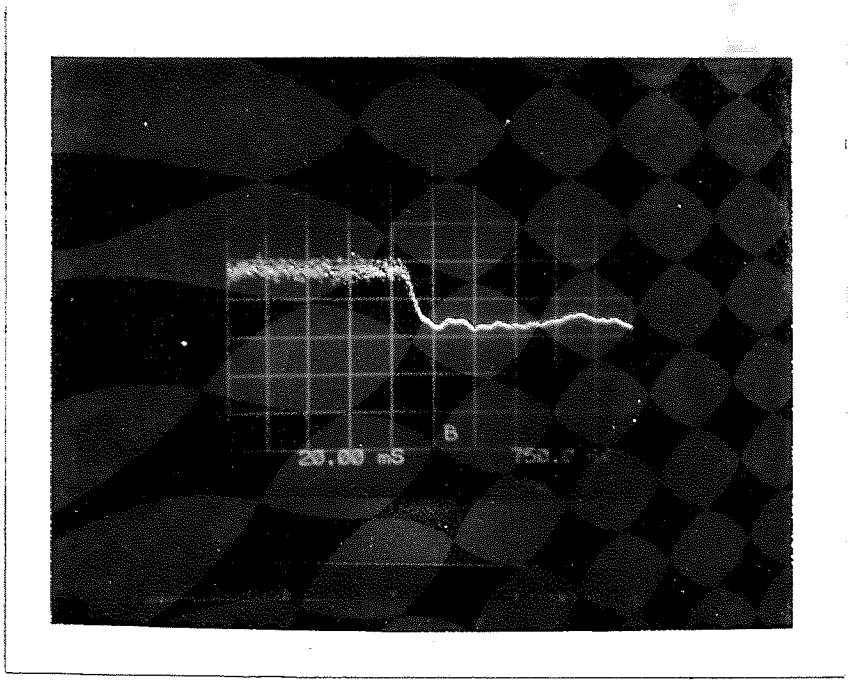

(a)

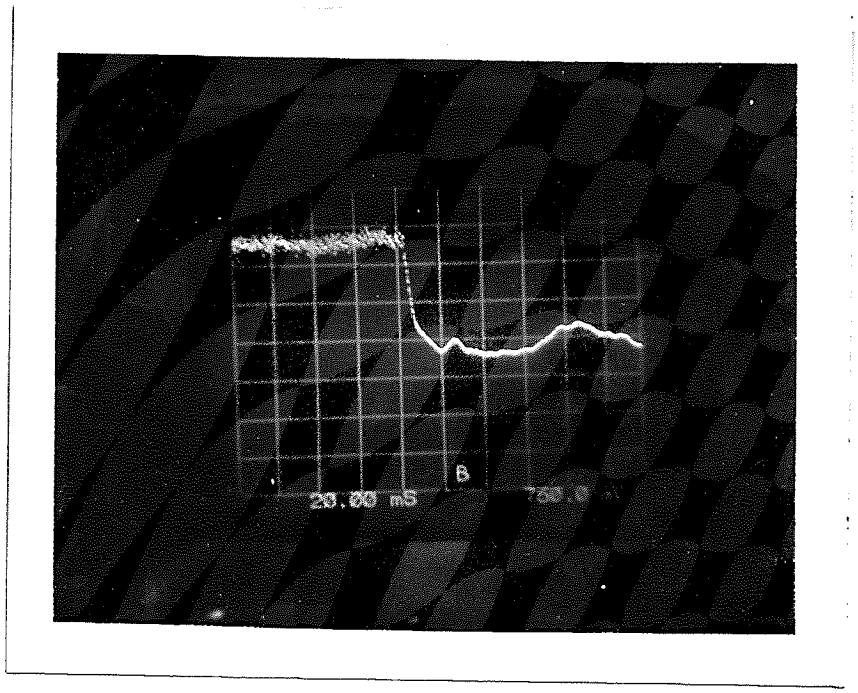

(b)

Fig. 5.92 Water force plate for (a) Noz 7-43W, F= 10.93 N and (b) Noz 7-63W, F=10.76 N at X= 25.4 mm.

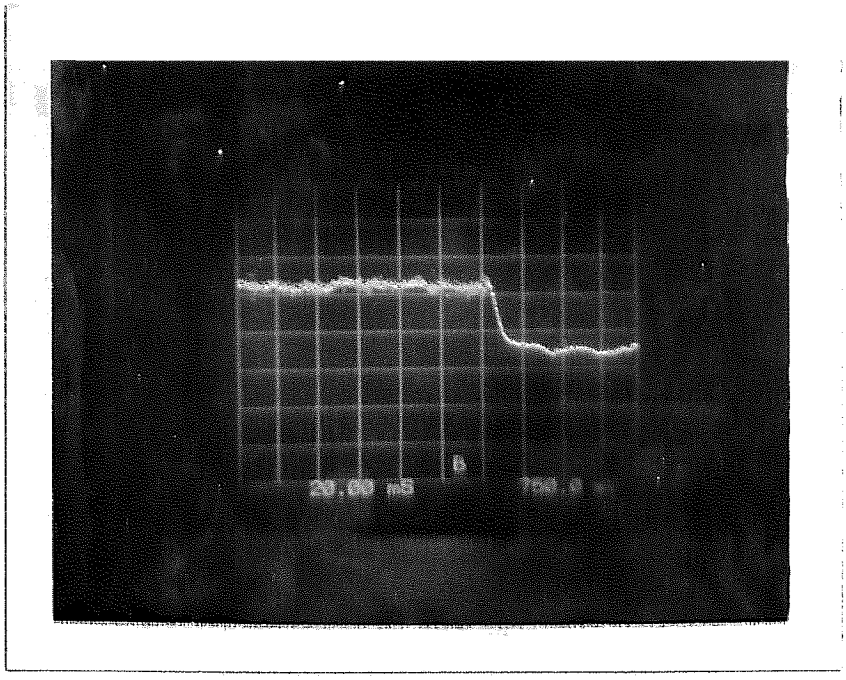

(a)

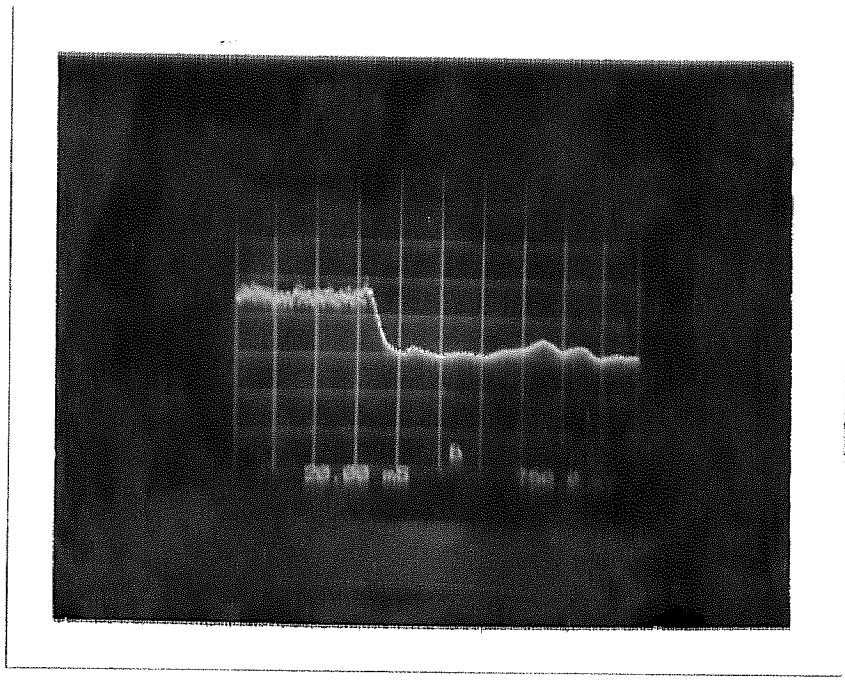

(b)

Fig. 5.93 Water force plate for (a) Noz 10-30W, F= 20.68 N and (b) Noz 12-30W, F=29.9 N at X= 25.4 mm.

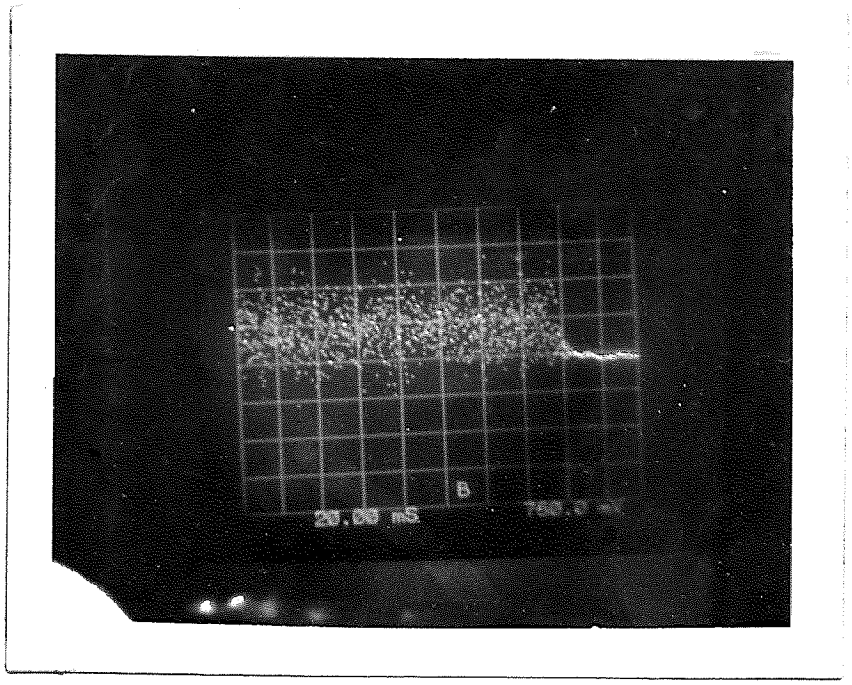

(a)

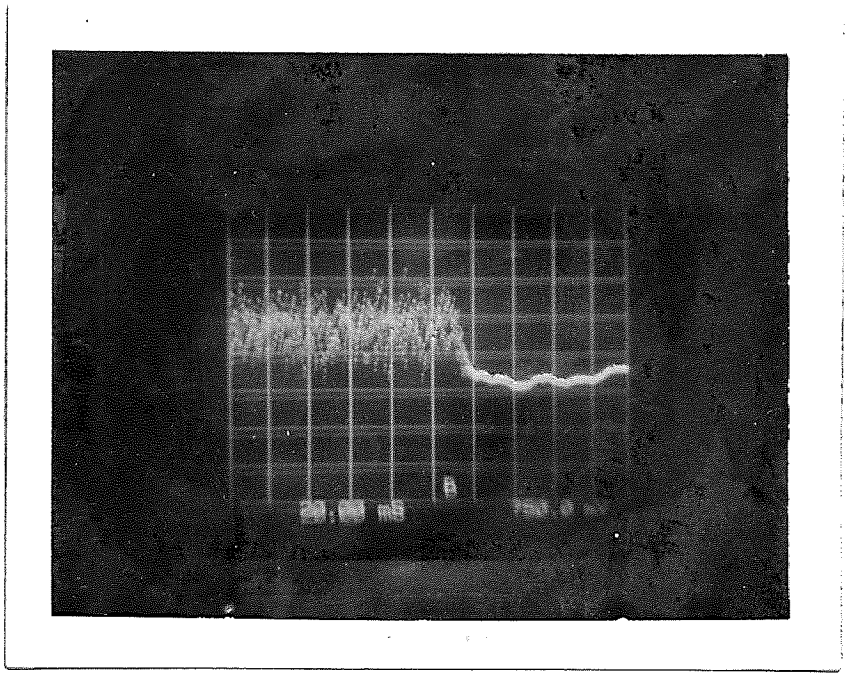

(b)

Fig. 5.94 Abrasive force plate for (a) Noz 7-30A, F'=7.48 N and (b) Noz 7-43A F'=8.84 N at X= 25.4 mm.

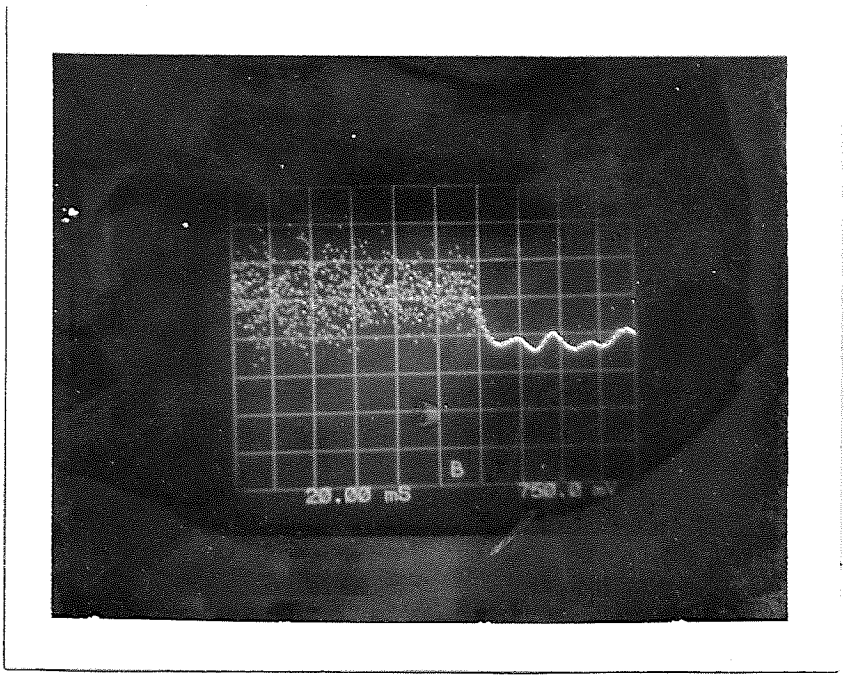

(a)

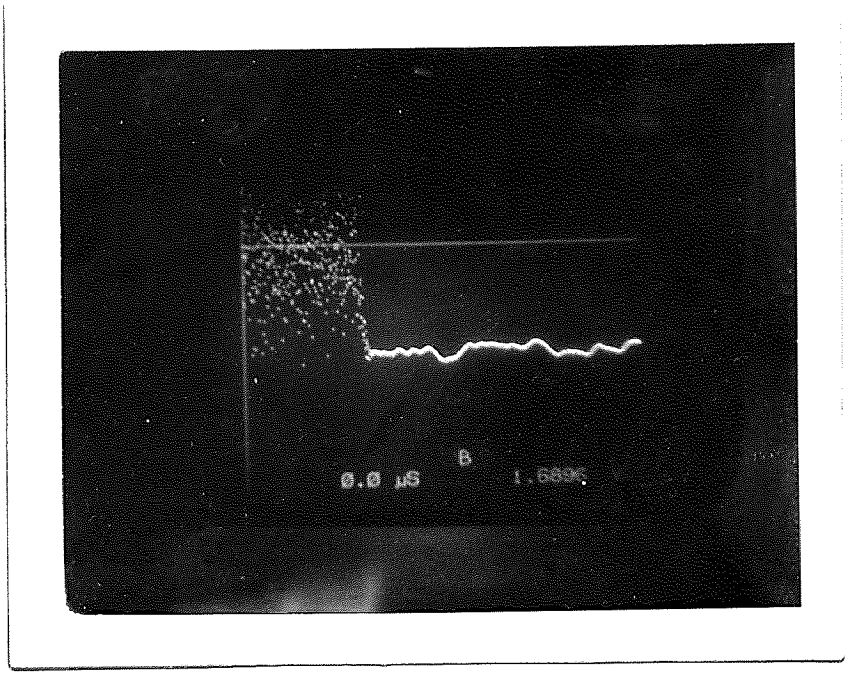

(b)

Fig. 5.95 Abrasive force plate for (a) Noz 7-63A, F'=10.08 N and (b) Noz 12-63A F'=26.08 N at X= 25.4 mm.

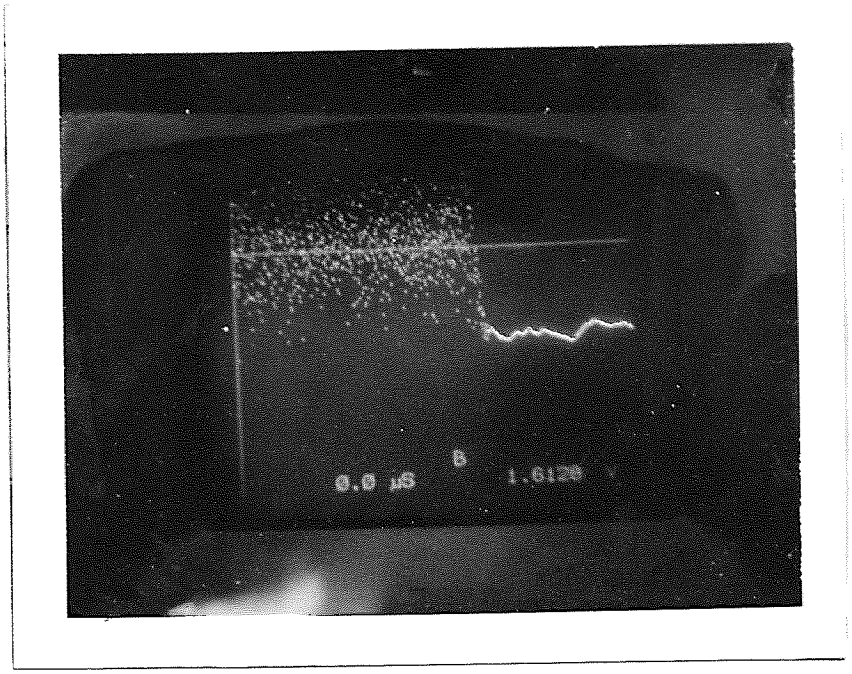

(a)

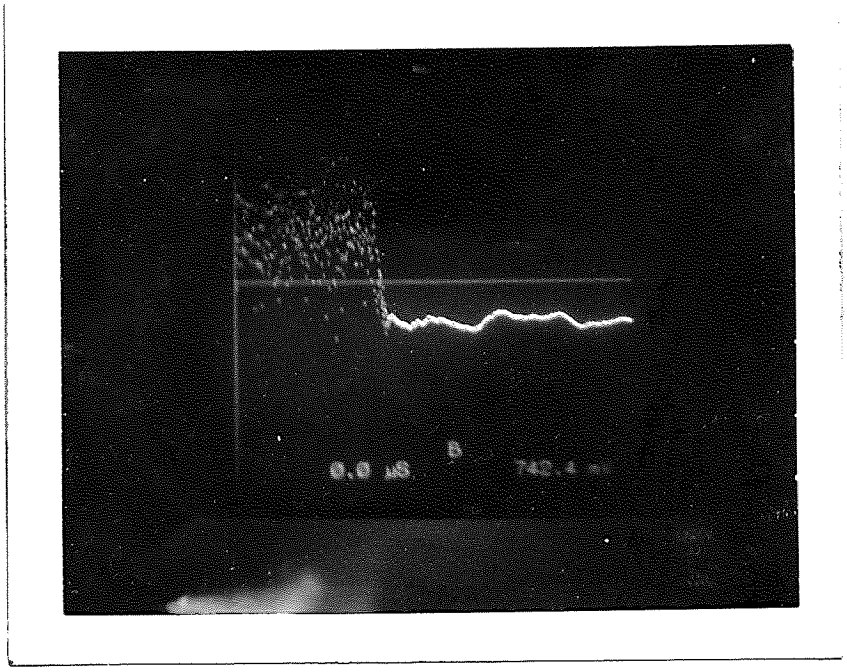

(b)

Fig. 5.96 Abrasive force plate for Noz 10-63A (a) F'=21.05 N at X=0.127 mm and (b) F'=19.23 N at X= 25.4 mm.

REFERENCES

1. Amano, R. S., and Neusen, K. F., "A Numerical and Experimental Investigation of High-Velocity Jets Impinging on Flat Plate", 6th Int. Symp. on Jet Cutting Tech., 6-8 April, 1982, PP.c3.107-c3.122.

2. Baker, C.R. and Selberg, B. P., "Waterjet Nozzle Performance Tests", 4th Int. Symp. on Jet Cutting Tech., April 12th-14th, 1978, PP. A.11-A.14.

3. Cady, W. G., "Piezoelectricity", Dover Publication, Vol. 1 & 2, 1964.

4. Curie, J. and Curie, P., Acad. Science (Paris), 91, 294 (1880); 91, 383 (1880).

5. Danon, H., Wolf S. M. and Hetsroni, G., "Numerical Calculations of Two-Phase Turbulent Round Jet", Int. J. Multiphase Flow, Vol. 3, 1977, PP. 223-234.

6. Davies, T. W., Metcalf, R. A. and Jackson, M. K., "The Anatomy and Impact Characteristics of Large Scale Waterjets", 5th Int. Symp. on Jet Cutting Tech., June 2nd-4th, 1980, PP. A2.15-A2.32.

7. Edwards, D. G., Smith, R. M. and Farmer, G., "The Coherence of Impulsive Water Jets", 9th Int. Symp. on Jet Cutting Tech., 6-8 April, 1982, PP. c4.123-c4.140.

8. Elghobashi, S., Abou-Arab, T., Rizk, M. and Mostafa, A., "Prediction of the Particle-Laden Jet with a Two-equation Turbulence Model", Int. J. Multiphase Flow, Vol. 10, 1984, PP. 697-710.

9. Fredrickson, "Principle and Applications of Rheology", Prentice Hall, 1964, PP. 214-221.

10. Gautschi, G. H., "Piezoelectric Multicomponent Force Transducers and Measuring System", Proc. Transducer, 1978, Conf., Wembly Conf. Canter, London, 1978.

11. Geskin, E. S., Chen, W. L., Chen, S. S., Hu, F., Khan, M. E. H. and Kim, S., "Investigation of Anatomy of An Abrasive Waterjet", 5th American Waterjet Conf., August 27-31, 1989, Toronto, Canada, PP. 217-230

12. Geskin, E. S., Chen, W. L., Chen, S. S., Hu, F., Khan, M. E. H., Kim, S. and Li, H. Y., "Study of the Abrasive Waterjet Cutting", Anual Research Bulletin of National Science Foundation, 1989.

13. Givler, R. C. and Mikatarian, R. R., "Numerical Simulation of Fluid Particle Flows: Geothermal Drilling Applications", Transactions of the ASME , J. of Fluid Engg., Vol. 109, Sept. 1987, PP. 324-331.

14. Gitis, M. B. and Shenker, A. A., "Pulsed Operation of a Flat Piezoelectric Transducer", Sov. Phys. Acoust., 27(6), 1982.

15. Gouesbet, G., Desjonqueres, P. and Berlemont, A., "Eulerian and Lagrangian Approaches to Turbulent Dispersion of Particle", Seminarie Int. Transient Phenomena in Multiphase Flow, May 1987, Int. Center for Heat and Mass Transfer, Dubrounic.

16. Hashish, M., "The Application of Abrasive Jets to Concrete Cutting", Jet Cutting Tech., Apr. 1982.

17. Hashish, M., "Steel Cutting with Abrasive Waterjets", Jet Cutting Tech., Apr. 1982.

18. Hishida, K., Nakano, H. and Maeda, M., "Turbulent Flow Characteristics of Liquid-Solid Particle Confined Jet", Int. Conf. on Mechanics of Two-Phase Flows, June 12-15, 1989, National Taiwan Univ., Taipei, Taiwan, ROC, PP. 207-214.

19. Hurlburt, G. H. and Cheung, J. B., "Submerged Waterjet Cutting of Concrete and Granite", Proc. 3rd Int. Symp. on Jet Cutting Tech., May 1976, Chicago, BHRA Fluid Engg., 1976, Cranfield, U.K.

20. Janakiram, K. S. and Rao, S. B. C., "Studies of the Characteristics of Flow and Erosion due to Plain and Cavijet Impingement", Proc. 5th Int. Conf. on Ersion by Solid and Liquid Impact, PP. 70.1-70.9.

21. Kesavan, S. K., Reddy, N. P. and Ardakani, S. Y., "Measurement of Dynamic Impact Thrust Exerted by High- Frequency Liquid Jet", Experimental Technical, Sep. 1985.

22. Lading, L., "Estimating Time and Time-Lag in Time-of-Flight Velocimetry", Applied Optics, 15 Nov. 1983, Vol. 22, No. 22.

23. Leach, S. J. and Walker, G. L., "The Application of High Speed Jets to Cutting", Proc. Roy. Soc., 260A, PP. 295-308, Organized by Royal Society, London, (1966).

24. Li, H. Y., "Investigation of Forces Developed in the Course of the Waterjet-Workpiece Interaction", MS Thesis, 1988, NJIT.

25. Loh, Y. and Tan, H., "A New Method for Processing the Signals from a Laser-Dual Focus Velocimeter", The Inst. of Physics, 1981.

26. Mason, W. P., "Piezoelectricity, Its History and Applications", J. Acoust. Soc. Amer., 70(6), 1981, PP. 1561-1560.

27. Melville, W. K. and Brag, K. N. C., "A Model of Two-Phase Turbulent Jet", Int. J. Heat Mass Transfer, Vol. 22, 1979, PP. 647-656.

28. Oliver, D. R., "The Expansion/Contraction Behavior of Laminar Liquid Jets", Can. J. of Chem. Engg., Apr. 1966, PP. 100-107.

29. Parathasarathy, R. N. and Faeth, G. M., "Structure of Particle-Laden Turbulent Waterjets in Still Water", Int. J. Multiphase Flow, Vol. 13, 1987, PP. 699-716.

30. Schneider, W. "Flow Induced by Jets and Plumes", J. Fluid Mech., 1981, Vol. 108, PP. 55-65.

31. Schneider, W., "Decay of Momentum Flux in Submerged Jets", J. Fluid Mech., 1985, Vol. 154, PP. 91-110.

32. Selbach, H., Lewin, A. C. and Goding, A. C., "Advancements in Laser Transit Anemometry using Fiber Probes", L.I.A. Vol. 63 ICALEO (1987).

33. Semerchan, A. A., Vereshchagin, V. F., Filler, F. M. and Kuzin, N. N., "Distribution of Momentum in a Continuous Liquid Jet of Supersonic Velocity", Sov. Phys.- Tech. Phys., Vol. 3, No. 9, Sep. 1958, PP. 1984-1903.

34. Shnitser, P. I., "Analysis of Oscilliations in an Open Acoustic Resonator with Reflective Piezoelectric Transducers", Sov. Phys. Acoust., 26(3), 1980.

35. Shuen, J. S., Chen, L-D and Faeth, G. M., "Evaluation of a Stochastic Model of Particle Dispersion in a Turbulent Round Jet", AIChE J., Vol. 29, 1983, PP. 167-170.

36. Swanson, R. K., Kilman, M., Cerwin, S. and Tarver, W., "Study of Particle Velocities in Water Driven Abrasive Jet Cutting", Proc. of 4th U.S. Water Jet Conf., 1987.

37. Szymczak, M., Tavoularis, S., Fahim, A. and Vijay, M. M., "Flow Visualization of High Speed Waterjets", Proc. of the 4th U.S. Water Jet Conf., Aug. 26-28, 1987.

38. Twigg, J. W., "High Pressure Water Jetting Techniques", Corrosion Prevention and Control, Apr. 1982.

39. Wernwt, M. P. and Edwards, R. V., "Implementation of a New Type of Time-of-Flight Laser Anemometer", Applied Optics, Vol. 25, No. 5, March 1986.

40. Wu, "Ben", W. Z., Summers, D. A., and Tzeng, M. J., "Dynamic Characteristics of Waterjets Generated From Oscillating Systems", Proc. of the 4th U.S. Water Jet Conf., Aug. 26-28, 1987.

41. Yanaida, K. and Ohashi, A., "Flow Characteristics of Water Jets in Air", 4th Int. Symp. on Jet Cutting Tech., April 12th-14th, 1978, PP. A3.39-A3.54.

42. Yanaida, K. and Ohashi, A., "Flow Characteristics of Water Jets in Air", 5th Int. Symp. on Jet Cutting Tech., June 2nd-4th, 1980.

43. Zauner, E., "Visualization of the Viscous Flow Induced by a Round Jet", J. Fluid Mech., March 1985, Vol. 154, PP. 111-119.